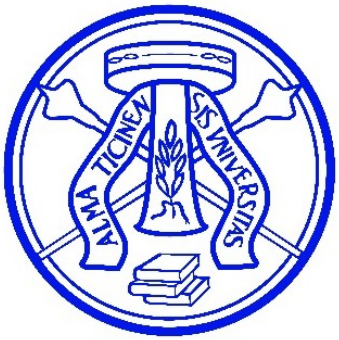

UNIVERSITÀ DEGLI STUDI DI PAVIA

DOTTORATO IN SCIENZE CHIMICHE E FARMACEUTICHE E INNOVAZIONE INDUSTRIALE

(XXXIV Ciclo)

Coordinatore: Chiar.mo Prof. Giorgio Colombo

THE KEY ROLE OF HIGH-PERFORMANCE ANODE MATERIALS IN LI- AND NA-ION BATTERIES

Tesi di Dottorato di
Daniele Spada

AA 2020/2021

Tutor
Chiar.ma Prof.ssa Marcella Bini

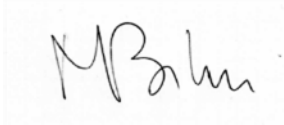

“Lithium-ion batteries have revolutionised our lives since they first entered the market in 1991. They have laid the foundation of a wireless, fossil fuel-free society, and are of the greatest benefit to humankind.”

The royal swedish academy of Sciences, press release: The Nobel Prize in Chemistry 2019

Riassunto

In questa tesi di dottorato, diversi materiali anodici per batterie agli ioni Li e Na con caratteristiche complementari sono stati studiati per avere una gamma di possibili candidati come materiali per batterie di nuova generazione. L'ossido ternario $ZnFe_2O_4$ ad alta densità di energia ha una reazione complessa e irreversibile con il Li, che è stata studiata con tecniche elettrochimiche e diffrazione operando, per comprenderne la ciclabilità. Alligazione e conversione-alligazione di Sn e SnO_x sono altre reazioni elettrochimiche ad alta densità di energia, che possono essere sfruttate sia in batterie al Li che al Na. Sono stati ottenuti risultati promettenti (anche a correnti elevate) da un elettrodo composito self-standing elettrospinnato. Alte densità di potenza sono la caratteristica prevalente di $FeNb_{11}O_{29}$, le cui sorprendenti caratteristiche cinetiche sono state studiate insieme al meccanismo di reazione, grazie a diffrazione operando e spettroscopia Raman in situ.

Abstract

In this PhD thesis, different anode materials for Li- and Na-ion batteries with complementary features were investigated to obtain a wide spectrum of candidate materials for next-generation batteries. The ternary transition metal oxide $ZnFe_2O_4$ offers high energy density, and its complex and irreversible reaction with Li was studied with electrochemical techniques and operando X-ray diffraction in order to understand the cycling behaviour of the material. Alloying and conversion-alloying of tin and tin oxides are also high energy density electrochemical reactions, that can be exploited in both Li- and Na-ion batteries. Promising results were obtained from an electrospun self-standing tin/carbon composite with enhanced rate capability. Higher power densities are shown by complex niobium oxides such as $FeNb_{11}O_{29}$, whose enhanced kinetic features were studied alongside the reaction mechanism, that was unravelled with operando X-ray diffraction and in situ Raman spectroscopy.

List of publications

The following list includes all the works published during the PhD. The contribution of the PhD student to each publication will be listed in the form of CRediT statement.

1. Spada D., Mozzati M. C., Albini B., Galinetto P., Quinzeni I., Capsoni D., Bini M. "Deepening the shear structure $FeNb_{11}O_{29}$: influence of polymorphism and doping on structural, spectroscopic and magnetic properties." Dalton Transactions 47.44 (2018): 15816-15826. **DOI: 10.1039/C8DT02896F** (First published on October 12th, 2018)

   Methodology; Formal analysis; Investigation; Writing - Original Draft; Visualization

2. Spada D., Quinzeni I., Bini M. "Orthorhombic and monoclinic modifications of $FeNb_{11}O_{29}$, as promising anode materials for lithium batteries: Relationships between pseudocapacitive behaviour and structure." *Electrochimica Acta* 296 (2019): 938-944. **DOI: 10.1016/j.electacta.2018.11.047** (First published on November 13th, 2018)

   Methodology; Formal analysis; Investigation; Writing - Original Draft; Visualization

3. Galinetto P., Spada D., Mozzati M. C., Albini B., Bini M. "Effects of reaction atmosphere on physico-chemical properties of V-doped $FeNb_{11}O_{29}$." Optical Materials 92 (2019): 373-378. **DOI: 10.1016/j.optmat.2019.04.035** (First published on May 8th, 2019)

   Methodology; Formal analysis; Investigation; Writing - Original Draft; Visualization

4. Bini M., Quinzeni I., Spada D. "The Doping of $FeNb_{11}O_{29}$ as a Way to Improve Its Electrochemical Performances." *ChemistrySelect* 4.19 (2019): 5656-5661. **DOI: 10.1002/slct.201901182** (First published on May 21st, 2019)

   Methodology; Formal analysis; Investigation; Writing - Original Draft; Visualization

5. Nuti M., Spada D, Quinzeni I., Capelli S., Albini B., Galinetto P., Bini M. "From tunnel NMO to layered polymorphs oxides for sodium ion batteries." SN Applied Sciences 2.11 (2020): 1-13. **DOI: 10.1007/s42452-020-03607-z** (First published on October 26th, 2020)

   Formal analysis; Writing – Original Draft

6. Spada D., Davino S., Girella A., Milanese C., Bini M. "Inside the failure mechanism of tin oxide as anode for sodium ion batteries." Journal of Solid State Electrochemistry 25.4 (2021): 1401-1410. **DOI:/10.1007/s10008-021-04919-9** (First published on February 24th, 2021)

   Conceptualization; Formal analysis; Investigation; Writing – Original Draft; Writing – Review & Editing

7. Leccardi F., Nodari D., Spada D., Ambrosetti M., Bini M. "Synergistic Effect of Polymorphs in Doped $NaNi_{0.5}Mn_{0.5}O_2$ Cathode Material for Improving Electrochemical Performances in Na-Batteries." Electrochem 2.2 (2021): 335-346. **DOI:/10.3390/electrochem2020024** (First published on June 4th, 2021)

   Conceptualization; Writing – Original Draft; Writing – Review & Editing

8. Spada D., Albini B., Galinetto P., Versaci D., Francia C., Bodoardo S., Bais G., Bini M. "$FeNb_{11}O_{29}$, anode material for high-power lithium-ion batteries: Pseudocapacitance and symmetrisation unravelled with advanced electrochemical and in situ/operando techniques." Electrochimica Acta 393 (2021): 139077. **DOI:/10.1016/j.electacta.2021.139077** (First published on August 12th, 2021)

   Conceptualization; Investigation; Formal Analysis; Visualization; Writing – Original Draft

Table of Contents

1. Introduction

"Chemistry is the discipline that deals with the matter. Energy is something that permeates chemistry, whether as driving force of a reaction, or as the reason why some compounds exist and others not, and so on… Energy can be extracted from the matter, and pushed back into it, in order to transform a compound into another, maybe more useful to mankind. The importance of knowing and managing energy is strongly bound to our technological advancement as a specie willing to survive on the planet."

The introduction of this thesis is devoted to energy at different scales, from a global perspective that embraces the previous and next decades, if not centuries. Firstly, a panoramic on the global scale of energy and related issues is given. Then the energy storage systems are briefly analysed, with regards to Lithium- and Sodium-ion batteries which are discussed in detail. A deeper focus is given to the materials' science and the state of the art of anodes for both kind of batteries, which are the research topic of this thesis.

1.1 Energy in the 3rd millennium

The work of this thesis can be ascribed to the field of "a subject that we have come to believe is unequivocally the most important technological problem in the world: our global energy future", to cite the words of prof. Nathan Lewis, (California Institute of Technology) on its plenary lecture called "Powering the Planet", held on April 11, 2007 at the Materials Research Society Spring Meeting in San Francisco. [1]

> "Compared with all the other technical issues facing us in the world today, why is energy the most important? I believe that energy, not the dollar, is the currency of the world. It is the joule that drives every economy and gives people a way out of poverty. Without energy, we cannot find or administer medicine to cure disease, we cannot purify water, we cannot drive our cars; we cannot go to work, operate computers, or even study at night. Because our modern lives run on various forms of energy, we need to find a way to manage our energy challenges before they begin to manage us." [1]

Energy-related issues…

Scaling the problem – One gigawatt is the electrical output rate of a typical nuclear fission power plant. [1] In order to satisfy the human energy consumption of these decades (higher than 10 TW), more than 10 thousand nuclear plants should be required (Fig. 1.1).

Figure 1.1 - Picture of the Earth from space

Fossil fuels – Fossil fuels are the cheapest energy source available on the world (Fig. 1.2). Proven reserves (the quantities that the U.S. Securities and Exchange Commission allows a company, with 90% confidence, to book and to tell its stockholders it has in the ground). Resources are instead fossil energy supplies that the U.S. Geological Survey (USGS), with 50% confidence, estimates are still left to be discovered in the ground. The proven reserves of oil, natural gas and coal could supply energy for centuries, [1] so the availability of fossil energy is not the main problem.

Figure 1.2 - Oil wells

CO_2 emissions and climate implications – The real energy problem is associated with the CO_2 produced when fossil fuels are burned. Atmospheric CO_2 is troublesome because it is already the most oxidized form of C in an oxidizing atmosphere. As a results, CO_2 is not converted in any environmental-friendly compound and has great staying power (500 - 5000 years) [1] because it has to move from the near-surface ocean to the deep ocean to be depleted from the air. Except from climate models, nobody knows what the effects of higher atmospheric CO_2 concentrations will be. However, anyone can see that every glacier on earth but a few is melting, that means that the sea level is predicted to rise. Also, the pH of the near-surface oceans is changing, and coral reefs are already suffering from the acidification of the oceans (Fig. 1.3). There is also the possibility of a non-linear effect caused by the melting of the permafrost, that releases methane and CO_2 trapped in the ice. In the Permian Era, this already happened and caused a massive release of CO_2, an increase of the temperatures and extinction of 90% of the existing species.

Figure 1.3 - Climate changes in the whole planet: from the poles to the tropics

… and solutions

Carbon-free energy – In order to stabilize CO_2 concentrations at reasonable levels, the energy obtained from oil, coal and gas combined must be produced instead from carbon-neutral sources such as nuclear power and renewable carbon-neutral energy sources.

Carbon sequestration – Another approach to producing carbon-free power is to sequester the CO_2. In this process, CO_2 would be captured when it is emitted from a power plant, and then sequestered in the ocean or in geological reservoirs, or converted to carbonates. Burial of CO_2 in the deep ocean would change the pH of the ocean, inducing ecological changes in the biosphere. Sequestration in geologic reservoirs seems more promising, but the leak rates must be very low over centuries. Otherwise, after decades of sequestration, the yearly emissions would be comparable to the emission levels that were supposed to be mitigated. Some existing fossil-derived power plants could be retrofitted and employed for sequestration but many others are too far from suitable geologic reservoirs, meaning that the CO_2 should be pumped for long distances. [1]

Nuclear power – As mentioned before, in order to satisfy the actual energy needs, 10 thousand reactors are required, which is unfeasible in the next 30-40 years (Fig. 1.4). Also, the reactor fuel is not so easily available: proven reserves of uranium could provide 10 years of operation for the ideal 10 thousand reactors. The uranium is too diluted to be mined from sea water, and uranium-thorium cycles are not yet been proven technically. Enough plutonium exists to be employed and reprocessed, but the implications of huge amounts required for the hypothetical thousands of power plants must be evaluated. [1]

Figure 1.4 - Nuclear plant

Renewable carbon-neutral sources - Leaving aside nuclear fission and clean coal, the other approach to producing carbon-neutral power is to use carbon-neutral renewables, of which there are six often-mentioned sources: hydroelectric, geothermal, oceans/tides, winds, biomass, and solar (Fig. 1.5). [1]

Carbon-neutral sources

Hydroelectricity - Hydroelectricity is a model renewable energy resource: relatively cheap, benign and fairly abundant. However, the total hydrological energy potential of the planet (including the water flow from every river, lake, and stream) is barely a half of the actual energy consumption. Moreover, it is unfeasible to build dams on every water source, and this means that the estimated technically and economically hydroelectrical energy that can be extracted is about 0.9 TW (of which 0.6 TW already installed). [1]

Figure 1.5 - The six renewable sources

Geothermal - In a few places on Earth, turbines can produce electricity directly from the geothermal energy from the ground. In the majority of the surface, however, it is necessary to exploit the 200 °C thermal gradient of the Earth by going down about 10 km, injecting cold water into a well, and having the hot dry rock heat it up and convert it to steam for running a turbine. If all the surface of the Earth was employed as a geothermal source, 11.6 TW of sustainable global heat energy could be obtained, without accounting for the efficiency in the heat engines. As a result, few TW can be extracted sustainably. [1]

Tides - In terms of oceanic and tidal energy, all the energy in all the currents, all the tides, and all the waves on our planet falls far short of the 10–20 TW needed. [1]

Wind - Wind could produce a significant fraction of our total carbon-free energy, but it has constraints. Considering the practically available land (urban areas and environmentally sensitive lands are excluded) and the optimal spacing between windmills, 2–4 TW of electricity could be obtained. The offshore electrical power potential of wind is even greater, but transmitting power from offshore installations to the land would be a major problem. Also, producing 2 TW of wind power would require the operation of 2 million state-of-the-art wind turbines. [1]

Biomass - Although biomass is attracting a lot of attention today, it is fundamentally inefficient. Plants using photosynthesis store less than 1% of the total incident energy they receive from sunlight, under optimal growing conditions, averaged over the year. In addition, to prevent oxidative damage, photosynthesis shuts itself down at higher light intensities. As a result, 30% of the total land on Earth would have to be covered with energy farms devoted solely to producing biomass. However, not all of that 30% of needed land can support crops, and the increase the amount of land employed for food production makes this hypothesis unfeasible. [1]

Solar - The sun is the most powerful energy source available: it provides Earth with 120000 TW, meaning that solar energy is the only renewable resource with enough energy to satisfy alone the 10–20 TW carbon-free supply constraint. A solar energy "farm" operating at 10% efficiency, at a representative mid-latitude, to supply 3 TW of power, would cover 1.7% of U.S. land, which is comparable to the land devoted to highways (Fig. 1.6). From a global perspective, few 3.3 TW boxes would be needed to represent the needed amount of land. Putting 10% efficient solar panels on every home rooftop would generate only 0.25 TW and would be quite costly. [1]

Figure 1.6 –Map of the U.S. (right) with the red square showing the amount of land needed for a solar energy farm operating at 10% efficiency to produce 3 TW of power

And so? - Even if a lot of work is still to be done for cost-effective solar energy to become a reality, the problem of producing enough carbon-free power to satisfy our energy needs would still not be solved: sunlight is intermittent, but our collective energy needs are continuous. The sun generates power at certain hours of the day, only on sunny days. This means that a viable cost-effective way to store massive quantities of solar electricity must be developed.

1.2 Energy storage

As mentioned, the development of advanced renewable energy technologies must be paralleled with good energy-storage systems (EES). [2] ESS have an important effect on overall electric systems: they provide continuous and flexible power supply to maintain and to enhance power as a result of congestion and interruption of transmission line for excessive demand; they ensure reliable services for consumers during power crises due to natural disasters, they lessens the prices of electricity to support the peak demand by storing energy during off-peak hours at low cost. [3]

Unfortunately, we currently only have the capacity to store around 1% of the energy consumed worldwide, most of which (98%) is through pumped-storage hydroelectricity. While such hydroelectricity is widely used, it has low energy density. Besides energy density, other important parameters include cost (construction and maintenance), scalability and safety. [2]

Classification

The classification of ESS is determined with the use of energy in a specific form (mechanical, electrochemical, chemical, electrical, thermal, and hybrid). These systems are classified into various types according to their formations and composition materials. [3]

Mechanical - Mechanical storage systems are pumped hydro storage (PHS), compressed air energy storage (CAES), and flywheel energy storage (FES). The most popular is PHS, which is used in pumped hydroelectric power plants: reserved water is pumped to a power turbine with a generator to produce electricity. As already mentioned, this storage system contributes approximately 99% of the world electric storage capacity. [3]

Thermal – Thermal storage systems store energy in the form of heat in an isolated depository from solar or electric heater for later use in electricity generation plants or different heating purposes. [3]

Chemical - Chemical storage systems store and release energy through chemical reactions. The fuel cell (FC) is a typical chemical storage system that converts chemical energy of fuel to electrical energy continuously, with 40–85% fuel efficiency and proven reduction in fossil fuel use and CO_2 emissions. FCs are composed of liquid or gaseous fuel as anode and oxygen, air, and chlorine as the oxidant in the cathode side. Hydrogen-based FCs (HFCs) are popular and available in the market. HFCs (Fig. 1.7) use a combination of hydrogen and oxygen to produce electricity. This combination could be regenerative and reversible from electricity and water. The overall chemical reaction in fuel cells is

$$2H_2 + O_2 \rightleftharpoons 2H_2O + \text{Electricity}$$

FCs are classified into several types based on fuel and oxidant combinations, electrolyte type, operating temperature, and applications; these types include alkaline FC (AFC), phosphoric acid FC (PAFC), solid polymer fuel cell-proton exchange membrane FC (SPFC-PEMFC), regenerative FC (RFC), solid oxide FC (SOFC), direct methanol FC (DMFC), and molten carbonate FC (MCFC). Other types of FCs include metal-air FC (MAFC) and microbial FC (MFC). [3]

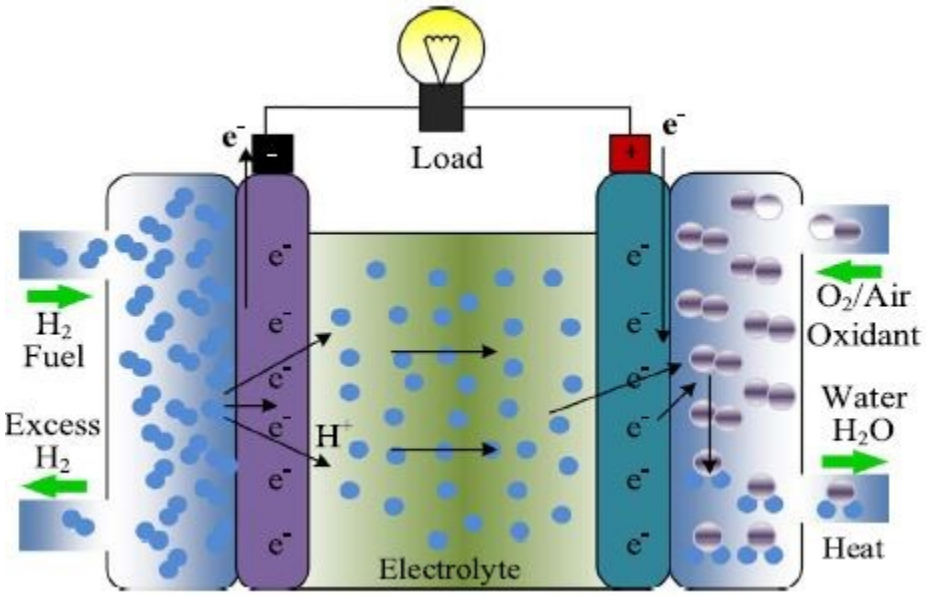

Figure 1.7 – Hydrogen fuel cell chemistry [3]

Electrical – Usually stores electrical energy directly as electricity in the form of electric field by separating charges or magnetic field by flux:

- *Ultracapacitors (UC)* – Also called supercapacitors, they are similar to normal capacitors in terms of structure and function. However, they can have a high energy capacity (kF). The specific power of UC is approximately 1000–2000 W/kg with 95% energy efficiency. Among all ESSs, UC has the longest lifetime (almost 40 years). They also do not require maintenance, and exhibit temperature insensitivity. UCs are used during electric braking and as energy source during rapid acceleration needed for hilling in EVs. UCs are found in three classes, namely, electric double-layer capacitors (EDLC, Fig. 1.8), pseudocapacitors, and hybrid capacitors, depending on the features of electrodes: EDLC electrodes (typically nanostructured, high-surface area and cheap carbon-based materials) store charges via ion accumulation to form electric double layers at the interface between electrode and electrolyte; pseudocapacitive electrodes store energy electrochemically through surface/near-surface reversible faradaic reactions. [4] UCs can be either symmetrical or asymmetrical configurations, [3] that is when there is any difference between the two electrodes (weight, thickness, material and so on). [5] The energy stored in capacitors is:

$$W_c = \tfrac{1}{2} CV^2 = \tfrac{1}{2} QV \qquad Q = CV \text{ and } C = \varepsilon A/d$$

where W_C is the electrostatic energy, C is the capacitance value of UC, V is the voltage across the electrodes, Q is the charge, ε is the permittivity of dielectric materials, A is the surface area of electrode, and d is distance between electrodes. [3]

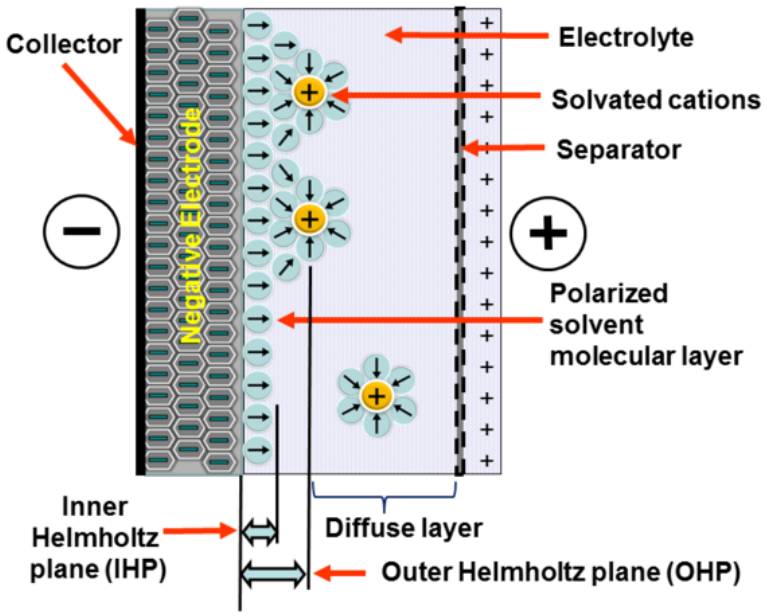

Figure 1.8 – Electric double-layer capacitor cell structure

- *Superconducting magnetic energy storage (SMES)* - SMES store electrical energy in the form of magnetic field, with a high energy storage efficiency (97%), full energy discharge capability, a

long life cycle of 100000, and quick response of milliseconds. However, the initial cost is high (even if lower than that of EDLC). The usual power rating of SMES is in kW to MW. Generally, SMES is utilized in UPSs, power quality applications, and grid systems. [3]

Electrochemical - All conventional rechargeable batteries can be classified as electrochemical storage systems, particularly flow batteries (FBs) and secondary rechargeable batteries. Energy is transformed from electrical to chemical energy and vice versa through a reversible process with energy efficiency and low physical changes. The main difference between an FC and a battery is that in a FC the fuel and oxidant are supplied externally, while in the battery they are integrated (except metal-air batteries). Batteries have the dual function of storing and releasing electrical energy by changing the charge and discharge phases with no harmful emission and little maintenance.

- *Secondary batteries* – They will be discussed in detail in the following section, being the focus of the thesis.

- *Flow batteries (FB)* – FBs are rechargeable, and in FBs, energy is stored in electroactive species. The electroactive species are dissolved in liquid electrolyte in tanks, and the liquid is pumped via electrochemical cell to convert chemical energy into electric energy. Redox flow (RFB, Fig. 1.9) and hybrid flow (HFB, which is the combination of a secondary battery and a redox flow battery) are examples of FBs. The total size of the tank of RFB defines the total energy of the battery. RFBs exhibit high life cycle stability, high efficiency, flexibility in power, and capacity demand, which make RFBs attractive in any autonomous and standalone grid systems. FBs have a life expectancy of 15–20 years, 4–10 h discharge range, and 60–70% efficiency. Nowadays, RFBs and HFBs are being designed for large-scale power storage for community energy storage and utility-scale application for enhancing power quality, UPSs, peak shaving, increasing security of supply, and integration with renewable energy systems. [3]

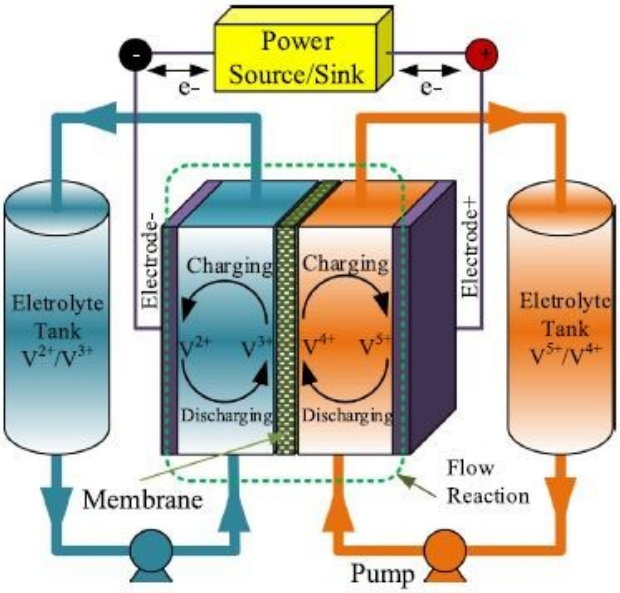

Figure 1.9 - Vanadium redox flow battery from [3]

Hybrid - Individually, all ESSs are incapable of providing all the features, such as energy density, power density, discharge rate, life cycle, and cost. Thus, ESS is needed to optimize features for balanced energy storage and delivery by combining two or more ESSs that have complementary characteristics, thereby ensuring the optimal performance of ESSs. Hybrid ESSs (HSS) have been developed, and they electronically combine the output power of two or more ESSs with complementary features. In HSS systems, the combination of a high-power-density ESS and high-energy-density ESS, or fast-response ESS and slow-response ESS, or high-cost and low-cost ESS are considered by power electronic configurations to deliver optimal power for loading. [3] For example the combination of supercapacitors and batteries, called battery-supercapacitor hybrid (BSH), offers a promising way to construct a device with merits of both secondary batteries and SCs (Fig. 1.10). In such a hybrid device, different charge storage mechanisms are implemented in the positive and negative electrode materials: one electrode (porous carbon) utilizes the double-layer storage mechanism while the other (transition metal oxides) stores charge by means of faradaic reactions. [5] As a consequence, bulk redox reactions occur at the battery-type electrode while ion accumulation/separation or rapid charge transfer happens at the capacitive electrode. Despite being asymmetric, BSH is different from conventional “asymmetric SCs,” in which both electrodes are capacitive but with asymmetric capacitive charge storage mechanism. [4] Recently, Li-ion capacitors (LIC) have been developed, which have the same high power density of UCs, but higher terminal voltage and energy density. [3]

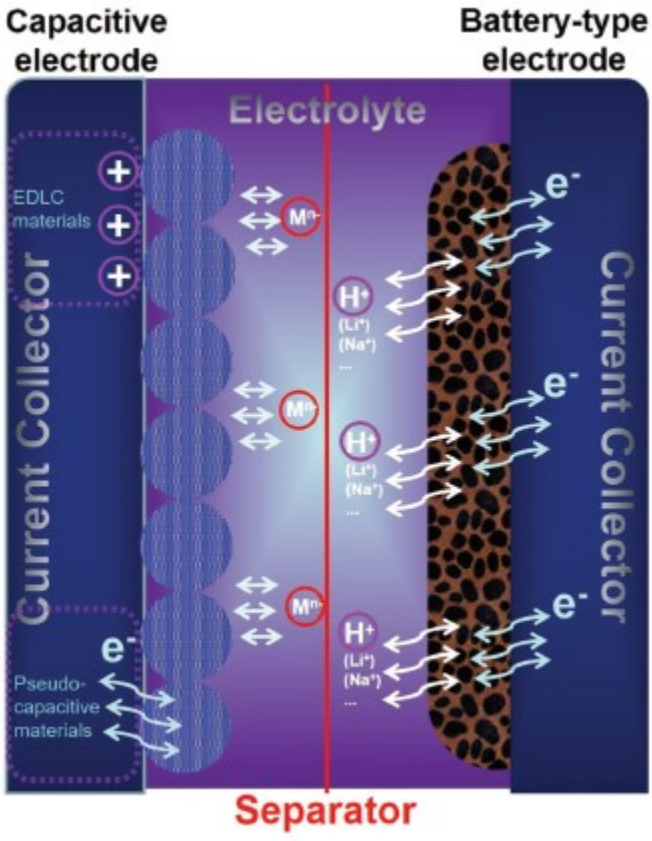

Figure 1.10 - General energy storage mechanism and device structure of a battery-supercapacitor hybrid [4]

Secondary batteries

Secondary batteries (SBs) dominate the market for portable energy storage devices for EVs and other electric and electronic applications. SBs consist of two electrodes (anode and cathode), an electrolyte, a separator and a case. SB possesses high specific energy, high power density, flat discharge profile, low resistance, negligible memory effect, and wide range of temperature performance. However, most batteries contain toxic materials. The various types of SBs mainly include lead-acid (LA), nickel-based (Ni-Fe, Ni-Zn, Ni-Cd, Ni-MH, Ni-H_2), zinc-halogen-based (Zn-Cl_2, Zn-Br_2), metal-air-based (Fe-Air, Al-Air, Zn-Air), sodium-beta (Na-S, Na-$NiCl_2$), high-temperature lithium (Li-Al-FeS, Li-Al-FeS_2), and ambient temperature lithium [lithium-polymer (Li-poly), lithium-ion (Li-ion)] batteries. [3]

Lead-acid batteries - LA batteries have been used as energy sources commercially since 1860. LA batteries are used in every internal combustion engine (ICE) vehicle as a starter and typically applied for emergency power supply, renewable energy storage, and grid storage because of their ruggedness, safe operation, temperature tolerance, and low cost. The battery (Fig. 1.11) consists of Pb as negative electrode, PbO_2 as positive electrode, and H_2SO_4 solution as electrolyte. The electrochemical reaction takes place in LA battery:

$$Pb + 2PbO_2 + 2H_2SO_4 \rightleftharpoons 2PbSO_4 + 2H_2O$$

The battery operates for 6–15 years with a maximum of 2000 life cycles and provides 70–90% efficiency. [3]

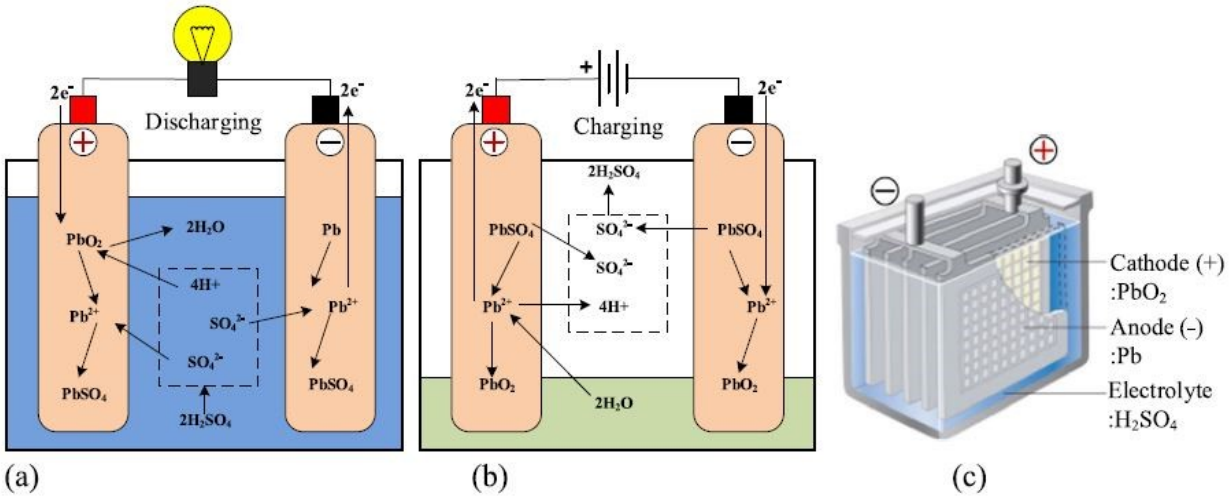

Figure 1.11 - Lead-acid battery chemistry: during (a) discharging, (b) charging, and (c) LA battery prototype [3]

Nickel-based batteries - Nickel-based batteries utilize nickel hydroxide as positive electrode, potassium hydroxide solution as electrolyte and different negative electrode materials (any metal Fe/Cd/Zn, MH, or H_2). Nickel-cadmium and metal hydride are currently used to power EVs because they have a high number of life cycles (2000 or more) and energy density. However, Ni-Cd has a high memory effect and price, which is more than 10 times the price of LA battery. By contrast, Ni-MH has low memory effect, negligible environmental effect, and a large operating temperature range. Environmental friendliness and its maintenance-free nature ensure that Ni-MH is more applicable than Ni-Cd for powering EVs

although it generates heat during operation and needs a complex algorithm and a costly charger. Ni-H_2 has a high capacity rate, a long lifecycle, and tolerance to overcharging or overdischarging without damage. However, this battery type is expensive, has self-discharge that is proportional to H_2 pressure, has low volumetric energy density, and is specially produced for space power. [3]

Zinc-halogen batteries - Zinc-halogen batteries include Zn-Br_2 and Zn-Cl_2, which was developed in 1970 for EV and static energy storages. Later, Zn-Cl_2 became applicable for power utility because of development changes for plumbing operation and maintenance. Zn-Br_2 batteries are suitable for EV energy storage because of their high specific energy, fast charging capability, and low material cost. However, this battery type has recently become slower in EV applications because of their low specific power, high reactivity of bromine, and large size for electrolyte circulation and temperature control. [3]

Metal-air batteries - Metal-air electrochemical batteries consist of electrodes of metal as anode and oxygen from inexhaustible air supply as cathode. In metal air batteries, Li, Ca, Mg, Fe, Al, and Zn are used as anode metal. Among these elements, lithium-air (Li-Air) battery has high theoretical specific energy, 100 times more than that of other batteries. However, this battery type has a high fire risk that could result from the combination of air and humidity. Overall, metal-air batteries are satisfactory for rechargeable storage application because of their low material cost and high specific energy. [3]

Sodium-beta batteries - Sodium (Na) is an attractive material for battery anodes. Sodium-beta batteries are the only batteries that use solid electrolyte. These batteries use beta-alumina (β-Al_2O_3) as electrolyte, which exhibits good Na^+ conductivity and electric isolation at high temperatures. Depending on cathode materials, sodium-beta batteries are classified into sodium-sulfur (Na-S) and sodium-metal halide. Na-S was developed by Ford, particularly for EV applications, in the 1960s. Later on, this battery type became commonly used for large-scale storage applications to support utility and electric grids. This battery has adequate energy and power density, a long life cycle of 4500, and high energy efficiency of 80–90%, and it is cheap and safe. However, this battery type suffers from high internal resistance and Na corrosion, and it needs to be heated at approximately 300 °C to maintain the molten state of electrodes. Na-S battery consists of solid sodium in molten form as anode and molten sulfur as cathode, partitioned by solid beta alumina ceramic electrolyte. Sodium-metal halide battery technologies have successfully powered EVs since the 1990s because they have a higher cell voltage than Na-S batteries. This type of battery is well known as Zero Emission Battery Research Activity (ZEBRA). A sodium-metal chloride (Na-$MeCl_2$) battery operates at a wide temperature range of 250–350 °C. ZEBRA batteries have the most attractive temperature for EV power because of their high energy density, less corrosion, intrinsic safety, and better tolerance to overcharging and overdischarging than Na-S because of the semisolid cathode, long life cycle, and lower cost than other batteries. However, ZEBRA batteries have a comparatively low specific power, and they need thermal management and self-discharge. $NaNiCl_2$ batteries are utilized especially for large- or medium-scale power storage applications. [3]

Lithium batteries – Lithium SBs are promising batteries for EV energy storage applications because of their high energy density, high specific energy and power, and light weight. Moreover, lithium batteries have no memory effect and no harmful effects unlike mercury or lead. However, this battery type is costlier than other battery types and needs protection for safe operation and cell balancing system to ensure consistent battery performance at the same voltage and charge level. Lithium batteries can be designed for high or ambient temperature applications: lithium-aluminum-iron monosulfide (Li-Al-FeS) and lithium-aluminum-iron disulfide (Li-Al-FeS_2) are high-temperature lithium batteries, with the highest energy capacity and the lowest weight among all other lithium batteries, at the cost of a comparatively low life cycle, need for thermal management and energy loss for maintaining operating temperature. Lithium-sulfur batteries operate at a temperature range of 375–500 °C. Other lithium batteries (Li-poly and Li-ion batteries) normally operate at ambient temperature. The main difference between Li-poly and Li-Ion batteries is the use of lithium metal as anode (exclusive of Li-poly). Li-poly batteries are useful for a variety of packaging shapes, have high specific energy and power but poor conductivity and power density. Li-ion batteries will be better discussed in the following section, but generally consist of lithium metal oxide ($LiMeO_2$, e.g., $LiCoO_2$, $LiMn_2O_4$, $LiNiMnCoO_2$, $LiNiCoAlO_2$) as cathode, dissolved lithium salts in organic carbonates as electrolyte, graphite carbon as anode, and a separator. The overall electrochemical reaction in Li-Ion battery is

$$LiMeO_2 + C \rightleftharpoons Li_{1-x}MeO_2 + Li_xC$$

Figure 1.12 shows the Li-ion battery chemistry during discharging and charging. When the cell is recharged, Li^+ travels from the cathode to the anode and a lithium atom is formed by combining with a charging electron (e^-) and deposited between carbon layers. During discharging, the processes are executed in reverse. [3]

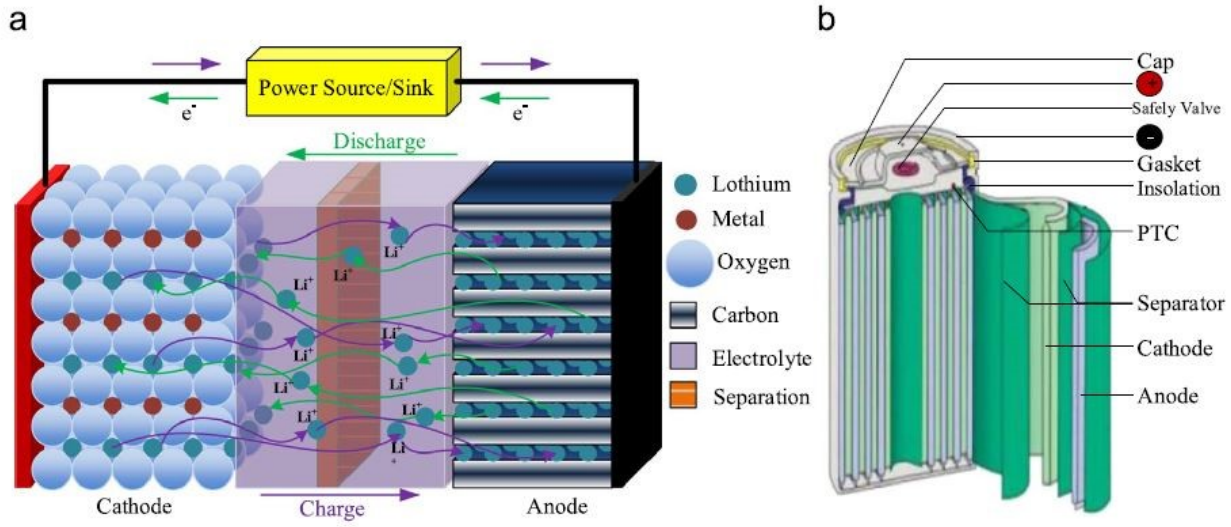

Figure 1.12 - Lithium-ion battery chemistry: (a) during discharging and charging and (b) cylindrical view of Li-ion battery [3]

Why Li-ion batteries? - In almost all aspects (specific energy, energy density, specific power, energy efficiency, battery life cycle, operating temperature range, per energy unit cost in US$), lithium batteries, especially Li-ion batteries, show better performance (Figure 1.13). In addition, the development of low-cost lithium battery materials and battery management systems has been advancing in terms of reducing manufacturing costs. [3] Their triumph in the portable electronics market is due to the higher gravimetric and volumetric energy densities offered by them compared to other rechargeable systems. The higher energy density is due to the higher operating voltages of ~4 V resulting from the use of water-free, nonaqueous electrolytes instead of aqueous electrolytes that limit the operating voltages mostly to less than 2 V. Lithium-ion batteries have also begun to enter the electric vehicle market and are being intensively pursued for grid energy storage as well. While energy density is the most important factor for portable electronics, cost, cycle life, and safety also become critical parameters along with energy density (driving distance between charges) for electric vehicles. On the other hand, cost, cycle life, and safety become more important than energy density for grid-energy storage. It is desirable to have a fast charge–discharge rate for all three applications. [6]

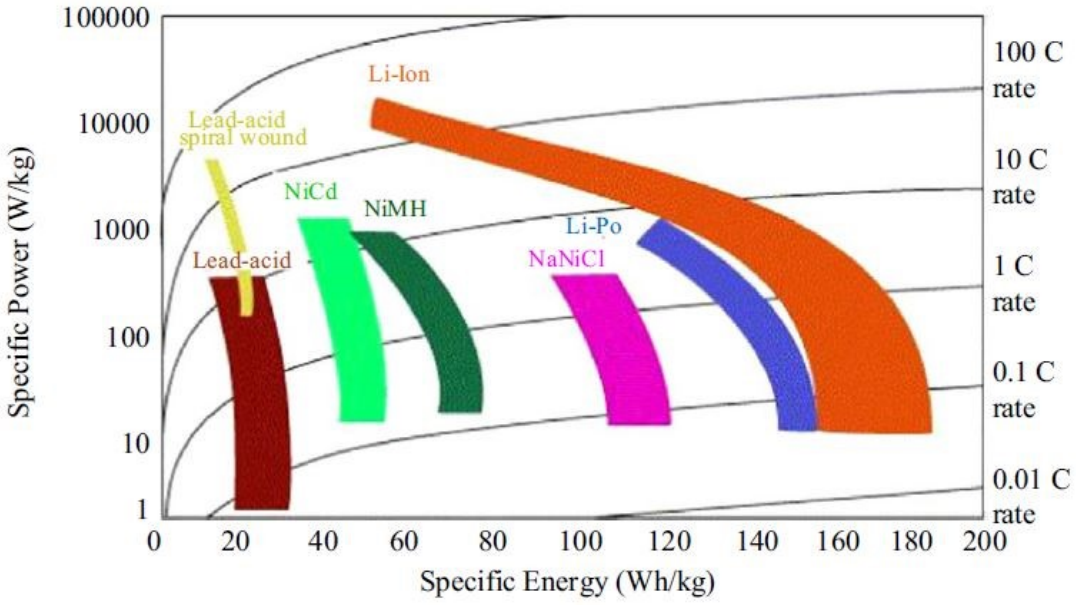

Figure 1.13 - Different electrochemical batteries according to their specific power and specific energy [3]

1.3 Lithium-ion and Sodium-ion batteries

Both Lithium- and Sodium-ion batteries (LIBs and SIBs respectively) are studied in this thesis. The history of LIBs, from the development of the concept to commercialization will be the first treated topic. Then, the basic concepts behind a LIB will be mentioned, before moving on to the topic of why Sodium-ion batteries are being developed. Then the materials' science of electrode materials will be treated thoroughly.

Brief history

In 1991, Sony Corporation announced a new product called lithium-ion battery. This announcement followed on the heels of a product recall of phones using Moli Energy lithium/MoS_2 batteries because of a vent with flame causing injury to the user. The improvement over previous aqueous systems was due to the high cell potential and low atomic weight of lithium compared to all other negative electrode materials that had been investigated. [7] While Sony was clearly the first to manufacture and sell lithium ion batteries, a number of previous studies were prelude to the 1991 product. [7]

The concept – The concept at the basis of lithium-ion battery was first demonstrated in the early 1970s by Whittingham employing metal dichalcogenides (e.g. TiS_2) as an intercalation compound (Fig. 1.14). The layered structure of TiS_2 comprising Ti and S sheets in a close-packed arrangement allows the intercalation of Li^+ into the host material. [8] The idea of a battery in which the lithium ion moved reversibly between the positive and negative electrodes using intercalation materials of different potentials for the two electrodes was first formulated by Armand in the late 1970s, and is often called a rocking chair battery because of the flow of lithium ions back and forward between the two electrodes. The idea was quickly taken up by Lazzari and Scrosati and implemented with a lithiated tungsten dioxide electrode and a titanium disulfide electrode. The potential range was only 0.8 to 2.1 volts and the electrodes both featured high molecular weights, but the important principle was established as the cell cycled for over 60 cycles although the charge voltage was limited to about 2.2 V and discharge to about 1.6 V. [7]

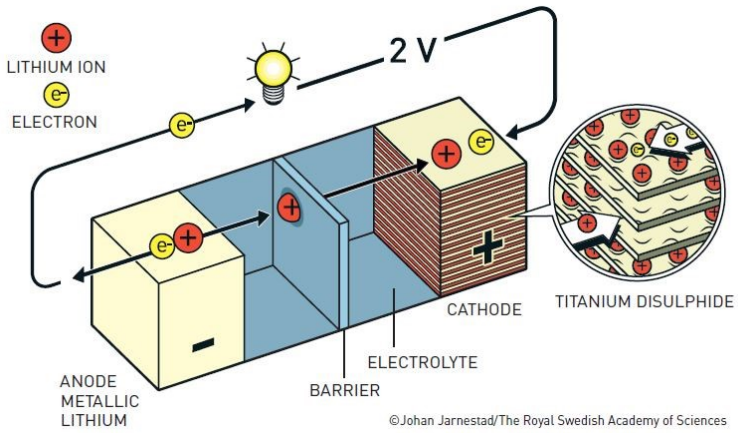

Figure 1.14 - Whittingham's battery [9]

Cathode - A seminal discovery by the Goodenough laboratory was the ability of the family of lithiated transition metal oxides of the $NaFeO_2$ structure (Fig. 1.15) to reversibly deintercalate and reintercalate lithium ions at relatively high potentials (but voltage was limited to prevent electrolyte oxidation). Nickel and cobalt as well as mixtures of these with Mn, Al, Fe, etc. were all found to have this ability and the later adoption of this patented material ($LiCoO_2$) formed the active positive material of Sony's lithium ion battery. [7]

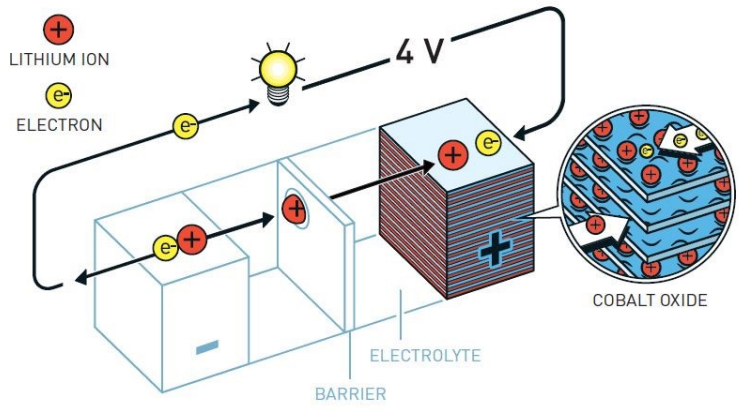

Figure 1.15 - Goodenough's battery [9]

Anode - The discovery of suitable negative electrode materials was somewhat more complicated than the positive electrode materials. Early work on graphite and carbonaceous materials had shown that lithium ions can be intercalated, the process was complicated by the cointercalation of solvent molecules, during which solvent reduction and disruption of the carbon structure occurred. Early work on graphite electrodes, such as the early patent by Basu of Bell Laboratories, or Yazami of University of Grenoble, did not take this issue into account and would have been unsuccessful in practical batteries. An important finding by Fong, Von Sacken and Dahn, showed that petroleum coke was much better than graphite for resistance to solvent co-intercalation and reduction, while addition of ethylene carbonate to PC greatly improved the resistance on both graphite and petroleum coke. The Dahn group also observed the severe corrosion of an aluminum positive electrode carrier with the $LiAsF_6$ electrolyte, that would have obviated the use of that salt in full cells. However, Yoshino and co-workers, from Asahi Kasei (a Japanese battery supplier of separators and electrolytes) had already described the benefits of lower temperature carbons such as petroleum coke in a seminal patent (lower temperature cokes and a $LiCoO_2$ material slightly modified from that suggested by Goodenough) that has resulted in identifying Yoshino as the true inventor of the lithium ion battery (Fig. 1.16). [7]

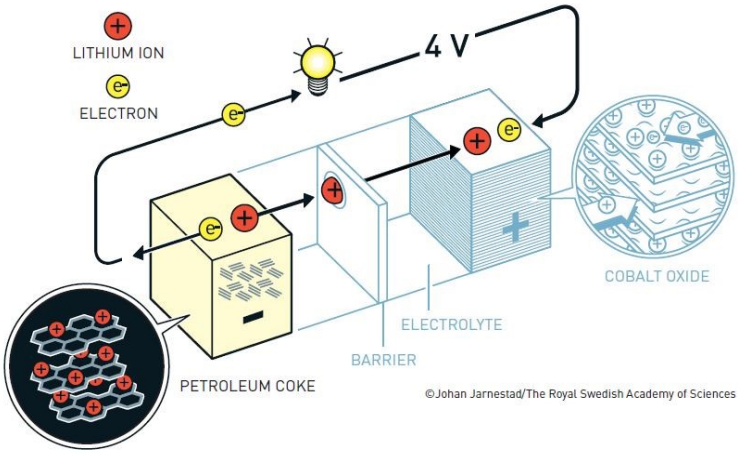

Figure 1.16 - Yoshino's battery [9]

The first battery companies - Asahi Kasei later formed a joint venture to create A&T Battery Corp. to make lithium ion batteries. A&T now operates as a subsidiary company within Toshiba. While the main elements of a lithium ion battery were laid out by Yoshino et al., there were many studies required to make a truly commercial battery with superior properties compared to nickel cadmium and the newly discovered nickel metal hydride batteries. The need was great, because of the deficiencies of these earlier batteries, particularly the memory effect, low specific energy, poor charge retention and environmental problems with the cadmium system. Also, the electronics industry was rapidly developing, particularly in the so called 3Cs (computations, communication and cameras). Sony was a leading company in consumer electronics and had shown a willingness to bring out inventive new products that had no previous market. Sony was a relative newcomer to the battery business, learning the alkaline primary cell technology and business via a joint venture with Union Carbide Battery Products Division, but severed the arrangement in 1986 and began work in earnest on rechargeable batteries. [7]

Upgrading the components - The works involved all the components in the battery. Negative electrodes with higher specific capacity, good safety and better rate capability were developed: hard carbon (second-generation batteries) and later the now commonly used mesophase carbon microbeads (MCMB). The positive electrode material, $LiCoO_2$, was carefully designed to have coarser particle size and good crystallinity. The binder was modified by grafting carboxylic acid anhydride onto the PVDF in order to improve the adhesion to the positive electrode. The electrolyte chosen was ethylene carbonate with a linear dialkyl carbonate (oxidation resistance up to about 4.5 V) and the salt was $LiPF_6$ of high purity and state of dryness. Subsequent improvements in electrolyte have mostly involved the use of additives to improve the passivating film on the negative material, improve the oxidation stability of electrolyte to the positive active material and in some cases reduce the flammability of the electrolyte. [7]

Commercial LIBs - The cell size selected was 18650, following the adopted nomenclature for cylindrical lithium primary cells: the first two numbers represent the diameter in mm and the remaining numbers

represent the height of the cell in tenths of mm (the common 2016 coin cell is 20 mm diameter and 16 tenths of mm in height). This choice is close to the volume of subC rechargeable nickel based batteries (the most popular size at the time for small electronic devices), but unique to lithium ion so that a 1.2 V NiCd or NIMH cell could not replace the lithium ion cell nor vice versa. The original Sony product with coke negative had energy density of 200 Wh/l and specific energy of 80 Wh/kg with a charge limitation of 4.1V. The cell with hard carbon negative had 295 Wh/l and 120 Wh/kg with a 4.2 V charge limitation. With the later use of MCMB negative material the energies were 400 Wh/l and 155 Wh/kg. While Sony remained the industry leader for some time, competition from many other producers finally led to a planned withdrawal of Sony from the battery market. [7]

Nobel prize – An element rarely gets to play a central role in a drama, but the story of 2019's Nobel Prize in Chemistry has a clear protagonist: lithium, an ancient element that was created during the first minutes of the Big Bang. Humankind became aware of it in 1817, when Swedish chemists Johan August Arfwedson and Jöns Jacob Berzelius purified it out of a mineral sample from Utö Mine, in the Stockholm archipelago. Berzelius named the new element after the Greek word for stone, lithos. Despite its heavy name, it is the lightest solid element, which is why we hardly notice the mobile phones we now carry around. On the 9th of October 2019, the Royal Swedish Academy of Sciences has decided to award the Nobel Prize in Chemistry 2019 "for the development of lithium-ion batteries" to (Fig. 1.17):

- John B. Goodenough, The University of Texas at Austin, USA
- M. Stanley Whittingham, Binghamton University, State University of New York, USA
- Akira Yoshino, Asahi Kasei Corporation, Tokyo, Japan Meijo University, Nagoya, Japan

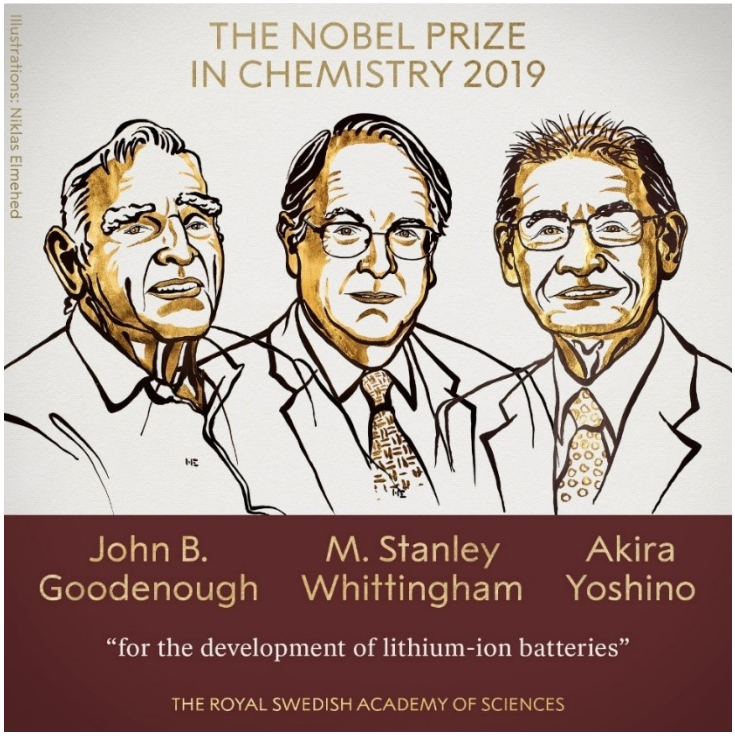

Figure 1.17 - Image of the Nobel prize 2019 winners [9]

The press release says: The Nobel Prize in Chemistry 2019 rewards the development of the lithium-ion battery. This lightweight, rechargeable and powerful battery is now used in everything from mobile phones to laptops and electric vehicles. It can also store significant amounts of energy from solar and wind power, making possible a fossil fuel-free society. [9]

Lithium-ion batteries are used globally to power the portable electronics that we use to communicate, work, study, listen to music and search for knowledge. Lithium ion batteries have also enabled the development of long-range electric cars and the storage of energy from renewable sources, such as solar and wind power. The foundation of the lithium-ion battery was laid during the oil crisis in the 1970s. Stanley Whittingham worked on developing methods that could lead to fossil fuel-free energy technologies. He started to research superconductors and discovered an extremely energy-rich material, which he used to create an innovative cathode in a lithium battery. This was made from titanium disulphide which, at a molecular level, has spaces that can house – intercalate – lithium ions. The battery's anode was partially made from metallic lithium, which has a strong drive to release electrons. This resulted in a battery that literally had great potential, just over two volts. However, metallic lithium is reactive and the battery was too explosive to be viable. John Goodenough predicted that the cathode would have even greater potential if it was made using a metal oxide instead of a metal sulphide. After a systematic search, in 1980 he demonstrated that cobalt oxide with intercalated lithium ions can produce as much as four volts. This was an important breakthrough and would lead to much more powerful batteries. With Goodenough's cathode as a basis, Akira Yoshino created the first commercially viable lithium-ion battery in 1985. Rather than using reactive lithium in the anode, he used petroleum coke, a carbon material that, like the cathode's cobalt oxide, can intercalate lithium ions. The result was a lightweight, hardwearing battery that could be charged hundreds of times before its performance deteriorated. The advantage of lithium-ion batteries is that they are not based upon chemical reactions that break down the electrodes, but upon lithium ions flowing back and forth between the anode and cathode. Lithium-ion batteries have revolutionised our lives since they first entered the market in 1991. They have laid the foundation of a wireless, fossil fuel-free society, and are of the greatest benefit to humankind. [9]

Sodium-ion batteries - The development of sodium ion cells paralleled that of Li ion batteries through the 1980s. The higher energy density of the lithium counterparts—owing to their higher potential and lower mass—resulted in their domination of both research and commercial fields and led to the exponential growth in the portable electronics market in the 1990s. However, for stationary applications, where gravimetric energy density is not so much of a concern (such as grid or minigrid storage), Na ion batteries are an equally viable technology. Recent reports have even shown that these cells can compete with Li ion batteries in terms of energy density. Research in sodium ion batteries has increased dramatically in the last few years and seems to grow exponentially. Nonetheless, several barriers need to be overcome before such cells can become a practical, commercial reality: insufficient cycle life and the need for the discovery of new materials for both the positive (and especially) negative electrodes to increase the performance. [10]

LIBs and SIBs: concepts

The discussion will focus on the main features of the components of LIBs and SIBs. It has to be noted that in this chapter, for better smoothness, only Li^+ ions and Li-ion batteries will be mentioned, but the same principles apply to Na^+ and Sodium-ion batteries.

Basics - Li-ion rechargeable batteries consist of two electrodes (named anode and cathode), immersed in an electrolyte and separated by a polymer membrane. This basic device configuration has remained unchanged from the earliest developed batteries. [11] The key concept behind a LIB is the capability of storing energy into the electrodes through chemical bonds, and releasing it when needed, with minimal energy losses. The energy density of a Li-ion battery is determined collectively by the Li-ion storage capacity (determined by the available space to accommodate the Li ions and by the capability of the electrode materials to change valence states) and the discharge potential of the cell, which is directly proportional to the difference between the electrochemical potentials of the two electrode materials. [11] Hence, in principle, the main difference between a cathode and an anode material is the electrochemical potential at which the Li^+ storage/release reaction occurs. The criteria for the identification of good electrode materials will be discussed later in this section.

Reversibility and stability - Maybe the most important parameter for a secondary battery is the reversibility of the reaction. Of course the structure of the electrode materials hosting Li^+ ions must be very stable to lithiation and delithiation cycles, with small volume changes, but as mentioned previously, also chemical compatibility between the components is needed: when side reaction (e.g. oxidation, corrosion, gas formation) occur, the cycle life of the battery is negatively affected.

Hysteresis - Even once found stable and compatible components, hysteresis is always observed between the charge and discharge curves in all charge/discharge measurements of electrode materials: the charge potential is greater than the discharge potential, probably because of the polarization arising from the internal resistance of the electrode materials; in addition, the internal resistance drop (iR drop) also leads to a drop in potential between the end of charge and the beginning of discharge. Further, overpotential is the driving force behind electrochemical phase transitions in the electrodes: during the discharge step, Li ions enter the interstitial space of the host lattice and electrons are accepted into the transition metal d orbital, followed by an energy decrease and phase stabilization. However, in reverse, more energy is consumed as ions and electrons must be promoted from the lower energy states. In particular, the energy spent during charge is slightly higher than that delivered during discharge. [11] If the electrode materials' resistance is harder to handle (only carbon coating can be effective), the overall resistance of the cell is easily minimized with highly conductive, low viscosity electrolytes in a high concentration. The choice for a proper electrolyte is given also by the compatibility with the other components, as mentioned before and discussed later.

(Not so…) secondary components - The separator must be a good electronic insulator (in order to prevent short-circuit between the electrodes) with high porosity and wetting properties. In solid-state batteries, no separator is needed because the solid electrolyte is already insulating the two electrodes, still allowing ionic conductivity. Other components, often neglected in the research, include the current collector, binding agent and conductive carbon. The current collector has to be highly conductive and low cost, keeping the compatibility with the other components. This is the reason why the current

collector for the anode side in LIBs is copper instead of the cheaper aluminum employed for cathodes, which would be corroded at low potentials. The importance of the binding agent is getting more and more attention, because of its environmental implications: it is needed in the electrode manufacture process, mixed with the active material (capable of forming bonds with Li^+ reversibly through electrochemical reactions) and conductive carbon (improving the electron conduction), in order to stick the mixture to the current collector giving mechanical stability. These powders are mixed and a solvent (to the binding agent, but not to the other components) is added in order to obtain a slurry to deposit onto the current collector as a thin film. The problem associated with the binder relies in the cost of the usually employed fluorinated compounds and in the toxicity of the solvents involved in the processing. Many efforts are being devoted to the development of low-cost aqueous binders (e.g. carboxymethyl cellulose) that can also improve the mechanical properties of the electrodes.

SIBs: why they are so appealing

LIBs and SIBs are related, sharing the basic principles, but the availability/performance balance makes them different in the commercial application.

LIBs and electric vehicles - Lithium-ion batteries (LIBs) are one of the greatest successes for energy storage applications of the last century. LIBs are light, compact and offer outstanding energy and power density, dominating the market for portable electronics, hybrid and electric vehicles (EVs). In view of the increasingly growing electrified automotive field, an increasing demand of lithium and cobalt has been observed with consequent price increase and related concerns about the future and long-term material availability. [12]

Lithium distribution - Indeed, the global lithium supply is concentrated in a few areas with the major lithium resources located in South America brine deposits and in the Greenbushes mine in Australia (Table 1.1). Moreover, the market managing lithium sources is dominated by few companies (Figure 1.18), altogether controlling around 50% of the lithium supply. [12] Albemarle Corporation (USA), American FMC Lithium (USA), Sociedad Química y Minera de Chile (SQM, Chile), and Talison Lithium (Australia), which is owned by Albemarle Corporation (49%) and Tianqi Lithium Industries (51%) from China have set a sustained price increase for the years to come: the prices of spodumene ($LiAlSi_2O_6$), which is the mineral source of lithium, have increased from $380/ton in 2014 to $480/ton in 2016 with peaks of $650/ton. The future does not look much better after Galaxy Resources signed a contract for 2017 at 830–905 US$/ton. Regarding the brine sources Li_2CO_3 and LiOH, the landscape is covered by doubts about supply and prices continuously increasing by 15% in 2016 with respect to 2015, up to $7200/ton. In summary, despite that Li resources are considerably large—an estimated 34 million tons—and the possibility of Li recycling could be opened in the future, they are concentrated in a small number of countries, unevenly distributed. [13]

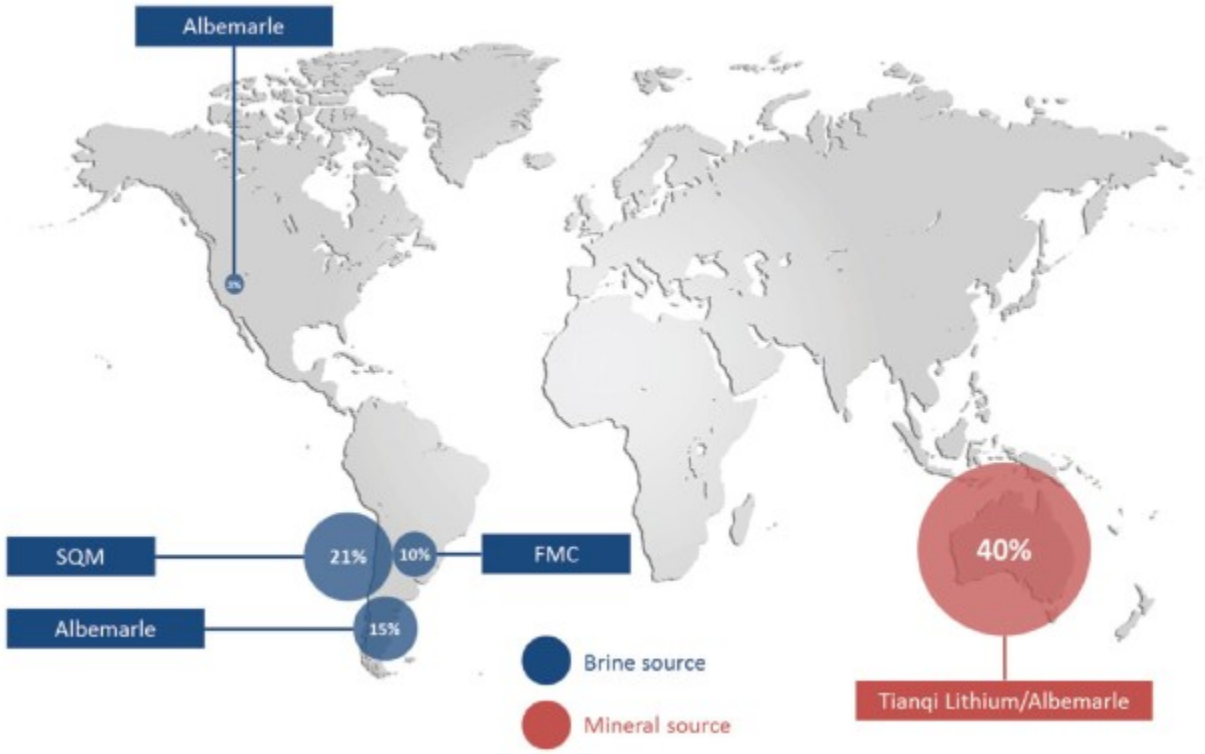

Figure 1.18 - Global distribution of lithium supply [13]

Country	Deposits (mill. Ton)	% of worldwide resources
Argentina	2.6	7.6
Australia	1.8	5.3
Bolivia	10.2	29.9
Brazil	1.0	2.9
Canada	0.4	1.2
Chile	6.3	18.4
China	5.4	15.8
Germany/Czech Republic	0.16	0.5
Serbia	1.0	2.9
USA	4.0	11.7
Zimbabwe	1.0	2.9

Table 1.1 - Geographical distribution of the estimated Lithium resources [13]

Alternative chemistry - This uncertain situation has led researchers to look for both new chemistries dealing either with monovalent (K^+, Na^+) or divalent (Mg^{2+} and Ca^{2+}) cations as well as means to efficiently recycle lithium. Sustainability wise, the most appealing alternative to lithium metal is sodium. The abundance of sodium in Earth's crust is about 23000 ppm (the fourth most abundant element in the Earth's crust) compared with a mere 20 ppm for lithium, which is concentrated in a few mineral sources. Sodium is also present in sea water at high concentration, rendering its overall resources practically unlimited. Its uniform distribution leads to lower economic and geopolitical impact. Na-ion chemistry is based on the rocking chair principle as LIBs, thus, it could benefit from the great advances done in the last 30 years, resulting in the accelerated knowledge-development and easy transition to manufacturing. Performance wise, sodium is three times heavier than lithium (23 g mol^{-1} compared with 6.9 g mol^{-1}) and is 0.3 V less electropositive, so relatively high gravimetric and volumetric capacity penalties (~15%) will have to be paid in moving from lithium to sodium batteries. [2] [12]

Benefits of Sodium-ion batteries - Nevertheless, if Na-ion technology could be achieved, early estimates predict a 30% cost decrease with respect to Li-ion technology while ensuring sustainability. Such a cost reduction takes into account, besides the cost of the raw materials, the possibility of using aluminum rather than copper as the current collector at the negative electrode and developing cheaper sodium-based electrolytes. Sodium salts (PF_6^-, $TFSI^-$, FSI^-) are much less toxic than their lithium counterparts, are also easier to obtain in their anhydrous state and easier to purify. [2]

Applications of SIBs – The lower cost of SIBs cannot balance the lower energy densities, making LIBs the viable choice for smart devices and transport applications. However, a major challenge is waiting for us in the near term: large scale and low-cost stationary energy storage. This will be crucial for boosting the efficiency, adaptability, and reliability of the next-generation power grid. The use of stationary energy storage systems coupled to the power grid will help to enhance the flexibility, minimize power fluctuations, and ease the integration of renewable power generation, which is intrinsically variable, into a stable and controlled grid. Given the current production costs of LIBs and the need of mining the raw materials, it is difficult that in the long term Li-ion technology can reach the target cost for the competitiveness with other energy storage systems. [13] There is great hope for grid applications, for which weight is not a concern, where Na-ion technology could stand as an attractive alternative to the presently commercialized high-temperature Na–S cells and Na–$NiCl_2$ ZEBRA-type systems. [2]

Chemistry of electrode materials

Several selection criteria of electrode materials must be considered, including societal, economical, and technical considerations: natural abundance, cost, lack of competition with other industrial applications, eco-friendly nature for processing, usage and recycle, while technologically the electrode materials must offer a large reversible storage capacity. [11]

An ideal choice procedure should involve all the following steps:

(1) Sustainability – which elements?

(2) Technical requirements - which compounds?

(3) Materials' science - how can the synthesis improve the performances?

It has to be noted that in most cases, these steps are interrelated, overlapped. Let us start with sustainability requirements:

Economics – Perhaps, the most important consideration in our market economy is the cost associated with producing conversion and storage devices (photovoltaic cells and batteries), which is now driven by both the abundance of the materials and the fabrication processes. Despite the very large discrepancy in reported LCA data regarding the relative impacts of materials production versus cell assembly, it is clear that 'materials production' is a main contributor to CO_2 emissions and energy costs. It includes various aspects such as mining, ore transport, ore transportation and processing, and so on. In fact, a large part of this energy is utilized in mining scarce elements and achieving the high temperatures required to make the electrode materials. [2]

Environmental aspects – It is also essential to consider sustainability, renewability and 'green chemistry' when selecting materials for storage devices, especially when used in applications with large markets and volume (vehicles, grid). LCA estimations taking into account the production of batteries, materials and recycling have revealed that more than 400 kWh are needed to make a 1 kWh Li-ion battery, resulting in the emission of about 75 kg of CO_2. In comparison, the production of 1 kWh of electricity from coal produces around 1 kg of CO_2. This means that in the current situation batteries will only begin to have an environmental benefit beyond hundreds of cycles. This also questions the benefits of developing batteries for electric vehicles to decrease greenhouse-gas emissions when we heavily rely on coal-fired plants to produce primary electricity: a standard internal combustion engine car can release less CO_2 per kilometre than an electric vehicle recharged with electricity coming from coal combustion. [2]

A sustainable and efficient energy storage device requires a lot of efforts for what concerns the materials' science. Let us survey the technical requirements involving Li- and Na-ion batteries.

Energy density - The output of a battery is a current I at a voltage V for a time Δt that depends on the total electronic charge Q transferred from the anode to the cathode in a full discharge at a constant operating current I. A critical parameter for a portable battery is the gravimetric energy density

$$E_g = QV/W,$$

where W is the weight of the battery. For a hand-held device, the volumetric energy density

$$E_v = QV/\text{volume}$$

is also important. It has to be noted that the voltage is reduced from its open-circuit value V_{oc} by the polarization $V = V_{oc} - \eta$. In order to minimize η, present-day lithium-ion rechargeable batteries use a liquid-carbonate electrolyte because these nonaqueous liquids dissolve a high concentration of Li salts to give a Li^+ conductivity $\sigma_{Li} \approx 10^{-3}$ S/cm. [14]

Voltage - Cell voltage is determined by the compatibility of the whole system, including the anode, cathode, and electrolyte. In particular, the difference in chemical potential between the anode (μ_A) and the cathode (μ_C) is termed as the working voltage, also known as the open circuit voltage, V_{OC}:

$$V_{OC} = (\mu_A - \mu_C)/e$$

where e is the magnitude of the electronic charge. This working voltage is also limited by the electrochemical window of the electrolyte (Figure 1.19) which is determined by the energy gap from the highest occupied molecular orbital (HOMO) to the lowest unoccupied molecular orbital (LUMO). The anode and cathode must be selected such that the μ_A of the anode lies below the LUMO and the μ_C of the cathode is located above the HOMO, otherwise, the electrolyte will be reduced on the anode or oxidized on the cathode to form a passivating solid electrolyte interphase (SEI) film. This SEI film offers both advantages and disadvantages: it permits the diffusion of Li ions through the film under a uniform electric field and reduces the overpotential and concentration polarization, preventing the aggregation of electrochemically active particles and maintaining a uniform chemical composition at the electrodes. However, the SEI film increases the internal resistance of the battery and consumes part of the Li ions from the cathode, leading to both power and capacity loss. In addition to the electrochemical window of the electrolyte, the p electron band of anions also determines the achievable voltage in the cathode. The anion (O^{2-}) will undergo oxidation to form gas (O_2) when the top of the anion p-band is located above the energy state of transition metal ions (e.g., Co^{3+}/Co^{4+}). [11]

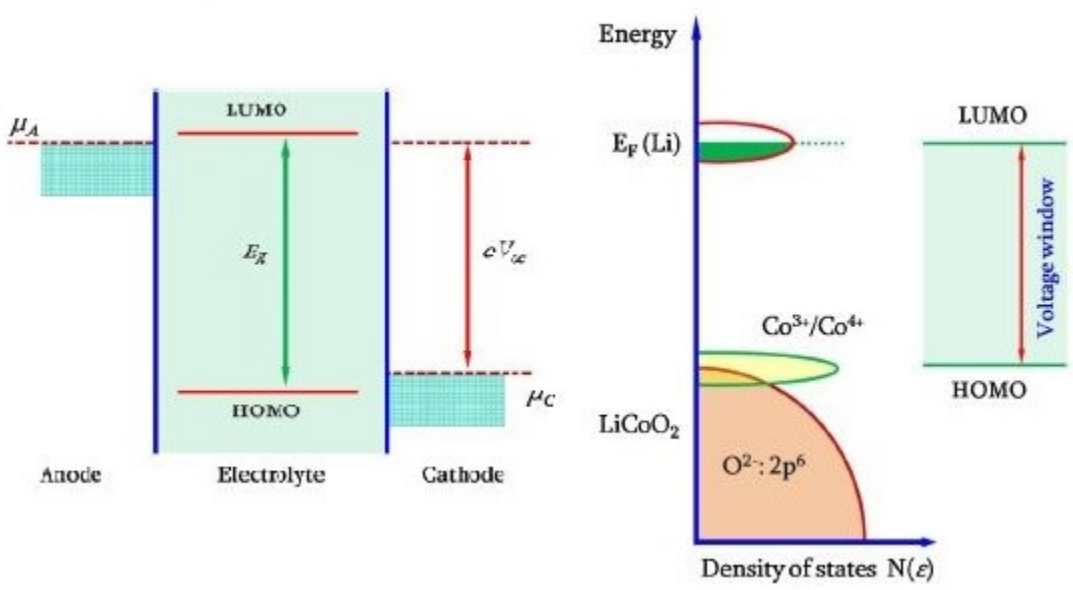

Figure 1.19 - Electrolyte stability window in relation with the electrochemical potentials of Li metal and $LiCoO_2$ [11]

Capacity - The theoretical capacity of electrode materials is:

$$C = nF/3.6M$$

where n is the number of reactive electrons per formula unit, M is the molar weight of materials, and F is the Faraday constant. The number of electrons is in turn correlated with the number of Li/Na ions accommodated in the host lattice. The equation implies that smaller molecular weight and accommodation of more electrons per formula unit can produce a higher capacity. For example, $LiCoO_2$ possesses a theoretical capacity of 273 mAh/g (1 Li^+/f.u.) and V_2O_5 has a higher capacity of 443 mAh/g (3 Li^+/f.u.). However, in practice, a capacity of 140 mAh/g is obtained as only half of the Li ions can be reversibly inserted into or extracted from the $LiCoO_2$ host. Nevertheless, lighter elements are favoured as electrode materials for their higher specific capacities. The advantages of transition metal oxides as cathode materials are incomparable, as their variable valence states facilitate more electron-storing sites. [11]

Electronegativity - Electronegativity is an essential factor that affects the electrochemical potential of electrodes. Electronegativity describes the tendency of an atom or a functional group to attract electrons (or electron density) toward itself. The difference in electronegativity will determine the character of chemical bonds formed between transition metal ions and anions or anionic ligands: a larger difference in electronegativity predicts the formation of a more ionic bond (dense structures), whereas smaller differences denote a more covalent bond (poorly packed structures). The structure density not only influences the phase stability of materials but also affects the specific site energy of Li ions, which is correlated with the electrochemical potential of materials. [11]

Electronic configuration - The electrochemical potential of electrodes increases with the number of electrons in d orbitals of transition metal elements of the same period: given the same coordination and valence, the ionic radius of the transition metal cations in the same row would decrease with increasing atomic number, as the electrons in the outer shell are more strongly attracted by atomic nuclei, resulting in higher energy consumption or release during electron transfer. Similarly, if the period increases in the same family, the binding energy of electrons and the electrochemical potentials of cathodes decrease, as the nuclei are not as strongly attracted to the 4d electrons as they are to the 3d electrons. As weaker attraction corresponds to a lower energy for electron transfer, the corresponding materials have a lower potential (Fig. 1.20). [11]

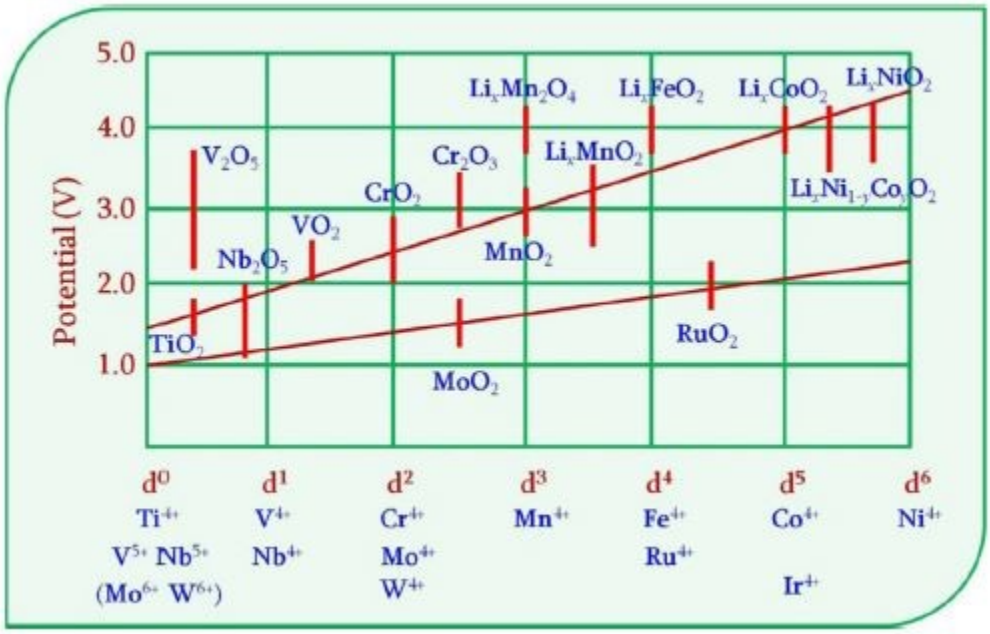

Figure 1.20 - Voltage range exhibited by transition metal oxides as a function of the amount of d electrons [11]

Anion - The selection of cations was discussed given that oxygen ions are the coordinating ligands to consider the energy for electron transfer, but different ligands alter the electrochemical potential. The presence of polyanionic groups with greater electronegativity that replace oxygen ions in the framework of electrode crystals would lead to more ionic M-X bonds (the inductive effect pulls some charge density out of M–X bonds to decrease their orbital overlap, increasing the ionic character of the bonds). This enhanced ionic character reduces the separation between the bonding and antibonding orbitals, which results in a decrease of the lowest unoccupied M-3d orbitals, that is, an increased electrochemical potential. The greater the electronegativity of the polyanionic group, the higher the increase in electrochemical potential. Phosphates, silicates and sulphates have higher electrochemical potential and better thermal stability than the corresponding transition metal oxides. Similarly, fluorides possess higher electrochemical potential than polyanionic compounds due to the strongly inductive effect of fluorine anions. [11]

Crystal structure - The crystal structure represents the symmetric arrangement of atoms that occupy positions in order to minimize the total energy of the crystal. Phase transitions are observed in the electrode materials during electrochemical reactions, and the change in Gibbs free energy determines the corresponding electrochemical potential. The electrochemical potential of electrode materials is directly correlated to the energy required to add or remove electrons (as mentioned above) but also lithium ions. Li ions occupy the tetrahedral and/or octahedral sites in intercalation electrode materials. Although both LiO_4 (r_{Li}/r_O = 0.415 >> 0.225) and LiO_6 (r_{Li}/r_O = 0.535 >> 0.415) are stable, the LiO_4 tetrahedron is much smaller than the LiO_6 octahedron, and the insertion/extraction of Li-ions to/from oxygen tetrahedrons and oxygen octahedrons result in different changes in the Gibbs free energy. For example, in the spinel crystal $Li_xMn_2O_4$, Li ions are inserted into the tetrahedral sites (at $x < 1$) and octahedral sites (at $x > 1$) at distinctive electrochemical potentials: 4.3 V relative to Li/Li^+ for the insertion of Li ions into smaller oxygen tetrahedrons and 3.1 V for Li ions to be inserted into larger oxygen octahedrons. [11]

Site energy - The Gibbs free energy is used to estimate the equilibrium potential of electrode materials. Site energy, the main component of the Gibbs free energy, is defined as the contribution of the enthalpy change (H) to the process of ion intercalation. The lower the site energy in a crystal lattice, the more external energy is consumed to transfer one ion from the occupied site to a free state. Different positions possess different site energies and produce different potentials when ions are inserted into or extracted from host materials. In both spinel and olivine crystals, oxygen anions form a robust framework of a closely packed anion sublattice with a densely packed atomic arrangement in three dimensions (3D), whereas layer-structured crystals consist of relatively loose stacks perpendicular to the 2D planes. When subjected to the insertion or extraction of lithium ions, the robust 3D frameworks of spinel or olivine crystal electrodes show negligible structural distortion, retaining the same site energy and displaying an almost constant electrochemical potential. However, the layered structures are distorted to a larger extent than are spinel and olivine crystals, leading to a slight increase in site energy and a sloping potential profile for lithium-ion insertion into layered structures. Sloping charge/discharge potential profiles can also arise from the non-equivalent site energy due to the disordered cations in the crystal lattices in solid solutions or in amorphous materials. [11]

Electronic structure - The electronic structure may be a determining factor for the displayed potential profiles of materials. Therefore, the crystal field theory (CFT) must be introduced, a model that describes the breaking of degeneracies of electron orbital states, usually d or f orbitals, due to a static electric field produced by a surrounding charge distribution (anion neighbors). The interaction between transition metal cation centers and ligands in a tetrahedron or octahedron will induce the splitting of d or f orbitals, as the charges of electrons in the d orbitals and in the ligand repel each other. Thus, the d electrons closer to the ligands will have a higher energy than those further away, which leads to the splitting of the energy of d orbitals. This splitting is affected by the following factors: (i) the nature of the metal ion; (ii) the oxidation state of the metal, with a higher oxidation state leading to a larger splitting; (iii) the arrangement of ligands around the metal ion; and (iv) the nature of the ligands surrounding the metal ion. The consequences of the electronic structure can be discussed with the example of the aforementioned discharge plateaus of spinel $Li_xMn_2O_4$ (Fig. 1.21), which are caused by a phase transition from cubic (tetrahedral Li sites occupied) to tetragonal (smaller octahedral sites)

driven by the Jahn-Teller effect: the intercalation of lithium ions will transfer a corresponding amount of electrons to the high-energy e_g orbital. This results in a strong electrostatic repulsion between the electrons in the p_z orbitals of the oxygen anion and the electron in the d_z^2 orbital of the Mn cation, which pushes the oxygen anions away from the Mn cations along the z-direction. This repulsive interaction causes the cubic spinel phase to transition to the tetragonal spinel phase. [11]

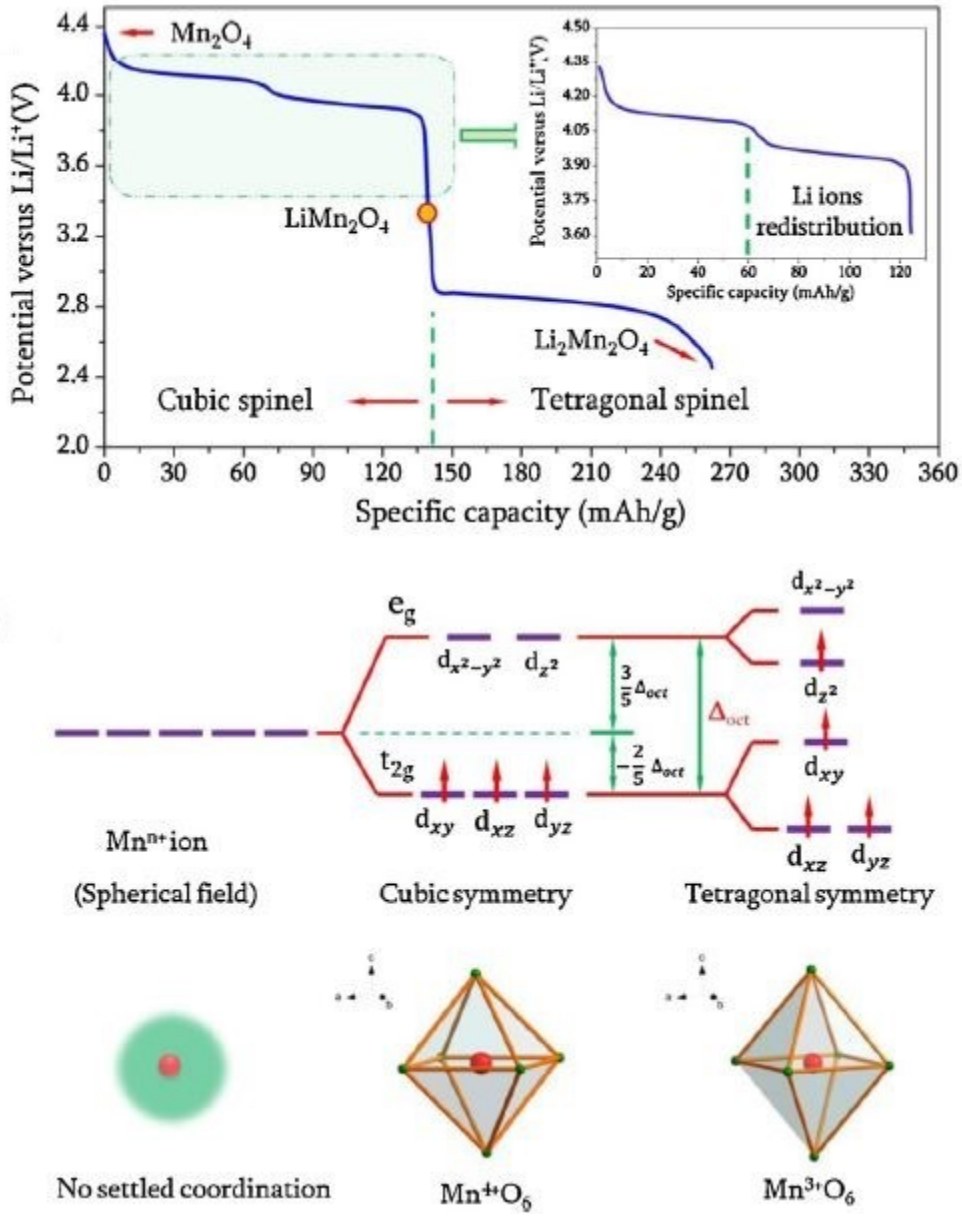

Figure 1.21 - Discharge profile in Lithium manganate, with the phase transition evidenced. Splitting in 3d orbitals induced by the reduction [11]

Once the candidate material has been selected, the synthesis step can still provide improved performances:

Nanostructure - In the past decades, several studies have synthesized and characterized various nanostructured materials for use as lithium-ion battery electrodes, because these nanomaterials have been shown to enhance the electrochemical properties considerably. Extensive studies have illustrated the benefits of nanomaterials as follows: (i) the enhancement of the reversibility of lithium-ion insertion and extraction reaction in nanostructured electrodes without destroying the crystal structure, impossible in micrometer-sized particles; (ii) the reduction in the diffusion or transport distance of the Li ions and electrons accompanying the Li-ion insertion and extraction reactions; (iii) the change in the site energy of Li ions occupying the host lattice, which affects the electrochemical potential of the electrodes. [11]

Defects - Although site energy is the main determinant of the potential plateaus of electrodes, defects are also a factor affecting the electrochemical potential of electrodes. These can be introduced through doping, atmosphere treatment and control of synthesis methods. Alien atoms replace the inherent atoms in the host to produce cation or anion vacancies, which in turn affect the electrochemical performance of the electrode due to the modified chemical pressure, lattice distortion or change in crystal field. Higher-valence cations can introduce cation vacancies, which can increase the corresponding charge storage capacity. Lower-valence cations introduce oxygen vacancies to maintain the electroneutrality and decrease the electrostatic repulsion between the cations, thus decreasing the Li site energy and increasing the potential of doped materials. The oxygen vacancies can play a role in the nucleation for phase transitions, which benefits the rate capability of electrode materials. Larger ions can expand the crystal lattice and increase the bond lengths, reducing the interaction between cations and anions. Thus, the site energy for Li ions decreases with a resulting higher potential. [11]

Amorphous state - Crystalline materials are considered suitable for ion insertion and extraction, because their regular atomic arrangement offers unique spaces for accommodating removable ions. However, an inferior degree of crystallinity has attracted increasing research interest, opening up avenues for developing the electrochemical performance of electrode materials. Mesoporous amorphous materials are conducive to the full infiltration of the electrolyte, which reduce the migrating distance of Na/Li ions, facilitate Na/Li-ion exchange across the interfaces, and tolerate the large volume change of the electrodes during Na/Li-ion insertion/ extraction. These factors greatly enhance the Na/Li-ion storage kinetics and structural stability. [11]

1.4 State of the art

As mentioned, the anode side offers very high storage capacities, but special care must be devoted when developing an anode material (as the history of Whittingham, Goodenough and Yoshino teaches). The most studied anode materials for both LIBs and SIBs will be described, with a deeper focus on the materials that will be investigated in the later sections of this thesis.

Improving the capacity of LIBs: TTMOs

Capacity issues –Graphite is the most used commercial anode material for LIBs because of its low and flat working potential, long cycle life, and low cost. However, the most Li-enriched intercalation compound of graphite has a stoichiometry of LiC_6, resulting in a less-than-desirable theoretical charge capacity (372 mAh g^{-1}) and a small practical energy density. [15]

$$6C + xLi^+ + xe^- \rightarrow Li_xC_6$$

Furthermore, the rate capability of graphite anodes are relatively low, which results in a low power density of the battery. [15]

Almost a decade ago, $Li_4Ti_5O_{12}$ attracted considerable attention as a potential anodic material for LIBs for use in electrochemical energy storage and electric vehicles. $Li_4Ti_5O_{12}$ is a lithium intercalation compound with a high lithium insertion/extraction voltage of approximately 1.55 V, well above the potential for formation of an SEI from the reduction of the organic electrolyte and for the formation of dendritic lithium, thus offering excellent safety. In addition to being nontoxic and relatively inexpensive, the material experiences little change in volume during the lithium insertion/ extraction processes and possesses high thermal stability, ensuring a long cycling lifetime. [16]

$$Li_4Ti_5O_{12} + 3e^- + 3Li^+ \rightarrow Li_7Ti_5O_{12}$$

However, $Li_4Ti_5O_{12}$ exhibits low electronic conductivity and low lithium-ion diffusion coefficient, which greatly limit its rate performance. Further, the generally accepted theoretical capacity is 175 mAh g^{-1}, even lower than the one offered by graphite. [16]

The reversible intercalation of lithium ions, which does not induce major structural changes, is mostly limited by the changes the crystal structure is able to withstand, and to the intrinsic limited redox activity (i.e., number of exchanged electrons) of the transition metals. There is general consensus that such limitation handicaps the device in terms of energy density, so that breakthroughs in performance will only come from the development of novel concepts in materials research. [17]

Ternary Transition Metal Oxides - Recently, Ternary Transition Metal Oxides (TTMOs) with general formula AB_2O_4 and spinel structure have been considered as novel alternatives for LIBs. In $M_2M'O_4$ (M= Co, Fe, Mn and Ni; M' = Sn, Ge and Si) system, during the first discharge process the active material is converted into its constituent elements (M and M'), followed by the formation of an amorphous Li_2O matrix and electrolyte decomposition at 0.6 to 0.7 V vs. Li/Li^+. Subsequently, the M' reacts with lithium to form Li_xM' (Li- alloying formation) at 0.1 to 0.3 V vs. Li/Li^+. During charging process, de-alloying reaction takes place at 0.5 to 0.8 V vs. Li/Li^+, and yields individual metals (M and M'). Subsequently, this

metal particles act as catalyst to decompose the Li_2O amorphous matrix and form the corresponding oxides (MO_x and $M'O_x$), according to conversion reaction mechanism. In the case of $MM_2'O_4$ (M = Ni, Mn, Co and Fe; M'=Ni, Mn, Co and Fe), the elements M and M' are involved in conversion reaction mechanism. During the first discharging process, the crystal structure destructed into individual metal particles accompanying with the formation of Li_2O matrix. As produced metal particles facilitate the electrochemical activity by means of formation/decomposition of Li_2O that give the way for conversion reaction mechanism. [18]

Compared with traditional metal oxides, TTMOs are attracting great research interest as anodes in LIBs owing to the combination of the advantages of both conversion and alloying reactions: the M_xO generated from the conversion reaction acts as a soft matrix to buffer the volume expansion of Li alloying/de-alloying; higher capacity is obtained thanks to the alloying reaction; higher electrical conductivity than simple metal oxides; higher environmental friendliness than the traditional metal oxides, particularly for cobalt oxides. [19]

Issues - The main issue of TTMOs is given by electrode pulverization, which is intrinsic to this class of compounds: in contrast to a generic insertion process of Li-ions in an open oxide framework (MO_2 +Li $\rightarrow$ $LiMO_2$) which comes with a 33% rise in the number of atoms, a dense metallic particle has to accommodate one Li per metal, with a 100% rise in the number of atoms. Also, the corresponding volume change is very high, due to the high atomic radius Li in its metallic state (2.05 Å), far higher than those of commonly studied host atoms (Sn: 1.72 Å, Si: 1.46 Å, Pb: 1.81 Å, Sb: 1.53 Å, Al: 1.82 Å). As a consequence, a lithiated particle will always have a much larger radius than the original unlithiated one. [20] In order to minimize volume changes, different strategies are possible: coating of the active material with an electrochemically inert material with good ionic and electronic conduction (carbon is the most common choice) or nanostructuration, that allows to accommodate the volume changes in the particles thanks to careful morphological design.

$ZnFe_2O_4$ - Among TTMOs, $ZnFe_2O_4$ (ZFO) stands out from the others because of its low cost, low toxicity, environmental friendliness and especially high theoretical specific capacity (1000.5 mAh/g) due to the combination of intercalation, conversion and alloying reactions:

I. Intercalation - $ZnFe_2O_4 + 0.2Li^+ + 0.2e^- \rightarrow Li_{0.2}ZnFe_2O_4$
II. Conversion – $Li_{0.2}ZnFe_2O_4 + 7.8Li^+ + 7.8e^- \rightarrow 4Li_2O + Zn + 2Fe$
III. Alloying – $Zn + Li^+ + e^- \rightarrow LiZn$
IV. Conversion – $Zn + Li_2O \rightarrow ZnO + 2Li^+ + 2e^-$
V. Conversion – $2Fe + 2Li_2O \rightarrow 2FeO + 4Li^+ + 4e^-$

Generally, the first cycle is considered to be an irreversible reaction, always showing high irreversible capacity due to the formation of the SEI layer together with amorphous-Li_2O. In later cycles, the discharge capacities decreased due to the volume expansion of the active material, caused by the alloying–de-alloying- and conversion-reaction mechanisms. [18]

However, there is no general consensus on the reaction sequence, because other authors [21] claim that the reaction sequence proceeds as follows:

I. Intercalation - $ZnFe_2O_4 + 0.5Li^+ + 0.5e^- \longrightarrow Li_{0.5}ZnFe_2O_4$
II. Intercalation - $Li_{0.5}ZnFe_2O_4 + 1.5Li^+ + 1.5e^- \longrightarrow Li_2ZnFe_2O_4$
III. Conversion - $Li_2ZnFe_2O_4 + 6Li^+ + 6e^- \longrightarrow 4Li_2O + Zn + 2Fe$
IV. Alloying - $Zn + Li^+ + e^- \longrightarrow LiZn$

With other side reactions that can occur during charge, alongside the reversed reactions I-IV:

V. $Zn + Li_2O \longrightarrow ZnO + 2Li^+ + 2e^-$
VI. $2Fe + 3Li_2O \longrightarrow Fe_2O_3 + 6Li^+ + 6e^-$

Spinel structure – The ideal spinel structure consists of a cubic close-packed array of anions in which 1/8 of the tetrahedral and ½ of the octahedral interstices are occupied by cations. The arrangement of atoms is such that, perpendicular to each three-fold axis, layers occupied only by cations in octahedral coordination alternate with others in which the tetrahedral and octahedral sites are filled in the ratio 2:1 (Fig. 1.22). The unit cell of $ZnFe_2O_4$ (s.g. $Fd\bar{3}m$) contains 8 formula units. [22]

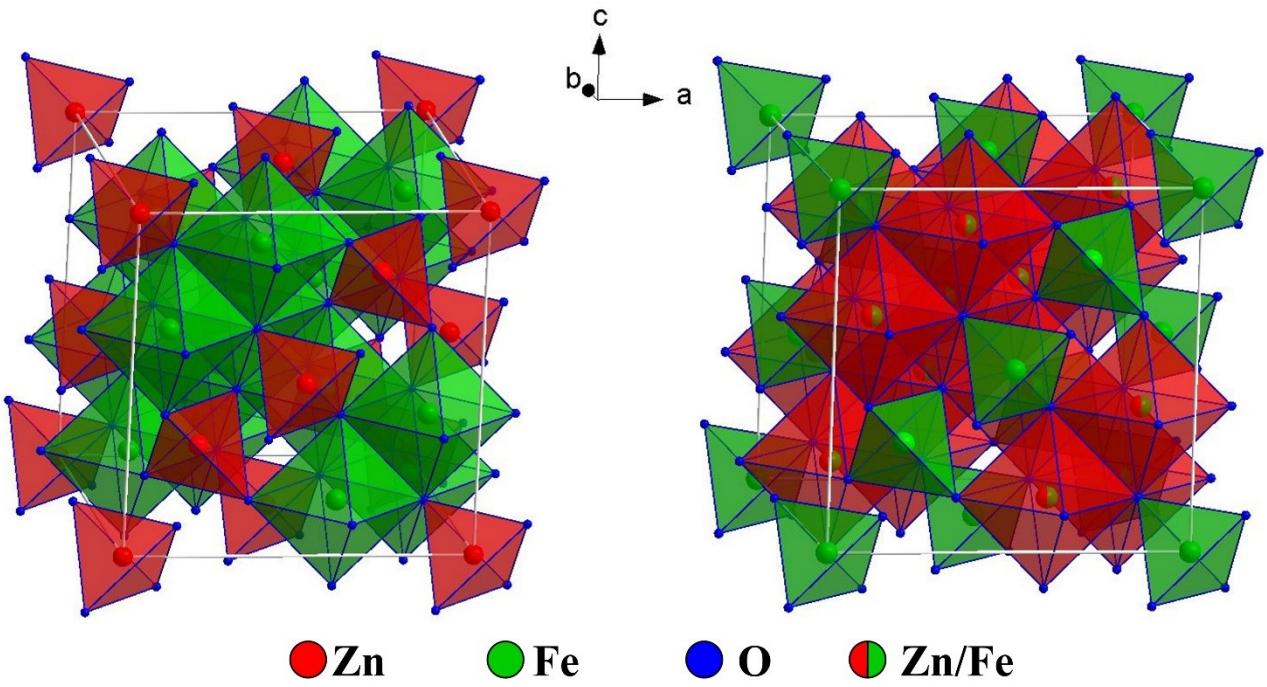

Figure 1.22 – The spinel structure of $ZnFe_2O_4$, with coordination polyhedra in the direct (left) and inverse (right) cation distribution.

The general formula in this kind of structures is often described as AB_2X_4, where A^{2+} occupies tetrahedral sites while B^{3+} occupies the octahedral sites in the cation distribution that is referred to as "direct" spinel. However, in this kind of structures, different distributions of cations are possible: the 'inverse' distribution $B[AB]X_4$, and all the intermediate cation distributions, represented as $(A_{1-x}B_x)[A_xB_{2-x}]X_4$, where x is the so-called degree of inversion, equal to zero and unity for the normal and inverse arrangements respectively. [22]

Even if the direct cation distribution is thermodynamically favoured, many factors can affect the degree of inversion, such as the thermal treatment during the synthesis and the grain size:
It is well known for bulk ZFO that the cation relocation is a temperature-dependent reversible process. Hence, increasing degrees of inversion can be obtained for the ZFO samples by calcination at growing temperatures followed by quenching. Although it is reported that the degree of inversion generally increases as the grain size decreases, it is also well known that particles with similar grain size can also exhibit different degrees of inversion. Therefore, the degree of inversion cannot be directly correlated to the grain size. [23]

Aim of the work – During my doctoral studies, the structural features of $ZnFe_2O_4$ prepared in different ways were investigated and correlated with the corresponding electrochemical performance of the $ZnFe_2O_4$-based electrodes. The complex reaction of $ZnFe_2O_4$ with Lithium was investigated with multiple electrochemical techniques, as well as *operando* X-Ray Diffraction.

Improving the capacity of LIBs and SIBs: tin and tin oxides

As already mentioned, improving the capacity of anode materials for LIBs is a relevant technological challenge. Alongside TTMOs, also tin and tin oxides are considered high-capacity anodes, that also have the benefit of reacting with both Li and Na. Since the charge storage mechanism shows little variations between the two chemistries, most of the introduction on tin and tin oxides will be focused on their activity in Sodium-Ion Batteries.

Anode materials for NIBs – Since Na metal suffers from dendrites formation on its surface, its use in NIBs is hampered and different kind of materials must be developed. The following list includes materials that can store Na^+ ions through intercalation, conversion and/or alloying reactions:

- *sp^2 carbons* - These are the most studied and promising carbonaceous materials as negative electrodes for sodium ion batteries. Although some reports can be found on sp^3 carbons as well, as nanostructures or thin films, they are generally not suitable as active negative electrode material as they tend to be wide band gap semiconductors with typically low electronic conductivity.

- *Organic compounds* – There are several organic compounds that react reversibly with Na^+ ions, C-H-, carboxylate- and C-N-based ones being the most interesting. Closely related hybrid organic–inorganic, or organometallic systems based on conversion reactions such as transition-metal carbodiimides (MNCN, M = Cu, Zn, Mn, Fe, Co and Ni) or metalorganic frameworks such as Prussian blue analogues are also mentioned. However, most of the problems inherent to the work with organics and polymers, such as the need of a large amount of conductive carbon or the large first-cycle coulombic inefficiency, mostly remain unsolved.

- *Transition-metal-based compounds* - Only Ti-based and V-based compounds undergo intercalation reactions at low voltage. Binary oxides based on Fe, Co, Ni, Cu, Mn, and Mo react with Na^+ through a conversion reaction, and although enormous specific capacities can be achieved through conversion, the large hysteresis, low coulombic efficiency, and poor cyclability are a major drawback that remains unsolved even for Li-ion batteries. Post-transition metal

oxides, for instance SbO_x, SnO_x, or ZnO, show conversion reaction followed by alloying, except Bi_2O_3, which exhibits a conversion–insertion mechanism. Niobium oxide, Nb_2O_5, exhibits the sodium intercalation reaction mechanism.

- *Sn, Sb and P-based compounds* - Despite that these are negative electrodes with proven performance in Li-ion lab cells, their potential applied to NIB technologies has not been fully demonstrated yet. Owing to their large abundance and very high capacity we consider them key materials for the developments of NIBs. Of course, negative effects associated to large volume changes (well above the 30% maximum volume change allowed for commercial applications) and stable cycling will have to be thoroughly addressed before these materials can reach the commercial stage, either in LIBs or NIBs.

Why tin and tin oxides for NIBs? - One of the most important players in the cyclability of NIBs is the electrode–electrolyte interphase (EEI): SEI in the negative electrode and solid permeable interface (SPI) in the positive electrode. The electrode surface passivation for Na-ion cells is less favourable than for Li-ion cells. This has been ascribed to Lewis acidity difference of Li and Na ions, which is higher for Li^+ than for Na^+. Surface films formed on noble metal electrodes when using Li salt solutions are more stable than when using Na salts, the origin being the higher solubility for Na-based compounds than for Li-based. From the comparison of the reversible and irreversible 1st cycle specific capacity of selected negative electrodes (Figure 1.23) it can be concluded that the irreversible capacity loss is a problem for most of them, hard-carbons and alloys being the most promising options. [13] Even though carbons are very interesting materials, they will not be discussed because the chosen research topic is alloying-based compounds.

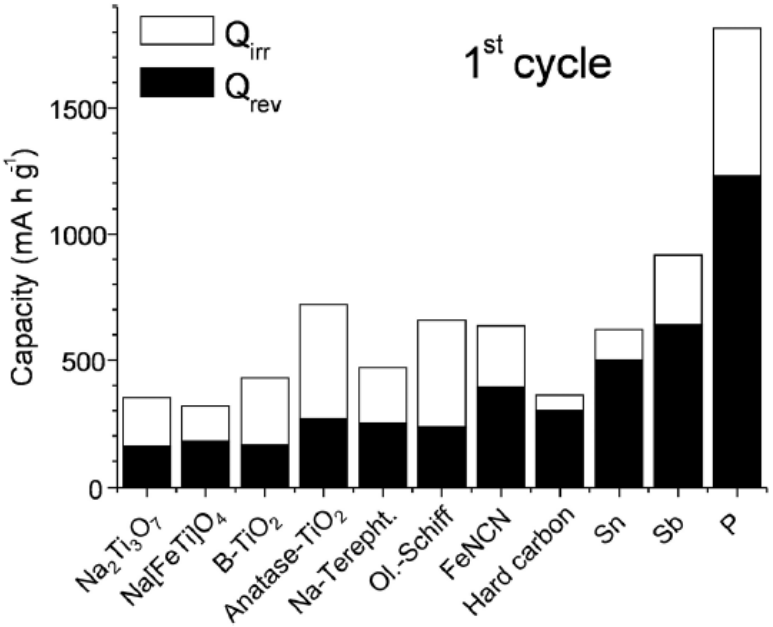

Figure 1.23 - Reversible and irreversible 1st cycle specific capacity for negative electrode materials in NIBs [13]

Alloying - A quite large number of metals and nonmetals such as tin, antimony, bismuth, lead, germanium, and phosphorus offer high theoretical capacity values as a result of the multiple electron exchange associated with the alloying process. However, it is well known that they suffer from severe structural changes upon cycling associated with large volume expansion and consequent electrode disintegration and capacity fading. The freshly exposed electrode material upon every alloying cycle implies a continuous electrolyte reduction, strongly affecting the overall Coulombic efficiency and cycle life. In addition, slow reaction kinetics lead to inferior rate capability and power performance with respect to insertion-based materials. To address these issues, enormous research and technological efforts in terms of nanostructuration have been devoted. [12] Alloy reactions of elements such as Si, Sn, Sb, Ge, or P with Li have been extensively studied as negative electrodes for Li-ion batteries because their theoretical specific charge is higher than that of carbonaceous materials. For similar reasons, these alloying elements are considered promising negative electrode materials for Na-ion batteries. [13]

Conversion-alloying - Recently an interesting group of oxides and sulfides based on group IV and V elements, herein named as conversion-alloying materials, have received increasing attention as anode materials. These compounds offer the possibility to reach high specific capacities while lowering the average working potential of conversion anodes, generally occurring above 0.4 V (vs Na/Na^+). In addition, the Na_2O formed during the conversion reaction may act as buffering matrix for the subsequent alloying reaction, generally occurring at lower potentials (Fig. 1.24). Moreover, these materials benefit from the enhanced conductivity of the electrode due to the formation of metallic nanoparticles upon the conversion reaction. The most studied conversion–alloying materials are SnO_x, SnS_x, Sb_2O_3, and Sb_2S_3. [12]

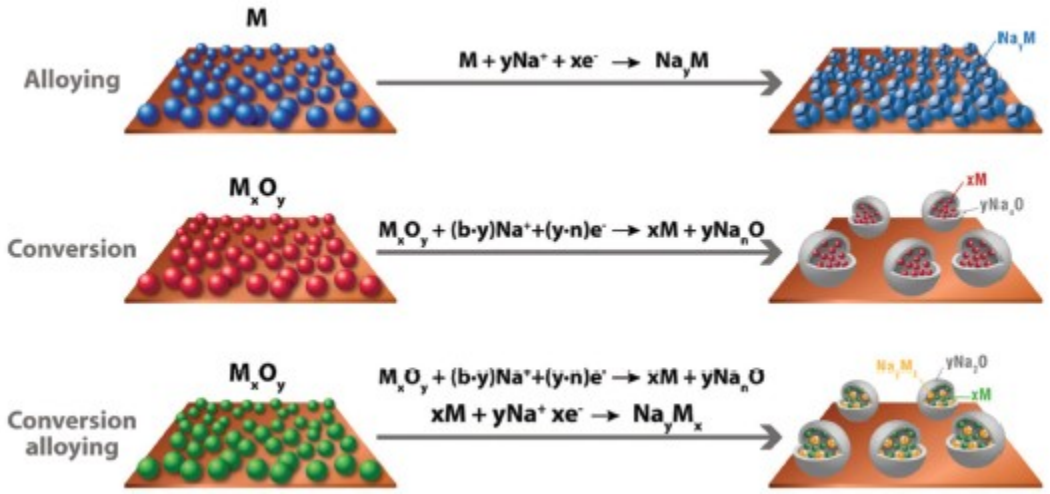

Figure 1.24 - Schematic reaction mechanisms of alloying, conversion and conversion–alloying [12]

Main challenges for both mechanisms – The alloying and conversion-alloying reactions show some problems that must be tackled with different strategies:

- *Nanostructuration* - Nanocrystallization is an important modification method to improve the cycling stability of Sn-based materials. Remarkably, nanoparticles can decrease the absolute volume change of every single particle with the rate of third power of particle diameter. As a result, the absolute strain is efficiently mitigated and the structural stability of the material is greatly enhanced. In addition, nanoparticles shorten the charge-diffusion route for both ions and electrons and supply abundant electrochemically active sites. The characteristic diffusion time of ions in active electrode materials can be represented as: $\tau = L^2/D$, where L is the ion diffusion distance, D is the ion diffusion coefficient. The diffusion time (τ) decreases with the square of diffusion distance (L^2), so the rate capability can be effectively improved by reducing the particle size. Furthermore, the interspace among nanoparticles can accelerate the infiltration of electrolyte and provide reserved buffer space for volume expansion. [24]

- *Aggregation or disgregation* - Nanoscale Sn particles suffer from aggregation after cycling, while some micron-sized particles coarsen after cycling and split away off the matrix, leading to the rapid deterioration of capacity. As schematic shows, the decline of nanoscale particles is mainly due to the limitation of kinetics resulting from the particle aggregation. In contrast, the loss of effective active materials in micron-sized sample resulted in unrecoverable capacity fading. Nanostructured Sn can promote the homogeneous lithiation/delithiation in a single particle and alleviate the volume mismatch, thus avoiding crack propagation and improving structural stability. However, because of the soft nature of Sn, aggregation inevitably occurs after cycling even in 30 nm Sn particles. [24]

- *SEI formation* - The first cycle irreversible capacity is exacerbated when getting to nanostructured electrodes, in which the higher surface area leads to increased amount of electrolyte decomposition. [12] The addition of fluoroethylene carbonate (FEC) could help to improve the cycling performance by forming high-quality SEI films and restraining side reactions. FEC could impede the superfluous SEI formation and reduce the irreversible Na+ exhaustion during cycling. The nano-Sn (5–10 nm) with FEC cycled steadily after the initial 15 cycles. In contrast, nano-Sn without FEC underwent a continuous capacity fade. However, the mitigating effect on capacity fade was not observed in micron-sized Sn (0.1–0.2 μm), which rapidly failed after 15 cycles even with FEC (Figure 1.25). The huge volume expansion caused cracks and the long ion diffusion path aggravated the crack propagation, leading to the particles pulverization and continuous SEI formation on the newly exposed surfaces. As a result, the protection mechanism of high quality SEI is invalid in microparticles. [24]

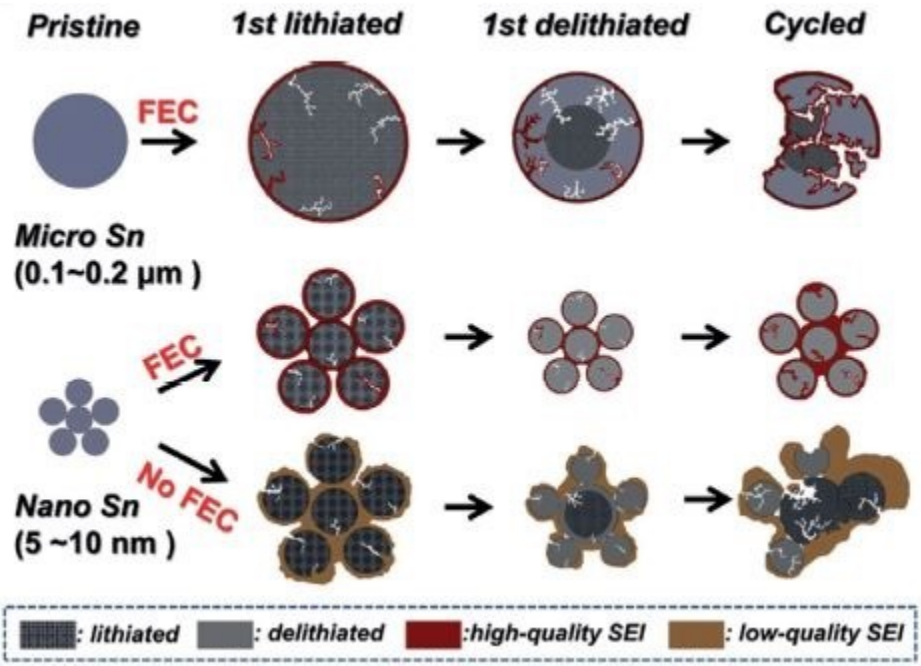

Figure 1.25 - Schematic illustration of the formation and degradation mechanisms of SEI films in Sn electrodes [24]

Tin - One of the most promising alloying materials for Na-ion batteries in terms of theoretical specific charge is tin (Sn, 847 mAh g^{-1}). The reversible (de)sodiation of tin shows several plateaus below 0.7 V, which correspond almost perfectly with the calculated reaction path through $NaSn_5$, NaSn, Na_9Sn_4, and $Na_{15}Sn_4$. Different authors with different techniques often found differences in intermediate phases ($NaSn_3$, $NaSn_2$…) and their crystallinity. Depending on the size of Sn particles present in the Sn:C:polyvinylidene fluoride (PVDF) electrode, the particles undergo different levels of morphological changes: low between 0.5 and 1.6 μm, high above 1.6 μm, and negligible below 0.5 μm. The cycling stability shown is fairly good despite that a degradation reaction of PVDF binder in Na-ion batteries has been reported. Nevertheless, poor capacity retention can be obtained from pure Sn nanoparticle electrodes, mainly due to the volume change of electrode material. In order to improve the stability of Sn, different composites with carbon and Sn-based active/inactive intermetallics have been synthesized. M-Sn intermetallics can convert to M/Sn composites with M providing electrical conductivity (inactive metals such as Co, Fe, Cu or Ni) and acting as a matrix to alleviate the strain produced by volume changes. [13]

Tin oxides - Tin oxides (SnO and SnO_2) have been considered as promising anodes for SIBs and recently attracted great interest due to their high theoretical capacity, environmental benignity, and low cost. Basically, SnO_x reacts with Na first via conversion reaction ($SnO_x + 2xNa^+ \rightarrow Sn + xNa_2O$) and then the reduced Sn metal alloys with Na through alloying reaction ($4Sn + 15Na^+ \leftrightarrow Na_{15}Sn_4$), both contributing to the high specific capacity. The Na_2O matrix accommodates the volume expansion of Sn nanoparticles and alleviates the agglomeration during alloying reaction. Although tremendous efforts have been devoted to improve the electrochemical performance, such as the implementation of nanostructured

electrodes and carbon coatings, still the reported specific capacity is much lower than the theoretical value, which may be due to the sluggish kinetics of the reaction with sodium. In addition, it should also be considered that Na_2O suffers, as many other oxides, from low electrical conductivity. Recent reports on SnO suggested it as a promising anode due to the properties of its layered structure and improved reversibility. However, SnO is thermodynamically less stable than SnO_2 and hence more difficult to be obtained. [12]

Aim of the work – In this work tin metal and tin oxides were tested as anode materials for LIBs and NIBs. The performance of the tin-based electrodes prepared in different ways will be compared and analysed, thanks to a combined approach. The carbonaceous matrix of tin/carbon composites will be characterized (alongside the active materials) with suitable techniques, and morphology-electrochemistry correlations will be established.

Improving the rate capability: Niobium oxides

Research interest - Any material that can reversibly store Li-ions with a suitable potential window can serve as anode material, giving birth to a wide range of selectivity. Based on the intercalation mechanism, numerous anode materials including carbon-based, TiO_2, and $Li_4Ti_5O_{12}$ are popular intercalation-type electrodes. Developing advanced intercalation-type anode materials can significantly enhance the electrochemical performances of battery systems. In addition, owing to the increasing demand for electric vehicles and hybrid electric vehicles, the hybrid supercapacitors (HSCs) have captured tremendous research interests. HSCs are made up of capacitor-type cathode and battery-type anode. However, the slow redox reactions derived from battery-type anodes hinder the electrochemical performances of the overall HSCs. Therefore, developing superior intercalation-type anode materials with fast charge–discharge storage capability has a vital role. [25]

Voltage issues – As mentioned before, the desirable features for an anode include low working potential but high capacity, safety and fast Li^+ ions conduction. Even if the Li metal anode has the lowest working potential possible in a LIB (being the reference reaction of the potential scale), and unpaired capacity (3850 mAh/g), the electrolytes are reduced by anodes having a voltage V < 1.0 V versus Li^+/Li unless the anode is passivated by a Li-permeable SEI layer. The SEI layer formed on a lithium anode prevents uniform plating out of Li during charge, and on repeated charge/discharge cycling, dendrites forming on the anode can grow across the separator to short-circuit a cell and set fire to the flammable electrolyte. So far, a lithium anode has only been used in a “half-cell” configuration at laboratory scale, to obtain the performance of a candidate electrode. Insertion of Li^+ ions into a graphitic carbon (Fig. 1.26) is a staging process of C to LiC_6, which gives a flat V ≈ 0.2 V versus Li^+/Li. Therefore, carbon or a carbon-buffered Li alloy is used as the anode where a high battery voltage is required. However, a LiC_6 charged anode forms a passivating SEI layer that, though permeable to Li, consumes Li^+ ions from the cathode unless the SEI layer is preformed on the anode before cell assembly. The solid cathodes of existing rechargeable lithium-ion batteries are all insertion compounds of limited capacity to receive Li^+ ions into their host structure, which means that formation within the cell of the SEI layer on a carbon anode reduces further the limited specific capacity of a cell. Moreover, the rate of Li transfer across the SEI layer must compete with the rate of Li plating on the surface of the SEI layer where the voltage

during charge raises the electron potential above that of Li^+/Li. If the Li transfer across the SEI layer is not fast enough to prevent plating out of lithium on the anode during a fast charge, dendrite formation may short-circuit the cell, which limits the safe charging rate of the battery. These problems associated with an SEI layer are found wherever the voltage of the anode is V < 1.0 V versus Li^+/Li. The spinel $Li_4Ti_5O_{12}$ is reported to be a stable anode operating on the Ti(IV)/Ti(III) redox couple located at 1.5 V versus Li^+/Li; it is capable of a faster charge and a long cycle life because no SEI layer is formed. However, it has a low specific capacity (~140 mAh/g), and the loss of 1.3 V relative to carbon reduces the energy density of a cell using this anode. Therefore, there is a motivation to identify a solid anode with a higher capacity and having a voltage in the range of 1.1 < V < 1.5 V versus Li^+/Li. [14]

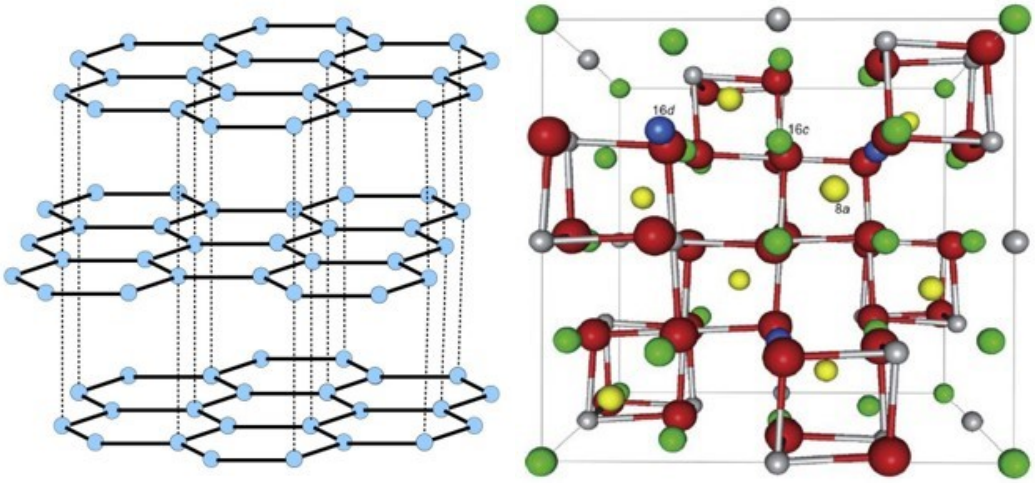

Figure 1.26 - Structures of graphite (left) and lithium titanate (right)

Niobium oxides - While strategies like nanostructuring have been used extensively to improve high-rate performance in materials like $Li_4Ti_5O_{12}$, this has many drawbacks, including high cost, poor stability, and poor volumetric energy density. However, nanostructuring is not necessary to obtain high rates. Recent works have shown that very high rates can be achieved in micrometre-sized particles of complex oxides of niobium. [26] Niobium-based oxides anodes are raising more and more attention with very high theoretical capacity (Nb_2O_5 ≈200 mAh g^{-1} and $TiNb_xO_{2+2.5x}$ compounds ≈ 388–401 mAh g^{-1}). Niobium- based oxides are a big family including Nb_2O_5, $TiNb_2O_7$, $Ti_2Nb_{10}O_{29}$, $TiNb_6O_{17}$, $TiNb_{24}O_{62}$ and so on. Most of them have a high working potential (>1.0 V vs Li^+/Li) that can prevent the formation of SEI film and lithium dendrites, ensuring the safety of the working batteries. Most of Ti–Nb–O family can be presented using the chemical formula as $TiNb_xO_{2+2.5x}$, with a Wadsley–Roth shear crystal structure, which are built by m × n × ∞ ReO_3-type blocks (Fig. 1.27). Among them, m and n represent the length and width of the blocks in numbers of octahedra, respectively. Moreover, all the Ti^{4+} and Nb^{5+} ions are disordered in octahedral sites sharing corners and edges. Such open Wadsley–Roth shear structure can lead to a large Li-ion diffusion coefficient, which shows promising applications in energy storage systems. In addition, $TiNb_xO_{2+2.5x}$ family have a high operating voltage of ≈ 1.6–1.7 V (vs Li^+/Li), which can match well with the lowest unoccupied molecular orbital (LUMO) of the organic liquid-carbonate electrolyte, avoiding the formation of SEI layer and lithium dendrite and ensuring the safety of

batteries. [25] Furthermore, as lithium does not alloy with aluminum until 300 mV vs Li^+/Li, copper foil can be substituted with significantly cheaper and lighter aluminum foil as the anode current collector. [27]

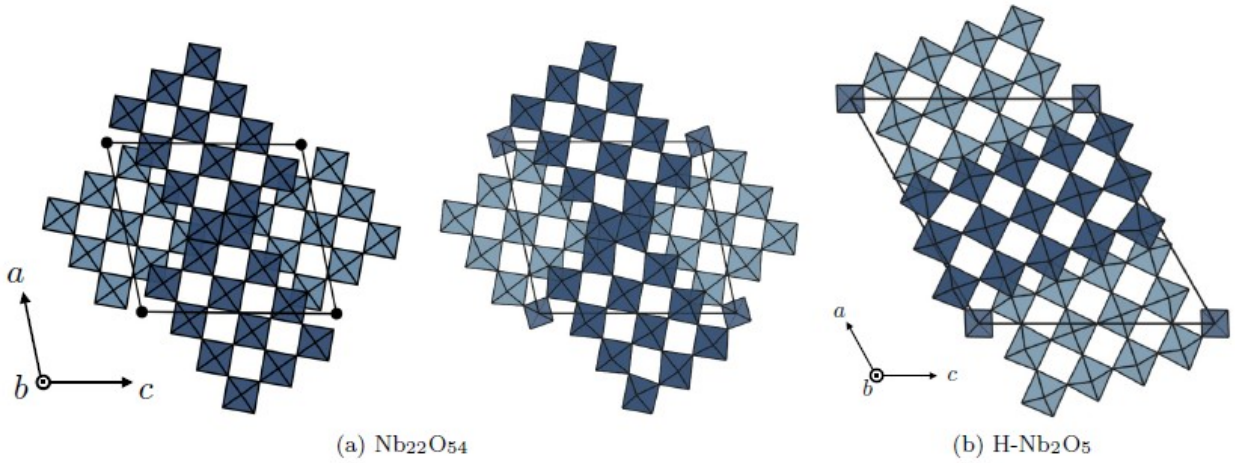

Figure 1.27 - Structure of example crystallographic shear niobium oxides [28]

M-Nb-O - However, the intrinsic low electrical conductivity and Li-ion diffusion coefficients hinder their practical applications in LIBs. In view of these two factors, exploring anode materials with similar structural merits to $TiNb_xO_{2+2.5x}$ compounds but with intrinsic higher electrical conductivity and larger Li-ion diffusion coefficients is significant and challenging. Moreover, it is well known that the shear ReO_3 crystal structure is open and stable, and all the transition metal ions are disordered in octahedral sites sharing corners and edges. In addition, the Li-ion diffusion coefficients are very sensitive to the unit cell volume. Therefore, using appropriate transition metal ions to replace M sites in M–Nb–O family can be expected to perform improved electrochemical performances. [25]

$FeNb_{11}O_{29}$ - The use of $FeNb_{11}O_{29}$ in electrochemical cells was suggested in 2014. [29] Taking advantage of the Niobium reductions (from 5+ to 4+ and 3+), it can store 23 Li^+ ions per formula unit, giving a theoretical capacity of 400 mAh/g, one of the highest among intercalation anodes. It shares the features of M-Nb-O oxides, such as safety, good rate capability and cycling stability, but also the main drawback of the poor electronic conductivity (just the electrons deriving from Fe^{3+} can participate to the electronic conduction). To tackle this issue, some articles attempted, successfully, the doping [30], [31] or the introduction of oxygen vacancies. [32] Another way of improving the performances is the nanostructuration, which is beneficial in terms of the reduction in the diffusion or transport distance of the Li ions and electrons. In 2019 $FeNb_{11}O_{29}$ nanotubes were employed both in test cells and in full cells with $LiCoO_2$, $LiMn_2O_4$ and $LiFePO_4$, showing good results. [33]

Superior intercalation materials for LIBs: pseudocapacitance

In this chapter the key features of pseudocapacitance will be explored, with particular reference to $FeNb_{11}O_{29}$. This will help the understanding of many experimental results that will be discussed later in the text.

Pseudocapacitance – Batteries keep our devices working throughout the day—that is, they have a high energy density—but they can take hours to recharge when they run down. For rapid power delivery and recharging (i.e., high power density), electrochemical capacitors known as supercapacitors are used. One such application is regenerative braking, used to recover power in cars and electric mass transit vehicles that would otherwise lose braking energy as heat. However, supercapacitors have low energy density. Batteries and supercapacitors both rely on electrochemical processes, although separate electrochemical mechanisms determine their relative energy and power density. During the past years, the energy storage field has witnessed a dramatic expansion in research directed at materials that might combine the high energy density of batteries with the long cycle life and short charging times of supercapacitors. The electrochemical processes occurring in batteries and supercapacitors give rise to their different charge-storage properties. In lithium ion (Li^+) batteries, the insertion of Li^+ that enables redox reactions in bulk electrode materials is diffusion-controlled and can be slow. Supercapacitor devices, also known as electrical double-layer capacitors (EDLCs), store charge by adsorption of electrolyte ions onto the surface of electrode materials. No redox reactions are required, so the response to changes in potential without diffusion limitations is rapid and leads to high power. However, the charge is confined to the surface, so the energy density of EDLCs is less than that of batteries. In the 1970s, Conway and others recognized that reversible redox reactions occurring at or near the surface of an appropriate electrode material lead to EDLC-like electrochemical features but the redox processes lead to much greater charge storage. This pseudocapacitance represents a second mechanism for capacitive energy storage. The most widely known pseudocapacitors are RuO_2 and MnO_2; recently this list has expanded to other oxides, as well as nitrides and carbides, as different pseudocapacitance mechanisms have been identified. Pseudocapacitive materials hold the promise of achieving battery-level energy density combined with the cycle life and power density of EDLCs. [34]

Intercalation pseudocapacitance - Intercalation pseudocapacitance occurs when ions intercalate into the tunnels or layers of a redox-active material accompanied by a faradaic charge-transfer with no crystallographic phase change. Electrochemically, pseudocapacitance gives rise to specific features that can be recognized on the basis of the response to (a) a voltage sweep, as in cyclic voltammetry; (b) constant current, as in galvanostatic cycling, and (c) alternating current, as in impedance spectroscopy. [35]

Intrinsic or extrinsic - Pseudocapacitance can be intrinsic to a material or extrinsic, i.e. the property can emerge through appropriate material engineering. Intrinsic pseudocapacitive materials display the characteristics of capacitive charge storage for a wide range of particle sizes and morphologies (e.g. RuO_2*nH_2O, MnO_2 and Nb_2O_5). On the other hand, extrinsic materials do not exhibit pseudocapacitance in the bulk state due to phase transformations during ion storage. With these materials, increasing the surface area through nanostructuring leads to improved high-rate behaviour due to a decrease in diffusion distances and in some cases, the suppression of a phase transformation (many transition metal oxides, e.g. the previously mentioned $LiCoO_2$, Fig. 1.28). [35]

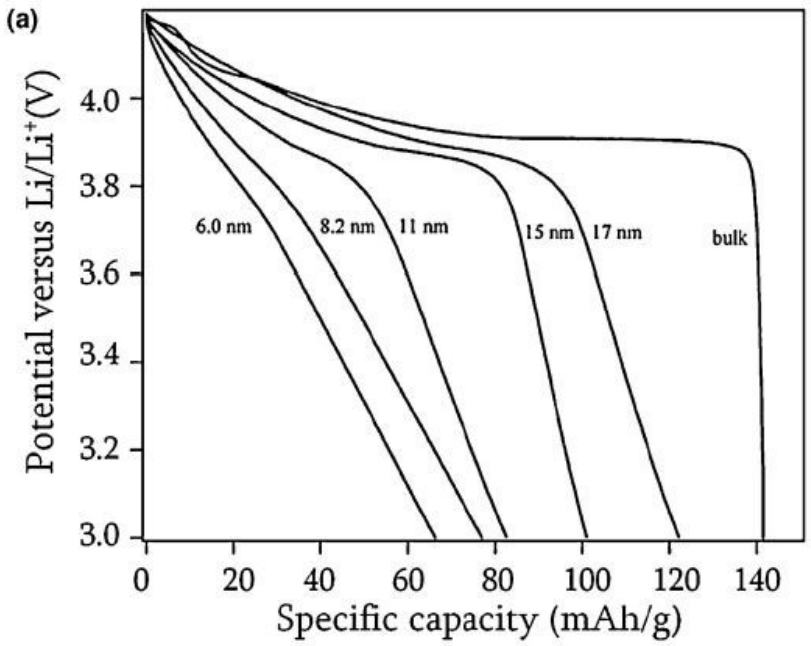

Figure 1.28 - Discharge profile of $LiCoO_2$ with different particle sizes [11]

Pseudocapacitance in T-Nb_2O_5 - While the electrochemical energy storage capabilities of Nb_2O_5 have been known since 1980, only recently has the pseudocapacitive behavior of orthorhombic T-Nb_2O_5 been identified. In general, the charge storage of T-Nb_2O_5 occurs due to the insertion of lithium ions in non-aqueous electrolytes at a potential of < 2 V vs. Li/Li^+. Based on the redox of the $Nb^{+5/+4}$ couple, charge storage occurs up to 2 Li^+/Nb_2O_5, and recent results suggest it as a promising material in lithium-ion non-aqueous electrolytes because at a timescale of 1 minute and utilizing a composite electrode with an active material mass loading of 1–1.5 mg cm^{-2}, the capacitance was 67% of the theoretical capacitance. Further, this type of intrinsic pseudocapacitor does not need high-surface areas (exposure of the surface of T-Nb_2O_5 to the electrolyte is not critical for high rate behavior), being a beneficial feature for practical devices. [35]

… and in other niobium oxides - The pseudocapacitive behavior in Nb_2O_5 is highly dependent upon the presence of a crystalline structure: amorphous Nb_2O_5 exhibits lower specific capacitance values than T-Nb_2O_5 despite the fact that the amorphous material has a much higher surface area. The structure of T-Nb_2O_5 consists of sheets of corner- or edge-sharing Nb^{+5} polyhedra along the (001) plane that are coordinated by 6 or 7 O^{2-}. Computations indicate that the (001) plane exhibits low energy barriers for lithium ion transport and gives rise to the pseudocapacitive behaviour observed in the material. [35] Many other niobium oxides share common structural features with Nb_2O_5, and indeed many other Nb oxides have been discovered to possess pseudocapacitive features (Fig. 1.29): recent works have shown that very high rates can be achieved in micrometer-sized particles of complex oxides of niobium, ternary Nb/W oxides, and ternary Ti/Nb oxides. Crystallographically, these complex oxides fall into two structural families: compounds with a tungsten bronze-type structure (T-Nb_2O_5 and $Nb_{18}W_{16}O_{93}$) and

Wadsley−Roth phases (compounds in the Nb_2O_5−WO_3 and Nb_2O_5−TiO_2 phase diagrams, in addition to pure Nb_2O_5 and Nb_2O_5−δ phases) with block-type structures. [26]

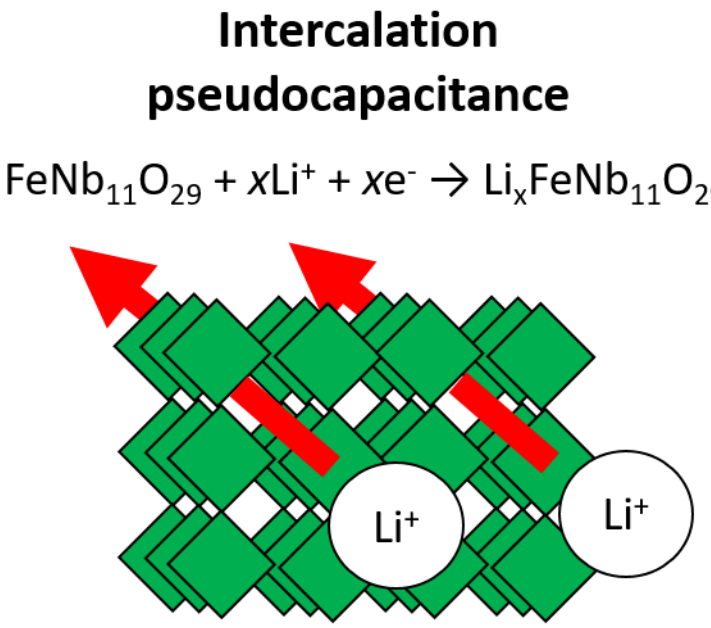

Figure 1.29 - Intercalation pseudocapacitance in the block-structure of $FeNb_{11}O_{29}$

Aim of the work – $FeNb_{11}O_{29}$ exhibits promising intrinsic pseudocapacitive features, however, many research works are still necessary before commercialization of a $FeNb_{11}O_{29}$-containing electrode. One of such research works, that holds particular relevance, is provided by the full comprehension of the intercalation reaction. In the master's degree thesis (as well as in already published papers), structural aspects related to the shear structures of $FeNb_{11}O_{29}$ [36], [37] and to the redox chemistry of the different polymorphs of the niobate [38] were investigated. In this work, the chemistry and electrochemistry of the intercalation of Li^+ ions in the structure of both the polymorphs of $FeNb_{11}O_{29}$ were investigated through advanced electrochemical techniques and with in situ/operando studies involving spectroscopic and diffraction analyses.

1.5 References

[1] N. S. Lewis, “Powering the Planet,” in *MRS spring meeting, San Francisco*, 2007, vol. 32, no. October, pp. 808–820.

[2] D. Larcher and J. M. Tarascon, “Towards greener and more sustainable batteries for electrical energy storage,” *Nat. Chem.*, vol. 7, no. 1, pp. 19–29, 2015.

[3] M. A. Hannan, M. M. Hoque, A. Mohamed, and A. Ayob, “Review of energy storage systems for electric vehicle applications : Issues and challenges,” *Renew. Sustain. Energy Rev.*, vol. 69, pp. 771–789, 2017.

[4] W. Zuo, R. Li, C. Zhou, Y. Li, J. Xia, and J. Liu, “Battery-Supercapacitor Hybrid Devices : Recent Progress and Future Prospects,” *Adv. Sci. News*, vol. 4, no. 1600539, pp. 1–21, 2017.

[5] M. R. Lukatskaya, B. Dunn, and Y. Gogotsi, “Multidimensional materials and device architectures for future hybrid energy storage,” *Nat. Commun.*, vol. 7, p. 12647, 2016.

[6] A. Manthiram, “An Outlook on Lithium Ion Battery Technology,” *ACS Cent. Sci.*, vol. 3, no. 10, pp. 1063–1069, 2017.

[7] G. E. Blomgren, “The Development and Future of Lithium Ion Batteries,” *J. Electrochem. Soc.*, vol. 164, no. 1, pp. A5019–A5025, 2017.

[8] T. Kim, W. Song, D.-Y. Son, L. K. Ono, and Y. Qi, “Lithium-ion batteries: outlook on present, future and hybridized technologies,” *J. Mater. Chem. A*, vol. 7, pp. 2942–2964, 2019.

[9] T. royal swedish academy of Sciences, “Press release: The Nobel Prize in Chemistry 2019,” 2019. [Online]. Available: https://www.nobelprize.org/prizes/chemistry/2019/press-release/.

[10] D. Kundu, E. Talaie, V. Duffort, and L. F. Nazar, “The emerging chemistry of sodium ion batteries for electrochemical energy storage,” *Angew. Chemie - Int. Ed.*, vol. 54, pp. 3431–3448, 2015.

[11] C. Liu, Z. G. Neale, and G. Cao, “Understanding electrochemical potentials of cathode materials in rechargeable batteries,” *Mater. Today*, vol. 19, no. 2, pp. 109–123, 2016.

[12] H. Zhang, I. Hasa, and S. Passerini, “Beyond Insertion for Na-Ion Batteries: Nanostructured Alloying and Conversion Anode Materials,” *Adv. Energy Mater.*, vol. 8, no. 17, 2018.

[13] M. Á. Muñoz-Márquez, D. Saurel, J. L. Gómez-Cámer, M. Casas-Cabanas, E. Castillo-Martínez, and T. Rojo, “Na-Ion Batteries for Large Scale Applications: A Review on Anode Materials and Solid Electrolyte Interphase Formation,” *Adv. Energy Mater.*, vol. 7, no. 20, pp. 1–31, 2017.

[14] J. T. Han, Y. H. Huang, and J. B. Goodenough, “New anode framework for rechargeable lithium batteries,” *Chem. Mater.*, vol. 23, no. 8, pp. 2027–2029, 2011.

[15] L. Ji, Z. Lin, M. Alcoutlabi, and X. Zhang, “Recent developments in nanostructured anode materials for rechargeable lithium-ion batteries,” *Energy Environ. Sci.*, vol. 4, no. 8, pp. 2682–2689, 2011.

[16] B. Zhao, R. Ran, M. Liu, and Z. Shao, “A comprehensive review of Li4Ti5O12-based electrodes for lithium-ion batteries: The latest advancements and future perspectives,” *Mater. Sci. Eng. R*,

vol. 98, pp. 1–71, 2015.

[17] J. Cabana, L. Monconduit, D. Larcher, and M. R. Palacín, “Beyond intercalation-based Li-ion batteries: The state of the art and challenges of electrode materials reacting through conversion reactions,” *Adv. Mater.*, vol. 22, no. 35, pp. 170–192, 2010.

[18] S. Yuvaraj, R. K. Selvan, and Y. S. Lee, “An overview of AB2O4- and A2BO4-structured negative electrodes for advanced Li-ion batteries,” *RSC Adv.*, vol. 6, no. 26, pp. 21448–21474, 2016.

[19] Y. Zhao *et al.*, “Recent Developments and Understanding of Novel Mixed Transition-Metal Oxides as Anodes in Lithium Ion Batteries,” *Adv. Energy Mater.*, vol. 6, no. 8, pp. 1–19, 2016.

[20] D. Larcher, S. Beattie, M. Morcrette, K. Edström, J. C. Jumas, and J. M. Tarascon, “Recent findings and prospects in the field of pure metals as negative electrodes for Li-ion batteries,” *J. Mater. Chem.*, vol. 17, no. 36, pp. 3759–3772, 2007.

[21] H. Hwang, H. Shin, and W. J. Lee, “Effects of calcination temperature for rate capability of triple-shelled ZnFe2O4 hollow microspheres for lithium ion battery anodes,” *Sci. Rep.*, vol. 7, no. March, pp. 1–10, 2017.

[22] R. J. Hill, J. R. Craig, and G. V. Gibbs, “Systematics of the spinel structure type,” *Phys. Chem. Miner.*, vol. 4, no. 4, pp. 317–339, 1979.

[23] L. I. Granone, R. Dillert, P. Heitjans, and D. W. Bahnemann, “Effect of the Degree of Inversion on the Electrical Conductivity of Spinel ZnFe2O4,” *ChemistrySelect*, vol. 4, no. 4, pp. 1232–1239, 2019.

[24] H. Ying and W. Han, “Metallic Sn-Based Anode Materials : Application in High-Performance Lithium-Ion and Sodium-Ion Batteries,” *Adv. Sci.*, vol. 4, p. 1700298, 2017.

[25] Q. Deng, Y. Fu, C. Zhu, and Y. Yu, “Niobium-Based Oxides Toward Advanced Electrochemical Energy Storage: Recent Advances and Challenges,” *Small*, vol. 1804884, pp. 1–26, 2019.

[26] C. P. Kocer, K. J. Griffith, C. P. Grey, and A. J. Morris, “Cation Disorder and Lithium Insertion Mechanism of Wadsley – Roth Crystallographic Shear Phases from First Principles,” *J. Am. Chem. Soc.*, vol. 141, pp. 15121–15134, 2019.

[27] K. J. Griffith, A. C. Forse, J. M. Griffin, and C. P. Grey, “High-Rate Intercalation without Nanostructuring in Metastable Nb2O5 Bronze Phases,” *J. Am. Chem. Soc.*, vol. 138, pp. 8888–8899, 2016.

[28] C. P. Koçer, K. J. Griffith, C. P. Grey, and A. J. Morris, “First-principles study of localized and delocalized electronic states in crystallographic shear phases of niobium oxide,” *Phys. Rev. B*, vol. 99, no. 075151, pp. 1–11, 2019.

[29] I. Pinus, M. Catti, R. Ruffo, M. M. Salamone, and C. M. Mari, “Neutron diffraction and electrochemical study of FeNb11O29/Li11FeNb11O29 for lithium battery anode applications,” *Chem. Mater.*, vol. 26, pp. 2203–2209, 2014.

[30] X. Lou *et al.*, “Exploration of Cr0.2Fe0.8Nb11O29 as an advanced anode material for lithium-ion batteries of electric vehicles,” *Electrochim. Acta*, vol. 245, pp. 482–488, 2017.

[31] M. Bini, I. Quinzeni, and D. Spada, “The Doping of FeNb11O29 as a Way to Improve Its Electrochemical Performances,” *ChemistrySelect*, vol. 4, pp. 5656–5661, 2019.

[32] X. Lou *et al.*, “Crystal Structure Modification Enhanced FeNb11O29Anodes for Lithium-Ion Batteries,” *ChemElectroChem*, vol. 4, no. 12, pp. 3171–3180, 2017.

[33] R. Zheng *et al.*, “FeNb11O29 nanotubes: Superior electrochemical energy storage performance and operating mechanism,” *Nano Energy*, vol. 58, no. January, pp. 399–409, 2019.

[34] P. Simon, Y. Gogotsi, and B. Dunn, “Where Do Batteries End and Supercapacitors Begin?,” *Sci. Mag.*, vol. 343, pp. 1210–1211, 2014.

[35] V. Augustyn, P. Simon, and B. Dunn, “Pseudocapacitive oxide materials for high-rate electrochemical energy storage,” *Energy Environ. Sci.*, vol. 7, no. 5, pp. 1597–1614, 2014.

[36] D. Spada *et al.*, “Deepening the shear structure FeNb11O29: influence of polymorphism and doping on structural, spectroscopic and magnetic properties,” *Dalt. Trans.*, vol. 47, pp. 15816–15826, 2018.

[37] P. Galinetto, D. Spada, M. C. Mozzati, B. Albini, and M. Bini, “Effects of reaction atmosphere on physico-chemical properties of V-doped FeNb11O29,” *Opt. Mater. (Amst).*, vol. 92, pp. 373–378, 2019.

[38] D. Spada, I. Quinzeni, and M. Bini, “Orthorhombic and monoclinic modifications of FeNb11O29, as promising anode materials for lithium batteries: Relationships between pseudocapacitive behaviour and structure,” *Electrochim. Acta*, vol. 296, pp. 938–944, 2019.

2. Experimental

This section describes the experimental procedures involved both during the synthesis and the characterization of the materials which were selected as research topic, with a deeper focus on the electrochemical side, with particular reference to combined techniques.

2.1 Synthesis

Solid state

The reference technique (for both feasibility and comparison purposes) for the preparation of oxides is the solid state synthesis. The reactants must be well ground and mixed in order to have the highest contact surface possible. Even in this way, very high temperatures (> 1000°C) and long reaction times are often required in order to allow the solid-state diffusion of heavy ions or atoms, favouring also the decomposition of organic precursors, when employed.

Stoichiometric amount of Fe_2O_3 and Nb_2O_5 were weighted and mixed by using a Fritsch ball milling apparatus in tungsten carbide jars at 600 rpm for 1 hours with an intermediate rest.

$$0.5Fe_2O_3 + 5.5Nb_2O_5 \rightarrow FeNb_{11}O_{29}$$

A portion of the mixture was treated in oven in air at 1100 °C for 4h to obtain the monoclinic polymorph, while the remaining powder was heated at 1300 °C for 4h to obtain the orthorhombic form, as schematized in Figure 2.1. The formation of these shear phases occurs at very high temperatures because the diffusion of heavy ions such as Fe^{3+} and Nb^{5+} is hindered by the decrease in the concentration of oxygen vacancies (the main medium for fast ionic diffusion) caused by the structural rearrangement involved in the formation of shear planes (Wadsley defects). $FeNb_{11}O_{29}$ is formed with a monoclinic unit cell at high temperature (above 900 °C), and then undergoes a polymorphic transition at 1250 °C, due to a structural rearrangement of the block structure towards higher symmetry. The orthorhombic phase is the highest-temperature phase reported up to date.

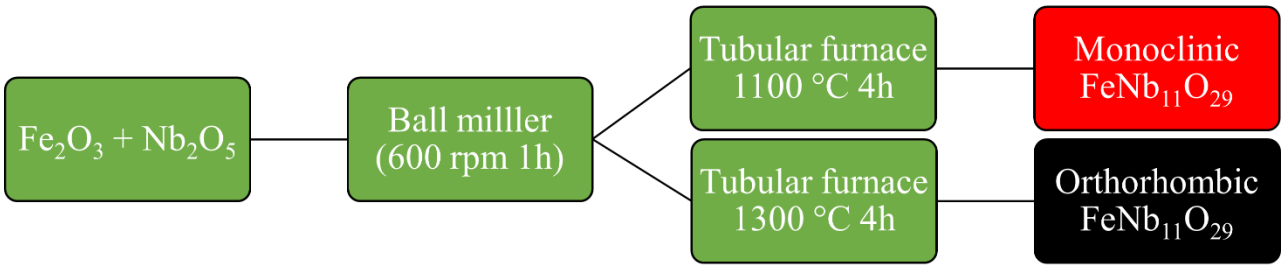

Figure 2.1 - Scheme of the synthesis of $FeNb_{11}O_{29}$

Co-precipitation

Co-precipitation methods consist in a chemical reaction between the precursors that leads to the formation of precipitates in the liquid medium in which the reactants were dissolved. The precipitates are usually dried and/or annealed in order to obtain the desired product.

$ZnFe_2O_4$ was synthesized in two different ways, as schematized in Figure 2.2. In the first case, the chemical reaction is an acid-base reaction which generates insoluble mixed hydroxides. 2 mmol of $ZnCl_2$ (Sigma-Aldrich, ≥ 98%) and 4 mmol of $FeCl_3 \cdot 6H_2O$ (Sigma-Aldrich, ≥ 98%) are dissolved in 50 mL of distilled water, then a solution of concentrated NaOH is added dropwise to the solution under magnetic stirring. Once the pH reaches 10, a brown-red precipitate starts to form. The solution is then kept for 2h at 80 °C inside an oil bath, in order to ensure a complete precipitation of the mixed hydroxides. After cooling to ambient temperature, the mixture is transferred in a Falcon and centrifuged for 5 min at 6000 rpm. The precipitate is then washed two times in distilled water and then in ethanol. The hydroxides are then dried in an oven at 80 °C overnight, ground in a mortar and finally annealed at 300 °C for 4h in an alumina crucible inside a tubular furnace.

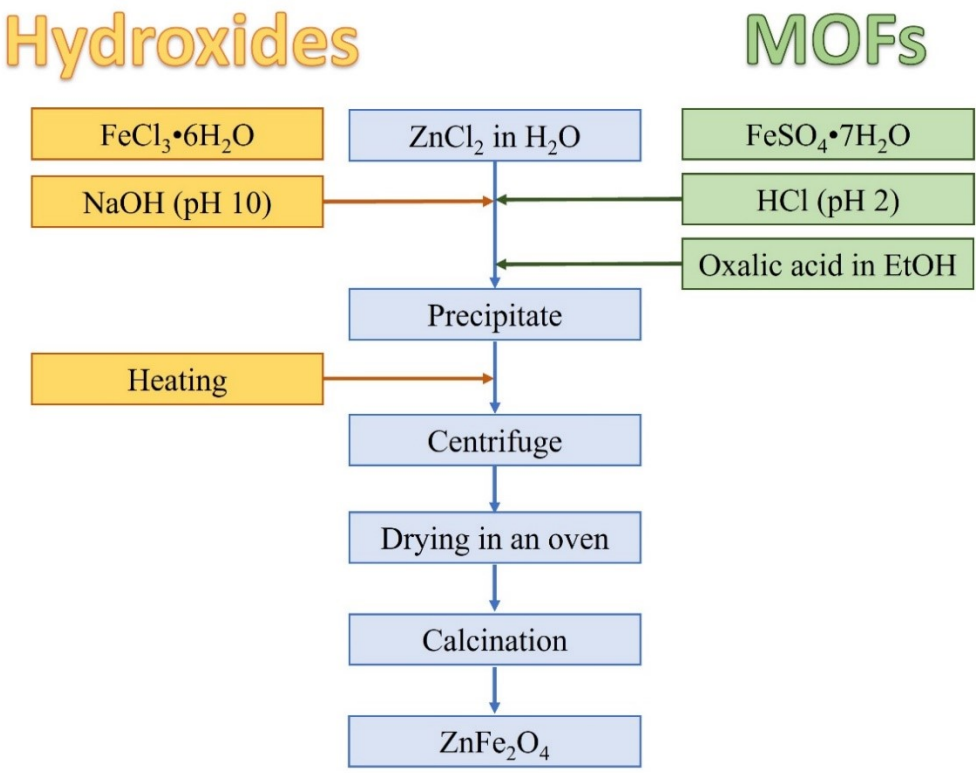

Figure 2.2 - Scheme of the syntheses of $ZnFe_2O_4$

In the second case, the chemical reaction involves the formation of a Metal-Organic Framework (MOF) between the metal cations and the oxalate anion. 2 mmol of $ZnCl_2$ and 4 mmol of $FeSO_4 \cdot 7H_2O$ are dissolved in 50 mL of distilled water, then a solution of HCl ca. 2.4 M is added dropwise until pH 2-3 is reached. When the solution turns from pale yellow to transparent, it is added dropwise under magnetic stirring to another solution of 1.6 M anhydrous oxalic acid (Sigma-Aldrich, ≥ 99.0%) in ethanol. Since the first drops, the solution turns yellow and gets opaque. The precipitate is then transferred in a Falcon

and centrifuged at 6000 rpm for 5 min, washed two times with distilled water and once with ethanol. The solid precursor is dried in an oven at 60 °C overnight, ground in a mortar and finally annealed at 500 °C for 3h in an alumina crucible inside a tubular furnace. This second synthesis is adapted from reference. [1]

Electrospinning

Electrospinning is a very simple but effective technique: a high potential difference is applied between a metallic plate (or a plate covered with aluminium sheet) and the metal needle of a syringe filled with a solution containing a soluble precursor salt and a soluble polymer (Fig. 2.3). The distance between the plate and the needle is kept a few centimetres in order to have a very high electric field, so that the polymer solution experiences high repulsive force due to concentration of similar charges. When the repulsive force exceeds the surface tension and the viscosity drag force of the polymer solution, a stream of fluid comes out automatically through the needle and subdivides further into millions of submicron to nano-sized jets which are deposited as nanofibers on the counter electrode. Increasing the electrospinning duration causes the randomly oriented fibers to build up in the form of thin sheet.

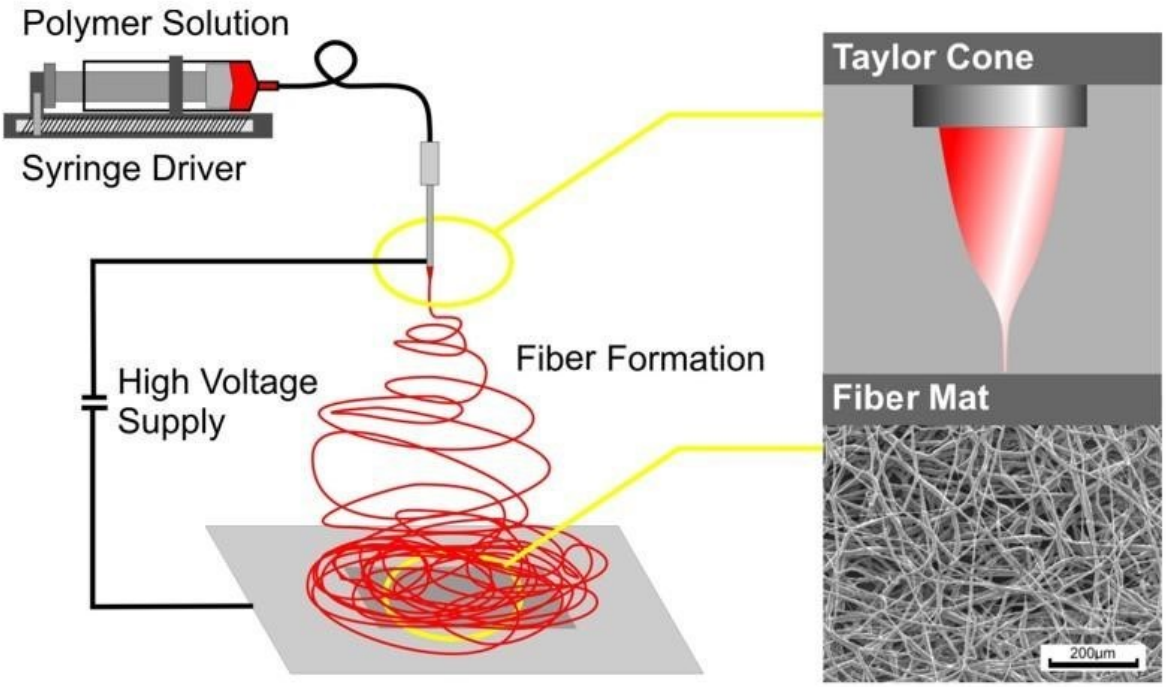

Figure 2.3 - General principles of the electrospinning technique. Reproduced from reference [2]

This technique was proposed for the preparation of polymer nanofibers, but in recent years it has been used for preparation of ceramic oxide nanofibers. Generally, the morphology of fibers prepared directly from inorganic salts, such as chlorides and nitrates, is poor due to interference of charges associated with anions. In order to overcome this problem, the inorganic salts are converted to organic precursors, e.g. acetates, citrates, etc for better fiber morphology. [2]

Polyacrilonitrile (PAN, Merck) was dissolved in N,N-Dimethylformamide (DMF, anhydrous, 99.8%, Merck) and stirred (magnetically) for 18 h at 60 °C to prepare a 9 wt% PAN solution. Then, SnO_2 (Aldrich, 99%) was added with vigorous stirring to obtain a homogenous solution at a nominal Sn/PAN loading of 33 wt. %, which was afterwards sonicated in a thermostated bath at 30 °C for 1 hour in total, alternating every 20 minutes, 20 minutes of simple stirring.

Nanofibrous membranes were spun on a custom-built laboratory device. The collector, covered with an aluminum foil, and the metal needle in a horizontal setting were positioned at a fixed distance of 22 cm, a height from the base of 18 cm and an inclination angle of 4-5°. The temperature, the relative humidity and the DC voltage applied were kept constant at about 25 °C, 35% and 20-22 kV respectively. The flow rate was set at 0.25 mL/h. As a reference, a plain 9 wt% PAN sample (without the addition of SnO_2) was electrospun with the same experimental set up at a 0.80 mL/h flow rate and 15 kV DC voltage.

Both membranes were stabilized in air for 1 h by heating at 5 °C/min up to 280 °C and then calcined in a 50 cc/min flow of Argon/Hydrogen (95:5) by heating at 10 °C/min up to 400 °C and at 5 °C/min to 700 °C with a final isotherm of 3 hours.

Some portions of the calcinated samples were ground at 250 rpm in a planetary mill (Retsch PM100) equipped with ZrO_2 jars and spheres, alternating 10 minutes of grinding with 10 minutes of pause for a total time of 2 h to obtain small and homogeneous fragments. As a consequence, the membranes were ground to a fine, electrostatic powder.

Electrodeposition

Electrodeposition, also known as electroplating, is the process of depositing material onto a conducting surface from a solution containing ionic species (salts). This fabrication technique is commonly used to apply thin films of material (metals or alloys, semiconductors) to the surface of an object to change its external properties such as to increase corrosion protection and abrasion resistance, improve decorative quality, or simply to deposit a layer. [3] The layer can also be removed from the conducting surface to synthesize morphologically controlled, nanostructured metals powders.

A typical setup consists of three electrodes, namely working, reference, and counter electrode. The electrodes, sitting within a vessel containing the liquid electrolyte (ionic species dissolved in it), are connected to a potentiostat. Being an electrolitic cell, external energy input is required for the reaction to progress. The overpotential (potential difference with respect to the equilibrium potential of the cathode and anode half-reactions) is the driving force for the current flow, allowing the oxidation at the anode surface and reduction at the cathode surface (the working electrode in an electrodeposition process).

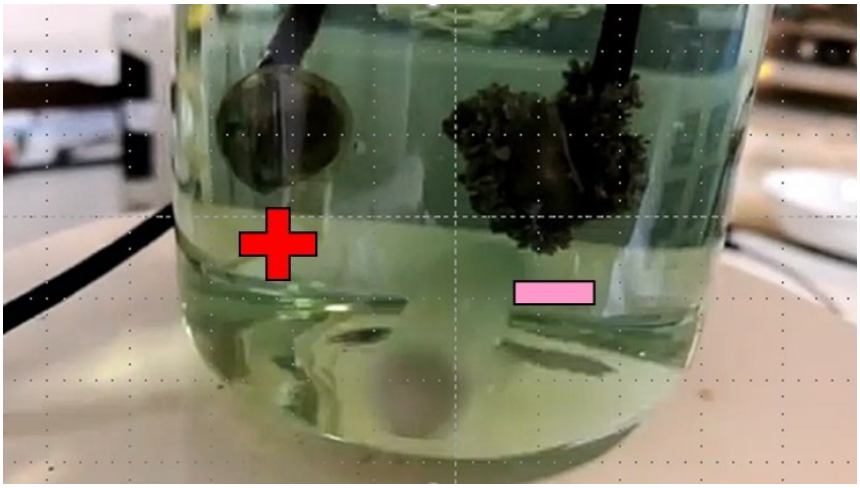

Figure 2.4 - Experimental setup for the electrodeposition of tin

In this work, Sn particles were electrodeposited from acqueous electrolytes containing different species but common concentrations (Fig. 2.4). The tin salt was 0.1 M $SnSO_4$, $SnCl_2$ or $SnCl_4*5H_2O$ and the corresponding acid was 0.7 M sulphuric or chloridric acid.

Anodic reaction	$O_2(g) + 4H_3O^+ + 4e^- + \rightarrow 6H_2O$	E_0 = +1.23 V vs SHE
Cathodic reactions	$Sn^{4+}(aq) + 2e^- \rightarrow Sn^{2+}(aq)$	E_0 = 0.15 V vs SHE
	$Sn^{2+}(aq) + 2e^- \rightarrow Sn(s)$	E_0 = -0.14 V vs SHE
	$2H_3O^+ + 2e^- \rightarrow H_2(g) + 2H_2O$	E_0 = 0.00 V vs SHE

By applying a voltage difference (7-10 V) between the electrodes (inox steel, ca. 1 cm distance, 0.8 cm^2 area each), a current of 1.8-1.9 A is associated with the evolution of bubbles of oxygen from the anode and the corresponding formation of Tin metal deposits on the cathode surface, between hydrogen bubbles that act as morphology modifiers. This synthesis was adapted from reference. [4]

2.2 Materials' characterization

XRPD (X-Ray Powder Diffraction)

X-ray Powder Diffraction holds the spotlight in the field of crystalline materials' characterization, because of its capability of identifying and quantifying the crystalline phases in powder samples. Through a structural refinement of a diffraction pattern, accurate details can be extracted (crystallites, cell parameters, atomic positions and thermal factors, as well as occupancies, defects, strains and so on).

The sample is irradiated with X-rays of a fixed wavelength deriving from the Coolidge tube: a W cathode emits electrons (thanks to thermoionic effect). The electrons are accelerated towards the anode (very high electric field) where the incident electrons eject electrons from the anode's core levels. Electrons from outer levels relax to the vacant core level, and the excess energy is emitted (among the other possibilities) as X-rays of fixed energy equal to the energy gap between the core and the outer level. The most common anode is Cu, whose most intense transition is the Kα, with a wavelength of 1.54 Å.

The incident beam can be scattered by the electrons of the atoms (with effectiveness proportional to the electron density of the atom) in the sample, if ordered in long-range (10^3 atoms) and hit by a proper wavelength (comparable to the interatomic distance between the planes of ordered atoms). By performing an angular scansion (changing the angle between the source and the sample), through complex calculations involving electron density maps, the lattice of each phase can be derived, and by modelling the shape and intensity of the collected pattern further informations about the phase can be extracted.

A Bruker D5005 diffractometer with Cu Kα radiation (40 kV, 40 mA), a graphite monochromator and a scintillation detector were employed for all the measurements. The patterns were collected in air, using a silicon sample holder with low background. Rietveld structural and profile refinement was carried out by means of TOPAS 4.0 software on the basis of the known crystal structure models of the synthesized materials. The background coefficients, scale factor, zero error, lattice parameters, crystallite sizes, isotropic thermal factors and atomic positions were refined.

SEM (Scanning Electron Microscopy) and EDS (Energy Dispersive Spectroscopy)

The morphology can be investigated with electron microscopies, the most common one being SEM. Together with morphological images, compositional analyses (identification, quantification and spacial distribution) can be performed if different detectors are employed.

The electrons generated through thermoionic effect (or field emission) by a W or LaB_6 cathode are accelerated in a vacuum chamber towards the sample, which is sputtered with gold or graphite (or sometimes fixed in a silver paste) when not already conductive. Many signals are emitted by the sample in response to the primary electron beam: secondary electrons are a surface signal deriving from anelastic scattering; backscattered electrons are higher-depth (higher energy) but less resolved signals deriving from elastic scattering; X-rays are also emitted as relaxation phenomenon, following anelastic scattering.

If secondary electrons are the highest resolution signal (low energy) employed for most of the SEM images, backscattered electrons provide less resolved images but with compositional contrast (scattering power of the nuclei). For the collection of X-rays longer exposure times are required, because their emission is less intense. The signals are even less resolved (higher depth) but allow the identification of elements (Moseley's law) and their quantification. Once the elements are identified, their distribution in the sample can be verified.

SEM measurements were performed with a Zeiss EVO MA10 microscope on powder samples, sputtered with gold. Micrographs at different magnifications were also collected on anodes before and after electrochemical measurements, in this case after disassembling the cell and washing the electrode with acetone.

Raman Spectroscopy

The Raman effect results from the inelastic scattering of monochromatic probing light when it interacts with a material. A typical Raman spectrum is a plot of the intensity of the scattered light as a function of its frequency difference from the incident probing light, and such a frequency difference is called the Raman shift. The Raman shift corresponds to the vibrational energy levels of the system, which are characteristic of the Raman-active modes for certain molecules or crystals.

Micro-Raman measurements on powder samples were carried out at room temperature in the Department of Physics at the University of Pavia, using a Labram Dilor spectrometer equipped with an Olympus microscope HS BX40. The 632.8 nm light from a He–Ne laser was employed as the excitation radiation. The cells pressed within the cell-holder were mounted on a motorized xy stage and tested with a 50× objective and with a laser spot of ∼2 μm diameter. The spectral resolution was about 1 cm^{-1}. A cooled CCD camera was used as a detector and the typical integration times were about 30 s.

ThermoGravimetric Analysis (TGA) and Differential Scanning Calorimetry (DSC)

Both techniques belong to the family of thermal analyses, which are very useful in the characterization of specific materials such as polymers, amorphous solids, composites etc. In the thermogravimetric analysis, the mass of the sample is measured with a precision balance while the temperature is changed (generally, at a constant rate) inside a furnace kept under different atmospheres (air, inert gas, oxidizing/reducing gas etc) depending on the target of the measurements. In the differential scanning calorimetry, the difference between the amount of heat required to increase the temperature of the sample and a reference compound is measured as a function of the temperature. This technique is particularly useful in the detection of reactions that involve heat exchange, such as phase transitions, crystallizations and glass transitions.

The samples were analysed with a SDT Q600 instrument, with a combined TGA and DSC measurement. The samples were heated from room temperature to 800 °C at a rate of 5 °C/min in air.

X-ray Absorption Spectroscopy (XAS)

X-ray Absorption Spectroscopy is a very powerful technique in probing the local symmetries and the electronic structures of complex samples, regardless from their aggregation state. One of the main features of the technique is the element-selectivity, that usually requires the use of tunable synchrotron radiation. In a typical XAS experiment, the energy of the beam is tuned to a range where the core electrons (often 1s electrons, K-edge, see Figure 2.5) of the investigated element are excited to higher-energy levels.

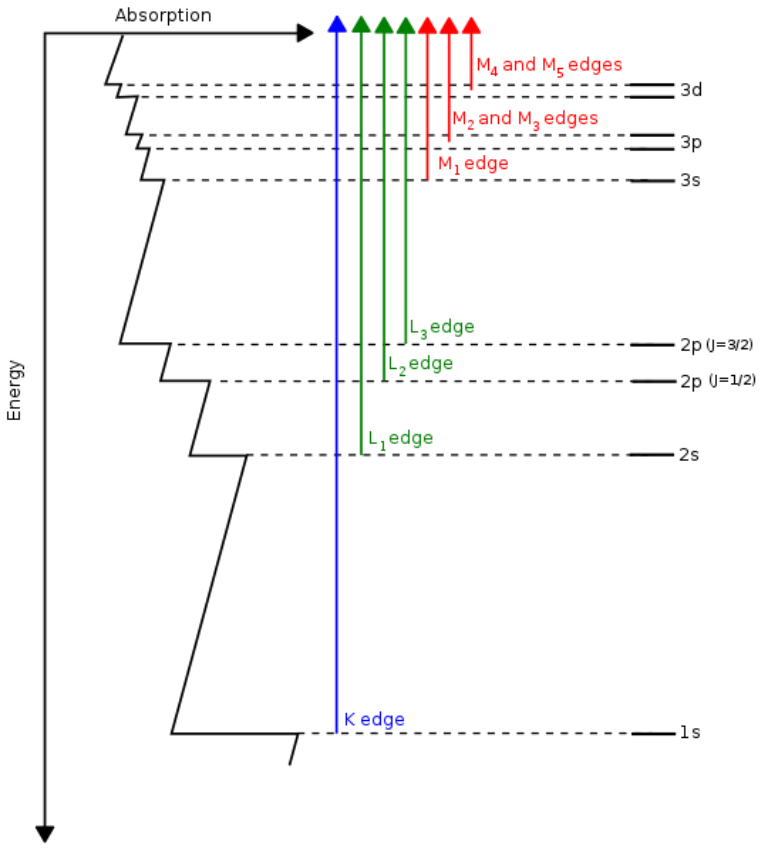

Figure 2.5 - Common XAS edges

There are two distinct XAS energy regions relative to the absorption edge (Figure 2.6), the region at ≈ 30 eV, near the absorption edge, is defined as the XANES, and the region above 40 eV extending to several hundred eVs is called the extended X-ray absorption fine structure (EXAFS). XANES provides information about the electronic structure, such as the oxidation states, and the site-symmetry of the absorbing atoms, while EXAFS provides quantitative local structural information, for instance, the bond length, degree of ordering, and the coordination number. [5]

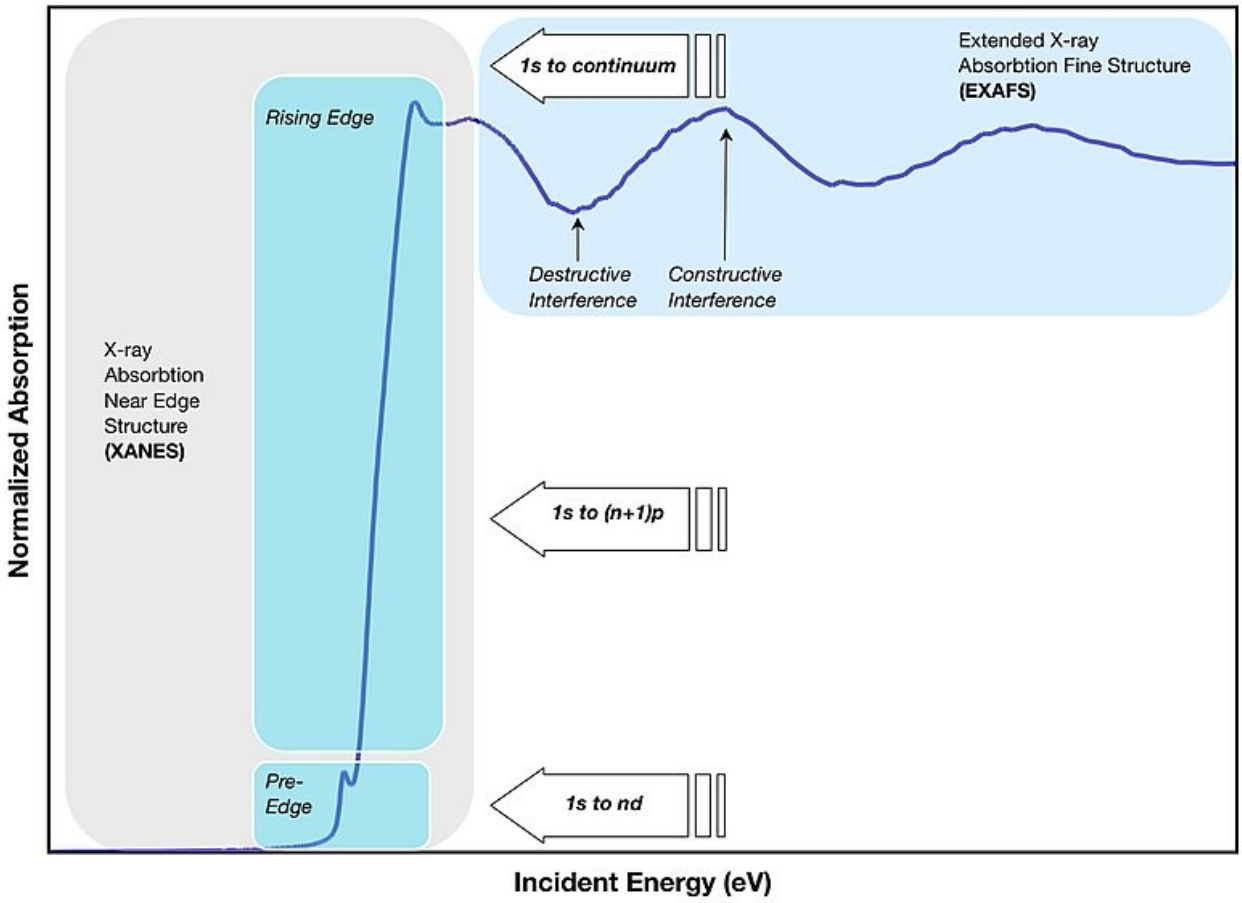

Figure 2.6 - Typical shape of XAS data for a K-edge

X-ray absorption spectroscopy measurements were performed at the Nb K-edge (18986 eV) and at the Fe K-edge (7112 eV) at the XAFS beamline operating at the Elettra synchrotron radiation facility in Trieste, Italy. A proper amount of sample, as to give a unit jump in the absorption coefficient μ, was pressed into a pellet. The two pellets of monoclinic and orthorhombic $FeNb_{11}O_{29}$ were then measured in the transmission mode at room temperature. The spectra of Nb_2O_5 and Fe_2O_3 were also acquired as reference. The energy calibration was performed measuring the absorption spectra of either Nb foil and metallic Fe pellet, placed in a second experimental chamber after the sample and after the I1 ionization chamber. The ring current and the energy were 200 mA and 2.4 GeV, respectively. A Si(311) double-crystal monochromator was used, while high-order harmonic rejection was obtained by detuning the second crystal. A water-cooled Pt-coated silicon mirror was used to obtain vertical collimation of the beam.

The data extraction and analysis were carried out by means of Athena, belonging to the set of interactive programs IFEFFIT. For the X-ray absorption near edge structure (XANES), the raw spectra were first background subtracted by using a straight line and then normalized to unit absorption above 800 eV. The EXAFS (Extended X-ray absorption fine structure) data analysis was performed by means of the Excurve code using a k2 weighing scheme.

Mossbauer Spectroscopy

Mossbauer Spectroscopy is a technique based on the emission and absorption of nuclear gamma rays in solids. As a consequence, this nuclear spectroscopic technique is very powerful but its application is limited to the characterization of few nuclei, the most common of which is ^{57}Fe. In a typical experiment, a ^{57}Co source decays by electron capture to an excited state of ^{57}Fe, that decays to ground state via emission of gamma rays. The source is accelerated towards the sample (velocities usually range in 1-10 mm/s) using a linear motor to produce a Doppler effect and perform an energy scan. The detector measures the intensity of the beam transmitted through the sample. The differences in the chemical environment of the sample are reflected in the nuclear transition energies (Fig. 2.7): isomer shift is a relative measure that describes the changes in the electron density in the s orbitals, which is affected by outer orbitals; quadrupole splitting is the consequence of the interaction of the nuclear energy levels (of nuclei with spin quantum number I > ½) with the electric field gradient deriving from an asymmetric electronic charge distribution or ligand arrangement. In the case of ^{57}Fe, the excited state has a nuclear spin of 3/2 and a doublet is observed (m_I = +- ½ and m_I = +- 3/2), and by applying a magnetic field the nuclear Zeeman effect causes further splitting of energy levels, resulting in a multiplet.

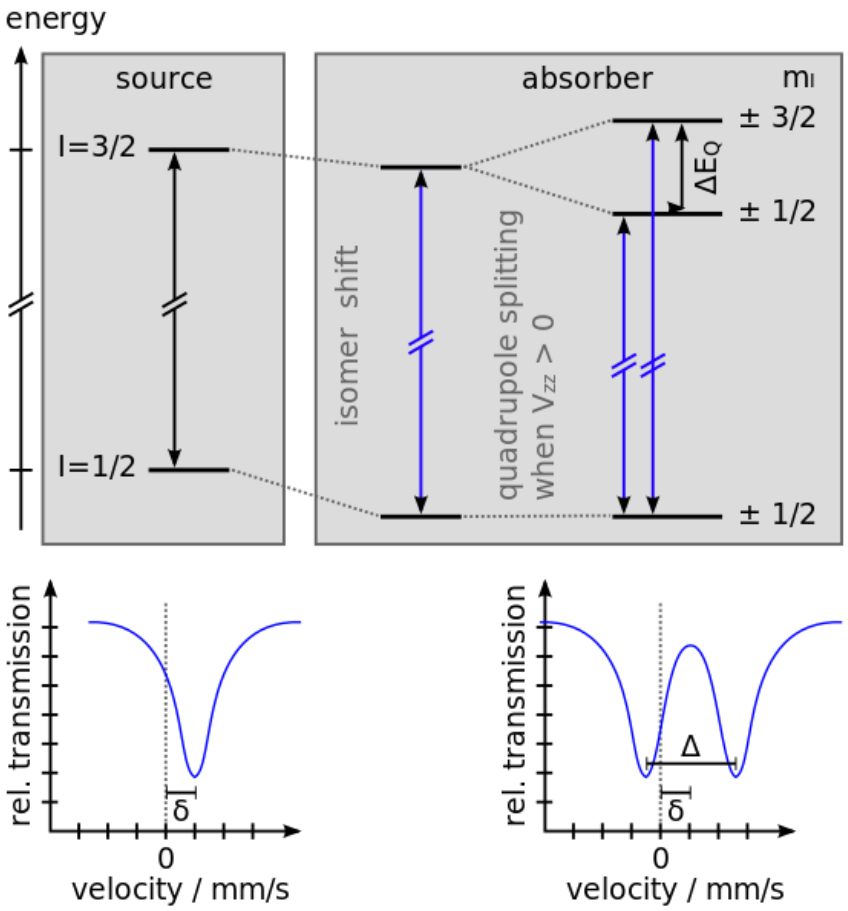

Figure 2.7 - Graphical explanation of isomer shift and quadrupole splitting

Mössbauer measurements on powder samples of monoclinic and orthorhombic $FeNb_{11}O_{29}$ were performed by means of a standard Mössbauer setup in transmission geometry. Mössbauer spectra were collected by means of a Kr-CO_2 proportional counter, FastTM electronics for gamma ray spectroscopy and a WisselTM spectrometer, which was run in sinusoidal acceleration mode (v_{max} = 6.0 mm/s) and calibrated by using a standard metal iron foil. The γ-ray source was a 25-mCi ^{57}Co in rhodium matrix with Lamb-Mössbauer factor f = 0.63. Approximately 47 mg/cm^2 of each compound were used for the measurements. The Mössbauer spectra were interpreted by means of a fitting procedure based on the evaluation of the transmission integral function, that takes into account the dependence of the Mössbauer spectra on the sample effective thickness. For both samples a rather good agreement between experimental and best fit data was obtained with χ^2 ~ 1000 for the 512 points.

Muon Relaxation Spectroscopy

Muons are elementary particles similar to electrons (electric charge -1 and spin ½) but with greater mass, i.e. 207 times the mass of the electron. The higher mass causes the muons to penetrate much deeper into matter, because they emit less bremsstrahlung, which is the main cause of energy loss for both electrons and muons. For example, cosmic ray muons can reach the Earth's surface and even deep mines.

Muon spin relaxation (μSR) is a very sensitive technique that probes the internal magnetic field using the magnetic moment of the muon. Muons are implanted in the sample where they penetrate a few hundred μm, rapidly thermalize due to electrostatic interactions and finally settle at a Coulomb potential minimum in the material. Appropriate electronic vetoing removes any double counts due to cosmic ray muons or if multiple muons are generated and become incident on the sample within one observation window. A thin muon detector is placed at the entry to the sample chamber. The thin muon detector starts a clock registering the entry time of the muon. The muon will spontaneously decay into a positron and two neutrinos with a lifetime of 2.2 μs. [6]

In this decay, the positron is emitted preferentially in the direction of the muon spin at the time of decay. The positron will be detected in one among the scintillators surrounding the sample and this will stop the clock and give a time from entry to decay. From the large ensemble of these events a histogram of positron counts in opposing detectors, NA and NB can be generated. Each positron counter will have an amplitude that fits the decay time of the muon with a signal representing the local field. By combining two opposing counters we can generate an asymmetry in the signal which is proportional to the spin polarization function. [6]

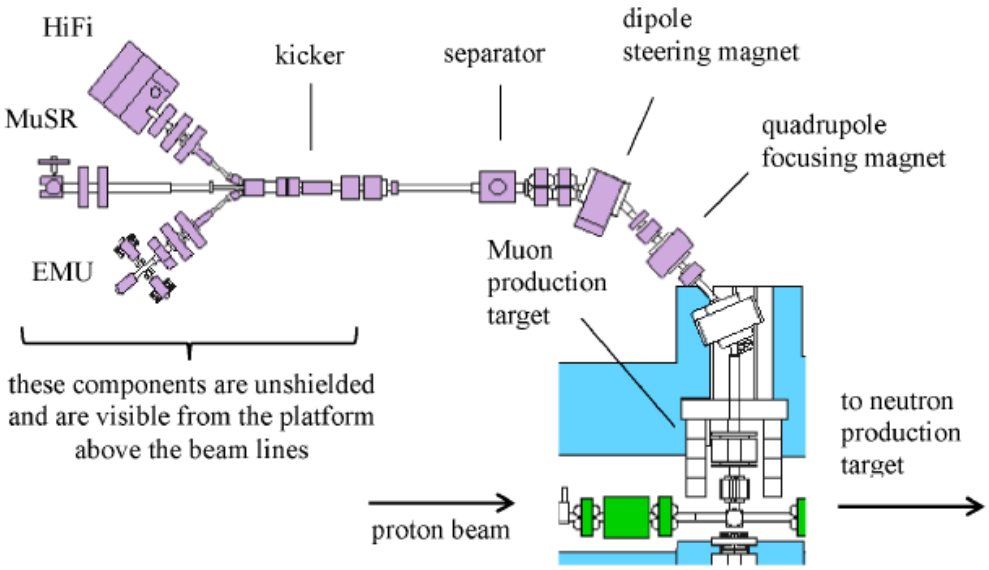

Figure 2.8 - General layout of the European Muon Facility at ISIS

The μSR experiment was carried out on the EMU experimental setup at the ISIS facility of the Rutherford Appleton Laboratory (Fig. 2.8), on powder samples (~ 500 mg) pressed into disks with 20-mm diameter and 3-mm thickness, then packed into an Au O-ring sealed titanium cell. The window of the cell was made of a Kapton film with 50-μm thickness. The cell was then mounted on the sample holder and cooled down to 50 K with a cryostat before starting the measurements. In order to explore the higher temperatures (up to 500 K), it was necessary to employ also an oven.

2.3 Electrochemical characterization

The electrochemical characterization is reported in separate paragraphs, describing the preparation of the electrodes and their use in electrochemical cells.

Electrode preparation

An electrode for LIBs or SIBs is a solid mixture of the active material (capable of forming bonds with Li^+ or Na^+ reversibly through electrochemical reactions) with conductive carbon and an electrically insulating polymer. In principle, the only essential component is the active material, but the powder alone would not stick on the current collector and, in most cases, would not have the required electrical conductivity. The polymer gives the mixture mechanical stability and sticks the electrode to the current collector, while the conductive carbon is added to improve the electron conduction. In order to obtain the most performing electrodes, these 3 components are mixed together, and a liquid is added. The liquid (organic or inorganic depending on the polymer) is solvent to the polymer but non-solvent to the other components, producing a black suspension with high viscosity, called ink or slurry. When the slurry is homogeneous, it is cast onto the current collector (a metal sheet or grid) thanks to a device called doctor blade, which consists in a blade with tuneable distance from the current collector. This step is necessary in order to have a homogeneous and thin layer of the slurry, which is then left to dry out, thanks to the vapour tension of the liquid, combined with the extractor hood. Once the electrode is solid, the eventual traces of liquid and the adsorbed water are eliminated through a vacuum oven.

The last step before the cell assembly is the hot pressing, that causes the polymer matrix to soften (the temperature is kept around the glass transition temperature) and improve the adhesion to the metallic current collector.

$FeNb_{11}O_{29}$ and $ZnFe_2O_4$ - The electrodes for conventional electrochemical tests in T-shape home-made Swagelock cells were obtained through magnetic stirring of the active materials mixed with the C65 carbon (Imerys) and polyvinyldifluoride (PVdF) in a weight ratio of 70:20:10 in N-methyl-2-pyrrolidone (NMP, Aldrich), thus obtaining the ink which was cast on a copper foil (Goodfellow) by using a homemade doctor blade, then maintained overnight at room temperature and dried in a vacuum oven at 100 °C for 1h. The self-standing electrodes instead were obtained with a modified phase-inversion procedure [7]: the ink (50:20:30) was cast onto a porcelain bucket in the shape of a foil, and then covered with distilled water. The phase inversion process causes the initial volatile solvent (NMP) to be replaced by the nonsolvent water, producing a solid porous PVdF structure through precipitation. This thin, flexible electrode limits the need for a metallic current collector as a physical substrate for the slurry, which would hamper in situ characterizations. Both the coated slurries and the self-standing electrodes were then hot pressed, respectively at 90 and 70 °C, and then stored in an Ar-filled glovebox.

Sn and SnO_2 – The procedure for the preparation of the electrodes based on powder samples was analogous to the one just described, with a different conductive carbon (350P) and different weight ratios (80:10:10). The preparation of the self-standing electrodes was instead already described in the synthesis by electrospinning.

Cell assembly

Provided that the available cell geometry is T-shaped (Fig. 2.9), the a.s. electrode must be cut in form of a disc. A half-cell employs as counter (and reference, when needed) electrode the corresponding metal (Li for LIBs and Na for SIBs) and an insulating separator, both in form of discs. The electrolyte is a liquid solution of a high concentration Li/Na salt with weak coordinative strength dissolved in an organic compound (or mixture) with the highest HOMO-LUMO gap as possible.

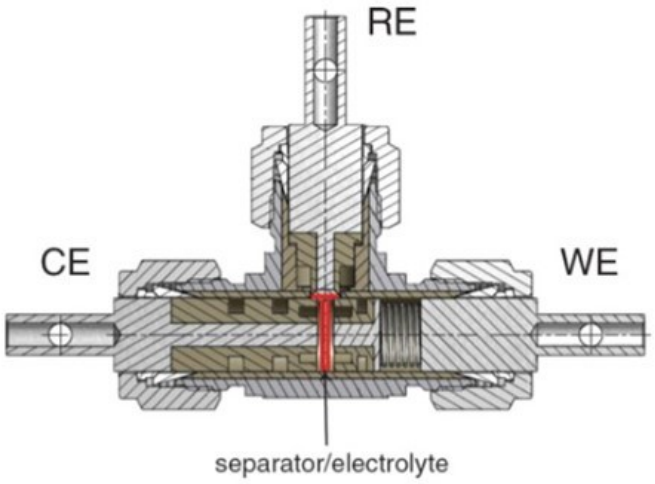

Figure 2.9 - Scheme of T-shaped cells, with the three electrodes (CE = counter electrode, RE = reference electrode and WE = working electrode)

Lithium-ion batteries - The electrodes were cut in form of discs (diameter 1 cm), with a mass loading in the range of 1.0-2.5 mg/cm^2. The Swagelok cells were assembled in a dry box under argon atmosphere (MBraun, O_2 < 1 ppm, H_2O < 1 ppm) using electrodes mentioned above as working electrodes, Li metal as the reference and counter electrode and a Whatman GF/A disc as the separator, soaked in 1M $LiPF_6$ in a mixture of ethylene carbonate/ diethylene carbonate (EC/DEC; 1:1 v/v) as the electrolyte (Aldrich).

Sodium-ion batteries – The procedure for the cell assembly was analogous to the one just described, with Sodium metal as counter electrode and 1M $NaPF_6$ in PC as electrolyte.

GCPL (Galvanostatic Cycling with Potential Limitation)

The most important parameter for an EES device is the reversibility of the reactions. To this aim, the electrochemical cells are subjected to a number of cycles of charge and discharge, in order to study the storage performances and their reversibility.

GCPL belongs to the family of chronopotentiometric techniques: a current pulse is applied to the working electrode and the resulting potential is measured against a reference electrode as a function of time. In this particular case the current is constant (Galvanostatic). When the current is first applied, the measured potential is abruptly changed due to the iR loss, and after that it gradually changes, because a concentration overpotential is developed as the concentration of the reactant is exhausted at the electrode surface. If the current is larger than the limiting current, the required flux for the current cannot be provided by the diffusion process and, therefore, the electrode potential rapidly rises until it reaches the electrode potential of the next available reaction, and so on. When a selected potential is reached (the limitation mentioned in the name of the technique), the current flow is reversed until the other limitation is reached. This process is then repeated for a selected number of cycles, in different possible ways: when firstly studying a new material, an overview of the kinetics associated with the electrochemical reaction is obtained with what is called rate capability test (i.e. the applied current is varied after some cycles), and then when a proper C-rate (charge rate, i.e. the reciprocal of the amount of hours required for the cell to have a full charge) is chosen, a capacity retention test can be performed for a higher amount of cycles (usually hundreds or thousands), keeping the same current for every cycle.

In both ways many informations can be obtained from the data:

- specific capacity – the amount of charge stored in the unit mass of the active material
- capacity retention – cycling stability, in terms of % of the 1st cycle capacity
- coulombic efficiency – the reversibility of the reaction, the ratio between the energy stored during charge and discharge, expressed as %.
- V vs t – allows to visualize the ohmic drop, the potential associated with the reactions and the problems associated with a poor cell manufacture, when occurring

- V vs Q – a normalized version of the former graph, establishing correlations between the potential of a reaction and the amount of Li/Na ions stored.
- dQ/dV – being a derivative curve, the determination of the potential associated with a reaction is more accurate

Rate capability test on Swagelok cells were performed with a Neware BTS battery tester at C-rates between 0.5C and 10C, in different potential ranges (usually between 0.01 and 3 V) depending on the features of the active material.

CV (Cyclic Voltammetry)

Voltammetry is basically referred to as techniques with the common feature that the potential of the working electrode is controlled through a reference electrode and the resulting current flow is measured against a counter electrode. In cyclic voltammetry the potential is linearly scanned over time in either the negative or positive direction (cathodic and anodic scan, respectively) and reversed when the end of the potential window is reached. Anodic and cathodic scans are repeated alternately a number of times. In some techniques, changing the sweep rate allows to extract kinetic parameters such as the pseudocapacitive contribution and the diffusion coefficient of Li/Na ions in the electrode. Even from a simple voltammogram, data such as the stored charge, the corresponding potential, the structural stability and the nature of the reaction can be easily extrapolated.

Cyclic voltammetry was performed by using an Autolab PGSTAT30 (Eco Chemie) at growing sweep rates, from 0.1 to 1 mV/s.

EIS (Electrochemical Impedance Spectroscopy)

In electrochemical impedance spectroscopy (EIS), the system under investigation (typically in the equilibrium state) is excited by a small amplitude ac sinusoidal signal of potential or current in a wide range of frequencies and the response of the current or voltage is measured. Since the amplitude of the excitation signal is small enough for the system to be in the (quasi-)equilibrium state, EIS measurements can be used to effectively evaluate the system properties without significantly disturbing them. Frequency sweeping in a wide range from high-to low-frequency enables the reaction steps with different rate constants, such as mass transport, charge transfer, and chemical reaction, to be separated.

For typical impedance measurements, a small excitation signal (e.g., < 20-30 mV) is used, so that the cell is considered as a (pseudo-)linear system. In this condition, a sinusoidal potential input to the system leads to a sinusoidal current output at the same frequency. As a matter of fact, the output current exponentially increases with the applied potential (or polarization, over-voltage), that is, the typical electrochemical system is not linear.

Being the excitation signal and the response sinusoidal waves, the Euler's relationship defined as $\exp(ix) = \cos x + i \sin x$, allows to express the system impedance as a complex function. A lot of useful information

can be visualized in quite a simple manner through the Nyquist plot: the real part of the impedance is plotted on the abscissa and the imaginary part on the ordinate. In the Nyquist plot a vector of length |Z| is the impedance and the angle between this vector and the real axis is a phase shift, x.

In spite of the wide use of the Nyquist plot, it has a weakness that we cannot know the frequency at which a specific impedance point is recorded in the plot. The Bode plot might be useful, in that the frequency information is explicitly shown. In the "Bode plot," the axis of the abscissa is the logarithmic frequency (log f) and the axis of the ordinate is either the absolute value of the logarithmic impedance (log |Z|) or phase shift (x).

The values of the resistance, capacitance, and the chemical diffusion coefficient of lithium into the active materials can be determined from the complex nonlinear least squares (CNLS) fitting method, by fitting the impedance spectra to an equivalent circuit model.

The Randles circuit is the simplest and most common electrical representation of an electrochemical cell. It includes a resistor (with a resistance of R_{ct}; an interfacial charge-transfer resistance) connected in parallel with a capacitor (with a capacitance of C_{dl}; a double layer-capacitance) and this RC electrical unit is connected in series with another resistor (with a resistance of R_s; a solution resistance). The equivalent circuit of insertion materials includes the diffusion impedance, originating from the solid-state diffusion of the active species. Assuming a semi-infinite diffusion process, the Warburg element with an impedance of Z_w is connected in series with the resistor representing the interfacial charge transfer, R_{ct}.

It should be mentioned that the capacitor (e.g., the double-layer capacitor in the Randles cell) in an impedance experiment frequently does not show ideal behavior. Instead, it acts like an electrical element with constant phase called a constant phase element (CPE). A few theories have been proposed to explain the deviation of the capacitive behaviour from ideality, including the surface roughness effect, but there is no general consensus on the origin of the CPE. This CPE can also serve to explain the pseudocapacitive contribution to the mass transport of Li/Na ions, which has faster kinetics than the solid-state diffusion.

The Electrochemical Impedance Spectroscopy (EIS) measurements were performed at room temperature by means of a Frequency Response Analyzer (FRA) Autolab PGSTAT30 (Eco Chemie) apparatus in the frequency range 0.01-10^6 Hz, with a perturbative sinusoidal wave of an amplitude of 30 mV. The spectra were collected in potentiostatic conditions, setting a 2h rest between applying each potential and recording the spectra, or at a single potential. The spectra were fitted with the help of the NOVA software.

GITT (Galvanostatic Intermittent Titration Technique)

The galvanostatic intermittent titration technique (GITT) is considered to be one of the most useful techniques in chronopotentiometry, because the equilibrium electrode potential is obtained as a function of lithium/sodium content, but most of all the chemical diffusion coefficient of the species in the insertion materials can be calculated as a function of the potential.

It should be noted that the classical application of the EIS and GITT techniques is related to systems in which the concentration of the intercalant changes monotonically as intercalation proceeds. Such a situation is valid only for topotactic solid-state intercalation reactions which lead to the formation of solid solution phases. When the intercalation/de-intercalation of Li^+ is accompanied by strong electron–ion interactions, the intercalation proceeds following one or several reaction fronts, and leads to the coexistence of two phases. Thus, the physical meaning of the chemical diffusion coefficient as a function of the composition in the situation of two-phase coexistence becomes obscure (apparent diffusion coefficient, as a measure of the intensity of long- and short-range interactions between the intercalated species). The electron-ion interactions in $FeNb_{11}O_{29}$ are very weak, with formation of a solid solution $Li_xFeNb_{11}O_{29}$, making the calculated diffusion coefficient a true diffusion coefficient. [8]

The GITT procedure consists of a series of current pulses, each followed by a relaxation time, in which no current passes through the cell. The current is positive during charge and negative during discharge. During a positive current pulse, the cell potential quickly increases to a value proportional to the iR drop. Afterwards, the potential slowly increases, due to the galvanostatic charge pulse, in order to maintain a constant concentration gradient. When the current pulse is interrupted, i.e., during the relaxation time, the composition in the electrode tends to become homogeneous by Li-ions diffusion. Consequently, the potential first suddenly decreases to a value proportional to the iR drop, and then it slowly decreases until the electrode is again in equilibrium (i.e., when $dE/dt \sim 0$) and the open circuit potential (V_{oc}) of the cell is reached. Then, the galvanostatic pulse is applied again, followed by current interruption. This sequence of charge pulse followed by a relaxation time is repeated until the battery is fully charged. The a sequence of negative current pulses, where the opposite holds, is applied. [9]

The Galvanostatic Intermittent Titration Technique (GITT) was performed with an Autolab PGSTAT30 (Eco Chemie) apparatus, employing the NOVA software. Galvanostatic discharge pulses with a current corresponding to a C-rate of C/20, each 10 minutes long, were followed by 10 minutes of relaxation time, from OCP to 1.0 V and then reversed and applied up to 2.7 V.

2.4 In situ/operando characterization

The growing interest in more advanced LIBs with higher energy and power density, longer cycle life and better safety characteristics is pushing towards the optimization of current electrode materials, as well as the discovery of novel electrode materials. Both require an in-depth understanding of the relationship between the structural changes of the battery materials and the performance of the batteries during electrochemical processes. [5]

The investigation of the materials alone cannot provide those information, and although ex situ characterization techniques can provide valuable information about the battery materials, the postprocess nature limits the ability to study the kinetic properties of the materials, such as the detailed structural changes and intermediate stages during charge–discharge cycling and heating. In addition, due to the sensitivity of working electrodes to air and moisture, the results from ex situ measurements about electrochemical processes, such as valence changes, surface, and interfacial reactions, may not fully reflect what is truly taking place. [5]

In situ measurements and, in particular, operando measurements (in situ means "in the natural or original position or place," and operando implies that the material is behaving as it would do in "real life," in other words, the experiment is carried out under the operating conditions) can reveal more valuable information about the electrode materials without disassembling the testing cells and can aid in exploring the correlation between structural properties and electrochemical performances. Each advanced technique has unique capabilities to study specific properties of the electrode materials (structure evolution, redox mechanism, solid–electrolyte interphase (SEI) formation, side reactions, Li-ion transport properties and so on). [5]

Involved techniques

The techniques that were employed in this work are quite different from each other, covering a wide range of material's properties.

Raman –Raman spectroscopy is sensitive to the ion oxidation state and local structure of the material, thus it is useful in monitoring valence and bond change, as well as strain and phase transformations of the electrode under operating conditions. Therefore, many aspects of the structural, mechanical, and chemical changes in the electrodes, the electrolyte, and the electrode/electrolyte interfaces (it can analyse both solids and liquids) during electrochemical cycling can be studied and understood via in situ Raman spectroscopy. Other advantages are: it is non-destructive and since Raman spectroscopy does not require long-range structural ordering, it can be used to analyse amorphous or poorly crystalline compounds or electrode materials that are otherwise difficult to study with XRD. [5], [10]

XRD - XRD is based on the scattering of X-rays, the interference of which produces diffraction patterns from crystalline or partial crystalline structured materials. XRD is widely used to study the crystal structures and phase transformations in electrode and solid electrolyte materials and in situ/operando XRD is used to monitor the structural changes of LIBs materials during (lithiation/delithiation) cycling or during temperature changes (heating/cooling). Compared to lab-sources, synchrotron-based X-ray sources provide higher intensities and larger photon energies, which result in larger penetration power,

shorter measurement times, and better signal-to-noise ratios, which are all favorable for in situ/operando studies. [5]

Pouch cells

Conventional electrochemical cells cannot be employed for in situ/operando studies, because its components are not transparent to the radiations. In order to minimize the presence of materials other than the active material, the "coffee bag" electrochemical cell was used, which consists of several flat parts assembled and sealed in an aluminum bag to make the cell air and moisture tight with an overall thickness of ≈ 1 mm. (see Figure 2.10). Depending on the beam-sample-detector geometry (reflection or transmission mode) the cells were assembled with a single or a double window. The main issue of such cells is the poor electrical contact between the electrode and the current collector, because the flexibility (or brittleness) of the materials prevents from applying a static and even pressure on the cell, especially near the windows. In addition, air and moisture can enter into the cell through the windows, which can affect the cell performance and limit the use of such cells to relatively short time experiments. [5]

To this aim, after a few failed experiments, we decided to solve this problem: together with the laboratories of the University of Pavia we designed a cell-holder with the aim of keeping constant and even pressure, through a couple of screws, with 1 (or 2) hole(s) for the beam, and a flat shape in order to easily handle the sample, keeping it still for the duration of the experiment. (Figure 2.10)

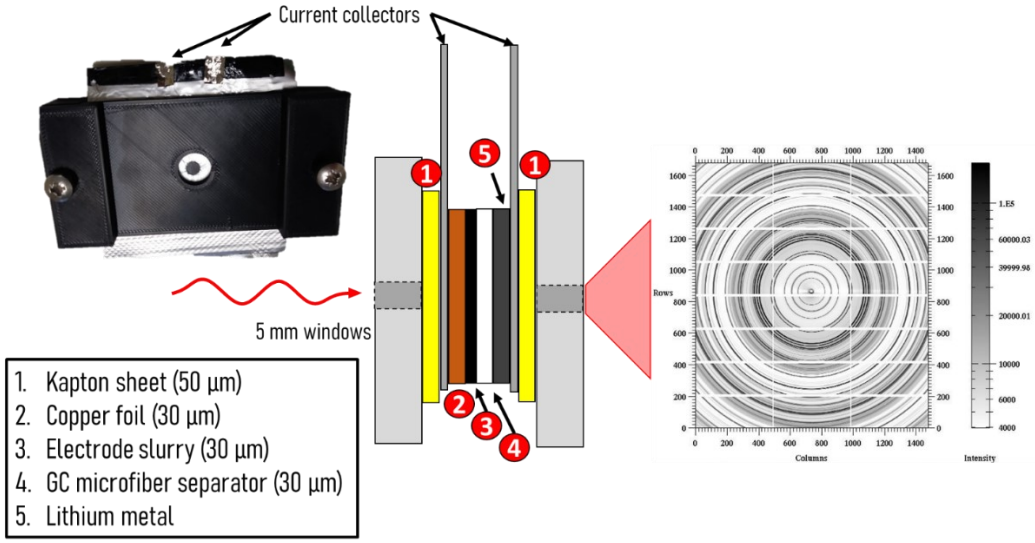

Figure 2.10 - General scheme of the pouch cells employed in this work

As one can guess, the material of the window has to be tuned according to the radiation involved in the experiment:

Visible light – Whether to probe the electrode or the electrolyte, the window must be transparent to a laser beam. The wavelength of most lasers is typical of visible light, hence the most diffuse window materials are glass or quartz. [5]

X-rays - Beryllium foil can be used as a window because of its X-ray transparency, and with some adjustments the oxidation of Be at high voltages can be prevented. However, the high toxicity of beryllium limits its application. Other common window materials are Kapton tape, a thin polymer film, amorphous or carbon or metal foil. Among them, the Kapton tape is widely used because it has a high transmissivity for X-ray, is easy to fabricate and is chemically inert. [5]

In situ/operando experiments

A key feature for in situ/operando experiments is the beam brilliance, which allows fast measurements, required for a combined study. Depending on the employed beam, its source can be available in laboratory or at synchrotrons. In the present work, the synchrotron light was employed thoroughly.

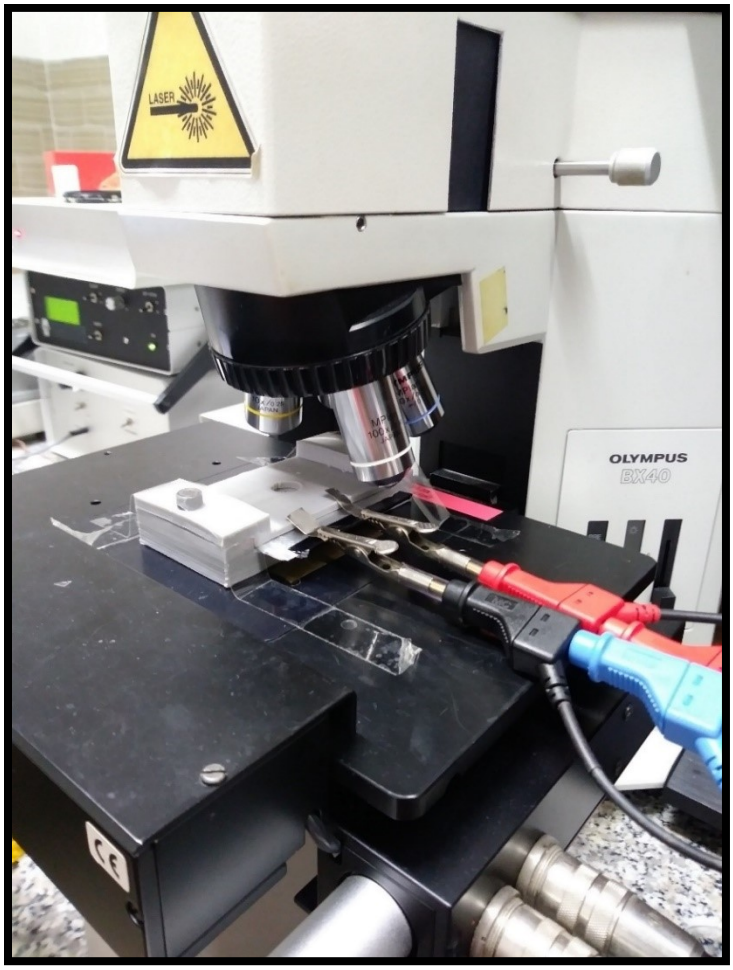

Figure 2.11 - Experimental setup for in situ Raman measurements

In situ Raman – In situ micro-Raman measurements were carried out using a Labram Dilor spectrometer equipped with an Olympus microscope HS BX40, with the experimental parameters already described above. The cells pressed within the cell-holder were mounted on a motorized xy stage (Figure 2.11) and the Raman spectra were recorded at fixed potentials, as soon as the current transient reached the plateau corresponding to equilibrium condition. The chronoamperometric steps were applied with an Autolab PGSTAT30 (Eco Chemie) apparatus, employing the NOVA software.

Figure 2.12 - Experimental setup at the beamline XRD1 of Elettra

Operando XRD – The experimental setup for the operando XRD measurements performed at Elettra, Basovizza (Trieste) is shown in Figure 2.12. The GCPL was performed at a C-rate of C/10 or C/2 in the range 1.0 - 2.8 V during the experiments on $FeNb_{11}O_{29}$, while C/8 in the range 0.01 – 3.0 V were the experimental parameters employed for $ZnFe_2O_4$. The detector available at the beamline XRD1 was a 2D Pylatus, set 200 mm away from the sample, with a beam spot around 200 microns. The exposure time was 10 s, and 4 series of patterns were collected on different spots of the cells, in order to have a complete characterization of the reaction (hundreds of patterns). As calibrant, a pattern of LaB_6 in a capillary was recorded before the measurements. Reference patterns of the pristine powder samples were also recorder in the same geometry, increasing exposure times and rotating the capillaries.

2.5 References

[1] X. Zhong *et al.*, "A novel approach to facilely synthesize mesoporous ZnFe2O4 nanorods for lithium ion batteries," *J. Power Sources*, vol. 306, pp. 718–723, 2016.

[2] M. Chandraiah, B. Sahoo, and P. K. Panda, "Preparation and Characterization of SnO2 Nanofibers by Electrospinning," *Trans. Ind. Ceram. Soc.*, vol. 73, no. 4, pp. 266–269, 2014.

[3] U. du Luxembourg, "Electrodeposition." [Online]. Available: https://wwwfr.uni.lu/recherche/fstm/dphyms/research_areas/photovoltaics/research/electrodeposition.

[4] T. H. Kim *et al.*, "One-step synthesis of multilayered 2D Sn nanodendrites as a high-performance anode material for Na-ion batteries," *J. Mater. Chem. A*, vol. 5, no. 38, pp. 20304–20315, 2017.

[5] D. Liu *et al.*, "Review of Recent Development of In Situ/Operando Characterization Techniques for Lithium Battery Research," *Adv. Mater.*, vol. 31, no. 1806620, pp. 1–57, 2019.

[6] T. J. S. Munsie *et al.*, "Neutron diffraction and μsR studies of two polymorphs of nickel niobate (NiNb2O6)," *Phys. Rev. B*, vol. 96, p. 144417, 2017.

[7] C. Kim *et al.*, "Long-term cycling stability of porous Sn anode for sodium-ion batteries," *J. Power Sources*, vol. 317, pp. 153–158, 2016.

[8] X. H. Rui, N. Ding, J. Liu, C. Li, and C. H. Chen, "Analysis of the chemical diffusion coefficient of lithium ions in Li3V2(PO4)3 cathode material," *Electrochim. Acta*, vol. 55, pp. 2384–2390, 2010.

[9] Metrohm Autolab B. V., *Galvanostatic Intermittent Titration Technique*. 2014, pp. 1–3.

[10] W. Zhu *et al.*, "Application of Operando X-ray Diffraction and Raman Spectroscopies in Elucidating the Behavior of Cathode in Lithium-Ion Batteries," *Front. Energy Res.*, vol. 6, no. 66, pp. 1–16, 2018.

3. Results and discussion

In the following section the research lines mentioned in the introduction are presented as separate chapters, devoted to $ZnFe_2O_4$, SnO_x/C, $FeNb_{11}O_{29}$ and Sn respectively.

3.1 Understanding the cyclability of $ZnFe_2O_4$ as anode material for LIBs

In the following paragraphs the investigation of the cycling behaviour of $ZnFe_2O_4$ with multiple techniques will be presented and discussed.

Characterization of the pristine material

$ZnFe_2O_4$ crystallizes in the cubic spinel structure (Franklinite, Fd-3m, see Introduction). In the X-ray diffraction patterns of both samples (Fig. 3.1.1), no secondary phases are detected, but the different annealing temperature causes marked differences in the crystallization degree: the MOF- $ZnFe_2O_4$ is quite crystalline, while the peak broadening of Hydroxides-$ZnFe_2O_4$ suggests the formation of nanocrystallites. The characteristic peak for the inversion of the spinel is clearly visible in the pattern of MOF-$ZnFe_2O_4$ (ca. 18°), while the combination of low intensity and peak broadening prevents its observation in Hydroxides-$ZnFe_2O_4$.

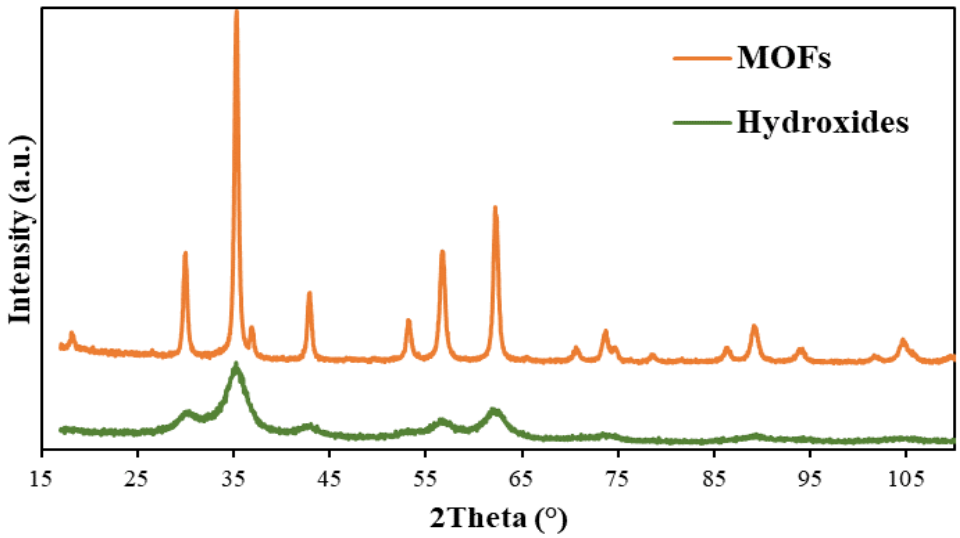

Figure 3.1.1 –Powder diffraction patterns of both $ZnFe_2O_4$ samples.

The results of Rietveld refinement of the powder diffraction patterns are reported in table 3.1.2. The agreement indices (R_{wp} and GOF) suggest reliable results. Lattice parameters and inversion degree are quite similar for both samples, that differ markedly only in the crystallite size, confirming the previous observation.

The thermodynamically most stable configuration of $ZnFe_2O_4$ at ambient temperature and pressure is the normal spinel, but the inversion degree strongly depends on the synthesis. The inversion degree cannot be correlated with the grain size, but it is already reported that an increasing annealing temperature causes higher inversion degrees. [1] This is confirmed by our Rietveld refinement, that calculated a slightly higher inversion for the MOF- $ZnFe_2O_4$.

Sample	*a* (Å)	Crystallites (nm)	Inversion degree *x*	R_{wp}/GOF
MOFs	8.4383(3)	26.63(67)	0.319(12)	$7.81/1.22$
Hydroxides	8.4493(35)	3.46(32)	0.259(30)	$7.37/1.16$

Table 3.1.2 – Main structural parameters and corresponding agreement indices calculated from the Rietveld refinement of the powder diffraction patterns shown in Figure 3.1.1.

The morphology of the particles of zinc ferrite is greatly influenced by the synthesis and, in particular, by the presence of complexing agents in the precursor's solution: SEM images of the powders of Hydroxides- $ZnFe_2O_4$ (Fig. 3.1.3, above) are dense aggregates of edgy particles ranging from tens to a hundred microns, while the powders of MOF- $ZnFe_2O_4$ (Fig. 3.1.3, down) are 2-3 microns long and ca. 500 nm wide nanorods.

This latter morphology is the result of the formation of MOFs between the Fe^{3+}, Zn^{2+} and the oxalic acid: the excess oxalic acid ethanol solution is used as a cosolvent with low dielectric constant that eliminates the solubility product difference of binary transition metal salts and guarantees the co-precipitation of zinc oxalates and iron oxalates. Oxalate ions can easily form planar complexes with metal cations, and ethanol in high concentration can inhibit the radial direction growth due to the effect of capping ligand. [2]

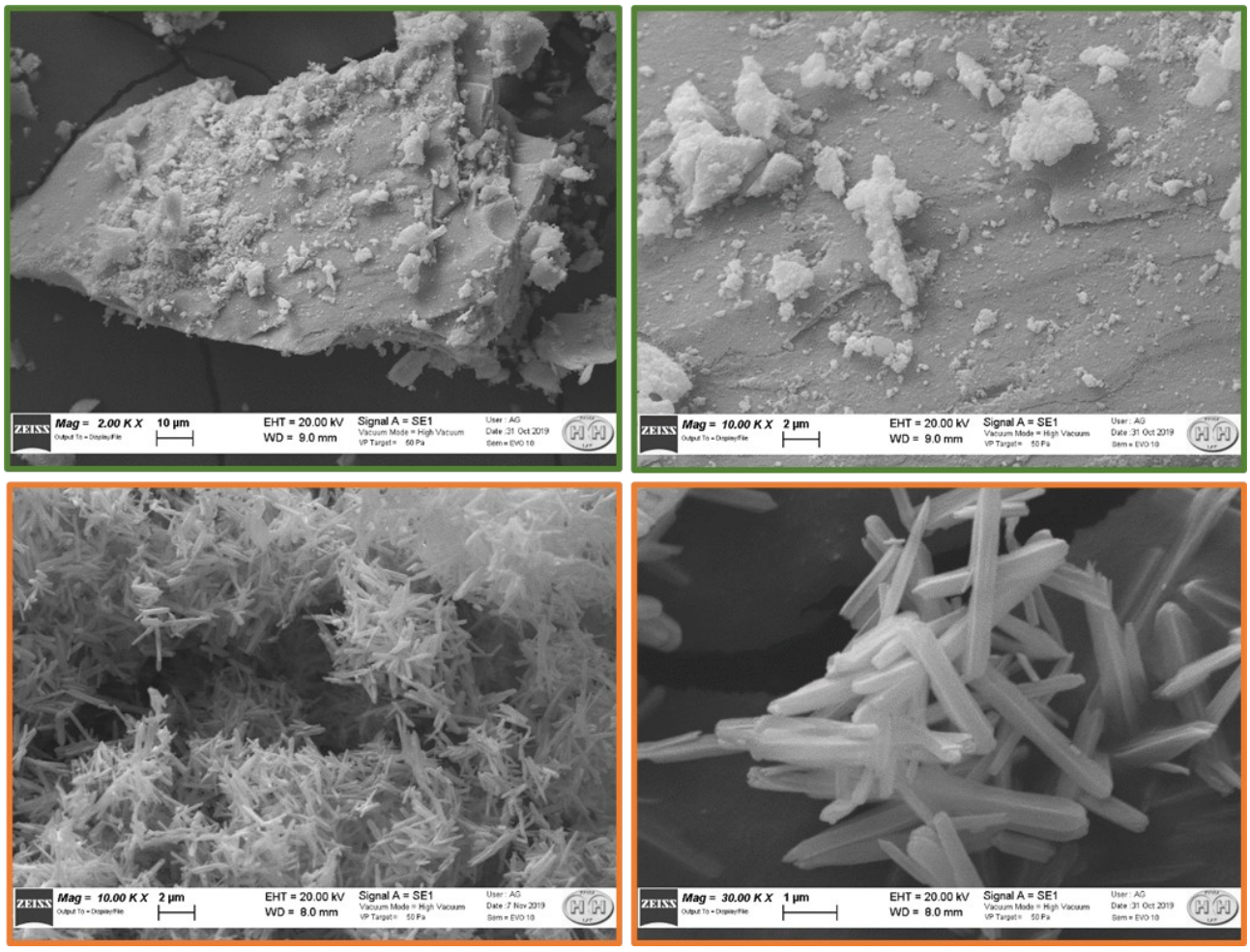

Figure 3.1.3 – SEM images of the Hydroxides-ZnFe2O4 (above) and MOF-$ZnFe_2O_4$ (down) powders.

Even if no secondary phases were detected, many oxides with different chemical compositions can crystallize with the spinel structure (e.g. Fe_3O_4), showing little differences in lattice parameters that prevent a clear identification of them by means of the X-ray diffraction alone. In order to exclude the precipitation of Fe and corresponding formation of Fe_3O_4 (Zn could have been washed away if not precipitated), EDS measurements were performed on both samples.

The EDS spectra and the corresponding atomic composition (Fig. 3.1.4) confirm the formation of crystalline $ZnFe_2O_4$: no elements other than Zn, Fe and O are detected, and the stoichiometric ratio between Iron and Zinc is close to 2, confirming the successful co-precipitation of both cations.

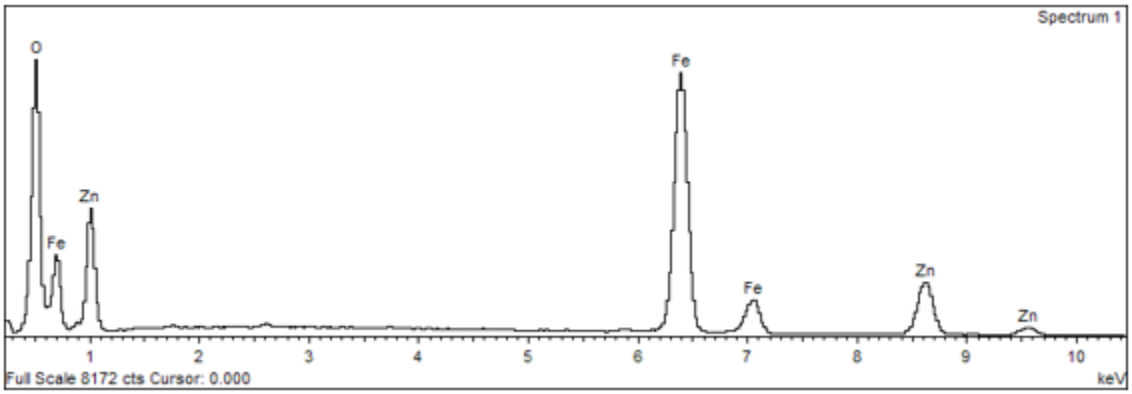

Sample	Atom% Zn	Atom% Fe	Fe/Zn ratio
MOFs	13.71	27.43	2.0007
Hydroxides	12.88	28.05	2.1778
Theoretical	14.28	28.57	2

Figure 3.1.4 – Example of EDS spectrum of $ZnFe_2O_4$ and elemental quantification of both samples.

Phase evolution of the electrodes

In order to investigate the phase composition of the $ZnFe_2O_4$-based electrodes upon cycling, operando XRD measurements were performed on pouch cells with Kapton windows, already employed in other researches. [3] The two series of XRD patterns are reported in Figure 3.1.5.

According to previous literature, the reaction of $ZnFe_2O_4$ is complex and challenging: no diffraction peaks are observed on deeply discharged and re-charged cells because the newly formed phases are poorly crystalline or amorphous. [4] This is one of the reasons why most papers dealing with the topic involve X-ray Absorption Spectroscopy. Furthermore, depending on synthesis and experimental parameters, marked differences are found concerning the phase evolution.

The first region of the voltage profile (from OCV to ca. 0.9 V) is ascribed to insertion of Li into vacant octahedral 16c sites of the spinel structure [5], [6], with a structural rearrangement that involves movement of Zn^{2+} from the 8a to 16c sites, in order to reduce the electrostatic repulsion between Li^+ ions in 16c sites and Zn^{2+} ions in the adjacent 8a sites. [6] Even if an angular shift in XRD patterns was recorded [6], no phase changes were detected from XAS at Fe and Zn K-edges. [7]

$$ZnFe_2O_4 + xLi^+ + xe^- \rightarrow Li_xZnFe_2O_4 \qquad (x < 2)$$

The main voltage plateau at 0.7 V corresponds to the conversion of the spinel to the metals and lithium oxide, together with the formation of SEI. [5] Li_2O is formed in near the active particles or in deep layers in the electrode, [5] homogeneously mixed with the other species. Different authors [7] report instead the compresence of monoxides which then convert to the corresponding metals. Residuals of partially inert ZnO were also detected.

$$Li_xZnFe_2O_4 + (8-x)Li^+ + (8-x)e^- \rightarrow Zn + 2Fe + 4Li_2O \qquad \text{(total capacity 890 mAh/g)}$$

In the last sloping region, the LiZn alloy is formed in the amorphous phases of highly dispersed Fe and Li_2O [5], [7]. However, some authors did not find evidence for the formation of LiZn alloy [6], while others found even intermediate species such as $LiZn_4$. [8]

$$Li^+ + e^- + Zn \rightarrow LiZn \qquad \text{(110 mAh/g)}$$

Upon recharging, ZnO and Fe_2O_3 [7] or FeO [6] are possible oxidation products.

$$Zn + Li_2O \rightarrow ZnO + 2Li^+ + 2e^-$$

$$2Fe + 3Li_2O \rightarrow Fe_2O_3 + 6Li^+ + 6e^-$$

$$Fe + Li_2O \rightarrow FeO + 2Li^+ + 2e^-$$

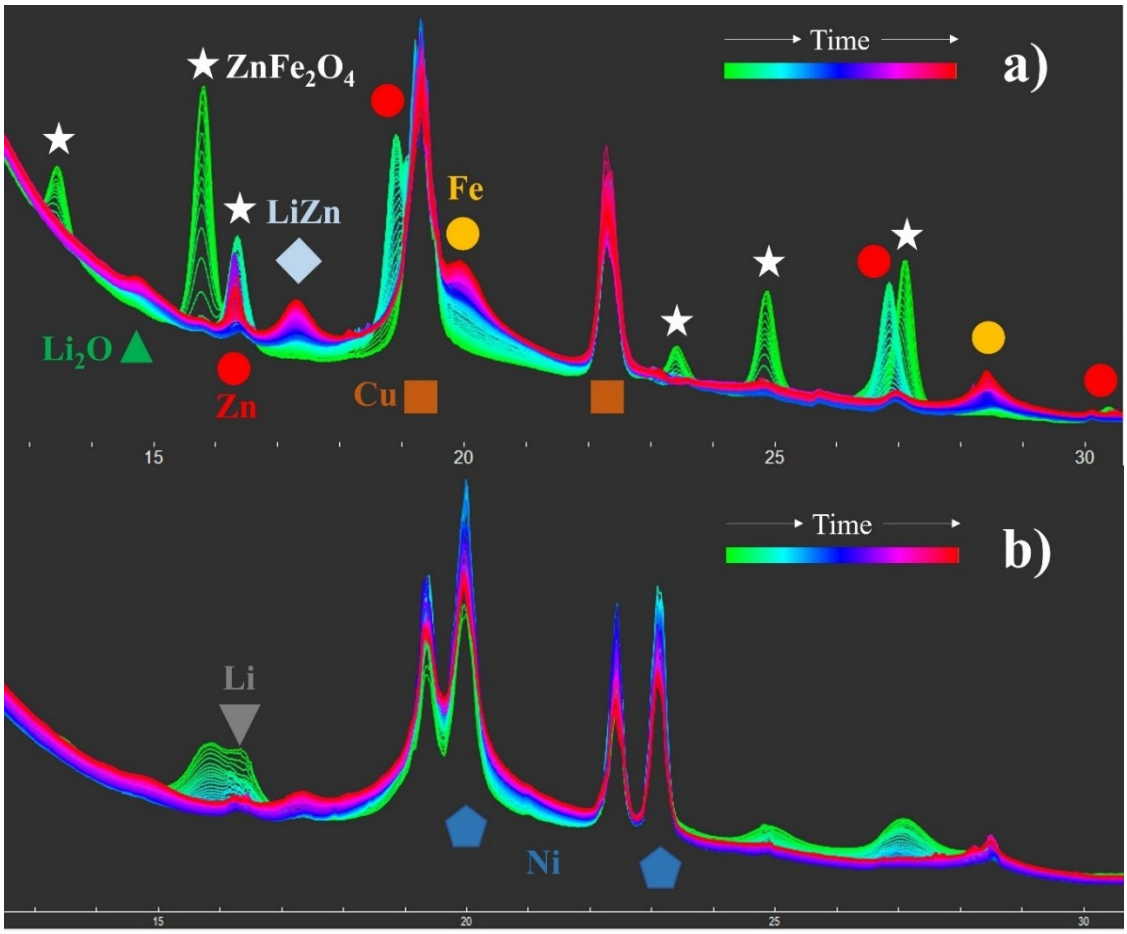

Figure 3.1.5 – Overall evolution of the *operando* XRD patterns of $ZnFe_2O_4$-based electrodes obtained from MOFs (a) and Hydroxides (b).

Our results are supportive of the theorized 1st discharge mechanism (without evidence of intermediate reactive ZnO or FeO) for both the investigated samples (Fig. 3.1.5). The crystallinity of the pristine phase has a great influence on the operando XRD patterns: the new species that are formed on the electrode surface are less crystalline, and this means that for the "MOF" sample, the observation of diffraction peaks corresponding to the reaction products is much easier. As a consequence, the reaction products of the "Hydroxides" sample are much harder to observe. Moreover, in that case the incident beam also hit single crystals of Lithium metal (spikes at ca. 16.5° and more) and the electrical contacts of Nickel (high-intensity diffraction peaks close to the ones of the Cu current collector).

In the following steps (Fig. 3.1.6), $ZnFe_2O_4$ is never formed back and the only reactive specie with significant crystallinity is Zn, which is the oxidized form of the LiZn alloy (forming during charge and disappearing during discharge). No significant differences in the reactivity are observed between the first and the second charge steps, that share the shape of XRD patterns and voltage profile. Also, the voltage profile helps the attribution of the phase transitions during the first discharge: at higher potentials no phase change is detected for the intercalation of Li into the spinel structure; then the main voltage plateau corresponds to formation of Li_2O, Fe and Zn, which reacts to form the LiZn alloy in the last sloping region.

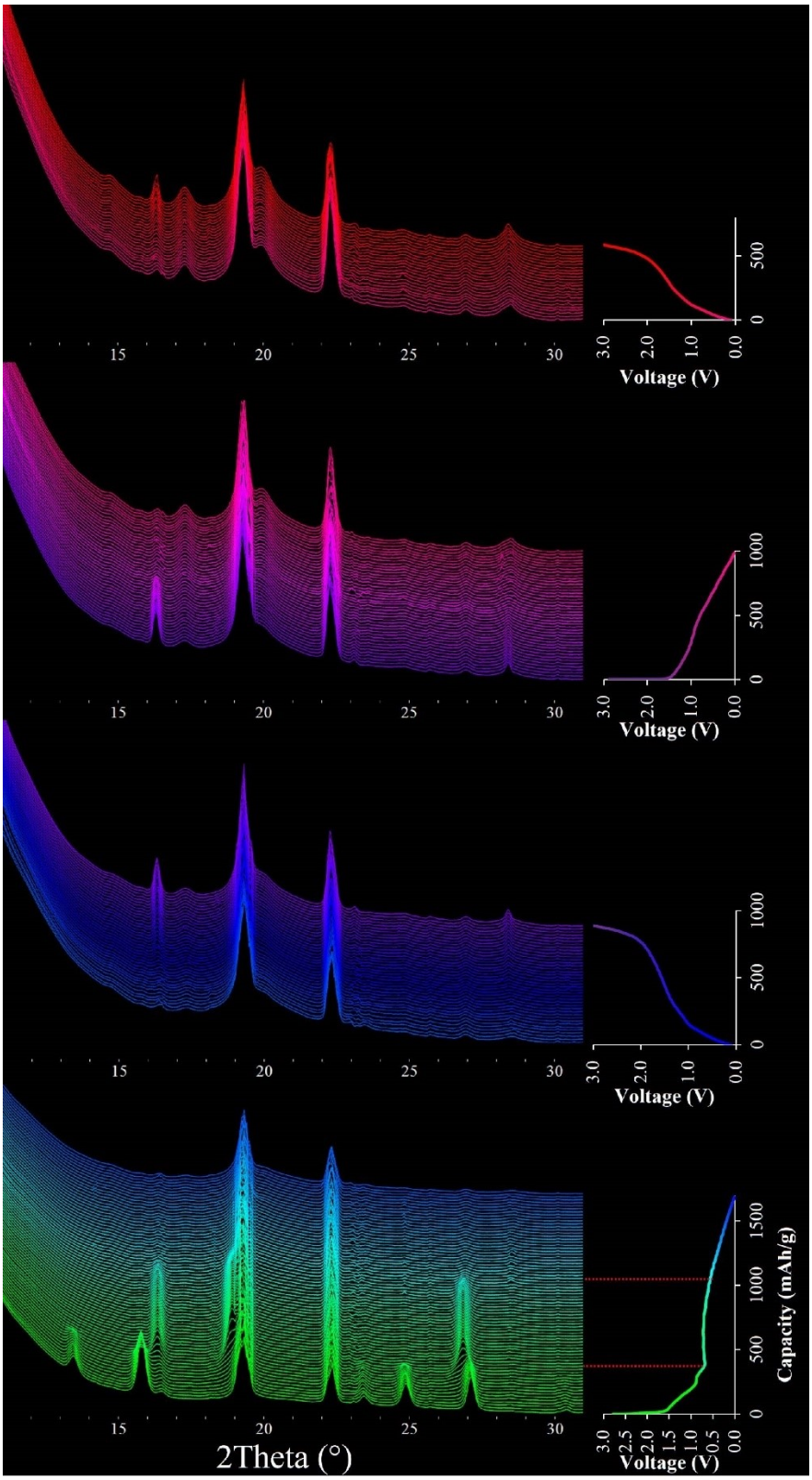

Figure 3.1.6 – Voltage profiles of MOF-$ZnFe_2O_4$ and corresponding operando XRD patterns during the first two cycles (from bottom to top).

However, the reaction of the observed crystalline species alone cannot explain the recorded capacities: the first cycle capacity exceeds the theoretical 1000 mAh/g, and the following steps exceed by far the reversible 110 mAh/g of the alloying/de-alloying reaction (Fig. 3.1.6)

A possible explanation is related to the intrinsic issue of the X-ray diffraction: reactions between amorphous (or nano-crystalline) phases cannot be detected due to the huge peak broadening. Fe, LiZn and Li_2O, for example, are already barely visible as an increase in the background in correspondence of the main diffraction peaks. Further reactions involving those species would be almost impossible to observe, and this means that the reversible oxidation of Fe to the corresponding oxide cannot be totally ruled out. Further analyses should be carried out, but our data (Fig. 3.1.7) seem to suggest that:

- Different reactivity of Fe and Zn is inferred, the latter being much more crystalline;
- Zn does not seem to be oxidized to ZnO, since the high crystallinity of Zn is expected to lead to detectable reaction products;
- Fe does not seem to be oxidized to FeO or Fe_2O_3, since the crystallinity of Fe slightly increases during all the steps, including charges;
- The crystallinity of LiZn increases upon cycling, and the crystallinity of Zn decreases accordingly.

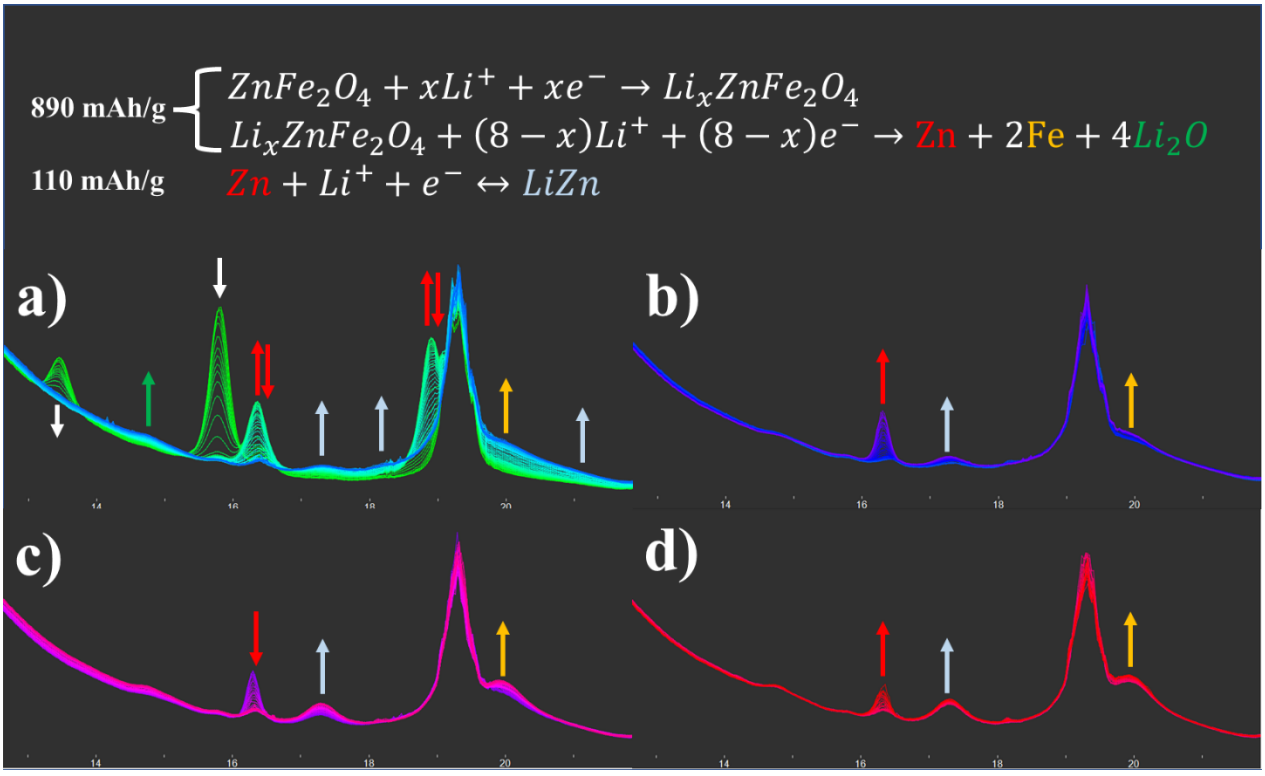

Figure 3.1.7 – Structural evolution during the a) 1st discharge, b) 1st charge, c) 2nd discharge and d) 2nd charge separately for MOF-$ZnFe_2O_4$.

Side reactions

The other possible explanation for the extra capacities involves side reactions. The SEI, which has been studied since the 80's, [9], [10] is a passivation layer formed on the surface of the anode at lower voltages, outside of the stability window of the electrolyte. The reduction of the electrolyte forms a protective film which is permeable to Li^+ ions but prevents further decomposition (electrically insulating properties) when a certain thickness is reached.

Previous studies confirmed that the lithium uptake of the spinel $ZnFe_2O_4$ is a superimposition of the conversion/alloying reactions and the Li storage in the SEI. [11] The decomposition of the electrolyte at voltages below 0.8 V results in LiF and $LiPF_x$ from the electrolyte salts and Li_2CO_3 from the electrolyte carbonates. [5] LiC_x from the intercalation of Li into amorphous conductive carbon is also present [11] alongside Li_2O and Li_2O_2 [10] and, at the lowest voltages, $ROCO_2Li$. [5]

The SEI forms in stages: in the first stage a thin SEI (less than 10 nm) is formed after electrolyte percolation, covering both the active material and the binder, then it preferentially grows over $ZnFe_2O_4$ particles. SEI is fully formed at the end of the voltage plateau (few tens of nm) and remains stable over the cycles. [5], [10], [11] At the initial stages, the SEI layer consist of LiF and Li_2CO_3. Below 0.7 V, Li_2CO_3 is covered by a superficial layer of alkyl lithium carbonates, and this layer grows down to the low-end voltage (5-7 nm). During de-lithiation this outer layer decreases thanks to reversible redox reactions (to Li_2CO_3). [5]

The combination of the capacity from the intercalation of lithium in the amorphous carbon and the reversible redox reactions of Lithium carbonate account for 250 and 300 mAh/g of excess capacity respectively. [5]

Cyclic voltammetry can provide great details on every kind of electrochemical reactions: thermodynamics and kinetics can be studied with suitable experiments. The voltammograms in Fig. 3.1.8 clearly show that the system is affected by huge irreversibility: all the 1^{st} cycle cathodic peaks except from the lower-voltage end are irreversible. Most of the redox chemistry of the following cycles is characterized by a high overpotential between the asymmetrical (and likely bi-component) cathodic peak centred at ca. 0.9 V and the anodic at ca. 1.6 V. The only partially reversible reaction is detected at lower voltages in the cathodic scan.

According to the operando XRD patterns in Figs. 3.1.5-3.1.7 and the corresponding discussion, the first cycle cathodic peaks above 0.8 V can be assigned to Li intercalation into the vacant sites of $ZnFe_2O_4$, accompanied by the cation redistribution of Zn. The main redox peak at 0.7 V corresponds to the voltage plateau, that is the conversion reaction to the metals and lithium oxide, and the lower-voltage end is attributed to the formation of LiZn alloy.

Following instead the previous discussion on side reactions, the sharp cathodic first cycle redox peak at 0.75 V, superimposed to the conversion reaction, could be assigned to the formation of most of the SEI (fluorinated species, Li_2CO_3 and Lithium oxides), while the sub-peaks at the lower end voltages can be attributed to the intercalation of Li into the amorphous carbon and to the redox reactions of Li_2CO_3 to the alkyl lithium carbonates. In the following cycles, the reversible alloying/de-alloying is accompanied by the redox reactions of carbonates and amorphous carbon. Reversible redox chemistry of Zn^{2+}/Zn and

Fe^{3+}/Fe or Fe^{2+}/Fe cannot be ruled out, even if XRD results cannot support this hypothesis. Moreover, the redox peaks are broader for the 1st charge and the following steps, because the newly formed phases are less crystalline than the pristine $ZnFe_2O_4$.

Most of the differences between the two samples can be ascribed to the crystallinity: sharper redox peaks are obtained for the most crystalline sample (MOF), while the differences in the high-voltage first cycle cathodic peaks can be ascribed to a slightly different inversion degree. Moreover, in the 2nd cycle the intensity ratio between the lower-voltage region and the main redox peak has opposite trends. The important variations in the lower-end voltage and in the SEI formation peak seem to suggest differences between the electrode areas.

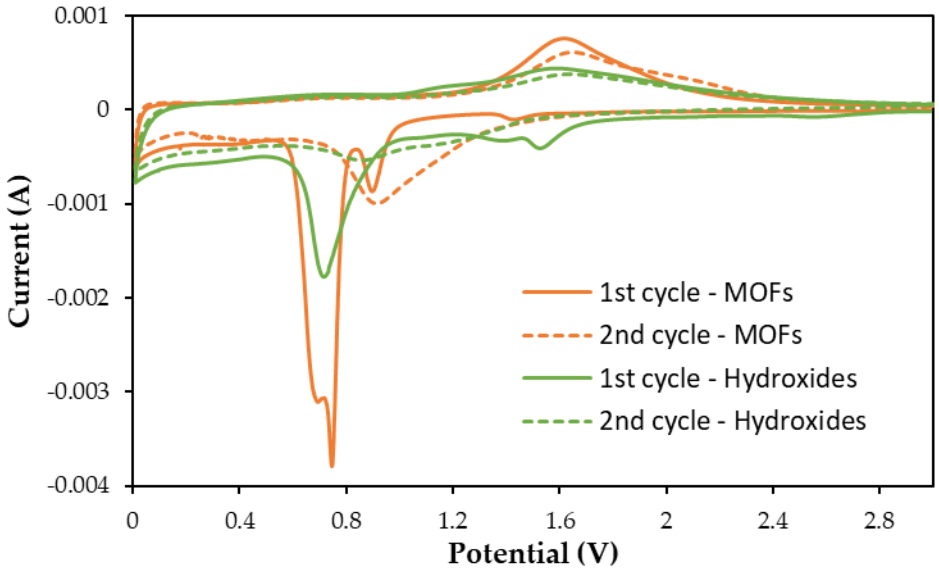

Figure 3.1.8 – Voltammograms for both samples of $ZnFe_2O_4$, recorded at 0.1 mV/s.

In recent years, the analysis of the kinetic behaviour of electrode materials is getting more common. With a simple voltammetric experiment performed at different sweep rates, the current from the semi-infinite linear diffusion can be separated from the pseudocapacitive current, when the following relation is adapted:

$i_{(V)} = k_1 v + k_2 v^{0.5}$

where v is the sweep rate, k_1 and k_2 are fittable parameters that describe the relative amounts of pseudocapacitive and semi-infinite linear diffusion respectively.

For $ZnFe_2O_4$ the pseudocapacitance is extrinsic, i.e. caused by the increase of surface area in nanostructured samples that show improved high-rate behaviour through reduction of diffusion distances. This means that higher pseudocapacitive contribution can be considered an indication of higher electrode area.

As previously inferred from the voltammograms at 0.1 mV/s (Fig. 3.1.8), different electrode areas are detected (as different pseudocapacitive contributions, see Fig. 3.1.10) between the two samples: the MOF- $ZnFe_2O_4$ shows 30-35% excess pseudocapacitive current, with values up to 84% at 1 mV/s, while the kinetics of the Hydroxides- $ZnFe_2O_4$ are much slower (27% at 0.1 mV/s). Since the passivation of the electrodes and the corresponding redox reactions occur at the electrode surface, having a higher electrode area is expected to lead to a higher contribution from SEI. This explains the observed differences in the voltammograms at 0.1 mV/s.

The pseudocapacitive current can be plotted as a function of the voltage (Fig. 3.1.9). Since pseudocapacitive currents indicate a surface-controlled kinetics, they can be attributed to a reaction involving the surface of the electrode, or to highly nanostructured particles. After the first cycle for which it is impossible to perform an accurate estimate of the pseudocapacitive current, the alloying of crystalline Zn formed during charge and observed with XRD is then attributed to the main cathodic peak, with an important contribution from semi-infinite linear diffusion. The cathodic peaks at lower voltages (below 500 mV) can then be attributed to redox reaction of SEI (Li_2CO_3 to alkyl lithium carbonates) and surface intercalation of Li into amorphous carbon, with a contribution from the alloying reaction of surface nanoparticles or the hypothetical reversible redox chemistry between Zn, Fe and the corresponding oxides.

The main anodic peak has again a significant contribution from semi-infinite linear diffusion, ascribed to crystallization of Zn, and the remaining peaks are attributed to surface reactions. In the sample Hydroxides, surface reactions (cathodic and anodic) are decreased because the particle size is much bigger, limiting the reaction kinetics.

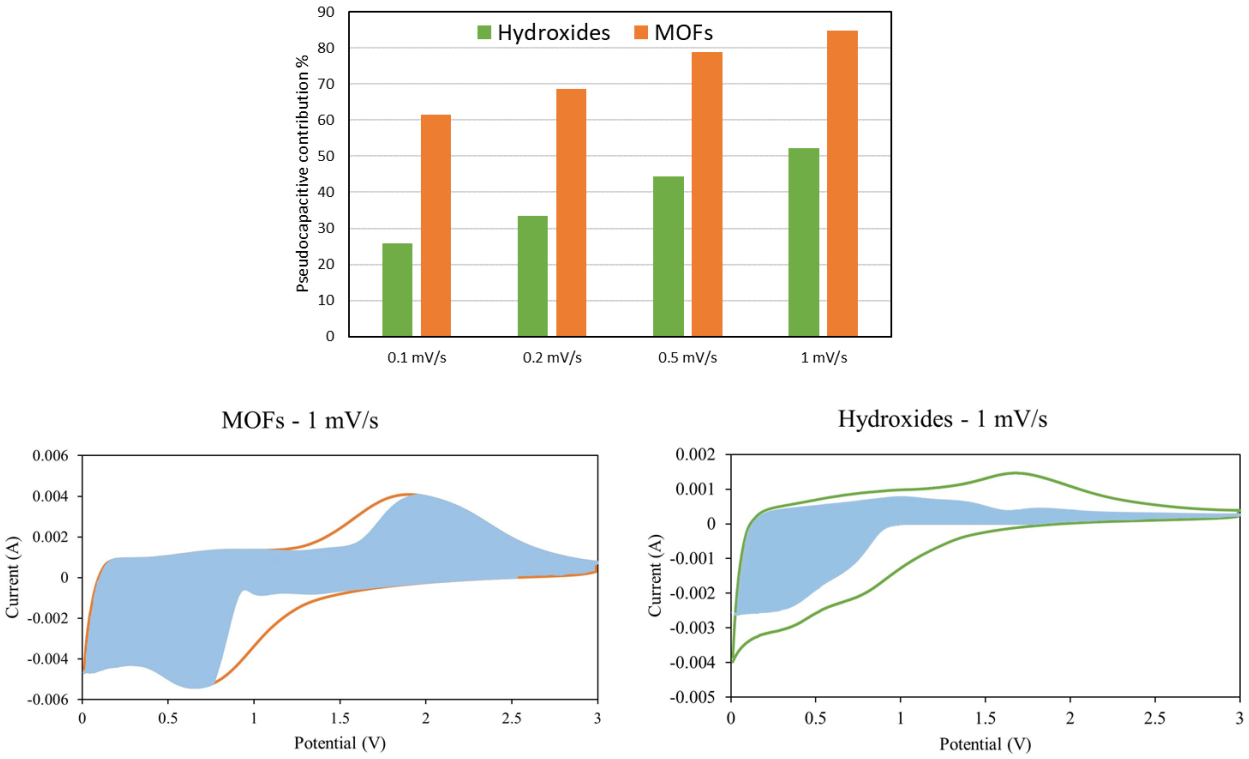

Figure 3.1.9 – Voltammograms recorded at 1 mV/s, corresponding pseudocapacitive current highlighted in light blue, and histograms showing the relative ratios between the pseudocapacitive current and the total current.

Electrochemical Impedance Spectroscopy (EIS)

Following the data obtained from voltammograms, EIS spectra were recorded at meaningful potentials, for 3 cycles of discharge and charge (Fig. 3.1.10). The first discharge irreversibility is clearly evidenced in the fitted values of the resistance and in the shape of the spectra. The overall trend is shared by both samples, even if some differences can be detected.

The pristine MOF-electrode exhibits less OCV resistance, and this can be ascribed to the resistivity of $ZnFe_2O_4$, which is reported to decrease at higher crystallinity and inversion degree, [1] but could also be lower due to the much smaller grain size.

The shape of the fitted values of resistance as a function of the voltage can be interpreted on the basis of previously shown voltammograms: at certain voltages corresponding to charge-transfer reactions (redox peaks), the current sharply increases because the charge-transfer resistance associated with that reaction decreases. During the first discharge, the minimum of the resistance at 0.7 V corresponds to the peak current associated with the conversion reaction. The increase of the resistance upon further discharge could be ascribed to the insulating properties of the SEI, whose direct observation as an extra semicircle in the Nyquist plot could be hindered by the overlapping of multiple charge-transfer reactions at similar frequencies, as the extreme broadening of the semicircles suggests.

During the following steps, resistance minima are detected at intermediate potentials, corresponding to the main redox reactions during the anodic (1.6 V) and cathodic (0.9 - 1.0 V) scans. The higher values recorded at the high-end voltages can be ascribed to the overpotential associated with charge-transfer reactions. The main contribution to the increase of resistance at low-end voltages can instead be ascribed to the reversible reactions involving SEI, which were inferred to be much more significant for the MOF sample because of its higher electrode area.

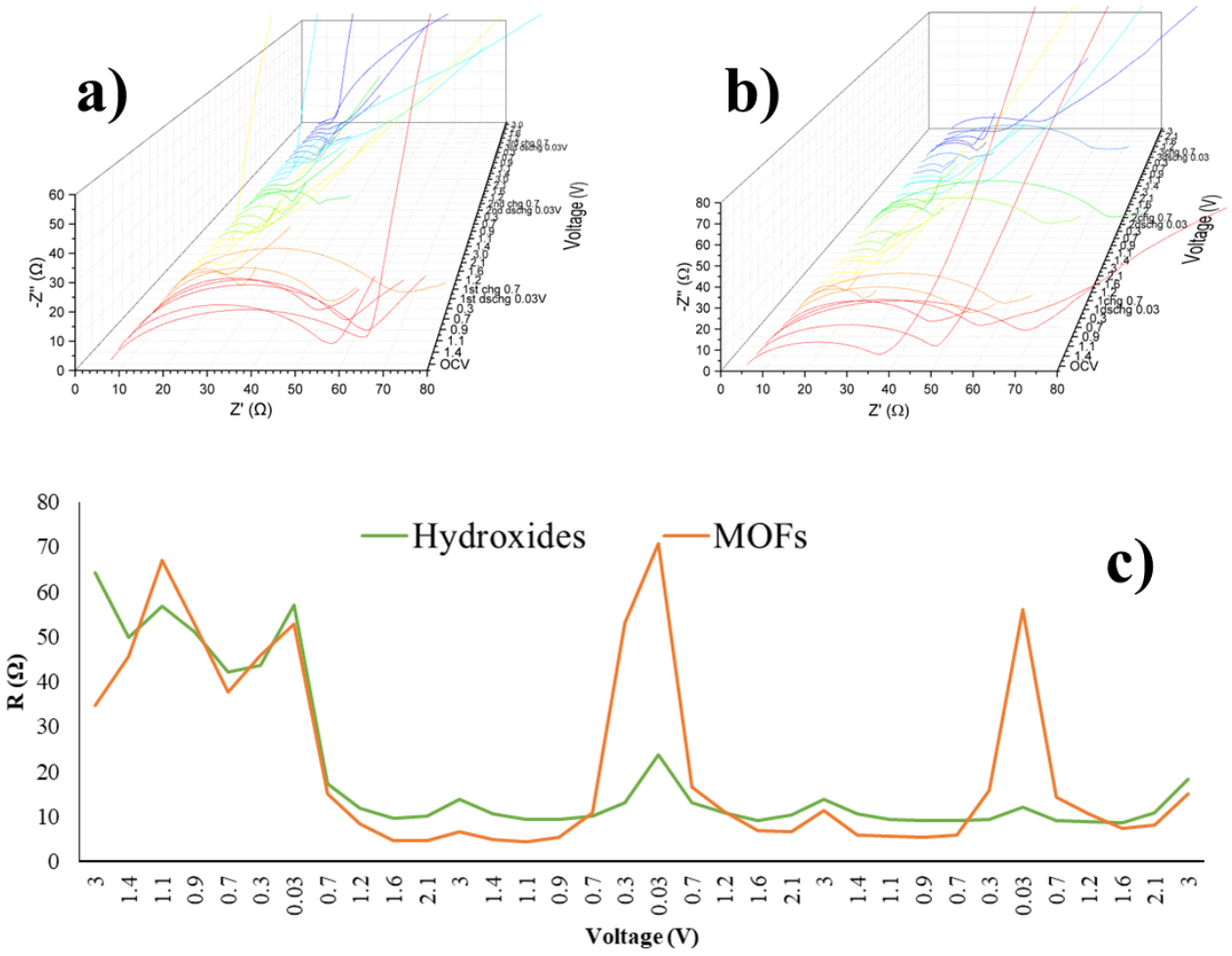

Figure 3.1.10 – Nyquist plot for Hydroxides-$ZnFe_2O_4$ (a), MOF-$ZnFe_2O_4$ (b) and corresponding fitted values of resistance (c) as a function of the voltage.

Galvanostatic cycling

All the previously employed techniques are useful for the explanation of the cycling behaviour of $ZnFe_2O_4$ (Fig. 3.1.11). The first cycle capacity largely exceeds the theoretical 1000 mAh/g expected for the intercalation/conversion/alloying reactions involving the active material. The only reasonable explanation is provided by side reactions that offer a significant contribution to the overall charge storage, namely formation of SEI and intercalation into amorphous carbon.

The capacity rapidly fades in the following cycles, even if the high values account for the reversibility of side reactions. Increasing the C-rate results in a capacity loss, which is attributed to kinetic limitations since the capacity recovery at C/2 after higher C-rates is good. This means that, after the first 10-20 cycles where the coulombic efficiency is quite low and the capacities drop regardless of the C-rate, slower C-rates are necessary for a satisfying reactivity, with > 95% coulombic efficiency.

In the rate capability test, the MOF-$ZnFe_2O_4$ performs better, with higher capacities at every C-rate and higher coulombic efficiency in the first cycles. At higher C-rates, the Hydroxides- $ZnFe_2O_4$ has better coulombic efficiency, probably caused by the lower capacity. In the long-term stability test, the same trend of the capacities is maintained, but the coulombic efficiencies are visibly higher for the Hydroxides-$ZnFe_2O_4$, and this accounts for the better cycling stability over the 200 cycles (> 99% coulombic efficiency after the first 80 cycles).

This last observation seems to suggest that the crystallinity of the active material is an important parameter: it seems that the higher electrode area offered by MOF-$ZnFe_2O_4$ (smaller particles) is responsible for the better reactivity in the first cycles, as discussed in the previous paragraphs. However, in the long term, a lower crystallinity of the active material (that leads to nano-crystalline reaction products) could lead to a better reversibility.

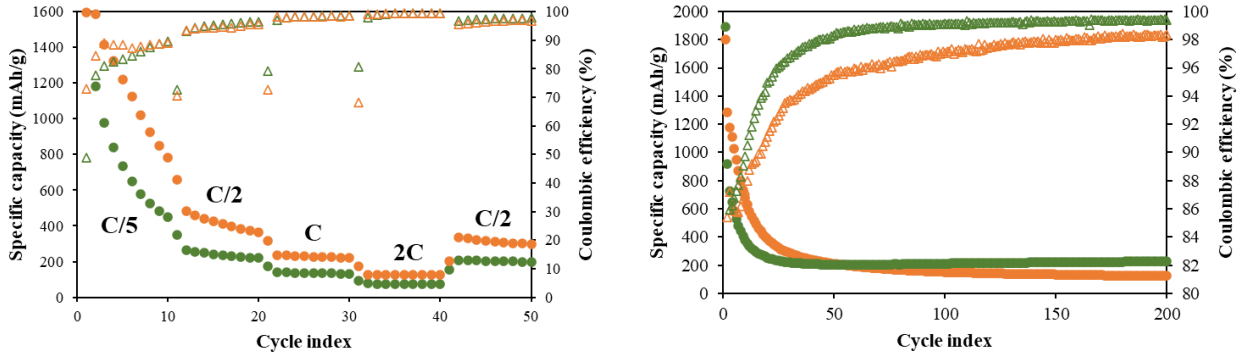

Figure 3.1.11 – Rate capability test and long-term cycling test at C/2 after a first cycle at C/5 for MOF-$ZnFe_2O_4$ (orange) and Hydroxides-$ZnFe_2O_4$ (green).

Conclusion

In conclusion, cubic $ZnFe_2O_4$ with partially inverted spinel structure was synthesized with two similar co-precipitation routes. The co-precipitation of hydroxides (basic pH) and the following thermal treatment at relatively low temperature caused the formation of big aggregates of edgy particles, formed by nanocrystals. The co-precipitation of MOFs (acidic pH) and the following thermal treatment at a higher temperature resulted in smaller aggregates of nanorods, more crystalline. The operando X-ray diffraction measurements confirmed the theorized reaction mechanism and its irreversibility, thanks to the observation of crystalline reaction products without recovery of the pristine phase. A low crystallinity of the reaction products seems to have a positive influence on the long-term performance, while a morphology with higher electrode area seems to perform better in the first cycles, where also side reactions provide a high contribution to the total capacity. The combination of operando X-ray diffraction, cyclic voltammetry and electrochemical impedance spectroscopy seems to be effective for the characterization of complex electrochemical reactions, and this study could be useful to improve the performance of $ZnFe_2O_4$ in the future years.

References

[1] L. I. Granone, R. Dillert, P. Heitjans, and D. W. Bahnemann, “Effect of the Degree of Inversion on the Electrical Conductivity of Spinel ZnFe2O4,” *ChemistrySelect*, vol. 4, no. 4, pp. 1232–1239, 2019.

[2] X. Zhong *et al.*, “A novel approach to facilely synthesize mesoporous ZnFe2O4 nanorods for lithium ion batteries,” *J. Power Sources*, vol. 306, pp. 718–723, 2016.

[3] D. Spada *et al.*, “FeNb11O29, anode material for high-power lithium-ion batteries: Pseudocapacitance and symmetrisation unravelled with advanced electrochemical and in situ/operando techniques,” *Electrochim. Acta*, vol. 393, p. 139077, 2021.

[4] D. Zhou *et al.*, “Local structure changes of nano-crystalline ZnFe2O4 during lithiation and de-lithiation studied by X-ray absorption spectroscopy,” *Electrochim. Acta*, vol. 246, pp. 699–706, 2017.

[5] S. J. Rezvani *et al.*, “Is the Solid Electrolyte Interphase an Extra-Charge Reservoir in Li-Ion Batteries?,” *ACS Appl. Mater. Interfaces*, vol. 9, pp. 4570–4576, 2017.

[6] Y. Zhang *et al.*, “Probing the Li Insertion Mechanism of ZnFe2O4 in Li-Ion Batteries: A Combined X-Ray Diffraction, Extended X-Ray Absorption Fine Structure, and Density Functional Theory Study,” *Chem. Mater.*, vol. 29, pp. 4282–4292, 2017.

[7] Q. Su *et al.*, “Study on the Electrochemical Reaction Mechanism of ZnFe2O4 by in Situ Transmission Electron Microscopy,” *Sci. Rep.*, vol. 6, p. 28197, 2016.

[8] Y. Ma *et al.*, “ZnO/ZnFe2O4/N-doped C micro-polyhedrons with hierarchical hollow structure as high-performance anodes for lithium-ion batteries,” *Nano Energy*, vol. 42, pp. 341–352, 2017.

[9] E. Peled, “The electrochemical behavior of alkali and alkaline earth metals in nonacqueous battery systems - The solid electrolyte interphase model,” *J. Electrochem. Soc.*, pp. 2047–2051, 1979.

[10] S. J. Rezvani *et al.*, “Local Structure and Stability of SEI in Graphite and ZFO Electrodes Probed by As K-Edge Absorption Spectroscopy,” *J. Phys. Chem. C*, vol. 120, pp. 4287–4295, 2016.

[11] A. Di Cicco *et al.*, “SEI Growth and Depth Profiling on ZFO Electrodes by Soft X-Ray Absorption Spectroscopy,” *Adv. Energy Mater.*, p. 1500642, 2015.

3.2 SnOx/C composites as anode materials for LIBs

In the following paragraphs, tin-carbon composites will be characterized from a structural and electrochemical point of view.

Physico-chemical characterization

The commercial tin oxide employed as starting material is a monophasic crystalline powder (Fig. 3.2.1, Cassiterite structure), constituted by aggregates of particles (up to tens of microns), as demonstrated by SEM images.

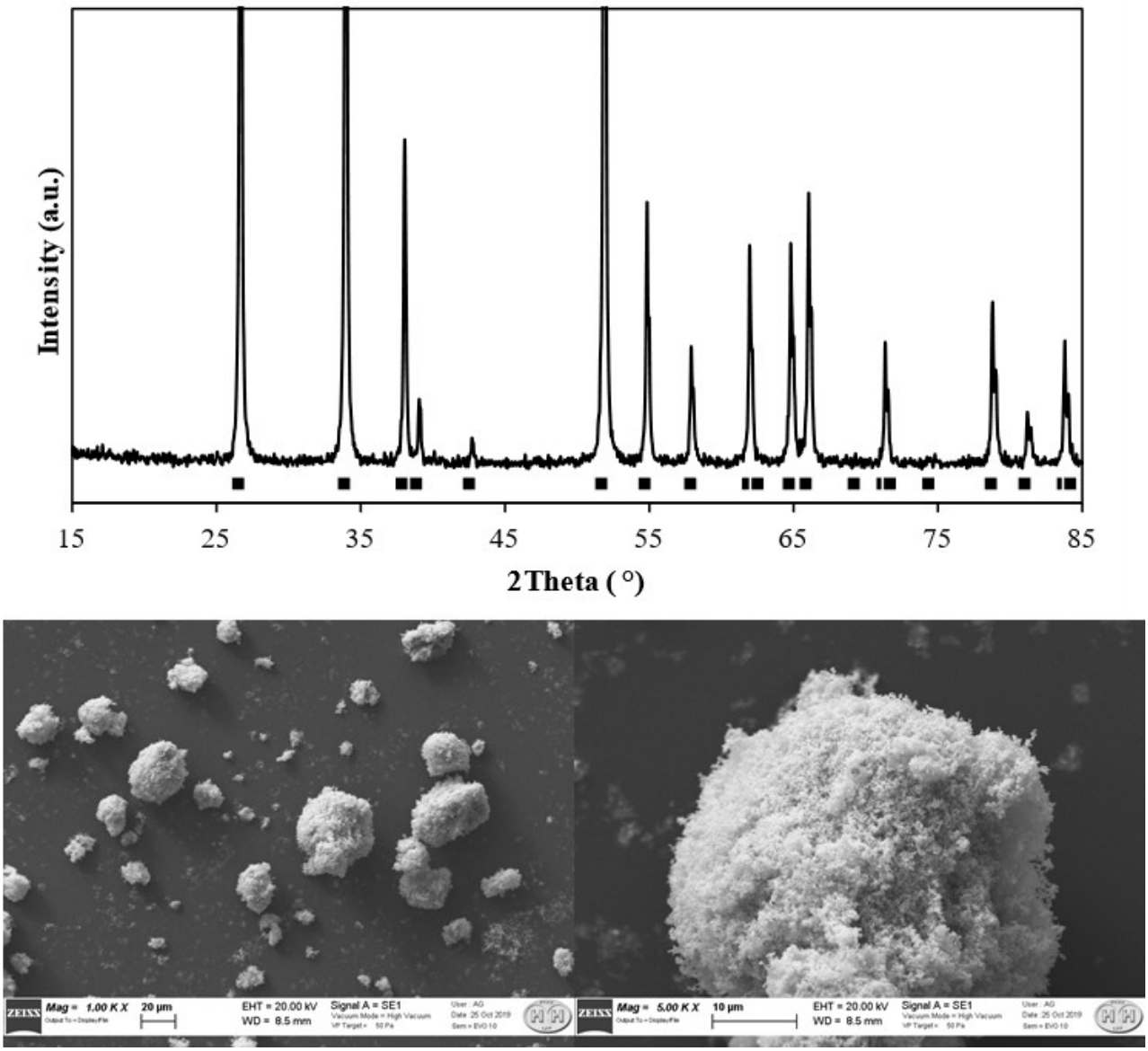

Figure 3.2.1 – XRD pattern, with reflections of Cassiterite (squares), and SEM images at two different magnifications of commercial SnO_2.

The self-standing sample obtained by electrospinning and the corresponding powder obtained after high energy milling (Figure 3.2.2, SnO_x/C – S and SnO_x/C-P) are constituted by different phases: SnO_2 (Cassiterite) and tetragonal Sn for the first, while in the second also the presence of SnO is detected. In both cases, the tin phases are well crystalline and dispersed in the carbonaceous matrix of carbonized PAN, amorphous or little crystalline. The formation of metallic tin is due to the calcination in Ar-H_2 atmosphere, which caused partial reduction of Sn(IV) without burning the carbon deriving from PAN. High-energy milling the sample promoted a mechano-chemical reaction that caused further reduction of SnO_2 to SnO (Romarchite) and Sn accompanied by oxidation of carbon to gaseous CO_2.

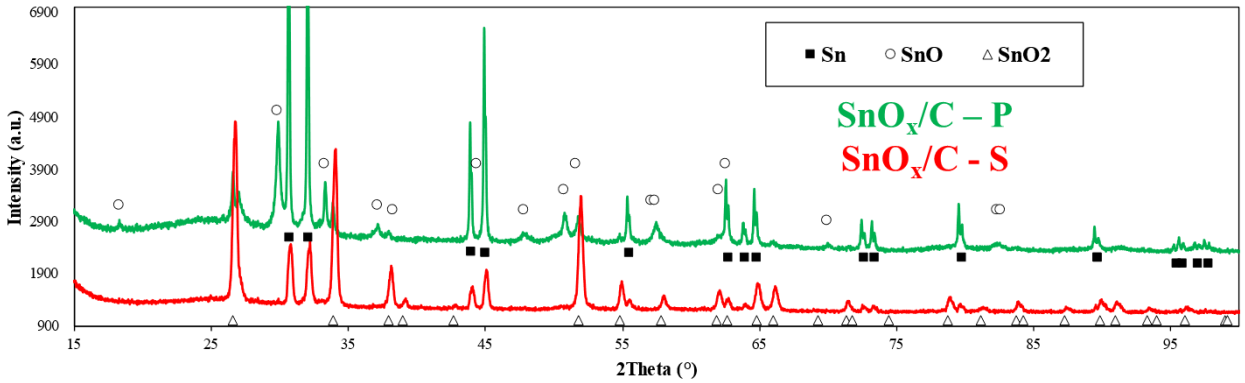

Figure 3.2.2 – XRD patterns of SnOx/C – S (red) and SnOx/C – P (green).

The precise quantification of the phases was performed on the powder diffraction patterns by Rietveld refinement, and the corresponding results are reported in Table 3.2.3. The GOF values suggest a reliable determination of the structural parameters. The SnOx/C-S is mostly constituted by SnO_2 (ca. 80%), with about 20% of metallic Sn formed after chemical reduction with Ar/H_2 (as previously explained). The mechano-chemical reaction instead seems to be much more effective in the reduction of Sn(IV), since the primary phase in the SnOx/C-P sample is tin metal (ca. 60%). The heating caused by friction during milling also promoted significant crystallization of tin (sharper peaks are detected and bigger crystallites are calculated for the ground sample, see also Fig. 3.2.2), together with the nucleation and growth of SnO. The residual SnO_2, instead, did not crystallize significantly.

	Sn (wt. %)	Cry. size (nm)	SnO (wt. %)	Cry. size (nm)	SnO_2 (wt. %)	Cry. size (nm)	GOF
SnOx/C - P	62.28(46)	120.9(12)	12.29(26)	33.53(65)	25.43(23)	45.9(19)	1.39
SnOx/C - S	21.80(19)	44.37(86)	/	/	78.20(19)	40.50(37)	1.74

Table 3.2.3 – Quantitative Phase Analysis performed with a Rietveld refinement on the XRD patterns of the tin/carbon composites. Calculated crystallite sizes and GOF values are also reported.

Carbon could be barely detected in the diffraction patterns (low scattering factor and low crystallinity) but gives distinctive Raman features (Fig. 3.2.4): for both samples, two broad bands are detected at 1330 and 1590 cm^{-1}, assigned to disordered/nano-crystalline sp^2 carbon (D band), and to single crystals of graphite (G band) respectively. [1] The relative ratios between Raman D and G bands, of about 3.5, suggest that carbon is highly turbostratic. The high interconnectivity of the PAN nanofibers and the low temperature of thermal treatment (relatively to graphitization) could have led to a high amount of defectivity in the resulting carbon.

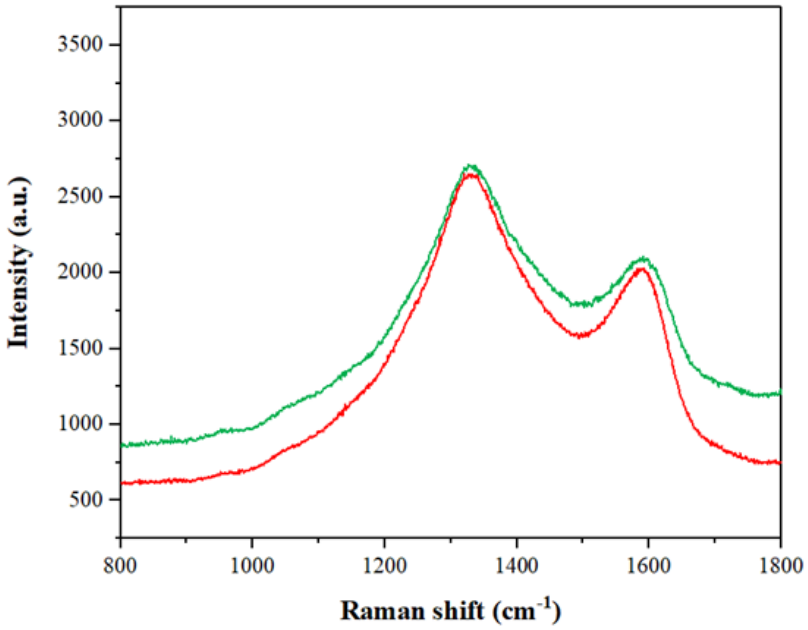

Figure 3.2.4 –Raman spectra of SnOx/C – S (red) and SnOx/C – P (green).

The chemical composition of the samples was verified thanks to the combination of EDS and TGA/DSC (Fig. 3.2.5): the spectroscopic quantification suggests a 34 and 35 wt. % of Sn in the sample, with the rest of the atoms provided by O and C, in agreement with the stoichiometric amount used during the synthesis. The gravimetric analysis determines a small loss of weight, completed at 100 °C, probably due to adsorbed humidity, followed by the exothermic combustion of carbon in air at ca. 500 °C. After the combustion, the mass of the sample is almost constant at 29% and 35%, i.e. the residual tin amount, confirming the aforementioned results.

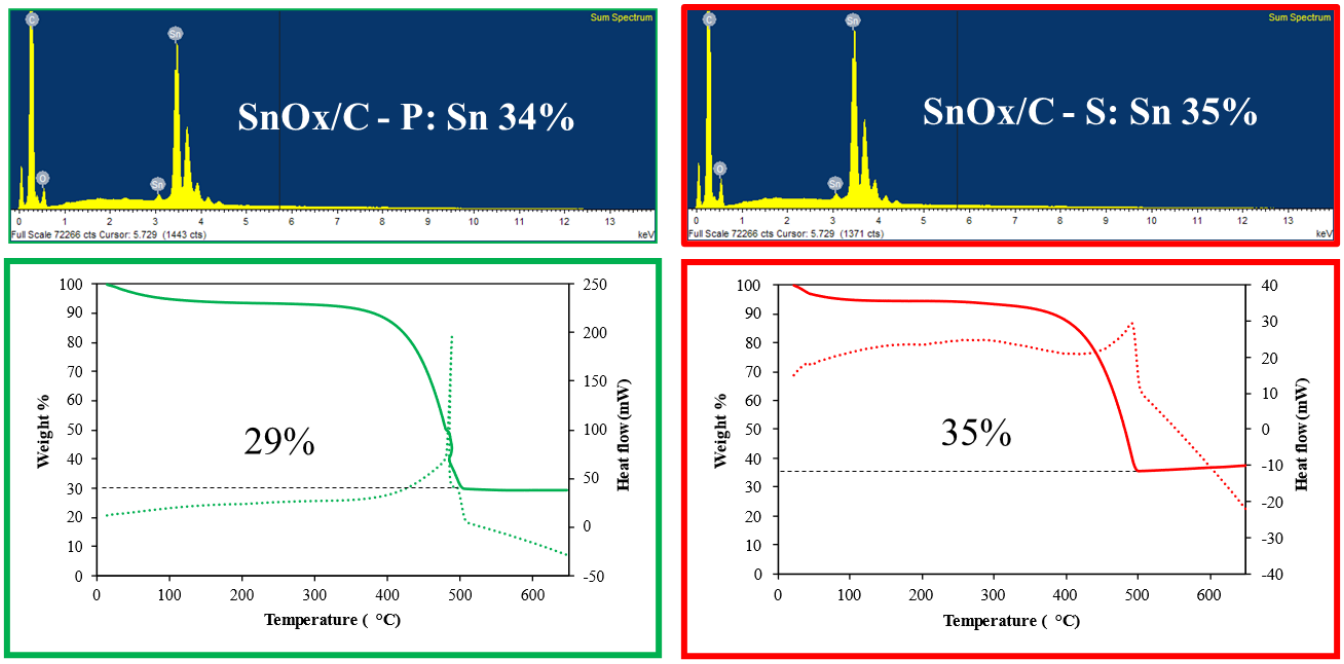

Figure 3.2.5 –EDS spectra of the composites and corresponding quantification of Tin (m/m %), together with TGA/DSC curves (full lines and dotted lines respectively) for SnOx/C – P (left) and SnOx/C – S (right).

The composite has the typical morphology deriving from electrospinning (Fig. 3.2.6): nanofibers are detected all over the sample, with a high degree of interconnectivity. The most evident change in the morphology of SnOx/C-P is the fragmentation of the fibers to nanorods, which are shorter and less interconnected. The cross-section SEM image allows to observe the thickness of the sample, which is around 90 microns.

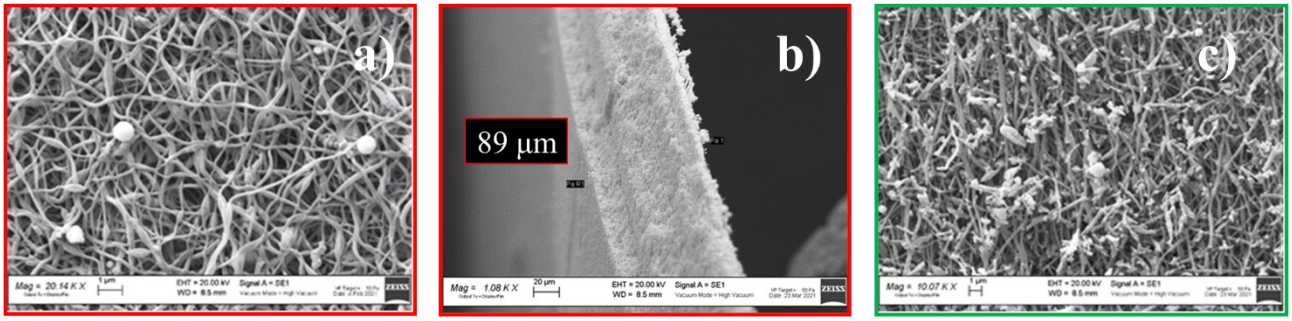

Figure 3.2.6 – SEM images of SnOx/C – S (a, and cross-section b) and SnOx/C – P (c)

Some beads seem to have slightly higher concentration of Sn (Fig. 3.2.7 – BSE images), but the overall distribution of tin atoms is homogeneous in the sample (Fig. 3.2.7 – EDS maps).

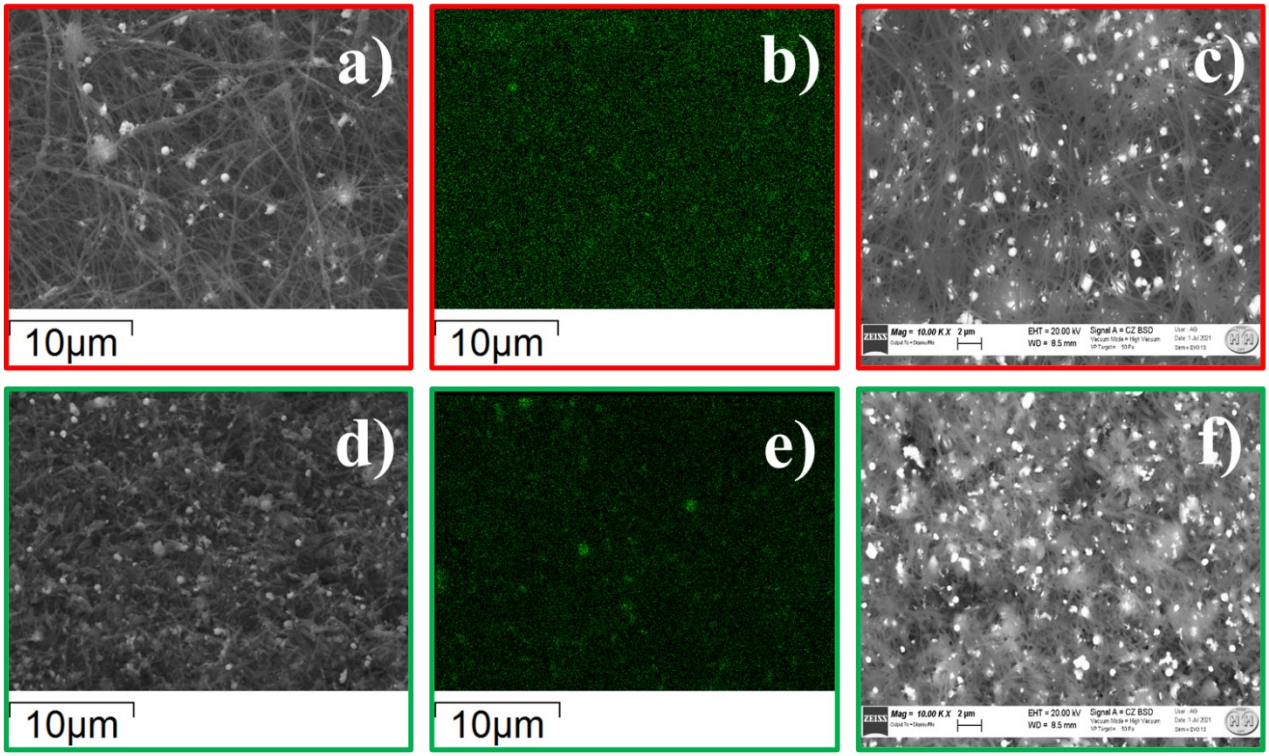

Figure 3.2.7 – SEM images collected from secondary electrons, corresponding EDS maps of Sn together with backscattered electrons SEM images for SnOx/C – S (a-c) and SnOx/C – P (d-f) respectively.

As a reference, a solution of bare PAN was electrospun and carbonized. The corresponding Raman spectra and XRD patterns are typical of turbostratic, low crystalline soft/hard carbons (Fig. 3.2.8) [2] which completely decompose during TGA/DSC measurements. The only significant difference between the samples resides in the morphology (Fig. 3.2.8, d-f): carbon nanofibers are organized as a well-interconnected web (f), which is partially fragmented after milling, resulting in aggregates of nanorods (d, e). Beads are not detected, confirming their higher concentration of tin.

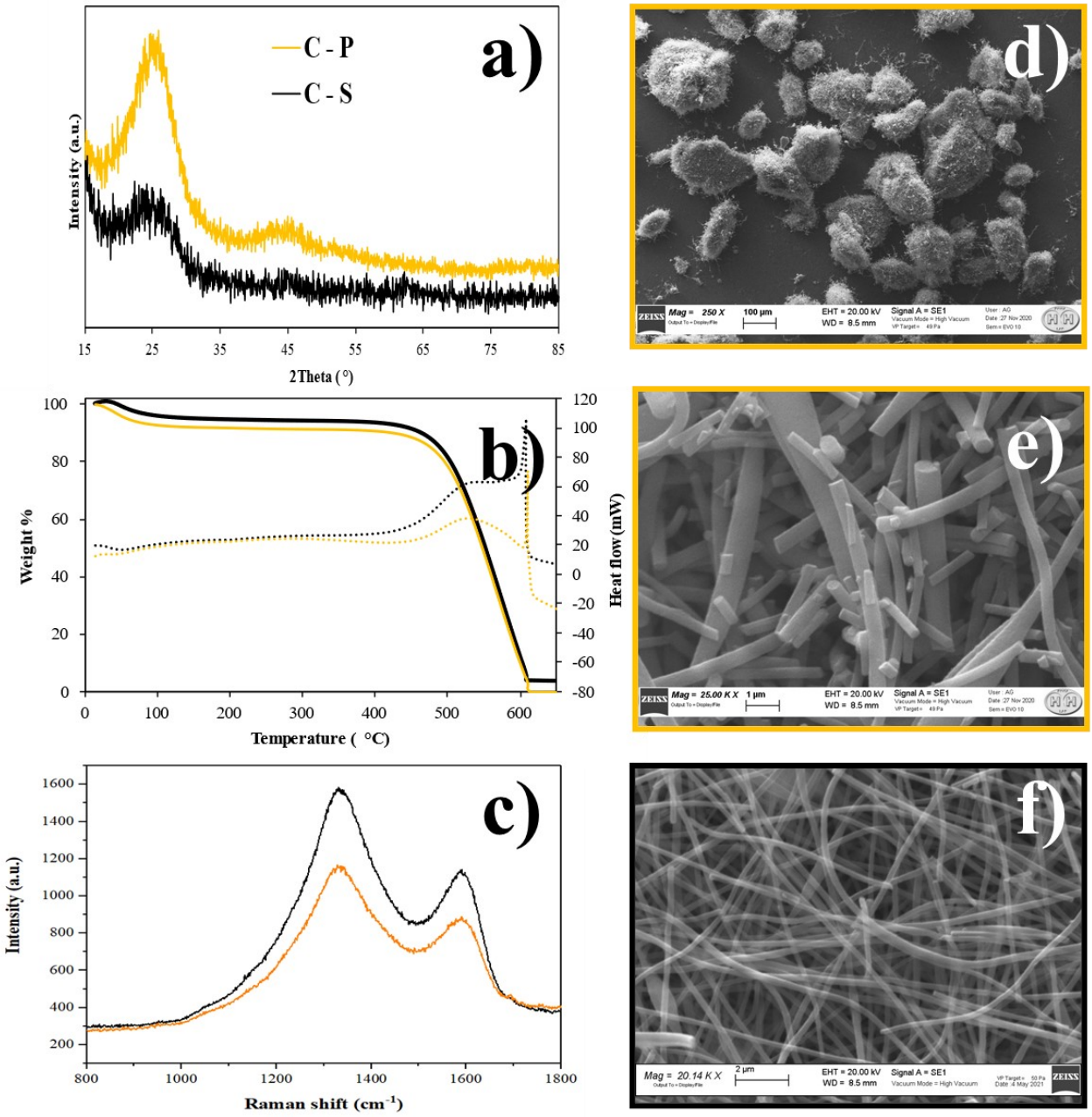

Figure 3.2.8 – Comparison between the XRD patterns (a), TGA (full lines)/DSC (dotted lines) curves (b), Raman spectra (c) and SEM images (d-f) of carbonized PAN samples (orange C-P, black C-S).

Electrochemical characterization

Cyclic voltammetry provides great insights into the Lithium intercalation reactions of electrode materials: both thermodynamics and kinetics of electrochemical reactions determine the shape of voltammograms and, through suitable experiments, valuable parameters can be extracted.

The voltammograms of the SnO_x/C samples and those of reference C samples are reported in Fig. 3.2.9. Since the two carbon samples are quite similar from a structural point of view, the differences in the voltammograms (Fig. 3.2.9a) are attributed to the morphology, which enhances electrical conductivity in the S sample. An irreversible cathodic 1^{st} cycle reaction is detected at 0.5-0.6 V for both samples, which is not attributed to electrolyte decomposition to form a SEI layer, since sharpness and peak position should be invariant between the two samples.

The voltammograms of SnO_x/C (Fig. 3.2.9b) are quite different: the irreversible cathodic peak at 0.7-0.85 V can be assigned to conversion reactions of SnO_2 (and SnO) to Sn and Li_2O, while the other peaks at lower potentials are related to the formation of $SnLi_x$ alloys with increasing Li:Sn ratio, up to $Li_{4.4}Sn$. In the following cycles, the curve of the P sample shows marked similarities with the carbon samples (Fig. 3.2.9a), suggesting that the reactivity of Sn is decreasing cycle by cycle. The S sample (Fig. 3.2.9b) shows instead a sharp and stable peak at 0.39 V, alongside multiple "edges" that differ from the broad and "hyperbole-like" curves of carbon samples. These features are also detected in the anodic branch, where the multiple peaks detected at 0.47, 0.61, 0.72 and 0.79 V are attributed to the de-alloying reactions. Analogous peaks are detected in the anodic branch for the P sample, even if much broader and at higher potentials.

The reversibility is a common issue for conversion-alloying reactions, and the comparison between SnO_x/C – P and SnO_x/C – S clearly suggests that the reversibility is greatly enhanced thanks to the morphology of the composite (Fig. 3.2.6). Well-interconnected webs are much more effective than the aggregates of cracked nanorods in tolerating the large volume changes that Sn particles are undergoing upon cycles of lithiation and delithiation. Further, the homogenous dispersion of tin into the carbonaceous matrix provides a high-conductivity substrate increasing the rate capability of the material.

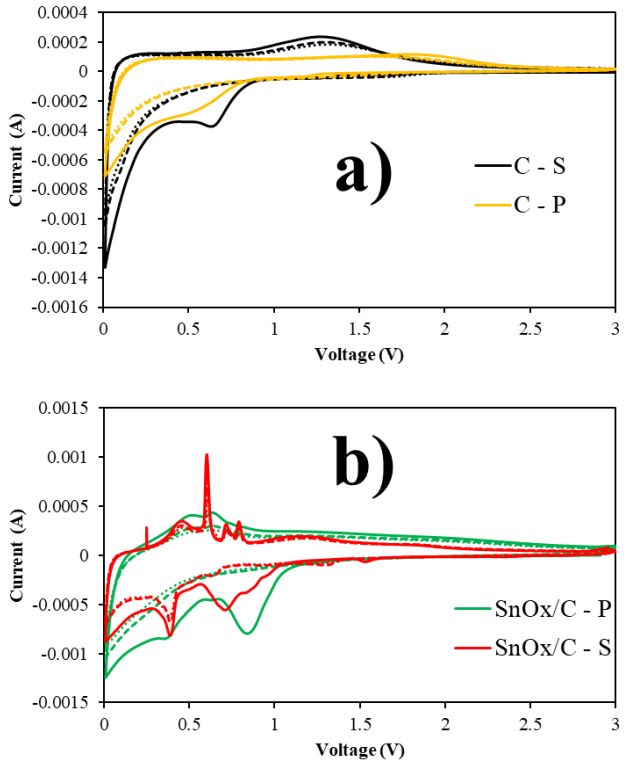

Figure 3.2.9 – Voltammograms of the first three cycles performed at 0.1 mV/s on (a) carbon samples and (b) SnOx/C composites. The first cycle is depicted with a full line.

A material is said to be pseudocapacitive when reversible redox reactions occur at (or near) the surface of a material in contact with an electrolyte, or when these reactions are not limited by solid-state ion diffusion. This feature leads to high energy density at high charge–discharge rates, and can be an intrinsic or extrinsic property to the material. Extrinsic materials do not exhibit pseudocapacitance in the bulk state due to phase transformations during ion storage. With these materials, increasing the surface area through nanostructuring leads to improved high-rate behavior due to a decrease in diffusion distances. [3]

In a cyclic voltammetry experiment, the timescale of the experiment is controlled by the sweep rate (v, mV s^{-1}). The current response to an applied sweep rate will vary depending on whether the redox reaction is diffusion-controlled or surface-controlled (capacitive). For a redox reaction limited by semi-infinite linear diffusion, the current response varies with $v^{1/2}$; for a capacitive process, the current varies directly with v. Therefore, the following general relationship, Equation (1), may be written for the current at a particular potential:

$$i(V) = k_1 v^{1/2} + k_2 v \qquad (1)$$

Solving for the values of k_1 and k_2 at each potential allows for the separation of the diffusion and capacitive currents. [3], [4]

Fig. 3.2.10 shows the voltammograms at different sweep rates (c, d) and the corresponding histograms (e), quantifying the pseudocapacitive contribution to the experimentally recorded current. Since the pseudocapacitance of tin and tin oxides is extrinsic, a higher pseudocapacitive contribution can be considered as an experimental proof of higher electrode surface. The self-standing composite (and the corresponding carbon sample, Fig. 3.2.10e) show higher pseudocapacitive contributions with respect to their powder counterpart, up to 90% at 1 mV/s, demonstrating that electrospinning is very effective in the improvement of the rate capability of electrode materials, which is especially advantageous for conversion-alloying reactions. Moreover, increasing the sweep rate (up to 10 times) did not cause the shape of the voltammogram of the self-standing sample to change significantly (Fig. 3.2.10c). On the contrary, most of the current recorded in the anodic scan in the powder sample (Fig. 3.2.10d) is shifted to higher potentials, which is detrimental for every anode material.

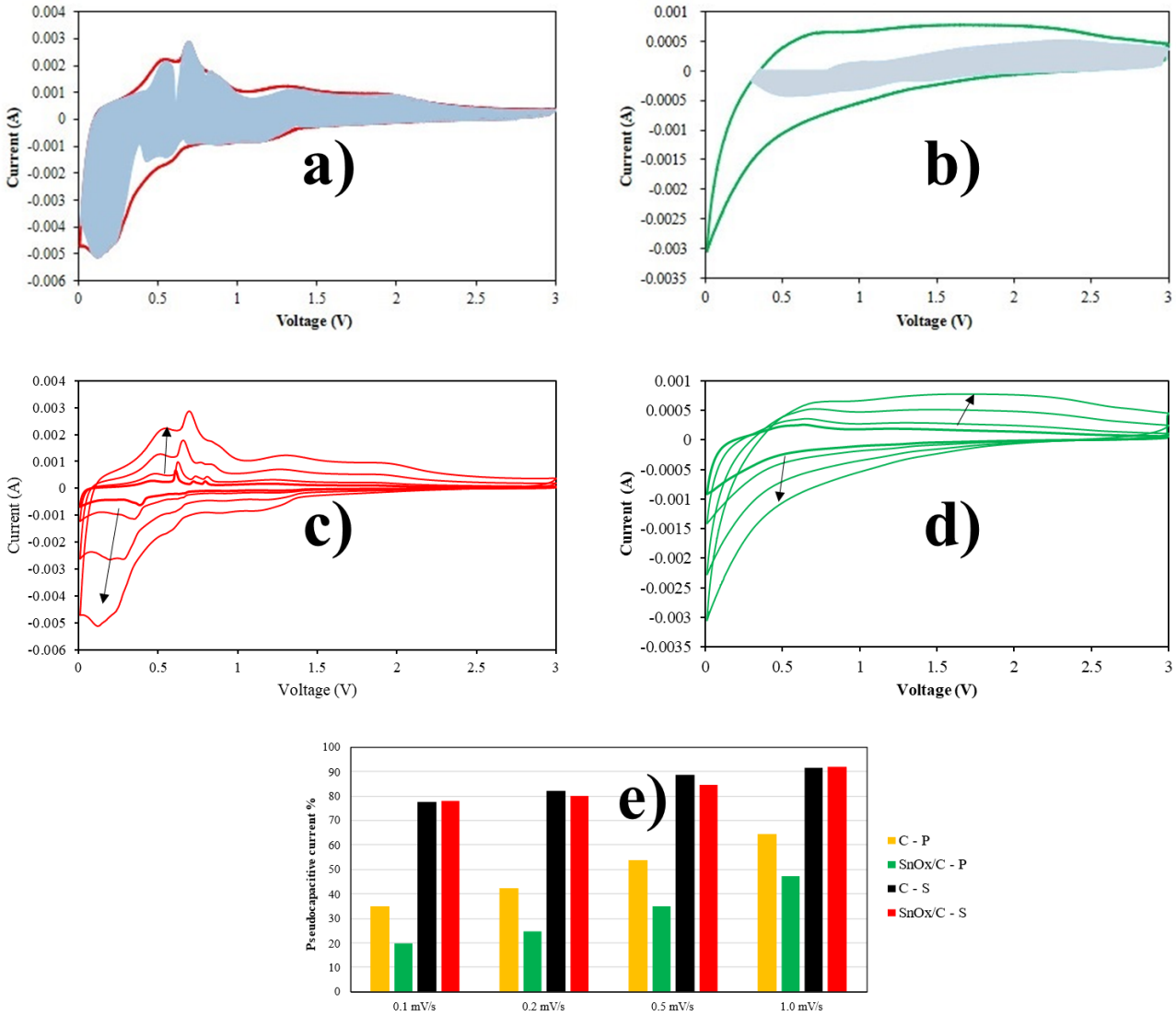

Figure 3.2.10 – Voltammograms at 1.0 mV/s with pseudocapacitive currents evidenced in light blue for SnOx/C – S (a) and SnOx/C – P (b) and corresponding voltammograms at the analysed sweep rates (c and d). Histogram of the total contribution of the pseudocapacitive current at all sweep rates for all the samples (e).

As a consequence of the higher pseudocapacitive contribution, better high-rate performance is obtained in the self-standing sample. Fig. 3.2.11a shows the results of the rate capability tests: the self-standing sample outperformed the corresponding powder sample by hundreds of mAh/g at every C-rate. The combination of higher electrode area and better interconnection of the carbon nanofibers enhances the reactivity of the active material, that results in better performance especially at higher C-rates. Also, the first cycle coulombic efficiency of SnOx/C – S is 77%, even higher than for carbon samples (Fig. 3.2.12, 66 – 69%), and the coulombic efficiency rapidly reaches values higher than 97%. Capacity values of SnO_x/C – S are higher than the theoretical capacity of graphite, which is the standard anode material in most commercial LIBs.

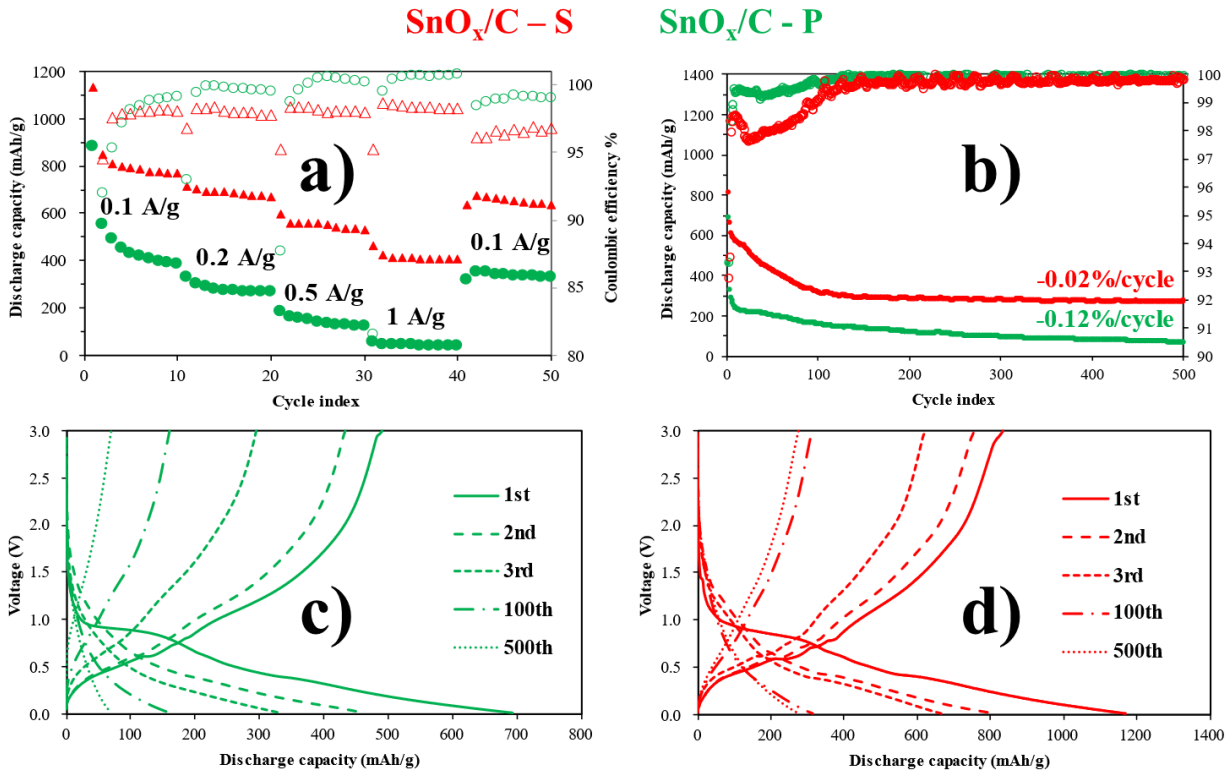

Figure 3.2.11 – Rate capability (a), long term tests performed at 0.5 A/g (b) and corresponding voltage profiles of SnOx/C – P (c) and SnOx/C – S (d). In the upper graphs, the empty markers refer to the coulombic efficiency (right axis), while the filled ones refer to the specific capacity (right axis).

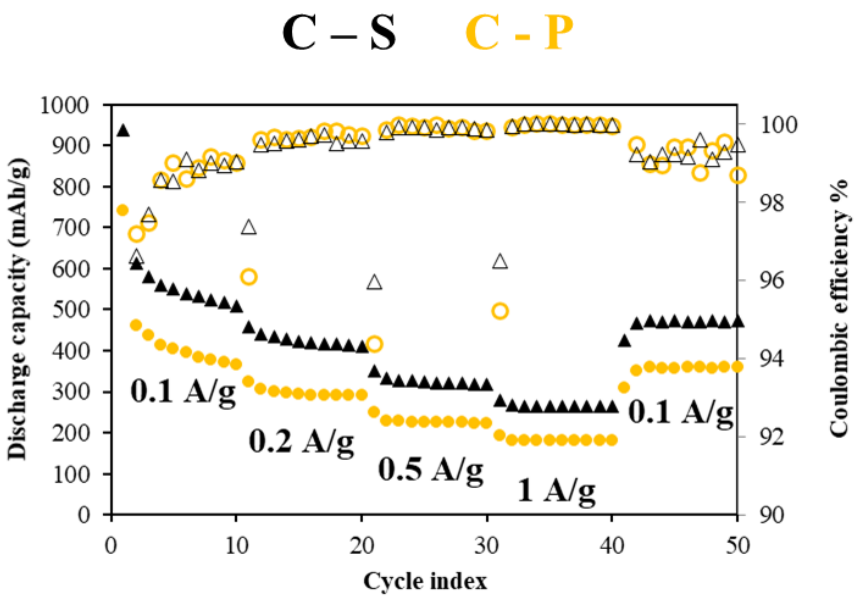

Figure 3.2.12 – Rate capability test performed on carbon samples. The empty markers refer to the coulombic efficiency (right axis), while the filled ones refer to the specific capacity (right axis).

Long-term stability tests (Fig. 3.2.11b) confirmed the better performance of SnO_x/C – S over 500 cycles: a stable and high capacity of 275 mAh/g is obtained at 0.5 A/g, with a coulombic efficiency of 99.8%.

The reactivity of the composite is enhanced over hundreds of cycles: the voltage profiles do not change shape after the 100th cycle in SnO_x/C – S (Fig. 3.2.11c), while the voltage profile gets progressively linear in the corresponding P sample (Fig. 3.2.11d). The reason for this improvement is again considered the flexible and more conductive carbonaceous matrix, which is also beneficial for the tolerance of volume changes.

In order to investigate the worse performance of the P sample, *ex situ* SEM images were collected on the electrodes after disassembling the cells (Fig. 3.2.13). The volumetric expansion and contraction during cycling did not pulverize the electrodes, as often reported for conversion-alloying materials. [5] It is likely that the rod-like morphology significantly tailored the mechanical stress that the electrodes are undergoing upon lithiation/delithiation. Since the loss of contact between the active material and the current collector is not responsible for the decrease in the performance, further analyses were carried out.

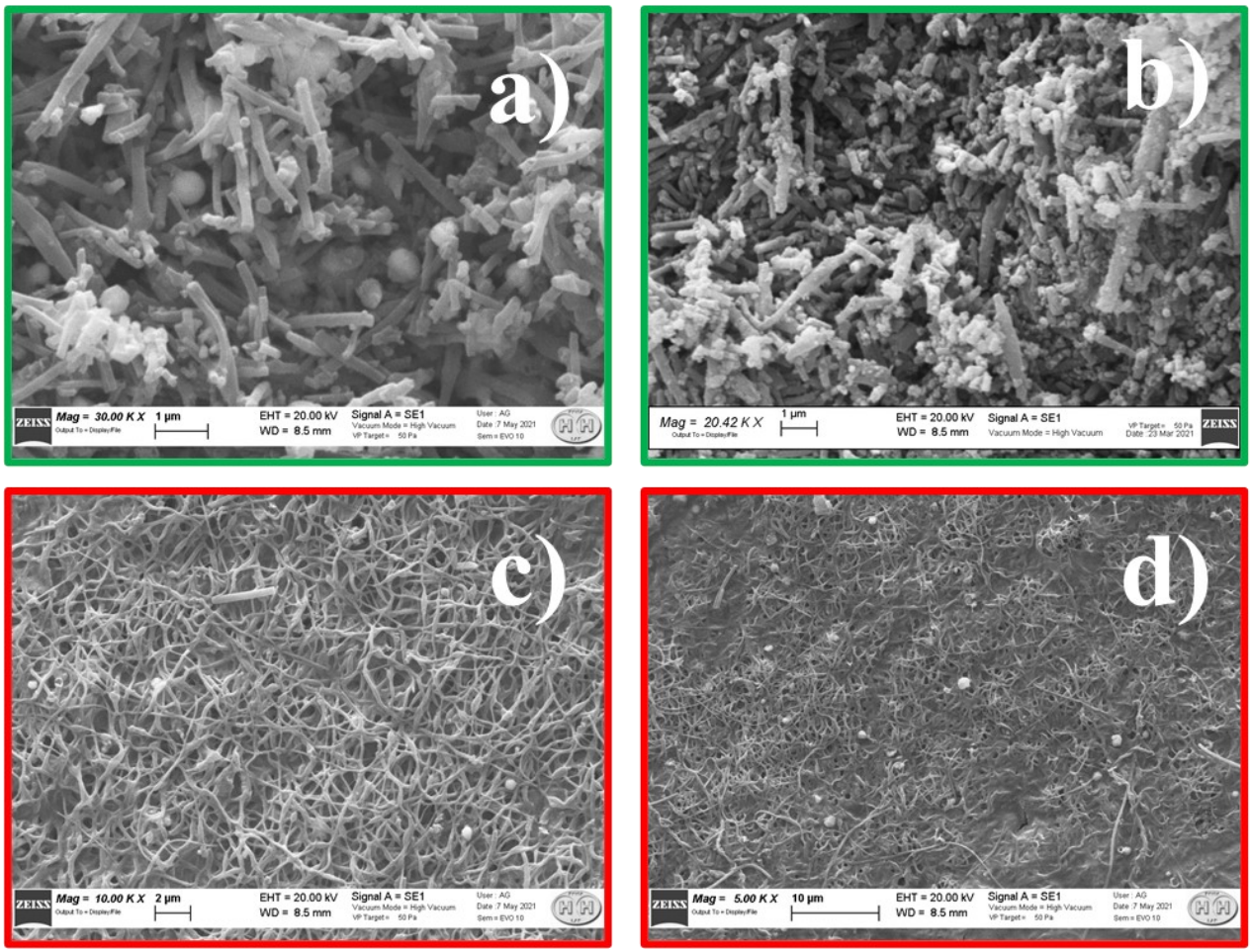

Figure 3.2.13 – *Ex situ* SEM images collected on the electrodes of pristine and post-mortem SnOx/C – P (a, b) and SnOx/C – S (c, d) respectively.

Electrochemical Impedance Spectroscopy has the great advantage of studying the charge-transfer reactions in an electrochemical cell separately. The Nyquist plot (Fig. 3.2.14) shows that from the Open Circuit Voltage onwards, the self-standing sample shows lower resistance. The higher resistance to the charge transfer of electrons (which occurs at high frequencies, i.e. 10^{3-4} Hz, see Fig 3.2.14c-d) reported for the powder sample is attributed to the need for insulating PVDF and to the worse interconnection of the carbon nanofibers.

After the 1st cycle, the impedance spectrum of the self-standing sample shows a significant decrease in the resistance (Fig. 3.2.14a), not detected in the powder sample, consistent with the irreversible conversion reaction of SnO_2 (semiconductor, the main phase in the S sample) to Sn (metal, the main phase in the P sample). This decrease in the resistance is accompanied by a significant shift of the charge transfer of electrons to higher frequencies (more than one order of magnitude, see Fig. 3.2.14c), again not evidenced in the powder sample. With these premises, the main origin of the constant and higher resistance offered by the P sample seems to be attributed to the insulating PVdF needed for the preparation of the electrode.

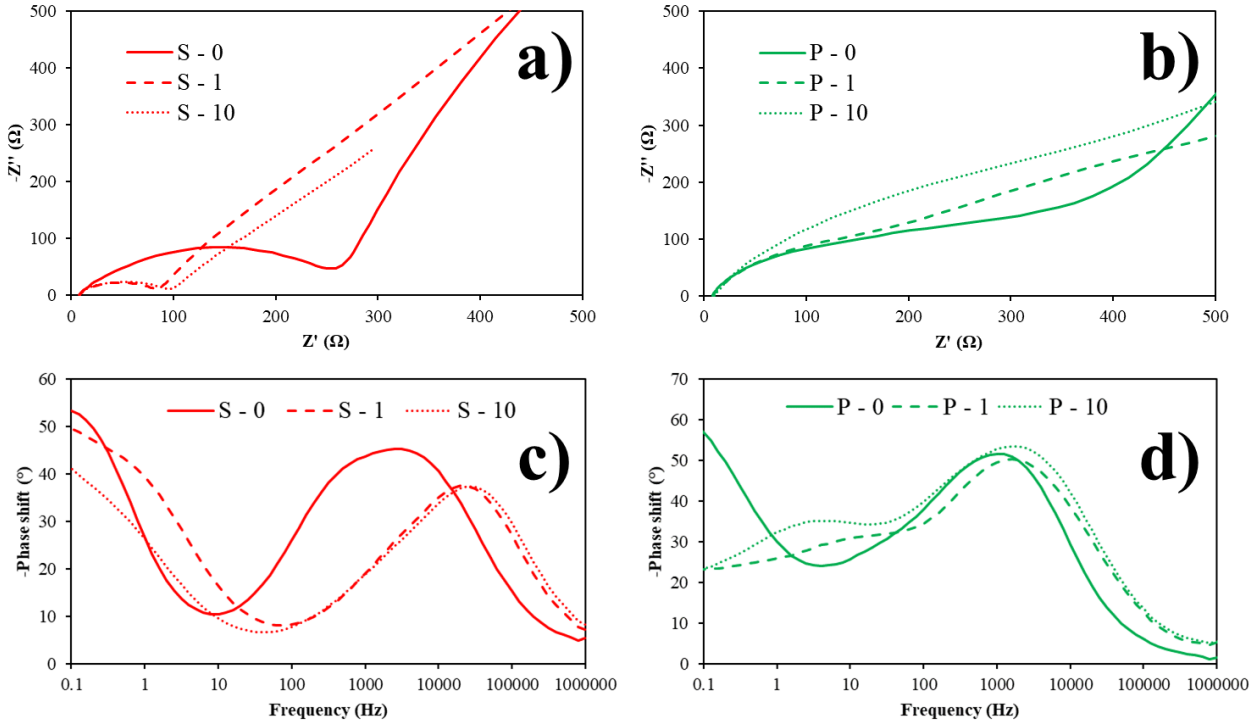

Figure 3.2.14 – Nyquist plot of SnOx/C – S (a) and SnOx/C – P (b) and Bode phase plot of SnOx/C – S (c) and SnOx/C – P (d). S - 0 stands for OCV conditions, S - 1 for the 1st cycle of discharge and charge, S – 10 for the 10th.

Conclusion

In conclusion, SnOx/C composites were successfully electrospun as self-standing sheets and then ground to obtain a powder. In the composites, the turbostratic carbonaceous matrix has a web-like morphology and the dispersion of tin within the samples is homogeneous. Crystalline Sn, SnO and SnO_2 are co-present in the samples, each having its own advantages in the electrochemical reactions with Lithium. The overall reactivity of the self-standing electrode is enhanced, with stable current peaks over the cycles and at different sweep rates (>90% of the current show surface-controlled kinetics). In the rate capability test, the self-standing tin-loaded electrode outperforms the powder sample by hundreds of mAh/g, maintaining the performance at higher current densities. The same sample was also subjected to 500 cycles of charge and discharge, obtaining a stable (0.02% loss/cycle) and high capacity of 300 mAh/g at a current density of 0.5 A/g. The electrodes did not pulverize after prolonged cycling, and the resistance offered by the self-standing electrode to the charge transfer of electrons is significantly lower than the corresponding resistance offered by the powder sample, because of the absence of insulating PVdF needed in the preparation of the electrode. According to all the involved electrochemical techniques employed in this study, the self-standing tin-carbon composite shows promising features as anode material for LIBs.

References

[1] N. Soin, S. S. Roy, S. C. Ray, and J. A. McLaughlin, “Excitation energy dependence of Raman bands in multiwalled carbon nanotubes,” *J. Raman Spectrosc.*, vol. 41, pp. 1227–1233, 2010.

[2] M. Á. Muñoz-Márquez, D. Saurel, J. L. Gómez-Cámer, M. Casas-Cabanas, E. Castillo-Martínez, and T. Rojo, “Na-Ion Batteries for Large Scale Applications: A Review on Anode Materials and Solid Electrolyte Interphase Formation,” *Adv. Energy Mater.*, vol. 7, no. 20, pp. 1–31, 2017.

[3] V. Augustyn, P. Simon, and B. Dunn, “Pseudocapacitive oxide materials for high-rate electrochemical energy storage,” *Energy Environ. Sci.*, vol. 7, no. 5, pp. 1597–1614, 2014.

[4] D. Spada, I. Quinzeni, and M. Bini, “Orthorhombic and monoclinic modifications of FeNb11O29, as promising anode materials for lithium batteries: Relationships between pseudocapacitive behaviour and structure,” *Electrochim. Acta*, vol. 296, pp. 938–944, 2019.

[5] A. P. Nowak, “Composites of tin oxide and different carbonaceous materials as negative electrodes in lithium-ion batteries,” *J. Solid State Electrochem.*, vol. 22, pp. 2297–2304, 2018.

3.3 Structural and functional properties of $FeNb_{11}O_{29}$: disorder, Li intercalation reaction and pseudocapacitance

This interesting material was characterized for all the three years of PhD, and the presentation of the corresponding results will be organized in sections for better clarity. Most of the discussed results were yet published, while some more are presented in the following pages.

Structural characterization of the pristine phase

$FeNb_{11}O_{29}$ was obtained as a green crystalline powder with high level of sintering, because of the thermal treatment required to obtain monophasic samples. Depending on the temperature, two different phases can be stabilized (Fig. 3.3.1). The characteristic feature of $FeNb_{11}O_{29}$ and other isostructural compounds ($M_xNb_{12-x}O_{29}$) is dimorphism (monoclinic or orthorhombic symmetry). Both the phases are classified as double shear: in their structures neighbouring blocks of octahedra share common edges, half of which at the level y = 0 and the other half at y = 0.5. The monoclinic and the orthorhombic phases differ by the manner in which individual blocks link: blocks can share *cis* (orthorhombic) or *trans* (monoclinic) corners with blocks at the same level.

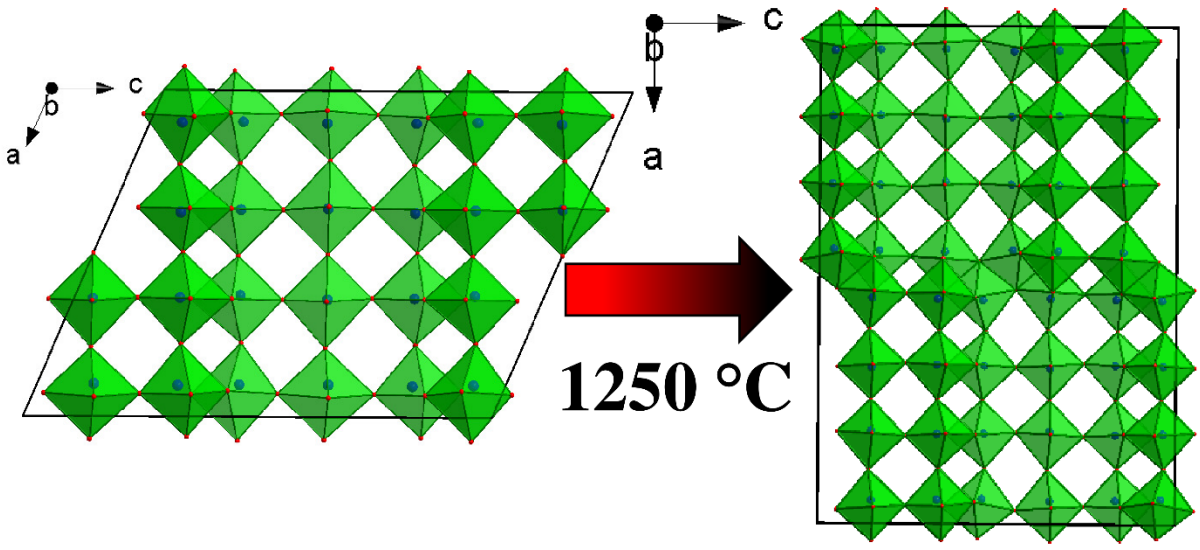

Figure 3.3.1 - Unit cell of both monoclinic and ortorhombic $FeNb_{11}O_{29}$.

The structures of monoclinic and orthorhombic are overall quite similar. However, little differences caused by the linking between blocks can be detected, as shown by the synchrotron XRD patterns in Fig. 3.3.2.

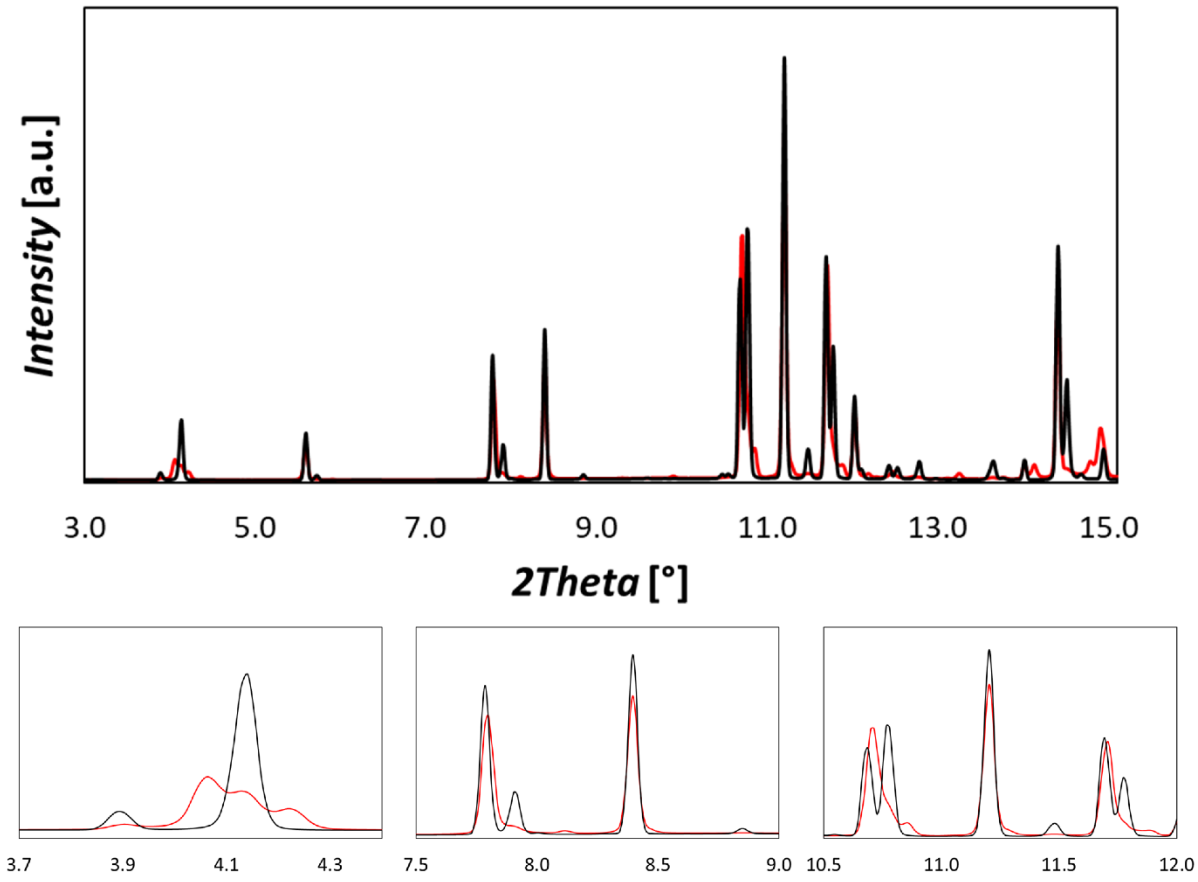

Figure 3.3.2 - Detailed view of the synchrotron XRD patterns of monoclinic (red) and orthorhombic (black) $FeNb_{11}O_{29}$.

In $FeNb_{11}O_{29}$, Fe^{3+} cations are distributed over multiple crystallographic sites, as demonstrated by the comparison between simulated and experimental patterns (Figure 3.3.3). This feature has an impact on the electrochemistry of the material: Li^+ ions intercalated in the shear structure experience different local environments from one unit cell to the next. This randomness in the potential energy landscape of Li^+ ions in a disordered structure suppresses lithium ordering and makes a larger number of sites available for occupation, enhancing electrochemical performances. [7]

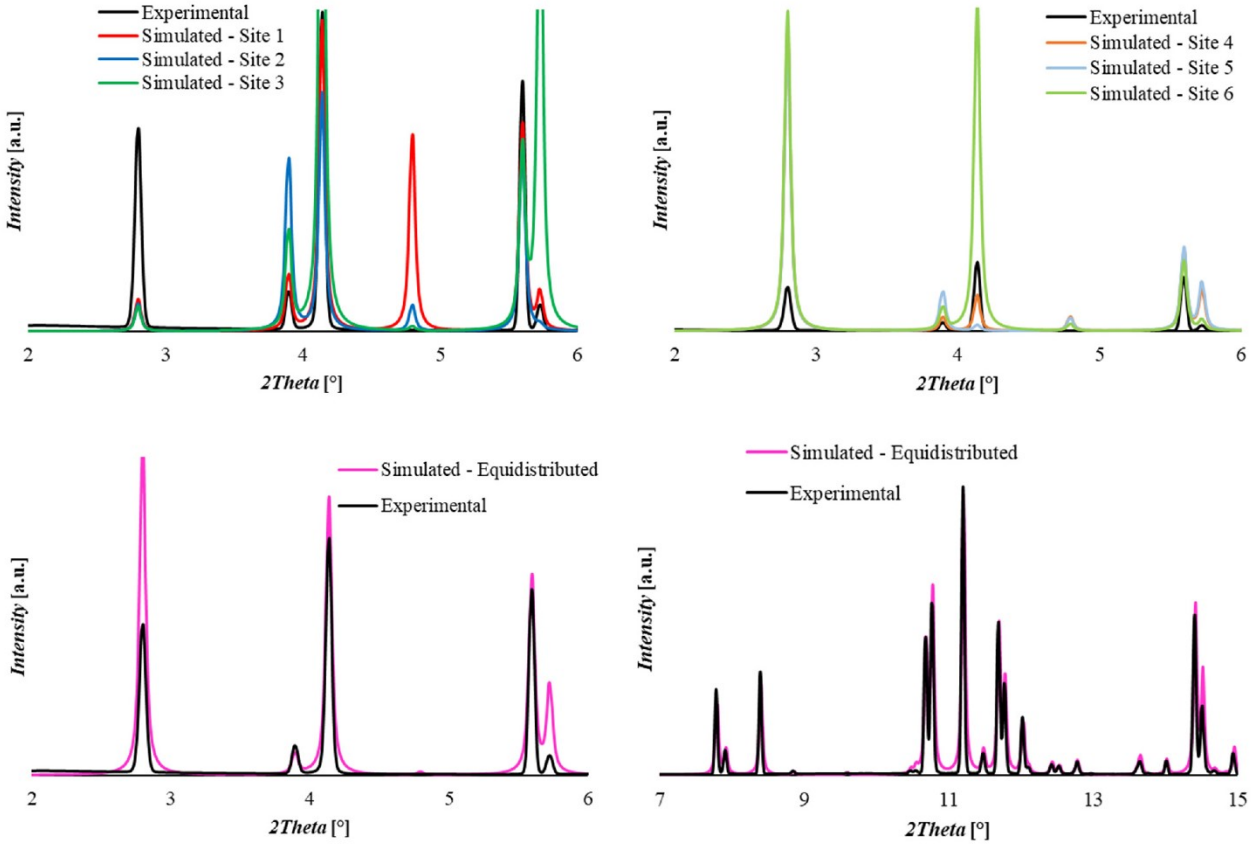

Figure 3.3.3 - Comparative plots between experimental patterns collected on powder orthorhombic $FeNb_{11}O_{29}$ (black) and simulated patterns for different orthorhombic structural models (coloured curves).

Simulated patterns are divided into groups: when Fe^{3+} occupies only site 1, 2 or 3 its low scattering factor makes the calculated structure factor for the 2 0 0 plane (d = 14.3 Å; 2θ = 2.8 °) insufficient. When instead site 4, 5 or 6 is occupied, the scattering factor of Nb^{5+} is too high for the experimental structure factor. When iron is equally distributed among the structural sites, a good compromise is obtained, even though the intensities still do not match perfectly.

In order to obtain a clearer picture of the situation of Fe cations in the structure of $FeNb_{11}O_{29}$, X-ray Absorption Spectroscopy was employed at the K-edges of Fe and Nb. The X-ray absorption near edge structure (XANES) spectra of monoclinic and orthorhombic $FeNb_{11}O_{29}$ at the Nb K-edge are shown in Fig. 3.3.4 (left panel), together with the spectrum of Nb_2O_5 taken as reference. In a XANES spectrum, the energy position of the rising edge is sensitive to the oxidation state of the element under investigation, while the spectrum profile can be considered as a fingerprint, allowing discriminating

between different species. As evident from the figure, the edge energy is the same for the three spectra, confirming that the oxidation state is Nb(V) in all cases. The spectrum profile is indeed nearly coincident for both the monoclinic and the orthorhombic phase, suggesting a very similar crystal structure.

XANES spectra of monoclinic and orthorhombic $FeNb_{11}O_{29}$ at the Fe K-edge are also shown in Fig. 3.3.4 (right panel) together with the reference Fe_2O_3. The position of the edges suggests a Fe(III) oxidation state in both polymorphs of $FeNb_{11}O_{29}$.

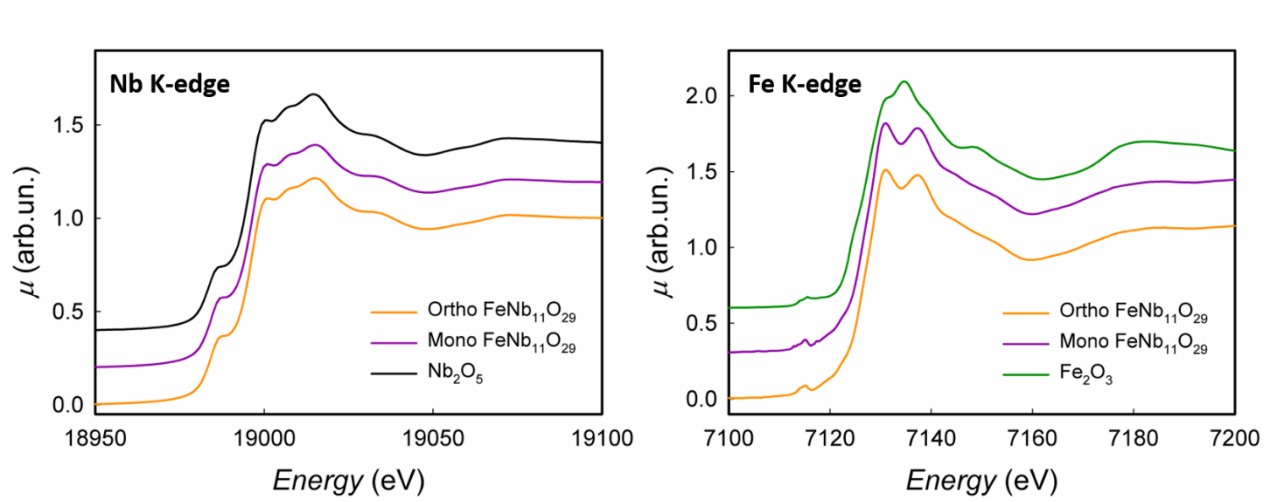

Figure 3.3.4 – (left panel) XANES spectra of orthorhombic and monoclinic $FeNb_{11}O_{29}$ and Nb_2O_5 at the Nb K-edge. (right panel) XANES spectra of orthorhombic and monoclinic $FeNb_{11}O_{29}$ and a-Fe_2O_3 at the Fe K-edge.

In order to investigate the local structure around Nb in the two phases, the EXAFS signals and the corresponding Fourier Transform were extracted (Figure 3.3.5). The experimental signal was fitted starting from a structural model accounting for either the monoclinic (space group: *A12/m1*) or the orthorhombic phase (space group: *Amma*). According to previous works [1]–[3], and to the simulated XRD patterns in Fig. 3.3.3, in both structures Nb atoms (with occupancy equal to 0.92) and Fe atoms (occupancy: 0.08) occupy six different crystallographic sites, each having a slightly different octahedral coordination. The two phases then differ in the connection in the network of octahedra. Due to the intrinsic complexity of this structure, an approximate model was obtained, where the average radial distribution function around the central Nb photoabsorber was estimated for both phases. The first neighbouring oxygen atoms are located at six different distances from Nb, one of which is lower than 2 Å, one is larger, and the other four are approximately around 2 Å. For this reason, four oxygen atoms were grouped together and fitted simultaneously.

The resulting model is shown in Table 3.3.6, together with the result of the fitting procedure. Even if simplified, it proves to be well representative of the structure, showing a nice agreement with the experimental, with an F factor around 10% for both phases.

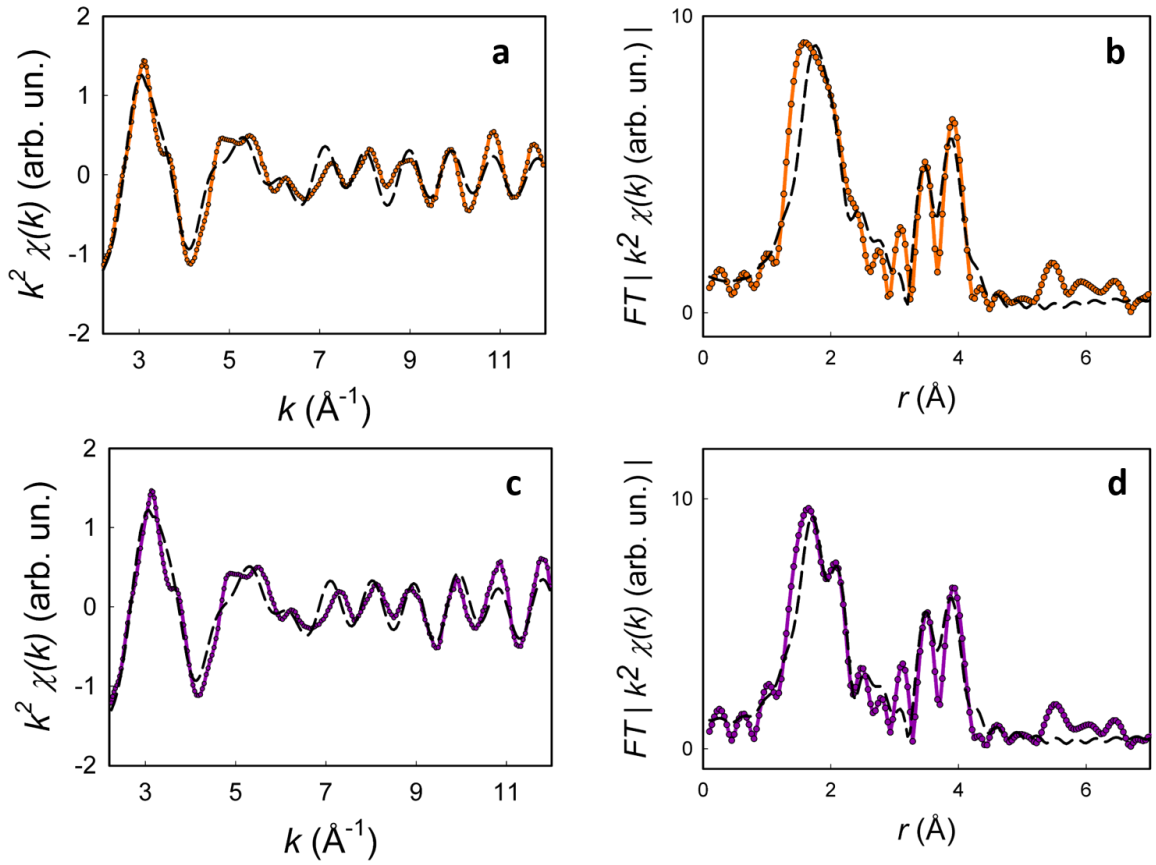

Figure 3.3.5 – EXAFS signal and corresponding Fourier transform (FT) of orthorhombic $FeNb_{11}O_{29}$ (a and b) and of monoclinic $FeNb_{11}O_{29}$ (c and d). The orange and purple dotted lines represent the experimental data, while the black dotted lines are the simulated curves.

In the Fourier transform signals (Fig. 3.3.5), the distances between Nb and the first six neighbouring oxygen atoms give rise to the first peak around 2 Å. For the orthorhombic phase, this peak is centred at 2 Å, with only a small asymmetry in the right side. Oppositely, for monoclinic $FeNb_{11}O_{29}$, a clear splitting is visible. Indeed, the fitting results reveal a different local structure in the two phases: for orthorhombic $FeNb_{11}O_{29}$, the Nb-O distances, even if all slightly different, are homogeneously distributed around 2 Å. For the monoclinic phase, instead, a significant contribution at higher distances (at *ca.* 2.4 Å, see Table 3.3.5) is clearly present.

This experimental observation confirms the results of the Rietveld refinement of XRD patterns already reported elsewhere [3], where the bond environment around Nb cations was determined to be more regular in the orthorhombic phase.

- **Orthorhombic $FeNb_{11}O_{29}$. F = 9.7%**

Shell	N	Atom	R(Å)	σ^2 (Å^2)	R (Å) crystallographic
1	1	O	1.87(2)	0.001(3)	1.808
2	4	O	2.19(4)	0.04(1)	1.991
3	1	O	2.03(2)	0.000(3)	2.288
4	4.130	Nb	3.64(2)	0.006(1)	3.550
5	0.380	Fe	3.6(2)	0.01*	3.550

- **Monoclinic $FeNb_{11}O_{29}$ F = 10.4 %**

Shell	N	Atom	R(Å)	σ^2 (Å^2)	R (Å) crystallographic
1	1	O	1.84(2)	0.002(2)	1.765
2	4	O	2.07(2)	0.014(2)	2.004
3	1	O	2.41(4)	0.005(5)	2.291
4	3.210	Nb	3.64(1)	0.004(1)	3.505
5	0.280	Fe	3.6(2)	0.01*	3.505

Table 3.3.6 – Structural parameters obtained after the EXAFS refinement for the orthorhombic and the monoclinic phase. N: coordination numbers (number of atoms in the shell): R: coordination distances; σ^2 : EXAFS Debye-Waller factors. The crystallographic distances are also reported. The values marked with an asterisk were not included in the refinement. The goodness of fit was evaluated through the F factor.

The role of iron

Since X-rays techniques could not give an accurate picture of the condition of Fe in the shear structure of $FeNb_{11}O_{29}$, Mössbauer spectroscopy was employed. In Figure 3.3.7, the Mössbauer spectra acquired at 293 K together with the corresponding fits are shown. For both samples, the Mössbauer spectrum is essentially the superposition of doublets, therefore indicating the absence of significant magnetic interactions between the ions in the samples (Fe^{3+} ions are diluted and distant in such a crystal structure). Clearly, the asymmetry and broadening of the two lines point to the presence of more than one contribution. For this reason, different contributions were considered in the fitting of the spectra. In particular, in both cases a good fit was obtained by considering five contributions, with different values of the hyperfine parameters (isomer shift (δ) and quadrupole splitting (Δ)) as well as the effective thickness (t_a). The same value of the linewidth (Γ), approximately coincident with the natural linewidth (~ 0.10 mm/s), was used for each contribution.

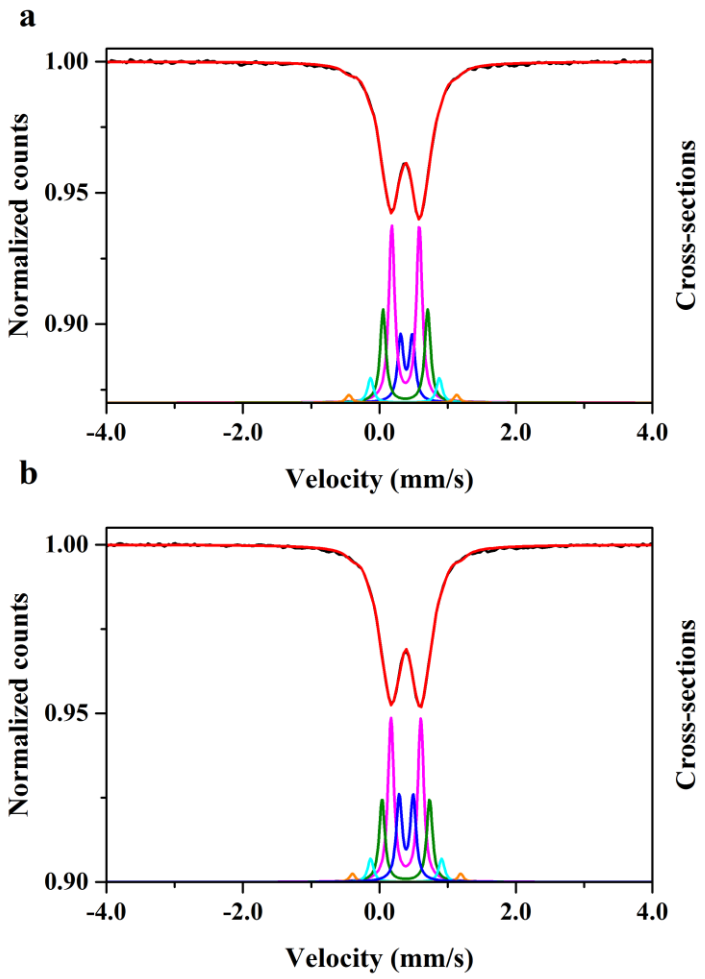

Figure 3.3.7 – Mössbauer spectra of the monoclinic (a) and orthorhombic (b) samples acquired at 293 K (black line) and corresponding fit (red line). The absorption cross-section of each contribution is also shown. The velocity range is restricted to emphasize the content of the spectra.

For each subspectrum, the values of the parameters extracted from the fit of the Mössbauer spectra of both samples are reported in Table 3.3.8, together with relative weight calculated from the values of t_a. For the monoclinic sample, all subspectra have a very similar value of the isomer shift, that is of the order of 0.16 mm/s. This value is associated to Fe^{3+} ions [4], in agreement with the results of X-Ray spectroscopies. However, the values of the quadrupole splitting of the subspectra are different and in particular an increasing trend is visible for the chosen labelling of the contributions. As the quadrupole splitting provides information about bond properties and local symmetry of the Fe site [4], these values indicate the degree of distortions from the ideal octahedral coordination. While for subspectrum 1 an octahedral geometry may be assumed, increasing distortions of this coordination are indicated for the other contributions. This is in line with the analysis of the crystallographic data that show the presence of six different coordination distances of the Fe-O ions. From the calculated relative weight, that can be considered as an evaluation of the population of each subspectrum, three main situations are evident. Subspectra 1, 2 and 3 are the majority contributions to the Mössbauer spectrum, with the population of subspectrum 2 that results to be approximately double than that of subspectra 1 and 3. Moreover, subspectra 4 and 5, that are characterized by the highest value of the quadrupole splitting, are minority contributions and their sum accounts to less than 10 % of the spectrum.

For the orthorhombic sample, similar considerations on the trends of the hyperfine parameters of the subspectra hold. Therefore, except for subtle differences in the values of the quadrupole splitting of each site, no substantial differences between the monoclinic and the orthorhombic samples are evidenced.

Sample	Subspectrum	δ (mm/s)	Δ (mm/s)	Γ (mm/s)	t_a	%
Monoclinic	1	0.394(2)	0.172(8)	0.10	0.113(7)	18
	2	0.3843(7)	0.404(5)	0.10	0.307(6)	48
	3	0.381(1)	0.655(7)	0.10	0.163(6)	25
	4	0.374(5)	1.01(1)	0.10	0.044(2)	7
	5	0.34(1)	1.58(3)	0.10	0.014(1)	2
Orthorhombic	1	0.393(1)	0.204(5)	0.10	0.122(5)	23
	2	0.3894(6)	0.437(5)	0.10	0.238(4)	45
	3	0.388(1)	0.698(6)	0.10	0.121(3)	23
	4	0.392(4)	1.04(1)	0.10	0.034(2)	7
	5	0.40(1)	1.59(2)	0.10	0.012(1)	2

Table 3.3.8 – ^{57}Fe Mössbauer parameters extracted from the fit of the spectra: isomer shift respect to α-Fe (δ), quadrupole splitting (Δ), linewidth (Γ) and effective thickness (t_a). The relative weight of each contribution is also reported.

In niobium-based shear structures, the 2nd order Jahn-Teller (SOJT) effect causes a spontaneous distortion of the edge-shared NbO_6 octahedra along shear planes. [3], [5] The cation-cation repulsion along shear planes has some implications when ions different from Nb are introduced in the structure: Ti^{4+} ions in $TiNb_2O_7$, though disordered, preferentially occupy shear plane sites. [6] Instead, W^{6+} is predicted to favour the tetrahedral position and the block-centre position of $Nb_{14}W_3O_{44}$. The preferential occupancy of tungsten on the purely corner-shared position is expected: the metal-metal distances are larger in the block centre, minimizing the electrostatic repulsion (W^{6+} vs. Nb^{5+}). Preferential occupation of tungsten on the tetrahedral site is due to the shorter M-O distances, which, together with the higher charge of the tungsten cations, lead to better covalency and stronger bonds. [7] Even if both W^{6+} and Ti^{4+} are d^0 ions, like Nb^{5+}, they tend to preferentially occupy different kind of sites because the high charge of W^{6+} ions has to be stabilized, while the smaller (compared to Nb^{5+}) charge of Ti^{4+} ions causes them to prefer edge-sharing octahedra.

Fe^{3+}, which is a non-Jahn-Teller high-spin configuration ion in $FeNb_{11}O_{29}$ [3] can be dispersed over more sites (at least at room temperature) because its smaller charge minimizes cation-cation repulsion in edge-sharing octahedra, while its coordination environment is energetically stabilized in the less distorted corner-sharing octahedra at the centre of blocks. The results of Mössbauer spectroscopy

seem to indicate that slightly distorted octahedra are preferentially occupied, confirming the importance of minimizing the coulombic repulsion along shear planes.

As already mentioned, this feature affects the electrochemistry of the material: the randomness in the potential energy landscape of Li^+ ions in a disordered structure suppresses lithium ordering and makes a larger number of sites available for occupation, enhancing the electrochemical performance. [7]

The presence of Fe^{3+} greatly affects the magnetic properties of a Niobium oxide (Nb_2O_5 is diamagnetic). Static magnetization data already reported in literature [3] disclosed a paramagnetic behaviour for both monoclinic and orthorhombic $FeNb_{11}O_{29}$ down to few K. A negative Weiss constant evidenced the system tendency towards antiferromagnetic correlations. [3] The local magnetic environment of $FeNb_{11}O_{29}$ was investigated by muon-spin rotation and relaxation spectroscopy (μ^+ SR). The zero-field data collected for the whole temperature range (Fig. 3.3.9) can be fitted with a model

$$A = A_0 + A_1 e^{-\lambda t}$$

The A_0 component reflects the muons that are stopped in the titanium sample-holder, and thus are not depolarising. A_1, instead, is subject to a lorentzian decay and probes the spin dynamics in $FeNb_{11}O_{29}$. Around 60% of muons is subject to a diamagnetic environment with no polarization variations (Titanium cell), while the remaining 40% is affected by a dynamic environment. This latter portion of muons seems to be subject to motional narrowing (Lorentzian profile function), that could indicate a movement of muons with respect to dipolar nuclear fields coming from the nuclei of Fe (nuclear spin I = ½) and Nb (nuclear spin I = 9/2), or could be explained with the presence of rapid spin fluctuations caused by the paramagnetic behaviour of the sample (unpaired 3d electrons of Fe^{3+} in high-spin configuration).

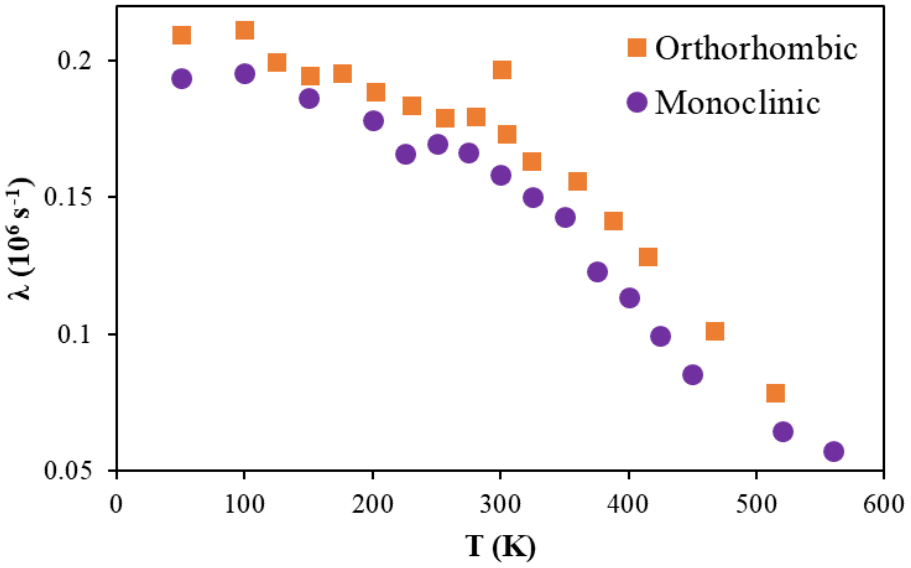

Figure 3.3.9 – Zero-field relaxation rate of muons as a function of temperature.

The temperature dependent behaviour of the relaxation rate, shown in Fig. 3.3.9, seems to suggest two different dynamic regimes for temperatures below and above ~300 K. In the lower temperature range, the muon seems to be experiencing fast, paramagnetic spin fluctuations. This interpretation is in agreement with SQuID magnetometry data collected elsewhere. [3] At T > 300 K the thermal energy is instead sufficient to overcome the energy barriers corresponding to the movement of muons between different crystallographic positions. For the parent compound $Nb_{12}O_{29}$, zero-field muon spectroscopy (ZF-μ^+ SR) measurements already discovered the presence of different interstitial sites for muons. [8] Even if muons are attracted to the most electronegative regions, they can stop in various interstitial sites in the complex shear structure, which contains several inequivalent sites with similar attractive energies. Muons located at each site will feel dipolar fields of varying strength, because of the different topology of the surrounding moment configurations. Since Fe^{3+} ions are distributed over multiple crystallographic sites, in different unit cells the same sites can feel different dipolar fields, depending on the location of Fe^{3+} in that unit cell.

Operando XRD

In situ/operando X-Ray Diffraction (XRD) is widely used to study the crystal structures and phase transformations in electrode and solid electrolyte materials for LIBs during cycling. [27]

Some XRD data on $Li_xFeNb_{11}O_{29}$ are already reported in literature, but up to date there was no systematic study on both the monoclinic and orthorhombic phase: in 2014 Pinus et al [12] performed neutron powder diffraction experiments on orthorhombic $Li_{11}FeNb_{11}O_{29}$, finding a volumetric expansion of +6.1% upon lithiation, while in 2019 Zheng et al [20] performed in situ XRD experiments on monoclinic $FeNb_{11}O_{29}$ nanotubes, confirming the volume expansion (6.92%) upon lithiation and determining the reversibility of the process.

In this work, operando XRD patterns were collected on both polymorphs of $FeNb_{11}O_{29}$ (Figure 3.3.10). The detailed analysis of the multiple components evidenced in the first pattern, collected at the open circuit voltage (OCV) of the cells, is reported in Fig. 3.3.11. The pattern consists of multiple peaks, deriving from both the crystalline $FeNb_{11}O_{29}$ and the current collector (copper metal), on a complex background of diffuse scattering, deriving instead from the conductive carbon, the kapton window, and the binder (in a smaller extent). The current collector is mandatory in order to have better electrochemical results, but in this case also serves as a reference: the position of the peaks of copper is not affected by the electrochemical reaction. Further, it also proves that the cell is not heating due to the flow of current nor X-ray absorption.

Aside from the current collector, the diffraction peaks can be assigned to $FeNb_{11}O_{29}$ for the duration of the whole measurements. Because of the solid-solution behavior manifested during Lithium intercalation, the lattice parameters of $FeNb_{11}O_{29}$ were refined vs the amount of Li intercalated in the structure of $FeNb_{11}O_{29}$ (which is directly proportional to the measured capacity). The structural models were adapted from monoclinic and orthorhombic $Nb_{12}O_{29}$ (*A2/m*, JCPDS 16-0733; and *Amma*, JCPDS 16-0734 respectively).

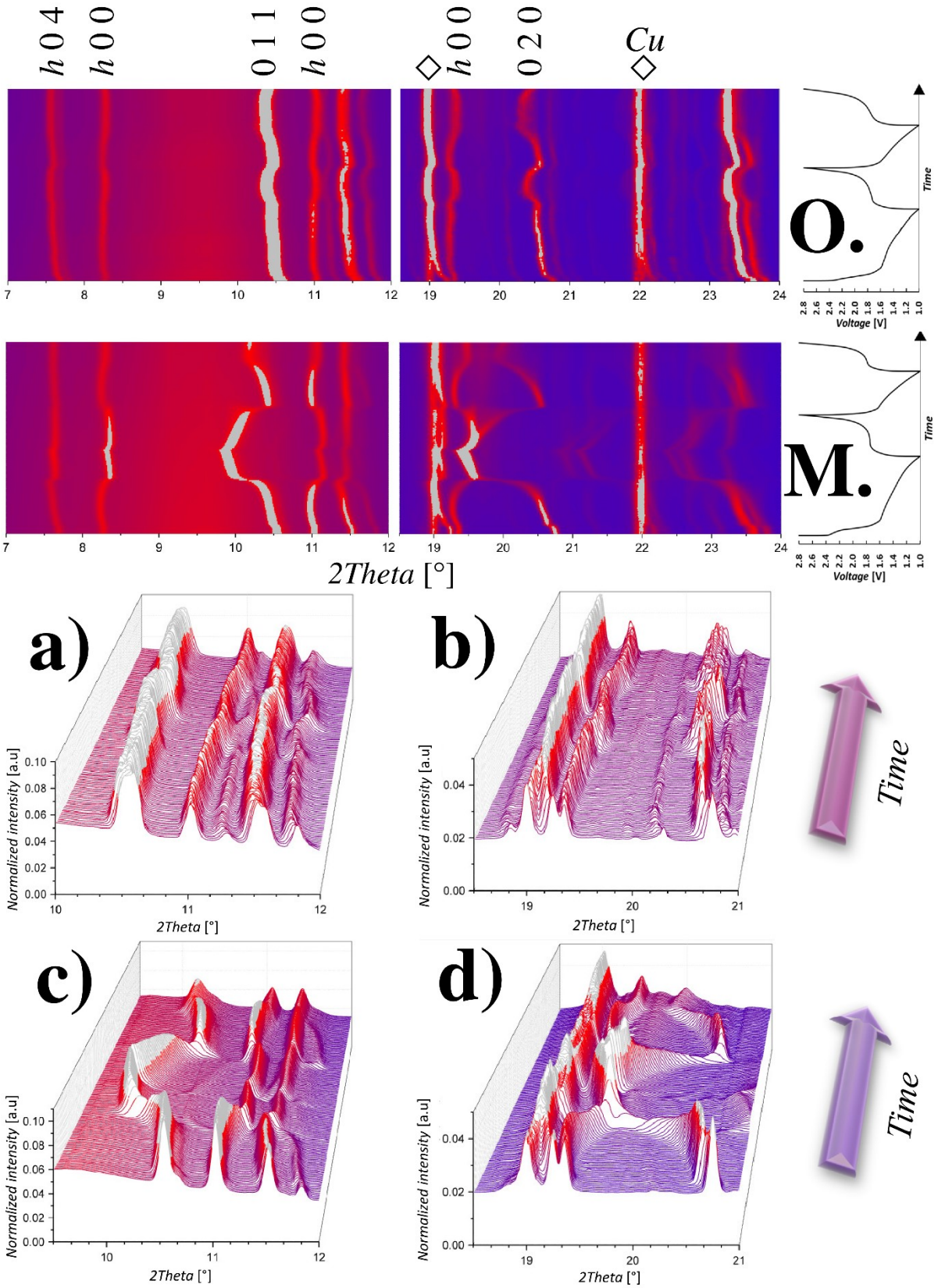

Figure 3.3.10 – Operando XRD patterns at C/10 with corresponding charge-discharge curves and hkl indices (above), with magnified regions of orthorhombic (a-b) and monoclinic (c-d) $FeNb_{11}O_{29}$.

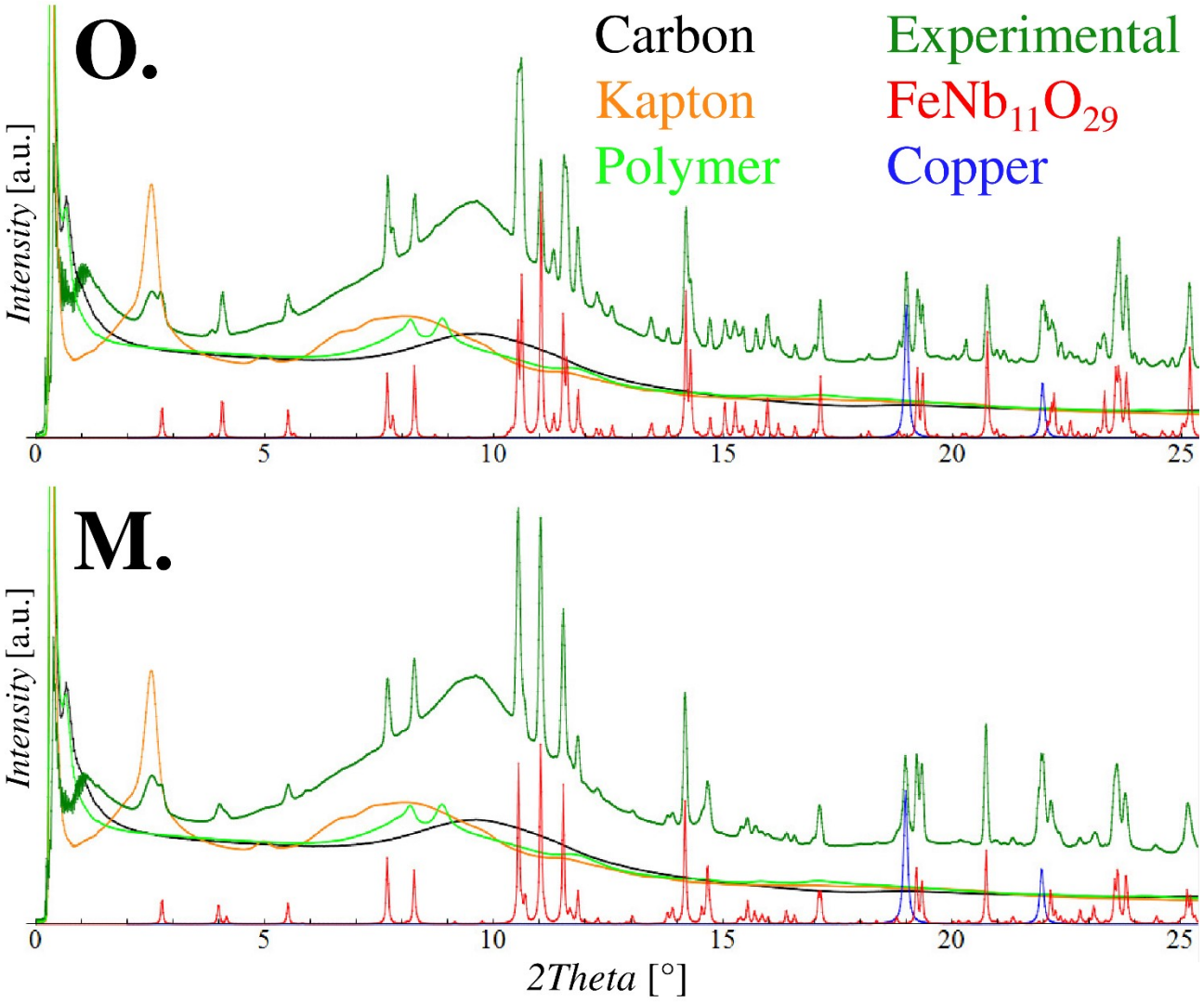

Figure 3.3.11 – XRD patterns collected at the OCV of the cells, together with the collected (carbon, kapton and polymer) or calculated ($FeNb_{11}O_{29}$ and Cu) patterns of the components of the electrodes.

The behaviour of the two polymorphs of $FeNb_{11}O_{29}$ will be discussed separately, due to their different lattice evolution (Fig. 3.3.12). The trend recorded for the monoclinic polymorph clearly shows analogies with DFT-calculated lattice parameters of similar oxides ($Nb_{12}WO_{33}$ and $Nb_{16}W_5O_{55}$) [7], but differs from the one already reported for $FeNb_{11}O_{29}$ nanotubes with in situ diffraction. [20] This discrepancy can be attributed to the particle sizes (micron- vs nano-sized), and to the timescale of the experiment, that can drastically affect the final results.

A first lattice expansion is followed by a contraction and by a second expansion. The final volume expansion at the end of the first discharge is +7.38%, due to the combination of the contraction of *a* (-0.55%) and the expansion of *b* (+7.05%) and *c* (+0.80%). The lattice parameters of monoclinic $Li_{11}FeNb_{11}O_{29}$ are in agreement with the ones found by Pinus et al. [12] for the orthorhombic sample, confirming the crystallographic similarities between the two structures.

During charge and in the following cycle of discharge and charge, the lattice parameters perform a sort of loop around the values refined for $Li_{11}FeNb_{11}O_{29}$ (see Figure 3.3.12).

The orthorhombic sample instead does not seem to undergo the lattice shrinking during the first discharge, where it only expands (*a* + 0.25%, *b* +1.11%, *c* + 1.27%). In the following steps, the drop in *a* and the further increase in the other parameters seem to suggest that the same trend recorded for the monoclinic polymorph is just delayed in the orthorhombic structure.

The lattice shrinking is beneficial for long-term cycling, but this kind of behaviour is often associated with phase transformation with slow kinetics. Operando XRD diffraction was also performed at a fivefold current (C/2), obtaining interesting results (Figure 3.3.13 and Figure 3.3.14, magnified regions): this time both polymorphs seem to follow the same trend, with a shrinking of the lattice parameters *a* and *c* clearly detectable at almost half of the discharge. Also, the hysteresis observed during the charge is reduced, confirming the increase in the coulombic efficiency already observed in charge-discharge measurements.

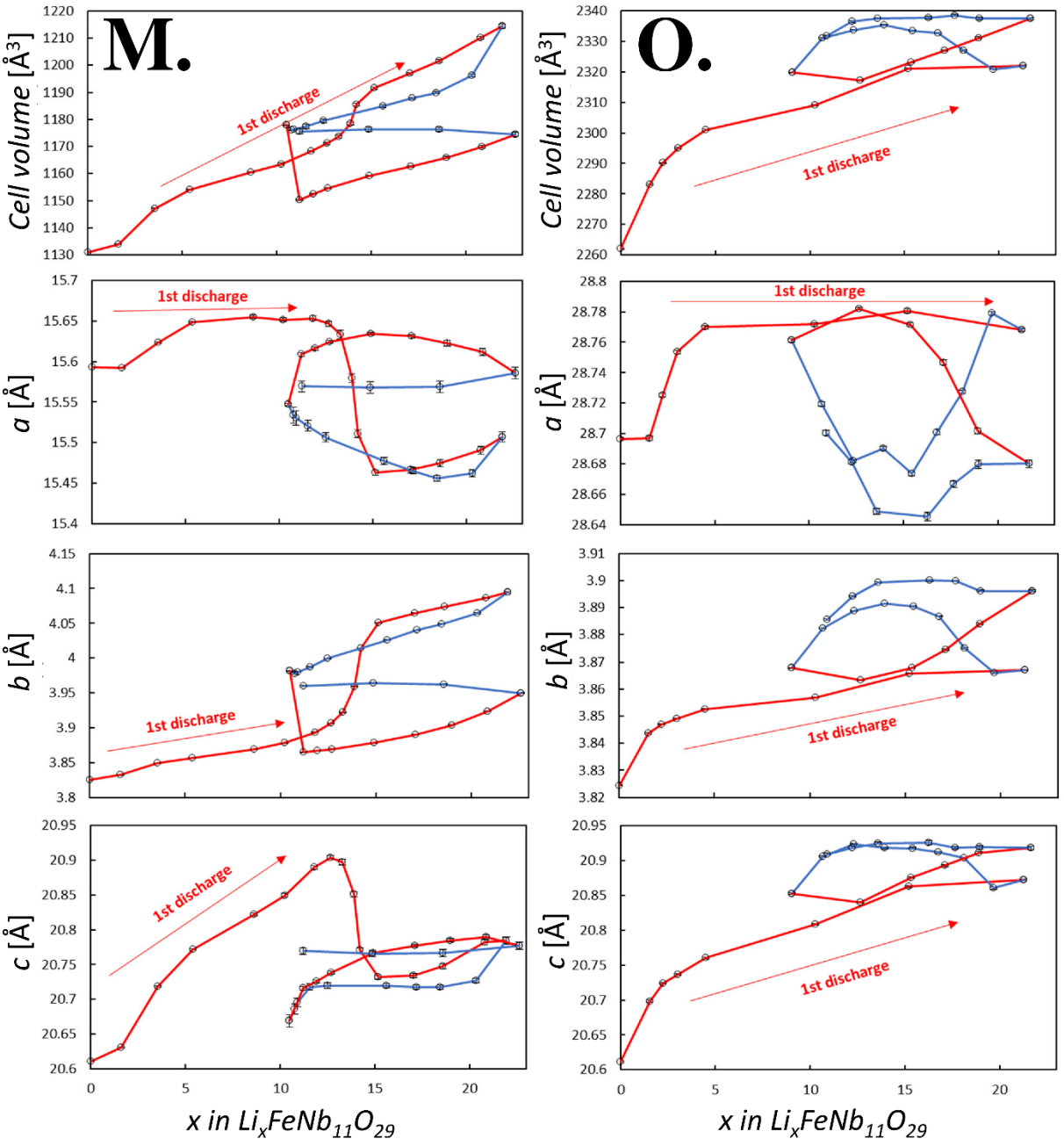

Figure 3.3.12 – Refined lattice parameters and cell volume during the operando XRD measurements at C/10, for monoclinic and orthorhombic $FeNb_{11}O_{29}$. Red/blue lines connect the refined lattice parameters during discharge/charge.

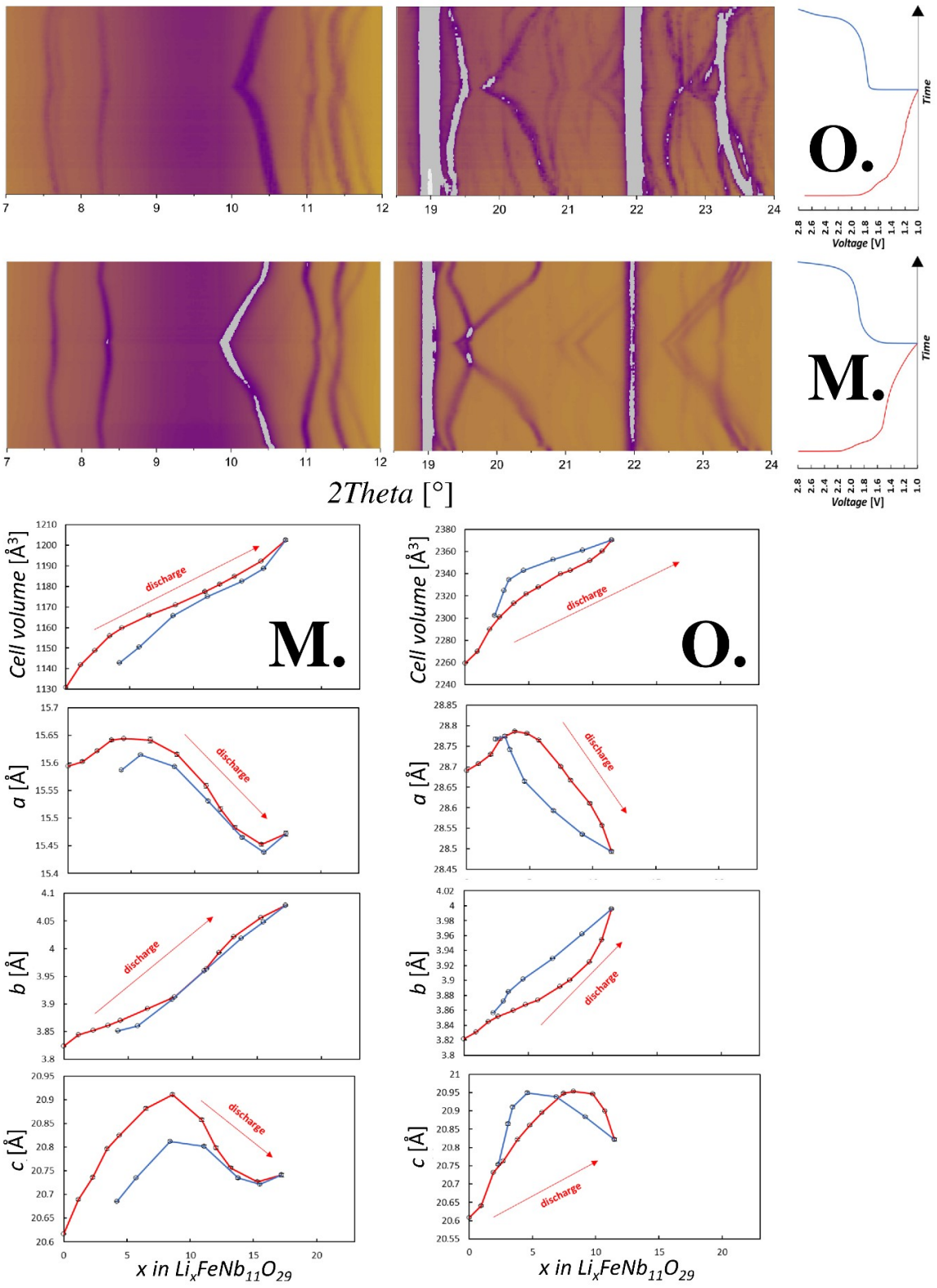

Figure 3.3.13 – Operando XRD patterns at C/2 of orthorhombic and monoclinic $FeNb_{11}O_{29}$, with corresponding charge-discharge curves and refined lattice parameters.

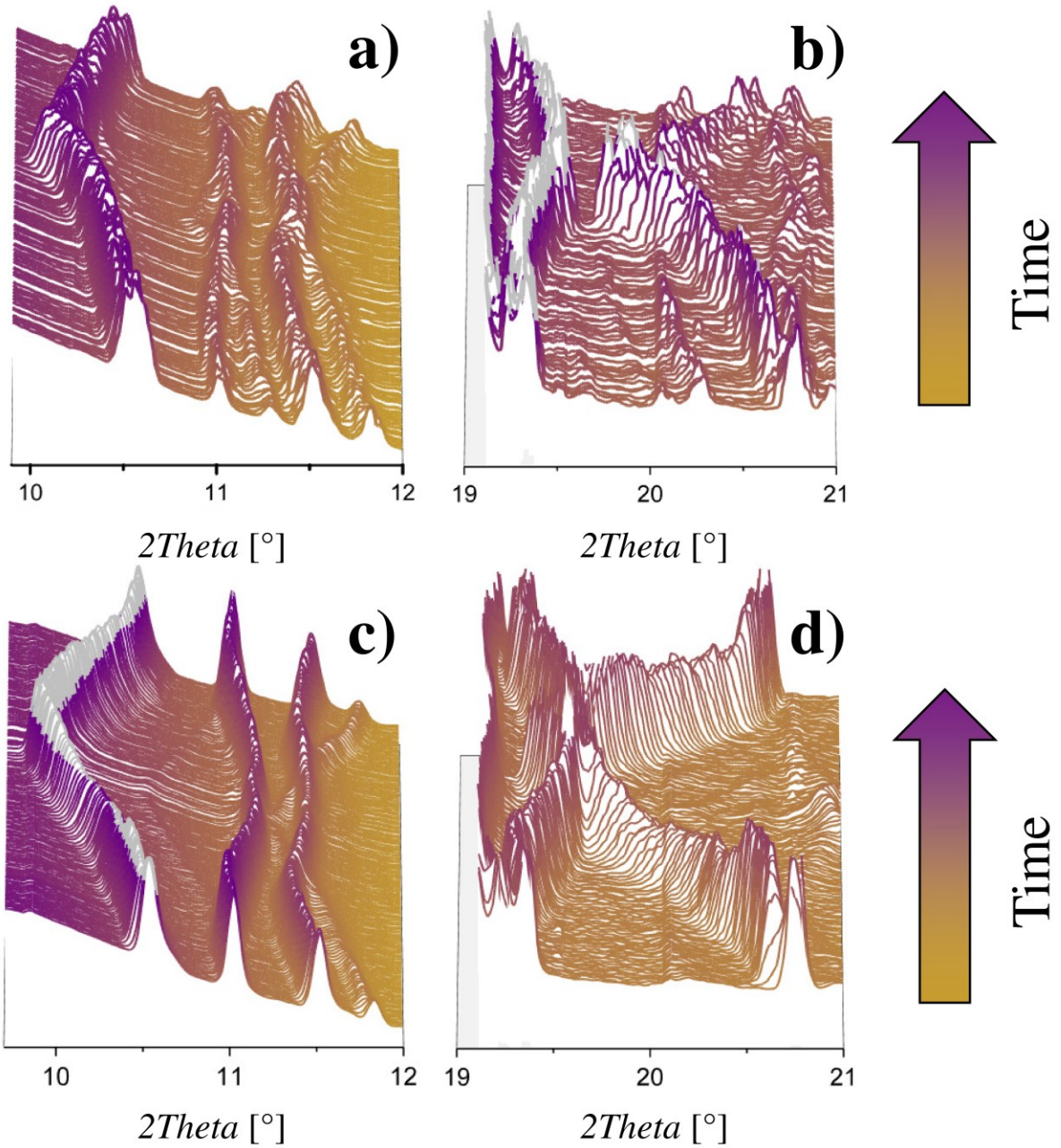

Figure 3.3.14 – Magnified regions of operando XRD patterns at C/2 of orthorhombic (a-b) and monoclinic (c-d) $FeNb_{11}O_{29}$ shown in Figure 3.3.13.

In situ Raman spectroscopy

Raman spectroscopy is very sensitive to the structure and bond order of transition metal oxides, especially in the region of metal-oxygen stretching modes, thus making the technique a very useful tool for in situ studies of electrode materials for secondary batteries. In situ Raman experiments on $FeNb_{11}O_{29}$ were never reported before, so, as reference, some Raman experiments on analogous compounds are mentioned.

The spectra of $FeNb_{11}O_{29}$ will mostly be discussed on the basis of the diatomic approximation. [15] In brief, the diatomic approximation allows a straightforward interpretation of the Raman spectrum of a crystalline metal oxide compound because it assumes that there are no vibrational interactions between neighboring metal-oxygen bonds in the lattice, allowing to determine the metal-oxygen bond lenghts directly from the observed Raman stretching energies. [28]

Here, we will follow the empirical formula, Equation (1), derived from ref. [28] in order to correlate the frequencies of the Raman modes with their bond distance:

$$v(\mathrm{cm}^{-1}) = 25922\, e^{-1.9168R} \qquad (1)$$

where v is the Raman shift corresponding to the stretching of a Nb-O bond with length equal to R (Å), 25922 and 1.9168 are the empirically derived pre-exponential and exponential factors.

The diatomic approach accounts well for the high energy Raman bands, i.e. for shorter Nb-O bonds, but some complication appears when longer Nb-O bonds are involved. Generally the site-symmetry model must be invoked when internal or external modes involving groups of three or more atoms are present in the crystal, and these modes are not accounted for in the diatomic approximation. Raman bands arising from symmetry-related modes almost always occur at low frequency, < 300 cm^{-1}, but seldom occur at high frequencies (molecules confined to a crystalline lattice and possessing a high degree of point-group symmetry). [28]

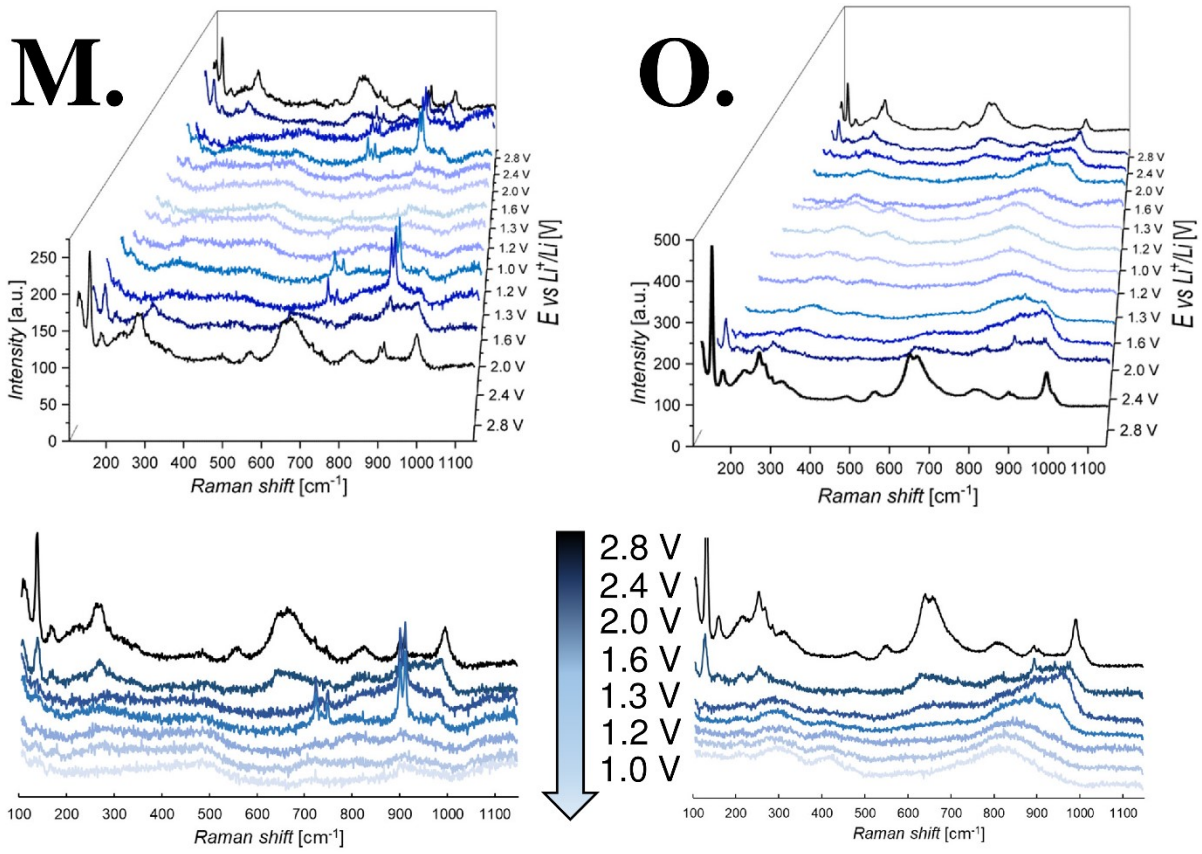

Figure 3.3.15 – In situ Raman spectra recorded at different potentials, for monoclinic and orthorhombic $FeNb_{11}O_{29}$ (above, 3D graph) and discharge trend (down, 2D graph).

The series of in situ Raman spectra for both polymorphs is reported in Figure 3.3.15. The reversibility of the intercalation reaction is confirmed by the recovery of the shape of the pristine spectrum after a full cycle of intercalation/deintercalation.

The Raman features are essentially dominated by the vibrational activities of Nb-O bonds in NbO_6 octahedra and the contribution of Fe is less relevant, in particular for symmetry-related modes in the lower energy Raman region. The Li-O interatomic distances (limited range centered around 2-2.1 Å) [12] in a diatomic frame bring the related Raman signature around 450-500 cm^{-1}, as evidenced in the low-voltage spectra. The modes deriving from the electrolyte are sometimes detected, depending on the amount of irradiated liquid in each measurement. They can be easily recognized by their sharpness and position, unaffected by the reaction. Their Raman shifts are located at 714, 739, 891 and 901 cm^{-1}, as one can figure out from the comparison between a powder $FeNb_{11}O_{29}$ and a $FeNb_{11}O_{29}$ particle totally wet with electrolyte, in the electrochemical cell (see Figure 3.3.16). This analysis also serves as a proof that the Raman spectrum of the sample in the cell in OCV conditions (2.8 V) is identical to the powder sample.

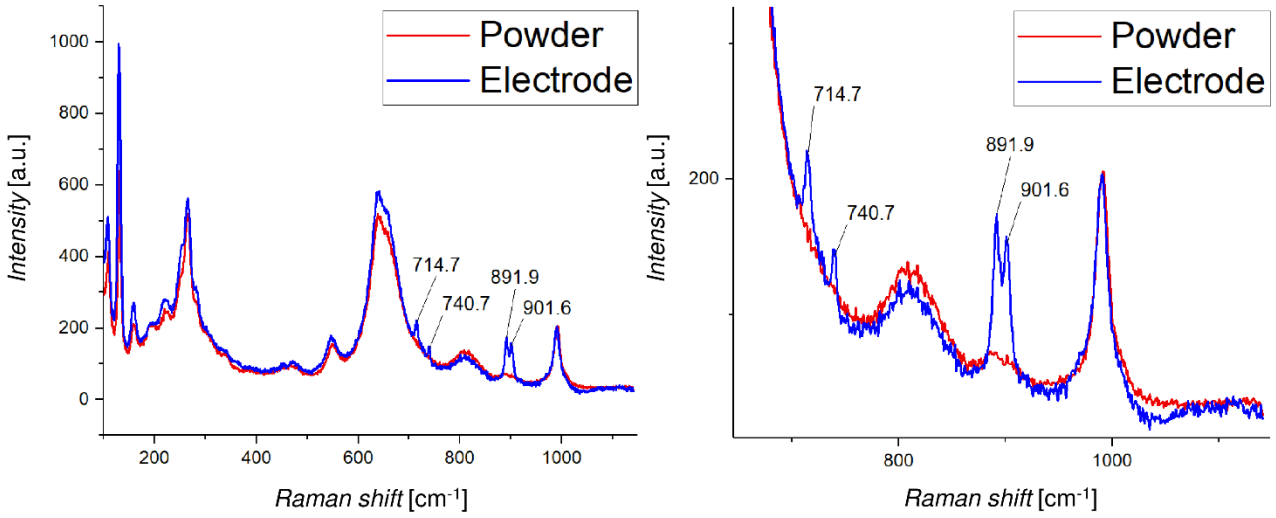

Figure 3.3.16 – Raman spectra of powder $FeNb_{11}O_{29}$ and $FeNb_{11}O_{29}$-based electrode inside a pouch cell, with detail on the region of interest.

In OCV conditions, multiple peaks arise in the different regions of the spectrum: in the high-frequency region peaks at 990 and 896 cm^{-1} correspond to the stretching modes of very short Nb-O bonds (respectively 1.70 and 1.75 Å), similar to double bonds because of their valence, associated with very distorted edge-sharing NbO_6 octahedra. The peak at 810 cm^{-1} is due to the symmetric stretching mode of collinear Nb-O-Nb bonds (1.80 Å) due to corner-shared octahedra. In the middle-frequency region there is most of the activity, given by the intense peaks at 660, 640 cm^{-1} with a shoulder at 550 cm^{-1} (corresponding Nb-O distances of 1.91, 1.93 and 2.01 Å), deriving from symmetric stretching of slightly distorted octahedra. The band at 478 cm^{-1} corresponds to the stretching of a Nb-O bond with length of 2.08 Å. In the low-frequency region, where the bending modes are active, multiple bands arise, the most notable one being centered at 130 cm^{-1}.

The spectrum of $LiFeNb_{11}O_{29}$ (2.4 V) is quite reminiscent of the pristine phase, with differences in the higher and lower energy regions of the spectrum. The most evident change is the decrease of the total Raman yield and a general broadening of the Raman features with a reduction in the number of peaks, heavily affecting the modes between 500-700 cm^{-1}. In addition, at higher energies, a blue-shift is clearly observed, consistent with a symmetrysation of the structure, accompanied by a distortion [29] that confirms the lattice expansion observed with XRD measurements.

The next spectrum, recorded at 2 V vs Li^+, is already typical of a high-symmetry phase, with few broad bands. The shape of lower-potential spectra is maintained, but some blue and red shifts prove that the symmetrised structure is being distorted. For these high-symmetry phases the diatomic approximation and the empyrical formula previously reported do not apply and the Raman activity at high wavenumbers (800-900 cm^{-1}) can be justified by the vibrations of highly symmetric groups of atoms.

However, the trend is significant: at the potential corresponding to the lattice shrinking (1.6 V), this Raman activity shifts to higher wavenumbers, because bond lengths decrease. After the symmetrisation/shrinking, bonds are elongated due to the expansion of the symmetrised structure, but

also due to the redox reactions involving Nb cations (lower-valence Nb cations will have longer bonds because of the Pauli' sum valence rule).

During the charge, the Raman activity is fully recovered, proving the structural stability of the host framework.

Symmetrisation explained

In the discussion of d^0 cations-containing stuctures, the 2nd order Jahn-Teller (SOJT) effect must be introduced: the energy of empty d orbitals is lowered as the cation becomes smaller and more charged. If the energy is lowered sufficiently, the empty d orbitals are able to mix with the filled p orbitals of the ligands. In extended structures this leads to a number of different electronic configurations with closely spaced energies. Any degeneracy in these configurations can be removed by a spontaneous distortion, and any lowering of the electronic energy caused by distortion has to compete with a possible increase in the structural energy (the principle of maximum symmetry is expected to work against distortions). The magnitude of this electronic effect depends inversely on the size of the energy gap between HOMO and LUMO. LUMO has cation d character, and is lowered in cations with higher charge and smaller size. Sc^{3+} and Zr^{4+} are dominated by structural energy, showing no tendency to distort, while V^{5+} and Mo^{6+} are dominated by electronic energy, and thus always distorted. In between Ti^{4+}, Ta^{5+} and Nb^{5+} are sometimes distorted, depending on the nature of structural energy. [30]

When two coordination octahedra share edges or faces, as in Niobium shear structures, the cations are brought into contact and tend to relax by moving away from each other, making distortions possible. [30] For $FeNb_{11}O_{29}$, it was already observed that different crystallographic sites posses different distortion degrees. The 6th site at the center of the building blocks (Figure 3.3.17), exclusively corner-sharing, is the less distorted because the Nb cations are far away from each other, while sites 1, 2 and 3 are more distorted than sites 4 and 5 because of the larger amount of shearing along the shorter side of the building blocks. [15]

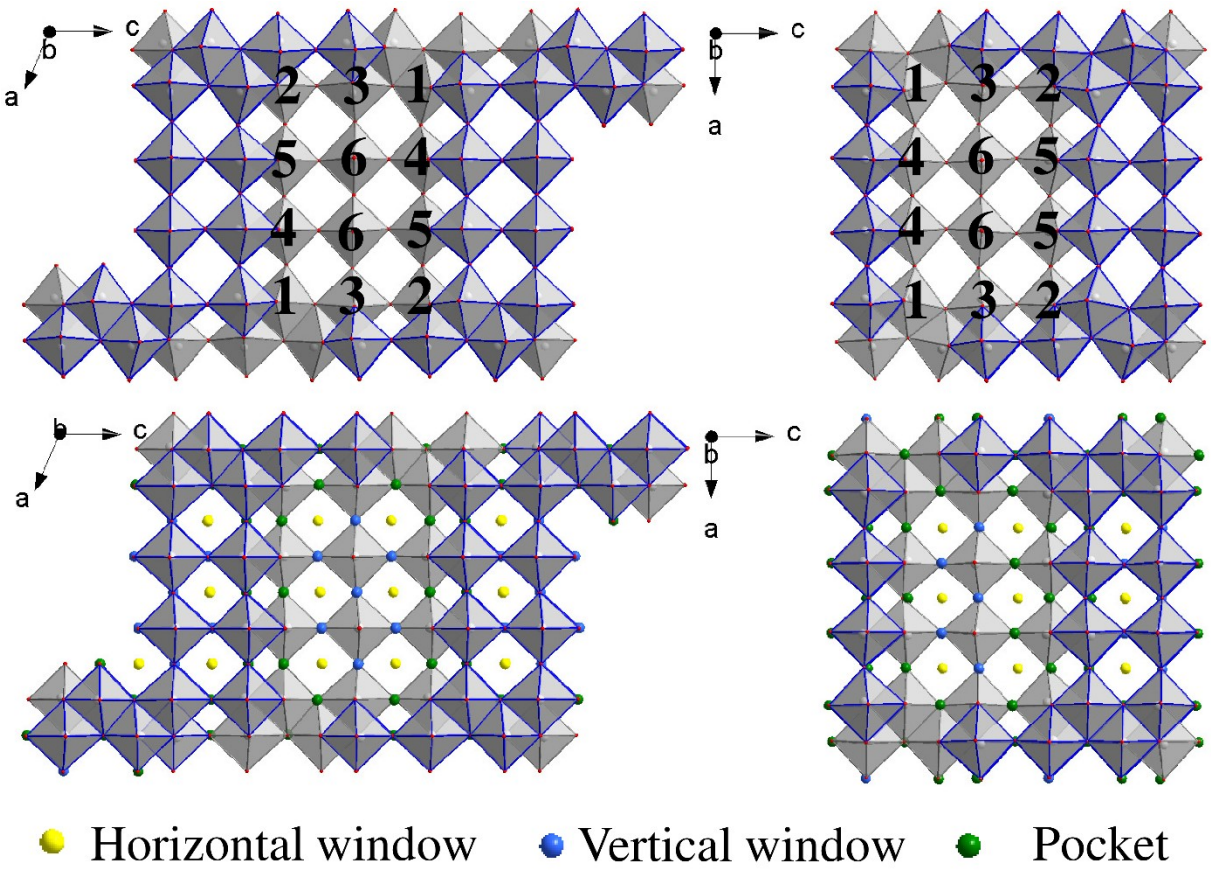

Figure 3.3.17 – Coordination environment of Nb^{5+} in $FeNb_{11}O_{29}$ (above) and Li^{+} ions in $Li_{23}FeNb_{11}O_{29}$ (down), in the monoclinic (left) and orthorhombic structures (right). Different kind of Li sites are highlighted with different colours.

In the lithiated phase ($Li_xFeNb_{11}O_{29}$), the electrochemical reduction of cations causes the lattice shrinking: while the d^0 (Nb^{5+}) edge-shared octahedra are heavily distorted because of the SOJT effect, both the d^1 and d^2 (Nb^{4+} and Nb^{3+}) are weakly distorted, because the degeneracy of electronic configurations is limited to the T_{2g} set of orbitals, not pointing towards ligands. This effect, together with the decreased electrostatic repulsion along shear planes, causes the symmetrisation of the octahedral framework, which is a displacive phase transition: the atoms slightly shift, retaining the symmetry of the crystal.

Structure and electrochemistry

Compounds with perovskitic cavities are studied since the 80's, because the empty space left by the lack of the cation A (if compared to a perovskite ABO_3) is suitable for Li insertion. In cubic ReO_3, upon lithiation, those cavities undergo an irreversible twisting that originates 2 smaller octahedral sites from a single cavity, because each cavity is too large for a proper coordination of a single Li^{+} ion. [31] In $FeNb_{11}O_{29}$ this twisting is prevented because edge-sharing octahedra make the structure less flexible,

giving wide, open tunnels weakly coordinating Li^+ ions. Even if cavities (first identified by Cava et al. [32]) are useful for the structural understanding of pristine shear phases, each cavity is associated with multiple lithium sites, making more accurate to describe the lithium insertion mechanism by the type of site (window, pocket) that is being filled. [7]

Lithium sites in block-type structures [33,34] are divided into three sets: fivefold coordinated `pocket' sites at the edge of the block, fourfold coordinated horizontal window positions, and four-fold coordinated vertical `window' positions (Figure 3.3.17). Horizontal window positions have a symmetric arrangement of oxygen atoms, while vertical window positions and some of the pocket sites are less symmetric. The insertion into fivefold coordinated sites is energetically more favourable, while insertion into vertical window positions is the least favourable because these sites are too large for fourfold coordination of lithium by the oxygen atoms. [7]

In lithiated $FeNb_{11}O_{29}$, up to 23 Li ions can be accommodated in the host lattice, corresponding to a theoretical capacity of 400 mAh g^{-1}. Among them, 10 Li^+/f.u. are accomodated in pocket sites (174 mAh g^{-1}) and the remaining 13 are accommodated in window sites (226 mAh g^{-1}).

The electrochemistry of $FeNb_{11}O_{29}$ is heavily influenced by the presence of this kind of Li sites: intrinsic pseudocapacitive features (i.e. also in the bulk state) are already reported in literature [19–21]. The pseudocapacitance reported in $FeNb_{11}O_{29}$ is termed intercalation pseudocapacitance and occurs when ions intercalate into the tunnels or layers of a redox-active material accompanied by a faradaic charge-transfer with no crystallographic phase change. [35] This phenomenon is possible because of the previously called perovskitic cavities, which are well interconnected and too large for a proper coordination of Li^+ ions, thus not limiting the kinetics of charge storage.

Thanks to previous works [19–21] and present results, the current peaks in a voltammogram can now be assigned to insertion of Li^+ into precise structural sites. Figure 3.3.18 shows the voltammograms obtained with a sweep rate of 0.01 mV s^{-1} ($1/10^{th}$ of the usual slowest sweep rate found in literature) for both the polymorphs of the iron niobate. Peaks are still overlapping, because the moltitude of possible sets of cation-cation neighbours deriving from the cationic disorder produces a distribution of site energies instead of single values, causing the peak broadening. The symmetrisation of the octahedra (main redox peak, at ca. 1.6 V) is responsible for most of the potential hysteresis that is recorded between the cathodic and anodic branches: during the discharge step, Li ions enter the interstitial space of the host lattice and electrons are accepted into the transition metal d orbital, followed by an energy decrease and phase stabilization. However, in reverse, more energy is consumed as ions and electrons must be promoted from the lower energy states. In particular, the energy spent during charge is slightly higher than that delivered during discharge. This energy difference is the source of the potential gap between the charge and discharge curves, or in this case between the two branches of the voltammogram. [36]

The peak around 2.5 V can easily be assigned to the $Fe^{3+}/^{2+}$ redox couple: in other isostructural materials with an electrochemically inactive transition metal ($GaNb_{11}O_{29}$ or $AlNb_{11}O_{29}$) that peak does not appear. [37,38] Further, the electrochemical potential of electrodes increases with the number of electrons in d orbitals of transition metal elements of the same period: the electrons in the outer shell are more

strongly attracted by atomic nuclei, resulting in higher energy consumption or release during electron transfer. Similarly, if the period increases in the same family, the binding energy of electrons and the electrochemical potentials of cathodes decrease, because the nuclei-4d electrons attractive force is weaker than the one between nuclei and 3d electrons. As weaker attraction corresponds to a lower energy for electron transfer, the corresponding materials have a lower potential. [36] All the other peaks below 2 V are then assigned to the $Nb^{5+}/^{4+}$ (E >= 1.6 V) and $Nb^{4+}/^{3+}$ (E < 1.6) redox couples. The shape of the voltammogram suggests more than one peak per redox couple. In order to discuss a possible correlation between peaks and Li insertion sites, we have to mention that different positions possess different site energies and produce different potentials when ions are inserted into or extracted from host materials. The lower the site energy in a crystal lattice, the more external energy is consumed to transfer one ion from the occupied site to a free state. [36] DFT calculations suggested that fivefold-coordinated sites are more energetically favourable than vertical window positions, hence the electrochemical potential of pocket sites is expected to be higher than vertical window sites. Further, the current detected in CV experiments is pseudocapacitive when Li^+ ions intercalate in the tunnels with no diffusion limitations: hence the sites involved in pseudocapacitive reactions are the window positions (corresponding to perovskitic cavities), with weaker coordinative bonds. By contrast, the diffusive intercalation should correspond to the 5-fold coordinated lithium sites, more stable.

The broad peaks above 1.65 V are pseudocapacitive, [18–21] with horizontal window positions involved. The multiple set of peaks involving Nb^{5+} reduction is likely caused by the different distortion degrees of different horizontal window sites, with possible contribution from pocket sites (the diffusive contribution).

The main redox peak involves the Nb^{5+}/Nb^{4+} redox couple with insertion of Li^+ ions in pocket sites, which are both symmetric and distorted, giving a splitting which is detectable only at slow sweep rates. This reaction is associated with the symmetrisation of the block, that makes previously distorted vertical window positions available. The main peaks are much sharper than any other peak, because they are associated with a phase transition, while the site energy associated with the other redox events is changing rapidly, due to the lattice expansion. The further reduction of Nb ions (Nb^{4+}/Nb^{3+}) is again pseudocapacitive, meaning that window positions are still involved (both the remaining horizontal and the freshly available vertical).

The reverse process is not exactly identical, as suggested by the analysis of the pseudocapacitive contribution in our previous paper. [21] This time the first oxidation (Nb^{3+}/Nb^{4+}) is diffusive, suggesting pocket sites are the first left by Li^+ ions. Pocket sites are involved until the main anodic redox peak, with a pseudocapacitive contribution in between suggesting that also some window sites are now free from Li^+ ions.

The little differences between the polymorphs detected in the voltammograms can be ascribed to both the different links between the structural blocks and to the different distortion degrees of the octahedra: the monoclinic polymorph usually shows a higher and broader redox peak for the Nb^{4+}/Nb^{3+} which, at higher sweep rates, prevails over the redox peak $Nb^{5+}/^{4+}$, because of the faster kinetics associated with pseudocapacitive reactions.

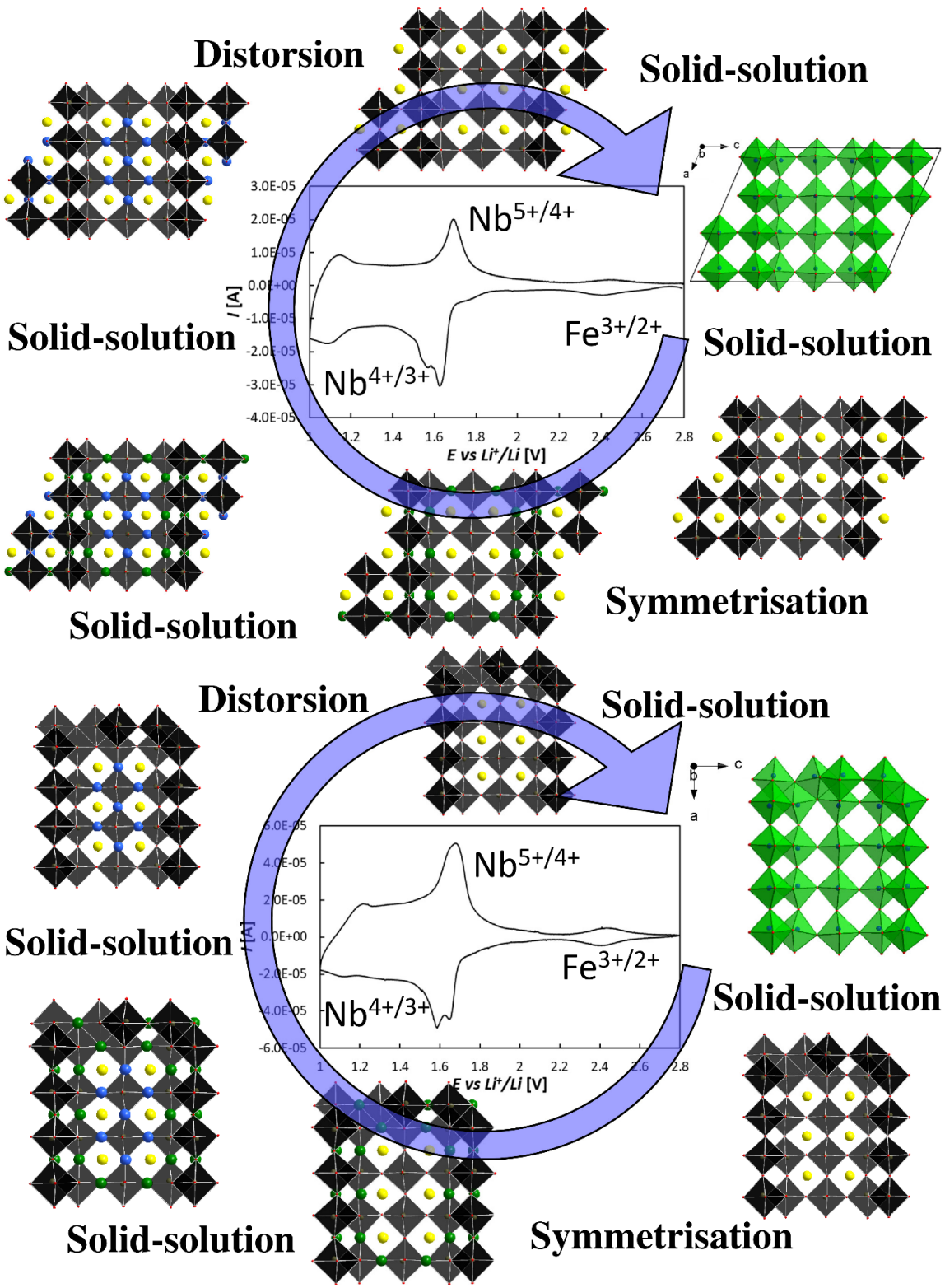

Figure 3.3.18 – 1st cycle of voltammetry of monoclinic (above) and orthorhombic (down) $FeNb_{11}O_{29}$, with corresponding structural changes. The pristine phase is pictured in green and the lithiated phases in black, while lithiation sites are consistent with Figure 3.3.17.

Electrochemical Impedance Spectroscopy and pseudocapacitance

While the Nyquist plot for an ideal capacitor is a vertical line (90° phase angle), deviations from a vertical line to phase angles of < 90° can indicate pseudocapacitive behaviour, which is often represented by a constant-phase element in the equivalent circuit. [35]

A series of spectra was collected applying different potentials to the $FeNb_{11}O_{29}$/Li cell (Figure 3.3.19) and allowing the cell to reach steady state conditions at each potential, before applying the excitation voltage pulses. For better clarity, both the Bode and Nyquist plots are shown, indicating respectively, the evolution of the shape of the spectra and the values of the resistances.

The pseudocapacitive nature of $FeNb_{11}O_{29}$ is evident: the continuous change in the oxidation states corresponding to the entrance/exit of Li^+ ions in/from the structure finds a correspondance in the spectra. At every potential (apart from high-end potentials where the overpotentials are too high for an ionic charge-transfer resistance) the spectra consist of a solution resistance (R_s), 2 charge transfer resistances (R_e and R_i, the first being electronic and the second ionic) and the mass transport, more or less detectable. An analogous model was reported for similar Niobium oxides. [39]

The evolution of the shape of the spectra shown with the Bode phase plot is representative of the process: the electrolyte resistance (at the high-end frequency of the spectra) is almost constant, indicating the good stability of the commercial electrolyte in the selected potential window.

At high frequencies (approx 10^3 Hz) the electronic charge transfer resistance is not much affected by the reaction, for what concerns the frequency of the process. The phase shift instead is slightly higher at the low-end potentials, indicating an increase in the capacitive contribution and thus a non-negligible contribution of the active material to the electron conduction. For most niobium oxides, wide band-gap insulators, lithiation/n-doping introduces electrons into the almost empty conduction band, resulting in metallicity (progressively stronger as the phase gets more lithiated), beneficial for high-rate battery performance and possible electrochromic applications. [7] The experimental data show that the electronic resistance and the phase shift even increase below 1.6 V, i.e. when Nb^{5+} cations are reduced. As the preferred electron transport direction is expected to be perpendicular to the block plane [7], the increase in R_e can be ascribed to the large expansion of the lattice parameter *b* (perpendicular to the block plane), that decreases the orbital overlapping and the electron transport along the favoured direction.

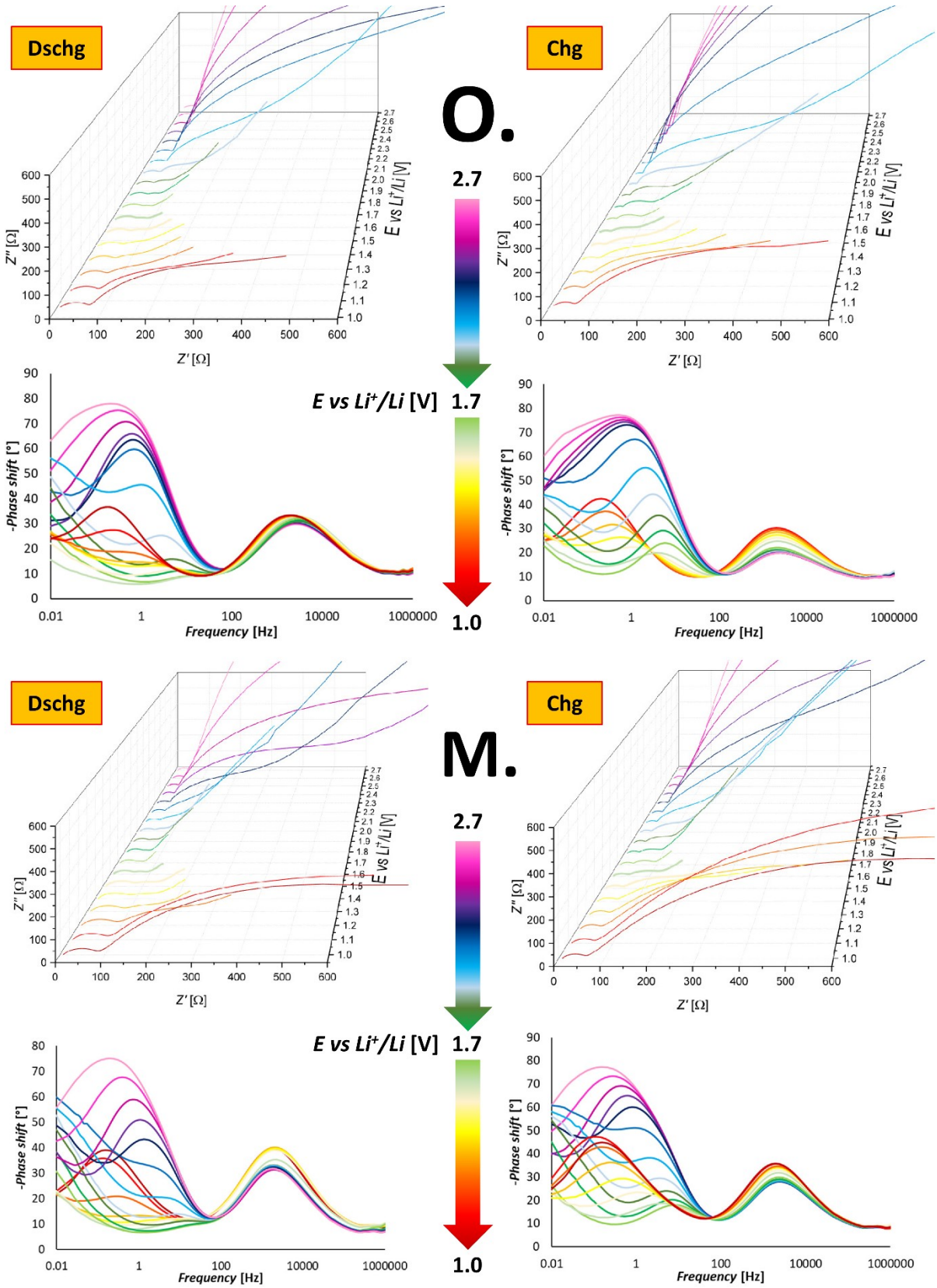

Figure 3.3.19 – Nyquist and Bode phase plots of the EIS measurements, for orthorhombic (up) and monoclinic (down) $FeNb_{11}O_{29}$. Both discharge (left) and charge (right) spectra are shown.

The ionic charge transfer instead shows consistent changes in the frequency of the process and in the phase shift. At higher potentials, the mass transport dominates the low-frequency region of the spectra. When the overpotentials associated with ionic charge transfer reactions (i.e. the already mentioned redox peaks) are progressively lowered, the low-frequency part of the spectra is a mix of mass transport and ionic charge transfer resistance. The capacitive resistance corresponding to the ionic charge transfer shows higher capacitive contribution (manifested as higher phase shifts, up to 70-80°) at high- and low-end potentials. The smallest phase shift (quite close to a pure resistance, that ideally has no phase shift) is obtained in correspondance of the highest redox peak (1.6 V), which showed maximum diffusive contribution in voltammetric analyses. [18,19,21] The consistent frequency shift (ranging from 10^{-1} to 10^{1} Hz), indicates faster charge transfer at potentials closer to the same redox peak. This is not surprising, because peaks in voltammograms correspond to higher reaction rates, i.e. faster charge transfers.

Of course the Nyquist plot shows the same trend, with constant and relatively little electrolyte and electronic-transfer resistances, followed by a huge Warburg impedance at higher potentials and a W-shaped trend in the ionic charge-transfer resistance, with a minimum in correspondance of the highest redox peak. The fitted values of the resistances, capacitances and the exponents of the frequency for the Constant Phase Elements (CPE) are reported in Table 3.3.20-3.3.21.

Monoclinic sample										
E vs Li^+/Li [V]	R_s [Ω]	R_e [Ω]	CPE_e [F]	N_e	R_i [Ω]	CPE_i [F]	N_i	CPE_d [F]	N_d	χ^2
2.7	6.9	37.8	7.14E-05	0.71	19552.0	1.00E-03	0.89			0.089
2.6	7.1	36.5	6.05E-05	0.73	4469.2	1.08E-03	0.86			0.041
2.5	7.0	34.5	5.73E-05	0.74	1412.6	1.14E-03	0.85			0.036
2.4	7.0	35.7	5.80E-05	0.73	694.2	1.18E-03	0.84			0.029
2.3	7.1	38.1	5.93E-05	0.73	453.8	1.35E-03	0.81			0.047
2.2	7.0	42.4	6.79E-05	0.71	125.5	1.02E-03	0.90	4.49E-03	0.68	0.027
2.1	7.0	44.1	7.15E-05	0.71	62.1	1.27E-03	0.88	1.04E-02	0.68	0.030
2	7.0	45.2	7.18E-05	0.70	40.4	1.91E-03	0.81	2.39E-02	0.71	0.031
1.9	7.0	47.0	7.55E-05	0.70	25.9	2.30E-03	0.82	3.27E-02	0.70	0.035
1.8	7.1	45.6	7.15E-05	0.70	20.3	3.31E-03	0.76	5.86E-02	0.68	0.028
1.7	7.1	45.2	7.07E-05	0.70	18.1	3.24E-03	0.77	7.96E-02	0.65	0.036
1.6	7.1	59.4	6.20E-05	0.70	25.9	1.51E-03	0.88	5.69E-02	0.54	0.037
1.5	7.1	79.2	5.10E-05	0.70	49.3	1.74E-03	0.78	3.61E-02	0.53	0.026
1.4	7.1	81.1	4.77E-05	0.71	68.0	2.56E-03	0.68	3.45E-02	0.55	0.026
1.3	7.1	78.1	4.32E-05	0.73	174.0	5.00E-03	0.50			0.022
1.2	7.2	81.2	4.47E-05	0.72	401.7	5.23E-03	0.54			0.034
1.1	7.2	83.9	4.97E-05	0.71	1000.0	4.12E-03	0.67			0.041
1	7.3	83.1	5.36E-05	0.70	1023.6	3.48E-03	0.71			0.062
1.1	7.3	56.3	6.03E-05	0.71	2291.1	3.19E-03	0.69			0.044
1.2	7.2	50.0	5.73E-05	0.71	1502.5	3.47E-03	0.66			0.029
1.3	7.4	48.4	5.27E-05	0.72	886.3	3.70E-03	0.62			0.030
1.4	7.3	47.2	5.51E-05	0.72	440.2	3.71E-03	0.61			0.028
1.5	7.4	43.4	5.67E-05	0.71	220.1	3.47E-03	0.61			0.032
1.6	7.3	42.0	6.47E-05	0.70	75.8	1.89E-03	0.76	4.43E-02	0.55	0.030
1.7	7.3	36.7	7.27E-05	0.69	50.0	1.31E-03	0.84	6.21E-02	0.60	0.030
1.8	7.3	34.6	7.54E-05	0.69	56.7	1.20E-03	0.86	3.25E-02	0.69	0.028
1.9	7.3	34.5	7.49E-05	0.69	73.5	1.11E-03	0.87	1.58E-02	0.71	0.027
2	7.3	33.7	7.44E-05	0.69	102.3	1.03E-03	0.89	9.38E-03	0.71	0.026
2.1	7.3	32.0	7.09E-05	0.70	163.7	9.76E-04	0.89	4.58E-03	0.70	0.023
2.2	7.3	30.9	7.01E-05	0.70	341.5	9.53E-04	0.89	1.89E-03	0.67	0.024
2.3	7.3	29.1	6.15E-05	0.72	1559.1	1.10E-03	0.84			0.039
2.4	7.3	31.1	6.75E-05	0.71	2343.5	9.82E-04	0.87			0.027
2.5	7.4	31.7	6.74E-05	0.71	4370.9	9.67E-04	0.87			0.037
2.6	7.4	32.2	6.61E-05	0.71	12315.0	9.56E-04	0.87			0.091
2.7	7.3	34.2	7.82E-05	0.69	33290.0	9.09E-04	0.89			0.049

Table 3.3.20 – All fitted parameters for the EIS data shown in Figure 3.3.19, for the monoclinic sample.

Orthorhombic sample										
E vs Li^+/Li [V]	R_s [Ω]	R_e [Ω]	CPE_e [F]	N_e	R_i [Ω]	CPE_i [F]	N_i	CPE_d [F]	N_d	χ^2
2.7	6.9	46.2	9.70E-05	0.65				7.83E-04	0.94	0.013
2.6	6.9	47.4	9.44E-05	0.65				8.16E-04	0.93	0.020
2.5	7.0	48.2	8.84E-05	0.65				8.74E-04	0.91	0.021
2.4	7.1	45.8	7.61E-05	0.67	2248.5	9.86E-04	0.90			0.064
2.3	7.1	46.6	7.42E-05	0.67	1862.0	1.04E-03	0.90			0.061
2.2	7.1	46.8	7.15E-05	0.67	1599.7	1.16E-03	0.87			0.057
2.1	7.0	48.6	8.10E-05	0.66	327.0	1.09E-03	0.92	3.42E-03	0.67	0.021
2	7.0	48.9	8.12E-05	0.66	91.6	1.21E-03	0.91	1.29E-02	0.64	0.024
1.9	6.9	49.9	8.20E-05	0.65	43.3	1.39E-03	0.91	2.25E-02	0.62	0.020
1.8	6.8	52.5	8.00E-05	0.65	23.6	1.40E-03	0.94	3.63E-02	0.57	0.012
1.7	6.8	58.1	8.11E-05	0.65	15.7	1.51E-03	0.97	4.98E-02	0.53	0.013
1.6	6.9	61.5	7.69E-05	0.65	19.4	2.41E-03	0.86	7.35E-02	0.50	0.016
1.5	7.0	64.2	8.15E-05	0.65	30.8	1.89E-03	0.91	4.06E-02	0.50	0.024
1.4	7.1	64.9	8.48E-05	0.65	39.1	2.26E-03	0.89	2.62E-02	0.50	0.028
1.3	7.1	64.8	8.66E-05	0.65	49.0	3.03E-03	0.84	2.52E-02	0.50	0.030
1.2	7.2	62.2	8.22E-05	0.66	170.5	6.33E-03	0.64			0.038
1.1	7.2	64.7	8.24E-05	0.66	315.3	5.86E-03	0.71			0.048
1	7.3	64.9	8.22E-05	0.66	545.4	5.21E-03	0.75			0.051
1.1	7.4	47.9	9.25E-05	0.66	791.4	4.61E-03	0.73			0.039
1.2	7.4	45.6	9.71E-05	0.66	531.1	4.86E-03	0.71			0.020
1.3	7.8	40.6	8.43E-05	0.68	345.6	5.01E-03	0.67			0.009
1.4	7.9	36.4	8.76E-05	0.68	221.2	5.04E-03	0.65			0.010
1.5	7.9	32.6	9.51E-05	0.67	141.3	4.64E-03	0.64			0.015
1.6	7.9	29.9	1.06E-04	0.66	55.9	2.15E-03	0.80	3.78E-02	0.50	0.011
1.7	7.9	24.7	1.32E-04	0.65	51.5	1.21E-03	0.90	5.09E-02	0.50	0.010
1.8	7.8	23.6	1.64E-04	0.63	56.8	8.55E-04	0.97	2.48E-02	0.50	0.014
1.9	7.9	22.5	1.53E-04	0.64	93.3	9.18E-04	0.94	1.63E-02	0.57	0.009
2	7.8	21.8	1.51E-04	0.64	156.4	8.69E-04	0.94	8.39E-03	0.59	0.008
2.1	7.4	20.2	1.46E-04	0.64	520.7	1.09E-03	0.87			0.064
2.2	7.4	19.6	1.43E-04	0.64	1820.5	9.70E-04	0.89			0.070
2.3	7.4	20.8	1.76E-04	0.62	3446.0	8.30E-04	0.92			0.023
2.4	7.3	21.2	1.85E-04	0.61	3995.1	7.83E-04	0.93			0.016
2.5	7.5	20.2	1.49E-04	0.64				8.21E-04	0.91	0.056
2.6	7.5	20.5	1.57E-04	0.63				7.99E-04	0.91	0.057
2.7	7.5	20.3	1.51E-04	0.63				7.73E-04	0.91	0.037

Table 3.3.21 – All fitted parameters for the EIS data shown in Figure 3.3.19, for the orthorhombic sample.

If we take into account Equation (2), employed in the circuit modeling for a conventional solid-state diffusion (Warburg impedance), the exponent of the frequency has a fixed value of 0.5 while for a CPE is variable, allowing a rough determination of the pseudocapacitive contribution: the closer the exponent to 1, the higher is the capacitive contribution.

$$Z_{CPE} = 1/[Y_0(i\omega)^N] \quad (2)$$

Where Z_{CPE} is the impedance, Y_0 is constant, ω is the frequency and N a fittable parameter.

The determined values, show a clear trend of pseudocapacitive diffusion at high potentials (N up to 0.95), with an almost solid-state diffusion at lower potentials (N very close to 0.5).

The graphs in Figure 3.3.22 clearly show that in the flatter region of the voltage profile (around 1.6 V) the ionic resistance is lower than the electronic one: at 1.7 V the electronic resistance is over 70% of the sum of R_e and R_i (called R_{tot}*). This serves as a confirmation of the incredible electrochemical properties of niobium shear oxides: the performance obtained with Nb-based electrode materials can be enhanced even more by improving the electron conductivity, because their conduction of Li^+ ions is already surprising. The trend of R_i also suggests that the more symmetrical are the previously called perovskitic cavities, the less resistance they offer to Li^+ solid-state diffusion.

During the charge the trend is similar, with a little hysteresis caused by the aforementioned symmetrisation, manifested with an increase in the internal resistance of the electrode.

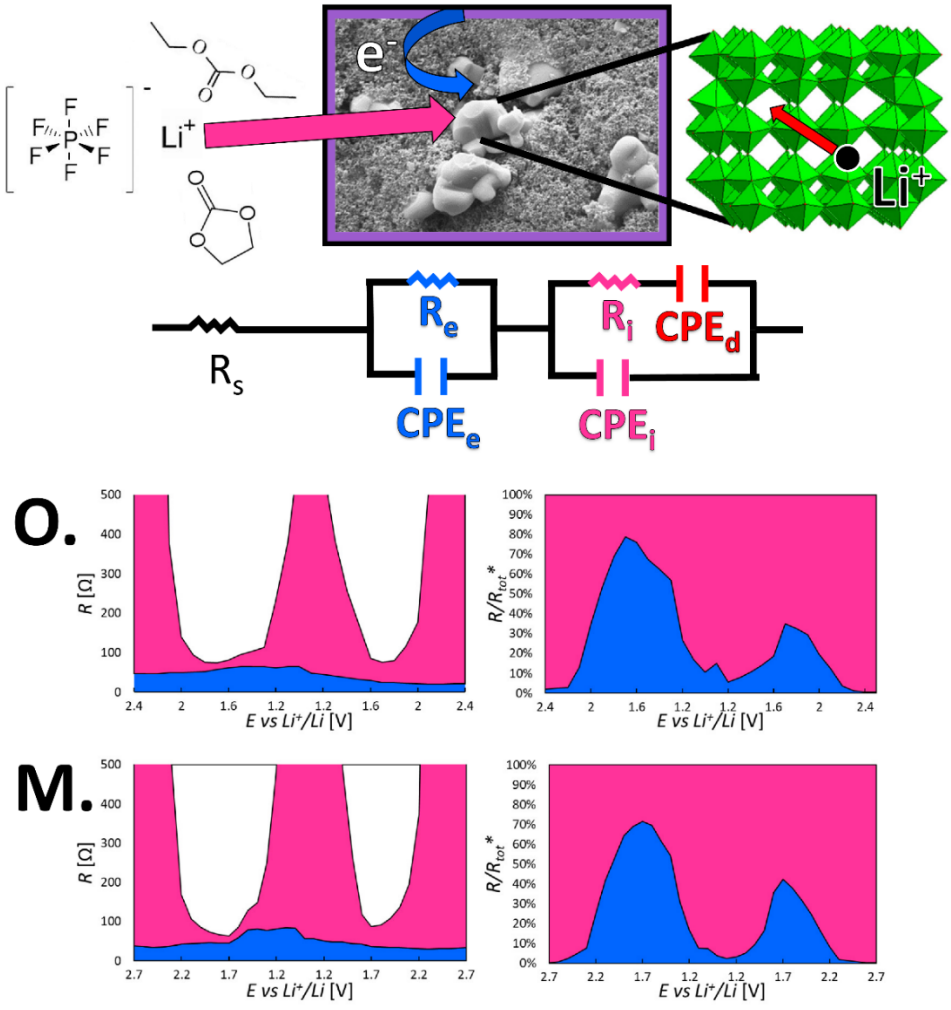

Figure 3.3.22 – Schematic representation of the electrochemical phenomena modelled with the equivalent circuit and *R* vs *E* plots, for monoclinic and orthorhombic $FeNb_{11}O_{29}$. Ionic (pink) and Electronic (blue) resistances are plotted separately on the left and their ratio with their sum (called R_{tot}*) is plotted on the right.

Galvanostatic Intermittent Titration Technique

Aside from the determination of the relative amount of solid-state diffusion and pseudocapacitive intercalation, it is very important to study the values of the diffusion coefficient of Li^+ ions into the electrode. One of the most useful techniques to this aim is the Galvanostatic Intermittent Titration Technique (GITT), which consists in a series of current pulses, each followed by a relaxation time. With a GITT procedure, during the pulse, the cell potential increases quickly due to the *iR* drop and then slowly due to the current pulse (in order to maintain a constant concentration gradient). During the relaxation time the composition of the electrode tends to be homogeneous through Li^+ diffusion, resulting in a sudden *iR* drop followed by a slow potential decrease until steady state conditions. By applying subsequent pulses until the cell is fully charged/discharged the *iR* drop can be eliminated in the calculation of the diffusion coefficient which, for very short pulse times and small currents, can be expressed as Equation (3):

$$D = (n_m V_m/S)^2 (\Delta E_s/\Delta E_t)^2 \, 4/\pi\tau \qquad (3)$$

Where τ is the duration of the pulse (s), n_m is the number of moles of the host oxide (mol), V_m is its molar volume ($cm^3\ mol^{-1}$) and S the contact area between the electrode and the electrolyte (cm^2), while ΔE_s and ΔE_t are two voltage differences (V), related to the steady state voltage change and to the pulse voltage change respectively. [23]

It is worth noting that the diffusion coefficient derived for $FeNb_{11}O_{29}$ is a true diffusion coefficient, because its solid-solution behaviour implies that the concentration of the intercalant ions changes monotonically as the intercalation proceeds. [40]

While for phase transition electrode materials a minimum in the values of the diffusion coefficient is observed in correspondance of voltage plateaus/CV peaks (because of the strong attractive interactions between the intercalating species and the host matrix) [40], $FeNb_{11}O_{29}$ shows an increase in the values of the diffusion coefficient (Figure 3.3.23) at some keypoint potentials, likely due to the weak interactions between Li^+ and the host structure. It has to be precised that with GITT the bare diffusion of Li^+ ions can be studied, thus excluding the pseudocapacitive contributions that affect the reactions below 1.6 V.

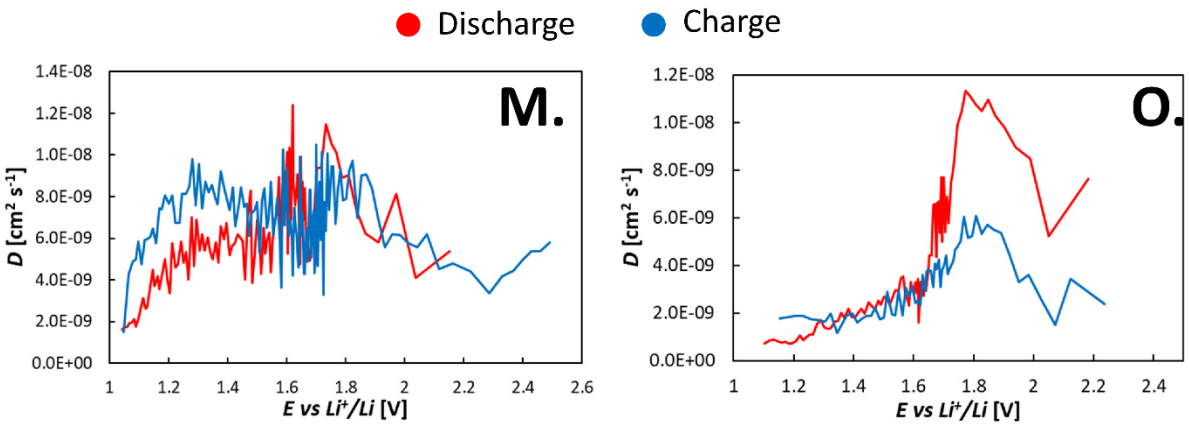

Figure 3.3.23 – Diffusion coefficient vs electrochemical potential, for monoclinic and orthorhombic $FeNb_{11}O_{29}$.

The high-end of the voltage of the *D* vs *E* curve cannot be studied in detail because of the non-equilibrium conditions of the cell (see the slope of the voltage profile), while in the two-phase-like region the diffusion coefficient shows 2 peaks corresponding to the first reduction of Nb^{5+} cations (approx. 1.8 V) and to the main redox peak (also a Nb^{5+} reduction) respectively. The low-end potential region shows a slower diffusion, with a peak for the monoclinic sample and a flatter shape for the orthorhombic sample. The intercalation reaction at 1.8 V allows very little charge storage when compared to the main redox peak, but the corresponding *D* values are the highest for the Nb^{5+} reduction. This suggests that the intercalation involves some entropic factors, with the empty channels being rapidly filled by Li^+ ions, causing the consistent decline in the diffusion coefficient in the following reactions. Further, another maximum of *D* is obtained at 1.6-1.7 V, confirming that in the most symmetrical structure the diffusion is really fast.

During charge, a similar trend is observed, with higher values of *D* at low-end potentials, for which a diffusive de-intercalation was determined in the previously mentioned voltammetric experiments. This suggests again that diffusion is faster in the symmetrical framework.

Conclusion

In conclusion, multiple complementary techniques were employed to study different structural and functional properties of $FeNb_{11}O_{29}$.

The dimorphism of the iron niobate did not reveal significant differences, except from a slightly higher octahedral distortion for the monoclinic polymorph. According to X-ray diffraction and Mössbauer spectroscopy, Fe^{3+} cations are disordered, even if with non-uniform occupation of the six cationic sites. The presence of Fe^{3+} and its random distribution give the material paramagnetic features and prevent Li ordering, making a larger number of Li^+ sites available for intercalation.

Upon Lithium intercalation, octahedral distortions are removed through symmetrisation, alleviating the volume changes and enhancing the already fast Li^+ conduction in the structural channels. The displacive phase transition that causes the symmetrisation explains the flatter region of the voltage profile: the

2nd order Jahn-Teller effect that causes the $Nb^{5+}O_6$ octahedra to be distorted is not present for $Nb^{4+}O_6$, causing Nb cations on shear planes to slide closer because of the decreased cation-cation repulsion. The intrinsic pseudocapacitance exhibited by $FeNb_{11}O_{29}$ is caused by the very weak Li-host matrix interactions: the huge tunnels in the structure provide mass transport that is mostly not limited by solid-state diffusion, showing capacitor-like kinetics and high Li^+ diffusion coefficients. The conduction of Li^+ ions is so fast, in the symmetrised structure, that the highest charge-transfer resistance in the cell is given by the charge-transfer of electrons.

These results provide a detailed structural investigation and explained thoroughly the Li intercalation reaction, correlating electrochemical and functional properties of an interesting anode material that has the potential to become a valid candidate for next-generation LIBs.

References

[1] I. Pinus, M. Catti, R. Ruffo, M. M. Salamone, and C. M. Mari, “Neutron diffraction and electrochemical study of FeNb11O29/Li11FeNb11O29 for lithium battery anode applications,” *Chem. Mater.*, vol. 26, pp. 2203–2209, 2014.

[2] D. Spada *et al.*, “FeNb11O29, anode material for high-power lithium-ion batteries: Pseudocapacitance and symmetrisation unravelled with advanced electrochemical and in situ/operando techniques,” *Electrochim. Acta*, vol. 393, p. 139077, 2021.

[3] D. Spada *et al.*, “Deepening the shear structure FeNb11O29: influence of polymorphism and doping on structural, spectroscopic and magnetic properties,” *Dalt. Trans.*, vol. 47, pp. 15816–15826, 2018.

[4] P. Gutlich, B. Eckhard, and A. X. Trautwein, *Mössbauer spectroscopy and transition metal chemistry: fundamentals and applications*. 2011.

[5] M. Kunz and D. Brown, “Out-of-Center Distortions around Octahedrally Coordinated d0 Transition Metals,” *J. Solid State Chem.*, vol. 115, pp. 395–406, 1995.

[6] K. J. Griffith *et al.*, “Ionic and Electronic Conduction in TiNb2O7,” *J. Am. Chem. Soc.*, vol. 141, no. 42, pp. 16706–16725, 2019.

[7] C. P. Kocer, K. J. Griffith, C. P. Grey, and A. J. Morris, “Cation Disorder and Lithium Insertion Mechanism of Wadsley – Roth Crystallographic Shear Phases from First Principles,” *J. Am. Chem. Soc.*, vol. 141, pp. 15121–15134, 2019.

[8] A. Lappas, J. E. L. Waldron, M. A. Green, and K. Prassides, “Magnetic ordering in the charge-ordered Nb12O29,” *Phys. Rev. B*, vol. 65, p. 134405, 2002.

3.4 Anode materials for NIBs

In this chapter, the study on tin metal as anode material for Na-Ion Batteries will be discussed. In addition, the results of preliminary tests in NIBs on materials that were already studied for Lithium-Ion Batteries will be reported.

Characterization of tin deposits

All the electrodeposits consist only of tin metal, which crystallized as tetragonal β-Sn. As evident from the diffraction patterns in Fig. 3.4.1, the crystallization pathways differed between the precursors. The intensity ratios between the different Bragg peaks (for example 2 0 0 and 1 0 1 in $SnCl_2$) suggest differences in the crystal shapes, more marked between the deposits obtained from $SnCl_2$ than in the other cases.

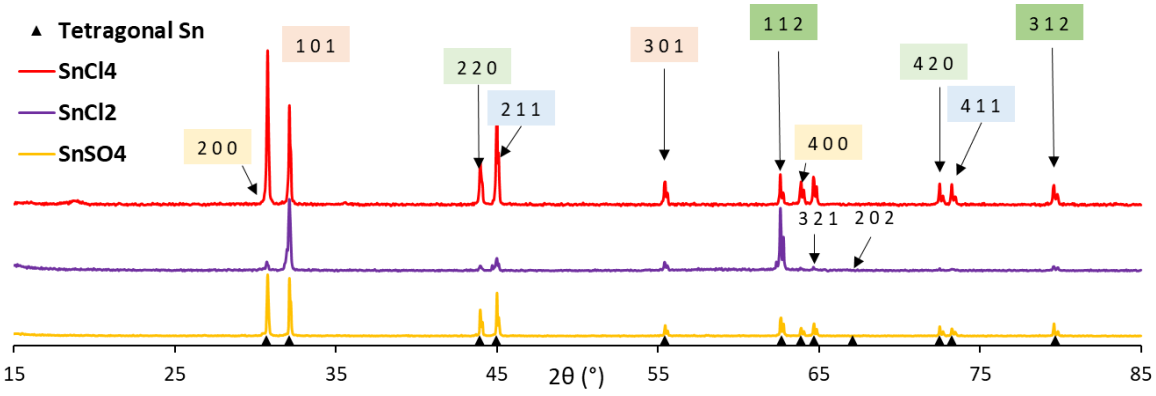

Figure 3.4.1 – XRD patterns of electrodeposited tin obtained from different precursors, with the expected reflections for tetragonal tin.

According to HRTEM + SAED data already reported in literature, [1] the 2D Sn deposits grow preferentially along the directions normal to the {2 2 0} planes. Therefore, when 2D Sn deposits grow layer-by-layer on the electrode surface, the reflections from the {2 2 0} planes (and from the 2 0 0, which lies in a parallel plane) are not collected, or drop in intensity. The same paper [1] suggests that the formation of perfectly two-dimensional dendrites with growth of primary branches perpendicular to a main stem is possible in a tetragonal crystal structure, since the (2 2 0) and (-2 2 0) planes are in one plane and normal to each other (Fig. 3.4.2).

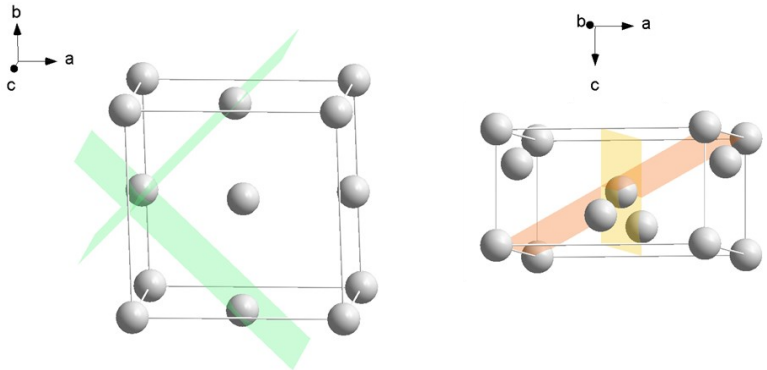

Figure 3.4.2 – Crystallographic planes in the unit cell of tetragonal tin. 2 2 0 and -2 2 0 (left, green), 2 0 0 (light orange, right) and 1 0 1 (dark orange, right)

SEM images (Fig. 3.4.3) show that in all cases, primary branches develop from a main stem. However, when $SnSO_4$ is reduced, the primary branches are very little defined and grown. The main stem grew much longer (tens or hundreds of microns) when $SnCl_2$ was employed and long, orthogonal primary branches are formed with good regularity in an overall 2D structure. The faster growth rate of the crystals could also be visible at bare eye: the deposits obtained from $SnCl_2$ were in higher amount, with the same duration of the process. A third morphology was obtained when $SnCl_4$ was chosen as precursor salt: leaf-like deposits were obtained with main stems of 10-20 μm, orthogonal primary branches and even secondary branches developing orthogonally to primary branches, resulting in 3D particles.

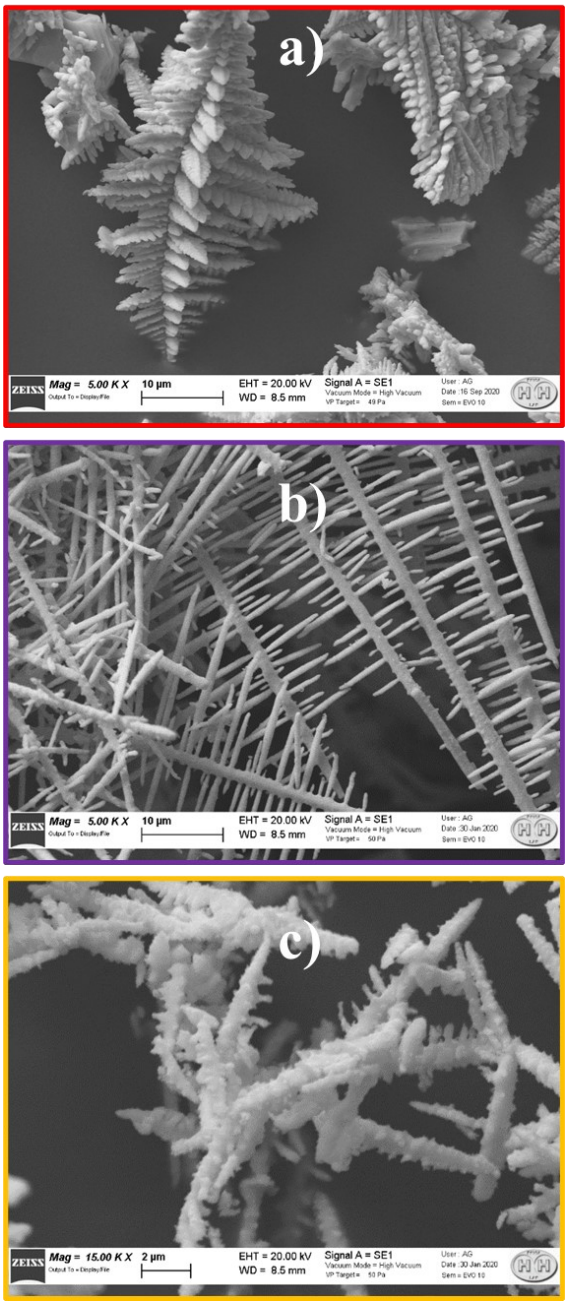

Figure 3.4.3 – SEM images of the electrodeposits obtained from a) $SnCl_4$, b) $SnCl_2$ and c) $SnSO_4$

The different resulting morphologies can be explained on the basis of the coordination environment of Sn cations: the sulphate anion (SO_4^{2-}) has weak coordinative strength on Sn^{2+}, meaning that in the $SnSO_4$ solution, tin is present as aquaion. In the other solutions instead, Sn-Cl species are found, with a higher coordinative strength. The experimental results seem to suggest that employing $SnCl_2$ favours the formation of 2D dendrites without the need for additives (such as coumarin) that is needed for tin sulphate. Also, the different coordination of Sn and the multi-step reduction of $SnCl_4$ affect the formation of deposits, preventing the formation of 2D dendrites and decreasing the growth rate.

Electrochemical results

All the results below are related to the most interesting sample, which is the tin electrodeposited from $SnCl_2$.

In the Sn-Na phase diagram, multiple phases can be electrochemically obtained after sodiation of tin metal, up to $Na_{15}Sn_4$ (Na:Sn ratio of 3.75). As a result, the voltammograms of tin-based electrodes (Fig. 3.4.4) are quite complex, with a multitude of cathodic peaks that are quite overlapped from 1 V downwards. The highest redox peak is found at the low-end voltages, corresponding to the formation of the terminal phase $Na_{15}Sn_4$, while the previous redox peaks can be ascribed to Na-Sn alloys with lower sodium content. The anodic peaks are significantly less intense and shifted in voltage, showing that the reaction is partially irreversible and kinetically hard. The shape of the following cycles and the huge decrease in the intensities confirm the lack of reversibility of the alloying-dealloying reactions.

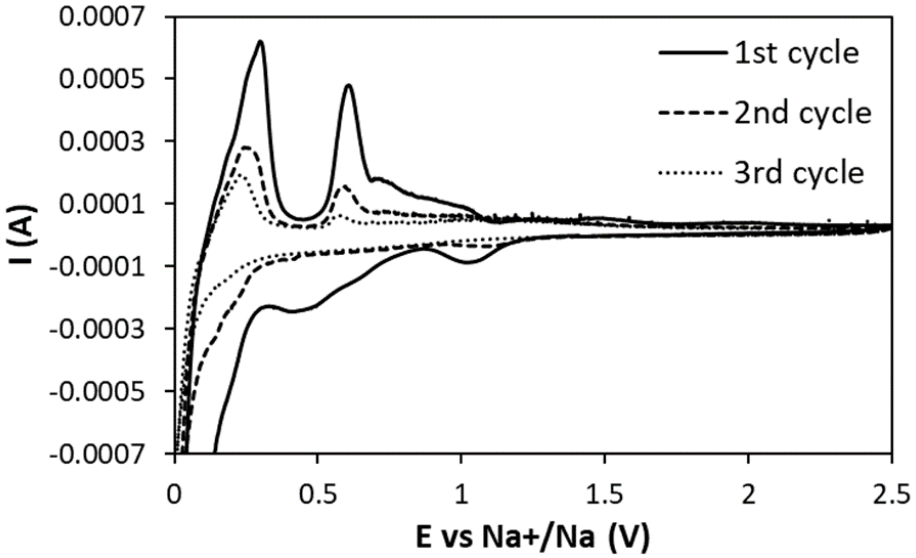

Figure 3.4.4 – First three cycles of cyclic voltammetry for Sn electrodeposits obtained from $SnCl_2$

The same lack of reversibility was recorded in the galvanostatic cycling (Fig. 3.4.5): after a good reactivity in the first discharge (theoretical capacity of 847 mAh/g), the following cycles are characterized by very low capacities, that decrease over time. In the rate capability test, the capacity does not decrease significantly at different C-rates, but the values are very low since 0.1C. The coulombic efficiencies reach quite good values only after ten cycles, and even at higher C-rates they do not exceed 97%. A constant decrease of the capacity is detected in the long-term test, where the coulombic efficiency reaches 98% after a hundred cycles, but the corresponding capacities are too low for being considered interesting. The main issue recorded in both cases is the first cycle coulombic efficiency, that is as low as 49%. This causes all the later cycles to have a huge drop in the capacity, which is even enhanced by the fact that the coulombic efficiency is still low for ten more cycles.

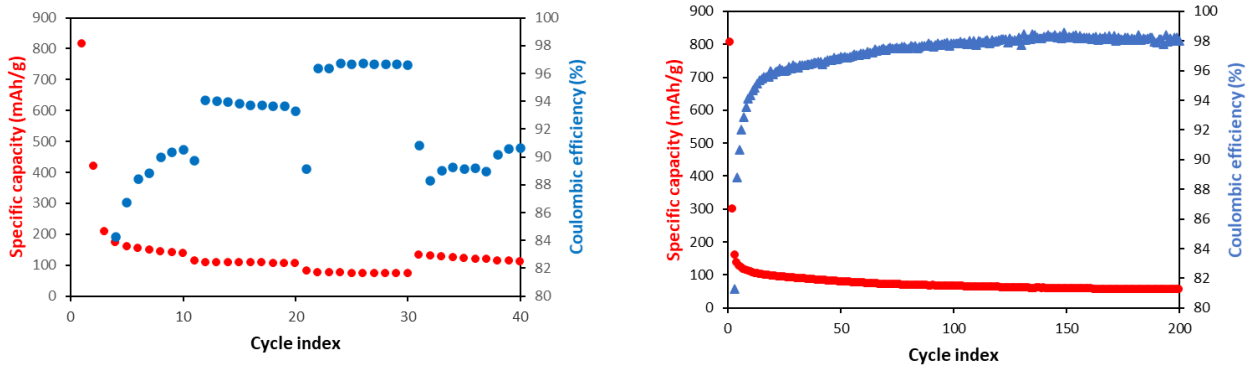

Figure 3.4.5 – Galvanostatic cycling of the Sn electrodeposits obtained from SnCl2. Rate capability test (left) at 0.1, 0.2, 0.5 and 0.1C, together with long term stability test (right) at 0.5C, after a first cycle at 0.1C. Coulombic efficiency is also reported on the right vertical axis.

As a consequence, a first attempt was to perform the galvanostatic cycling in a restricted voltage range, in order to have a better trade-off between capacity and reversibility: even if the theoretical capacity is expected to decrease (from Sn to Na_3Sn provides 80% of the theoretical capacity, equal to 676 mAh/g), the reversibility of the reaction is expected to increase thanks to the lack of a phase transformation (Na_3Sn to $Na_{3.75}Sn$). The corresponding results (Fig. 3.4.6) suggest that the main problem associated with the irreversibility of the reaction does not involve the discharge step: regardless of the discharge state, the first cycle coulombic efficiency is incredibly low (46%), and the capacities decrease without corresponding increase in the reversibility.

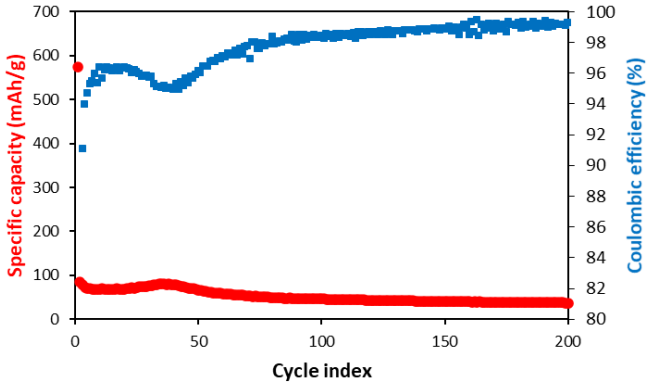

Figure 3.4.6 – Long term stability test of the Sn electrodeposits obtained from $SnCl_2$ performed at 0.5C, after a first cycle at 0.1C, in the voltage range from 0.1 to 2.5 V

A parallel attempt was to add 5% FEC to the electrolyte, keeping the extended voltage range down to 0.01 V (Fig. 3.4.7). The addition of fluoroethylene carbonate (FEC) can improve the cycling performance by forming high-quality SEI films and reduce the irreversible Na^+ exhaustion during cycling. Even though FEC has a positive effect on nano-sized particles, a rapid capacity fade was observed in the electrodeposited Sn-based electrodes. Cracks are caused by the huge volumetric expansion of Sn, and in micron-sized particles this leads to pulverization and continuous SEI formation on the newly exposed surfaces. As a result, the protection mechanism of high quality SEI is invalid in microparticles.

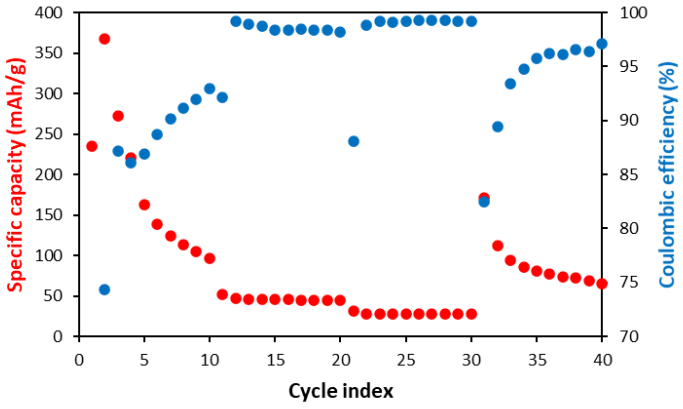

Figure 3.4.7 – Rate capability test of the Sn electrodeposits obtained from $SnCl_2$ performed at 0.1, 0.2, 0.5 and 0.1C with the addition of FEC to the electrolyte.

The reasons of the failure

The main cause of the failure of Sn-based electrodes seems to be related to the particle size: in this kind of electrochemical systems, micron-sized particles are associated with a lot of irreversibility, since the diffusion time of ions depends on the square of the diffusion distance. Also, micron-sized particles often detach from the electrode surface, resulting in unrecoverable capacity fading.

Post-mortem SEM images (Fig. 3.4.8) show that the particles of active material are quite big, and not well incorporated in the conductive carbon matrix. This is again a consequence of the particle size, which prevents a proper dispersion of the active material in the electrode slurry. Further, some residuals of chlorine that are not detected in the X-ray patterns are responsible for the degradation of the current collector and form flower-like particles of $CuCl_2$ that cover some portions of the surface of Cu.

The loss of morphology of the active material is also observed with SE and BSE detectors: the well-defined main stem with primary branches is still visible after cycling, but was damaged by the volumetric changes upon sodiation.

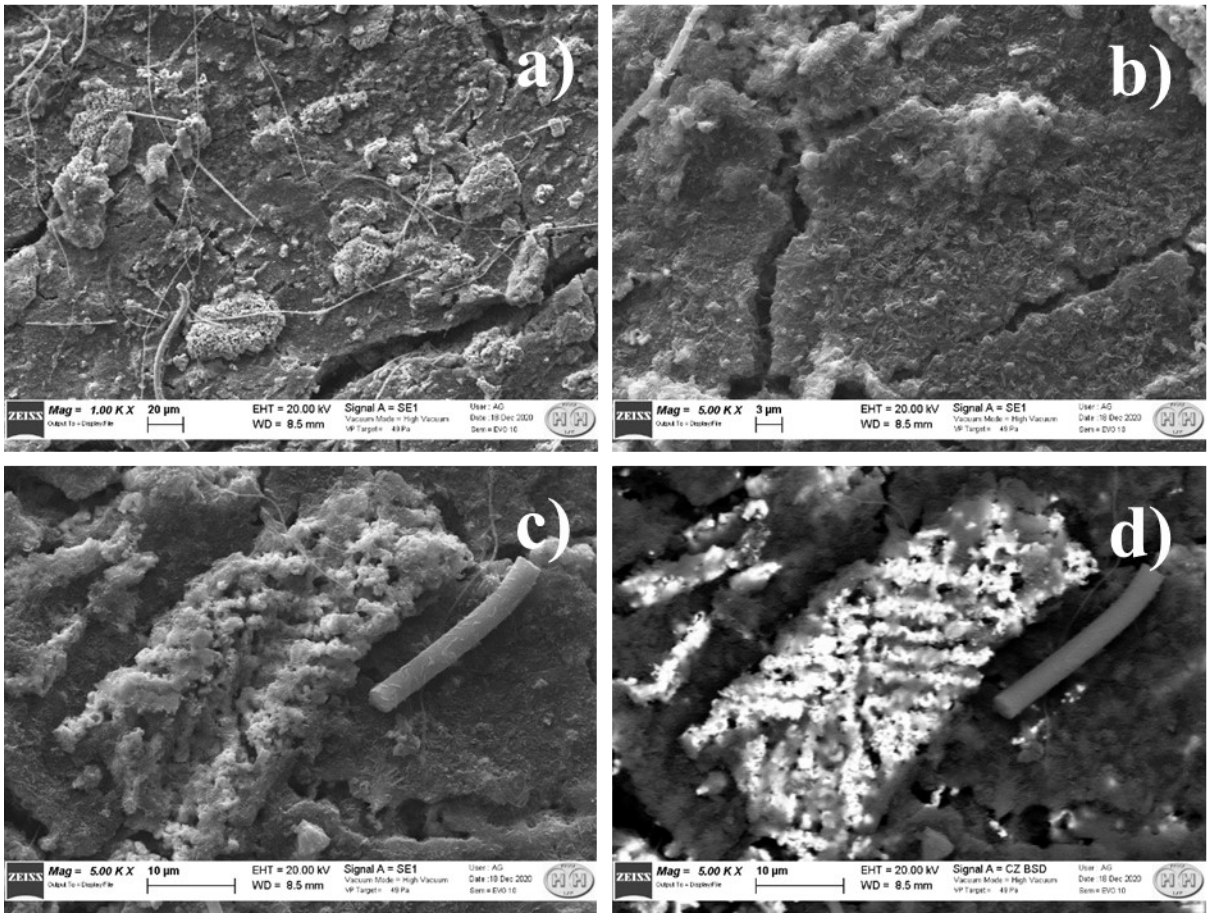

Figure 3.4.8 – Post-mortem SEM images of the electrodes at low magnification (a-b) and detailed region with a tin particle observed with secondary electrons (c) and back-scattered electronds (d)

Perspectives

Since the available electrodes and instrumentation for the electrodeposition process offered limited possibilities, the control over the electrodeposits was not enough for a detailed study. Future studies could deepen the control over particle size, implementing some additives (such as coumarin), that could 1) reduce the diameter of hydrogen bubbles formed during electrodeposition, resulting in a higher density of nano-branches and 2) suppress the formation of Sn branches in the vertical direction, making them bi-dimensional in all the cases. Also, the behaviour of the electrodeposits obtained from other salts could be explored.

From an electrochemical perspective, more experiments involving different binding agents, electrolytes (with or without additives) could improve the performance of these systems.

SnOx/C in NIBs

As mentioned in the introduction, tin and tin oxides can react with both lithium and sodium. Since the parallel work on tin-carbon composites produced interesting results in LIBs, the most interesting sample was subjected to an explorative rate capability test in NIBs (Fig. 3.4.9). The discharge capacities are much lower than the corresponding ones in LIBs, demonstrating how challenging the studies on NIBs are. The reactivity of the tin-carbon electrospun self-standing composite is barely better than the corresponding electrode prepared with a conventional slurry from micron-sized particles. The coulombic efficiencies are higher, with values higher than 99%, but the capacities are unsatisfactory. Since this composite showed the best performance with Lithium among the other electrospun samples, no further studies were carried out on the topic.

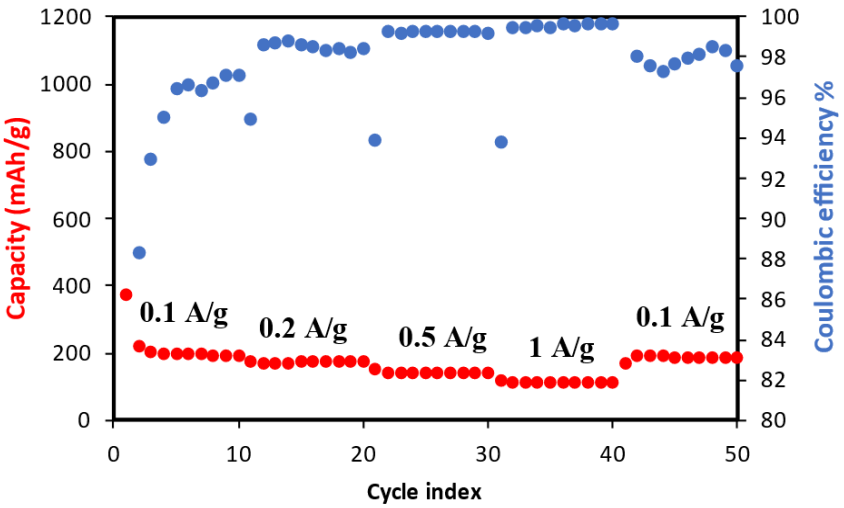

Figure 3.4.9 – Rate capability test performed on the SnOx/C – S sample, at different current densities.

$FeNb_{11}O_{29}$ in NIBs

Niobium oxides are interesting anode materials also in NIBs. T-Nb_2O_5 exhibits interesting energy storage properties in both LIBs and NIBs. Even if the kinetics of its charge storage are not as favourable as for Li intercalation (some pseudocapacitive contribution is still detected), the large interplanar spacing of 3.9 Å for the (0 0 1) planes in T-Nb_2O_5 could accommodate a certain amount of sodium. The redox couple Nb^{5+}/Nb^{4+} was determined to be reversible, whereas Nb^{2+} is irreversibly formed in the first discharge. [2]

The electrochemical properties of $FeNb_{11}O_{29}$ in LIBs are known since 2014, [3] but no reports about NIBs are found in literature. To this aim, we performed a first explorative cyclic voltammetry experiment (Fig. 3.4.10) in a suitable voltage range, comparable to the corresponding often explored in LIBs. We decided to extend the range to the lower-end, expecting an overvoltage associated with the diffusion of a bigger ion. This first experiment provided interesting results, such as a non-zero current detected at both voltage ends. A lot of irreversibility was already hypothesized from the difference between cathodic and anodic intensities, and the absence of an anodic peak in correspondence of the main cathodic peak at 0.75 V.

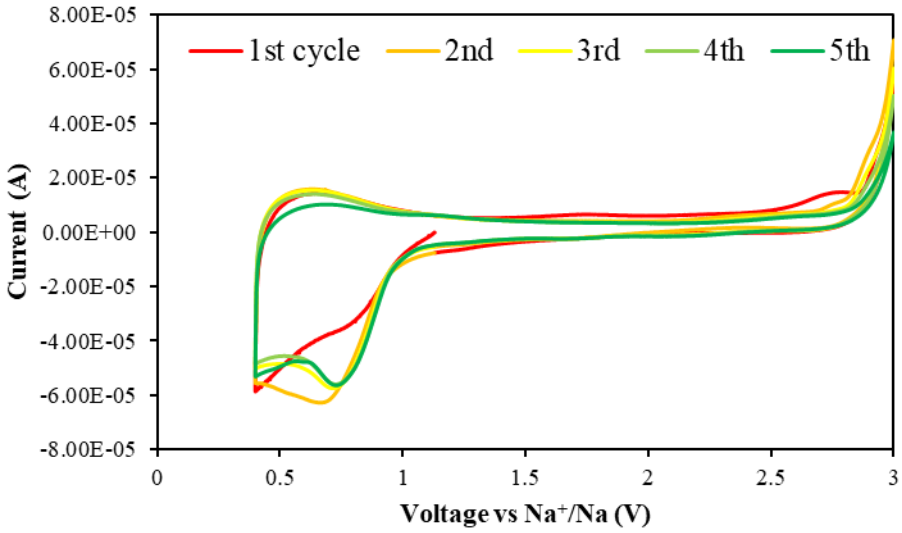

Figure 3.4.10 – Explorative cyclic voltammetry of $FeNb_{11}O_{29}$ in the range from 0.4 to 3 V.

In order to explore the residual current at 3 V, we performed another cyclic voltammetry experiment up to 4 V (Fig. 3.4.11), but the only detected reaction was the irreversible electrolyte oxidation, starting at 3 V. As a consequence we performed the following experiment at lower voltages in the range from 0.01 to 2.5 V. In this case, a huge first cycle irreversibility was detected from a peak centred at 0.5 V (ascribed to irreversible redox reactions involving Nb^{5+} and/or SEI formation), and another main redox peak at the low-end voltage, which can be attributed to electroplating of Sodium metal on the anode surface. The lack of reversibility can be inferred from the anodic scan, which shows the oxidation of the surface electroplated Na and a flat profile.

These hints prevented further investigation on the topic, and the main reason seems to be intrinsic to the structure of $FeNb_{11}O_{29}$: the channels for Li^+ diffusion are not big enough for Na^+ diffusion. As a consequence, the little amount of intercalated Sodium is not reversibly released during the oxidative scan, making the material useless for Sodium-Ion Batteries.

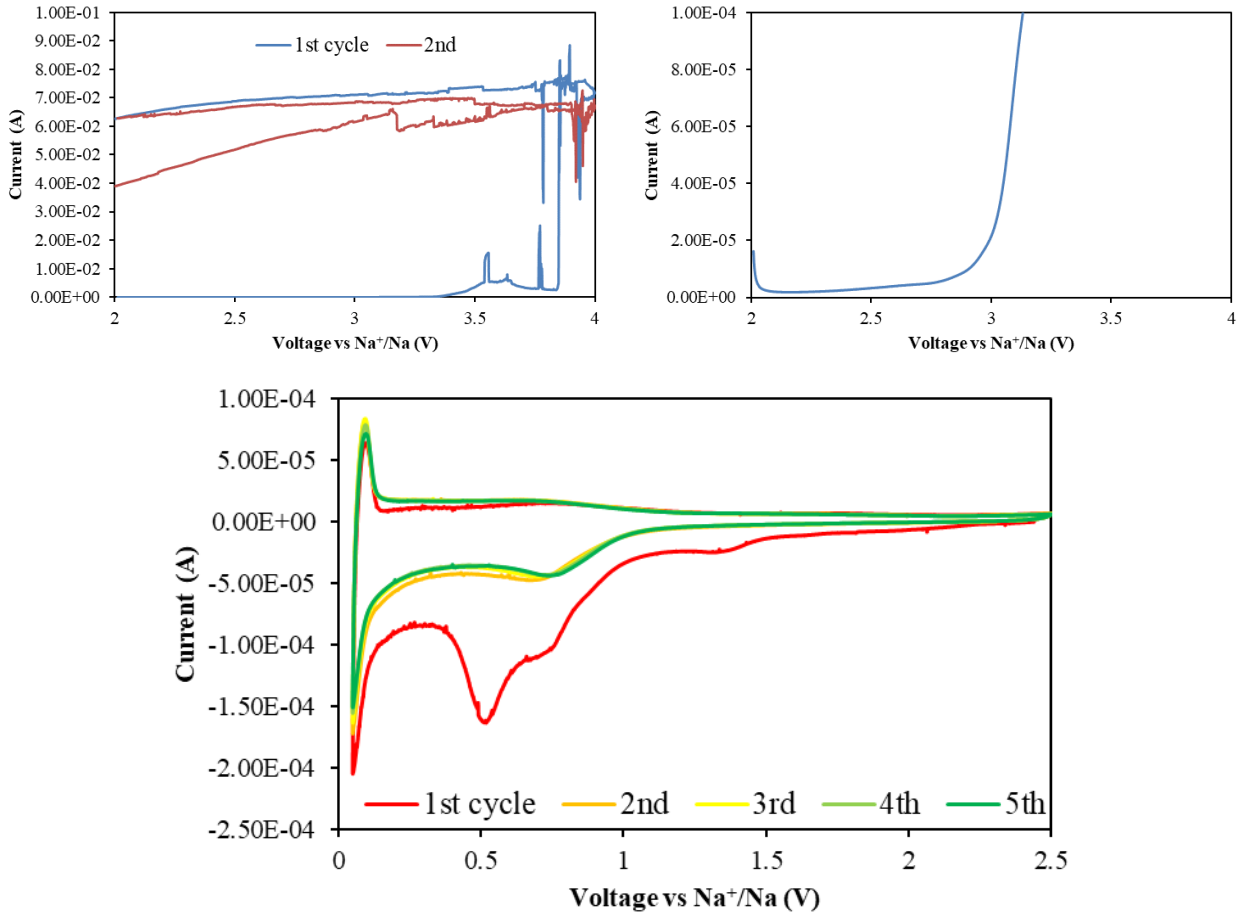

Figure 3.4.11 – High-voltage (above) and low-voltage (down) extensions of the previous voltammograms.

Conclusion

In conclusion, tin was successfully electrodeposited from different precursor salts, obtaining peculiar morphologies and no secondary phases. The performance of the electrodeposits in Sodium-ion batteries were studied, finding a good first cycle reactivity but a significant irreversibility in the following cycles. Following the results of some experiments, the main issue seems to be the de-alloying process of micron-sized particles, that causes loss of morphology and, likely, capacity loss due to pulverization. Discouraging performance was obtained from the iron niobate and the tin-carbon composite previously tested in lithium-ion batteries, finding irreversible reactions with sodium ions.

References

[1] T. H. Kim *et al.*, "One-step synthesis of multilayered 2D Sn nanodendrites as a high-performance anode material for Na-ion batteries," *J. Mater. Chem. A*, vol. 5, no. 38, pp. 20304–20315, 2017.

[2] Q. Deng, Y. Fu, C. Zhu, and Y. Yu, "Niobium-Based Oxides Toward Advanced Electrochemical Energy Storage: Recent Advances and Challenges," *Small*, vol. 1804884, pp. 1–26, 2019.

[3] I. Pinus, M. Catti, R. Ruffo, M. M. Salamone, and C. M. Mari, "Neutron diffraction and electrochemical study of FeNb11O29/Li11FeNb11O29 for lithium battery anode applications," *Chem. Mater.*, vol. 26, pp. 2203–2209, 2014.

4. Conclusions and perspectives

During the 3 years of PhD, the complex world of anode materials for Lithium-ion batteries and Sodium-ion batteries was investigated with a combined materials science-electrochemistry approach. A variety of synthetic pathways was explored, and the most important structural/morphological features of every material were studied alongside the resulting electrochemical properties. This approach led to collaborations with multiple departments of different Universities throughout Italy. A milestone of this thesis project was the setting of the beamline XRD1 (at the Italian synchrotron Elettra, Trieste) to perform *operando* X-ray diffraction measurements, never realized before, and now available in Italy for the entire academic community. Moreover, *in situ* Raman measurements on electrode materials were performed for the first time at the University of Pavia, in collaboration with the Department of Physics.

The materials studied in this thesis offer interesting alternatives to the anode materials currently employed in present batteries, since changing the chemistry of electrode materials offers a range of possibilities:

- employing mixed Ternary Transition Metal Oxides such as $ZnFe_2O_4$ or alloying materials such as Sn helps improve the charge storage capability of the batteries, that can power devices for longer times, or help designing lighter or smaller devices. In terms of electric vehicles, this increase in the energy density would be translated as longer travels between recharges.
- Employing carbon composites (SnOx/C) or pseudocapacitive materials (niobium oxides), can at the same time improve the power density, meaning that electric cars powered in such a way could travel faster or carry heavier loads.

The interesting reactivity of $ZnFe_2O_4$ towards Lithium was investigated with operando X-ray diffraction and multiple electrochemical techniques, confirming the theorized reaction mechanism of conversion-alloying and directly observing the irreversibility associated with the conversion reaction. Side reactions that contribute significantly to the total capacity were inferred and the implications of morphology and crystallinity on the short- and long-term performance were discussed. These findings can help tailoring the synthetic conditions in order to obtain better performance in the future.

Electrospun tin-carbon composites (SnOx/C) with homogeneous distribution tin in a matrix of well-interconnected turbostratic carbon nanofibers showed promising results: the self-standing sample exhibited positive kinetic features (high extrinsic pseudocapacitive contribution) with stable and high capacities recorded at a high current density (0.5 A/g). The production of self-standing electrodes is scalable and outperforms the corresponding electrodes prepared from powders by hundreds of mAh/g, over hundreds of cycles, resulting in a promising candidate for high power and energy density Lithium-ion batteries.

$FeNb_{11}O_{29}$ has peculiar structural features, which were studied for both the monoclinic and the orthorhombic polymorph alongside its electrochemical behaviour. Fe^{3+} cations were determined to be disordered over multiple crystallographic sites, affecting the magnetic properties of the material.

Operando X-ray diffraction combined with in situ Raman spectroscopy allowed to unravel the key point of the lithium intercalation reaction into $FeNb_{11}O_{29}$: second-order Jahn-Teller octahedral distortions are alleviated when Nb^{5+} cations are electrochemically reduced, resulting in a symmetrisation of the structure that undergoes a displacive phase transition when the cation-cation repulsion over shear planes is decreased by lithiation. This phase transition was determined to be reversible and not limiting for the high-rate performance of the material. A detailed model for Lithium intercalation was provided and the implications of having different Li sites in the structure were discussed alongside the characterization of the corresponding charge-transfer reactions, that clearly showed the promising electrochemical features of this oxide. Its intrinsic pseudocapacitive features make $FeNb_{11}O_{29}$ a valid alternative to conventional electrode materials.

Sn was electrodeposited from different precursor salts, resulting in crystalline tin with peculiar morphologies. The corresponding reactivity obtained from the electrodes tested in Sodium-ion batteries was unsatisfactory: after a high capacity during the first discharge, the capacity dropped to discouraging values. The reasons behind this failure seem to be related to the particle size, which could not be controlled in detail. Future studies on the topic could lead to the discovery of an ambient temperature, scalable and fast way to produce high-performance electrode materials for Sodium-ion batteries.

In conclusion, multiple materials possessing unique electrochemical features were studied in detail, showing the importance of the combination of experimental techniques, obtaining fundamental information and promising performance that brought the knowledge of the scientific community a little further towards a more efficient electrochemical energy storage.